2013-03-30

An Investigation into Ground Moving Target Indication (GMTI) Using a Single-Channel Synthetic Aperture Radar (SAR)

Joseph W. Winkler
Brigham Young University - Provo

An Investigation into Ground Moving Target Indication (GMTI) Using a Single-Channel Synthetic Aperture Radar (SAR)

Joseph W. Winkler

A thesis submitted to the faculty of
Brigham Young University
in partial fulfillment of the requirements for the degree of

Master of Science

David G. Long, Chair
Richard W. Christiansen
Brian D. Jeffs

Department of Electrical and Computer Engineering

Brigham Young University

March 2013

ABSTRACT

An Investigation into Ground Moving Target Indication (GMTI) Using a Single-Channel Synthetic Aperture Radar (SAR)

Joseph W. Winkler
Department of Electrical and Computer Engineering, BYU
Master of Science

Synthetic aperture radar (SAR) was originally designed as an airborne ground-imaging radar technology. But it has long been desired to also be able to use SAR imaging systems to detect, locate, and track moving ground targets, a process called Ground Moving Target Indication (GMTI). Unfortunately, due to the nature of how SAR works, it is inherently poorly suited to the task of GMTI. SAR only focuses targets and image features that remain stationary during the data collection. A moving ground target therefore does not focus in a conventional SAR image, which complicates the process of performing GMTI with SAR systems.

This thesis investigates the feasibility of performing GMTI with single-channel, unsquinted, broadside stripmap SAR despite this inherent limitation. This study focuses solely on the idealized case of direct energy returns from point targets on flat ground, where they and the airborne radar platform all move rectilinearly with constant speed.

First, the various aspects of how SAR works, the signal processing used to collect the SAR data, and the backprojection image formation algorithm are explained. The effects of target motion are described and illustrated in actual and simulated SAR images. It is shown how the backprojection (BPJ) algorithm, typically used to image a stationary landscape scene, can also focus on moving targets when the target motion is known *a priori*. A SAR BPJ ambiguity function is also derived and presented.

Next, the time-changing geometry between the airborne radar and a ground target is mathematically analyzed, and it is shown that the slant range between the radar and any ground target, moving or stationary, is a hyperbolic function of time. It is then shown that this hyperbolic range history causes the single-channel SAR GMTI problem to be underdetermined.

Finally, a method is then presented for resolving the underdetermined nature of the problem. This is done by constraining a target's GMTI solution using contextual information in the SAR image. Using constraining information, a theoretical way is presented to perform limited GMTI with a single-channel SAR system by using a modified form of the BPJ imaging algorithm, and practical considerations are addressed that complicate the process. Instead of focusing on stationary pixels, this GMTI method uses the BPJ ambiguity function to search for moving targets on a straight path, such as a road, by performing matched filtering on a collection of moving pixels in a position-velocity image space. Nevertheless, it is concluded that for moving point targets, general GMTI with no path constraints is infeasible in practice with a single-channel SAR.

Keywords: SAR, GMTI, hyperbola, backprojection, ambiguity function, matched filter

ACKNOWLEDGMENTS

First and foremost I want to thank Dr. David G. Long for recognizing my potential and making this research opportunity available to me, and for mentoring me in the ways of SAR. You were not only my graduate advisor, but also a good friend. You helped me wrap my mind around difficult concepts and clear muddy waters where needed. I also want to thank you for giving me this interesting research problem, and I feel lucky to have landed this particular research topic since I was the only one in your group to work on it. And I feel especially lucky to have had you as my advisor. You are the reason BYU is one of the top radar schools in the country.

I want to thank Space Dynamics Laboratory for funding my research and making it possible. I also want to thank Scott A. Anderson and Chad Knight in particular for bringing me out to Logan for a summer internship, and for everything you taught me about teamwork, project development, and working in a dynamic environment. And I want to thank you and the RASAR team for making me, a student researcher with no real-world experience at the time, feel so appreciated to be there working with you.

I want to thank my Mom. I love you very much, and I am fully aware of the sacrifices you made to be the best you could be in the face of extreme challenges during my life. You've also sacrificed to help me financially at times when I needed it most. I'm forever grateful for your love.

I also want to thank my other best friends I met at BYU. In alphabetical order by first name, I want to thank Anthony Bastian, Cameron Wright, Edwin Miller, Jessica Zeltner, Joseph Blanch, Lisa Kell, Ryan Johnson, Tania Uribe, and Todd Wight. You always made me feel appreciated. Thank you for being who you are.

TABLE OF CONTENTS

LIST OF TABLES

LIST OF FIGURES

NOMENCLATURE

*	Complex conjugation operator
^{H}	Hermitian conjugation operator
$\star$	Cross-correlation operator
a	Scale factor for real-aperture beamwidth, determined by the physical antenna shape and the phase and amplitude illuminations across it
$a(t)$	Amplitude modulation
A	Pulse transmit amplitude
A_{target}	A target vehicle's ground footprint area (m^2)
A_{cell}	Image resolution cell area (m^2), defined as $A_{cell} = \Delta R_g \cdot \Delta AZ$
AF	Ambiguity function
AGL	Above ground level
α	Scale factor that absorbs the effects of spreading loss predicted by the radar equation [Eq. (2.1)]
BPJ	Backprojection
BW	Bandwidth (Hz)
BW_D	Doppler bandwidth (Hz)
c	Speed of light (m/s)
C	Arbitrary nonzero scale factor, comes out of the matched filter derivation (mentioned, but not covered in this thesis)
$\chi(\cdot)$	Matched filter response integral, used to derive the ambiguity function
CPI	Coherent processing interval
CW	Continuous Wave
d	Along-track distance (m) flown by the SAR since the radar was turned on at time zero
D	Antenna azimuth dimension (m), referred to as simply "antenna size" for this thesis
δ	Nominal incidence angle of the radar beam on the ground, determined by the boresight look angle
δR	Apparent range error (m) induced by target Doppler shift for an LFM pulse
ΔAZ	Azimuth resolution (m)
ΔF_D	Doppler resolution (Hz)
$\Delta\phi$	Phase mismatch (rad) caused by an echo delay mismatch, defined as $\Delta\phi = \omega_0 \Delta\tau$
ΔR	Range resolution (m)
ΔR_g	Ground range resolution (m)
Δs	Linear position difference (m)
$\Delta\tau$	Echo delay mismatch (s) between an arbitrary echo and a target's true echo delay, defined as $\Delta\tau = \tau - \tau_T$
$\Delta\tau(x,y,z,n)$	Echo delay mismatch history
Δt	Time difference (s) relative to the matched filter's peak output time t_{MF}, defined as $\Delta t = t - t_{MF}$
ΔV	Velocity difference (m/s)
ΔV_x	Cross-track velocity component mismatch (m/s)
ΔV_y	Along-track velocity component mismatch (m/s)
Δx	Cross-track positional difference (m)
Δy	Along-track positional difference (m)

DBS	Doppler beam sharpening
f_0	Radar center frequency (Hz)
F_D	Doppler shift (Hz)
FT	Fourier transform
G	Antenna gain
GMTI	Ground moving target indication
GPS	Global Positioning System
h	SAR altitude AGL (m)
$h(t)$	Real matched filter's impulse response
$H(\omega)$	Fourier transform of $h(t)$
ICW	Interrupted continuous wave
IMU	Intertial measurement unit
IPR	Impulse response
j	Imaginary unit ($\sqrt{-1}$)
k_r	Frequency ramp rate for a linear frequency modulated pulse (rad/s^2)
λ	Radar wavelength (m), computed using f_0
$L_a(R)$	Range-dependent atmospheric loss
L_s	System loss
LFM	Linear frequency modulated
LOS	Line-of-sight
MF	Matched filter
N_0	Thermal noise power (W) in the matched filter
ω	Frequency (rad/s)
ω_0	Radar center frequency (rad/s)
ω_d	Doppler shift (rad/s)
ϕ	Phase shift (rad), defined as $\phi = \omega_0 \tau$
ϕ_0	Initial phase (rad) of the radar transmit pulse, ignored for this thesis
ϕ_T	Phase shift (rad) of a radar echo from a particular target of interest, defined as $\phi_T = \omega_0 \tau_T$
$\psi(t)$	Analytic radar transmit waveform
$\psi_r(t)$	Analytic received echo waveform
$\psi_0(t)$	Analytic matched filter output when the analytic radar echo $\psi_r(t)$ is applied to the analytic matched filter $z(t)$
P_t	Power transmitted (W) from the radar antenna in a single pulse
P_r	Power received (W) to the radar antenna from the radar echo
PRF	Pulse repetition frequency (pulses/s or Hz)
PRI	Pulse repetition interval (s)
R	Slant range (m)
R_g	Ground range (m)
RAR	Real-aperture radar
RC	Range compressed
RCS	Radar cross section (m^2)
RMC	Range migration curve
SAR	Synthetic aperture radar
SCR	Signal-to-clutter ratio

SNR	Signal-to-noise ratio
SCS	Single-channel SAR
σ	Radar cross section (m^2)
σ^0	Normalized radar cross section (m^2/m^2, unitless)
$s(t)$	Real radar transmit waveform
$s_r(t)$	Real received echo waveform
t	Time (s)
t_0	Time zero, when the radar turns on and data collection begins
t_{MF}	The time instant when the matched filter's output is at its maximum
τ	Echo delay (s)
τ_T	Echo delay (s) between the SAR and a particular target of interest
T	Pulse length (s)
θ	Heading relative to due north
θ_{3dB}	Mainlobe azimuth beamwidth
θ_{cone}	Cone angle
θ_N	Nadir azimuth angle
$\theta(t)$	Frequency modulation
ϑ	Integration angle
$U(\omega)$	Unit step function in the frequency domain
v_{LOS}	Relative radial velocity (m/s) along the LOS between the radar and a target
v_{SAR}	SAR platform speed (m/s)
$\mathbf{v}_{SAR}$	SAR platform velocity vector
v_T	Target speed (m/s)
$\mathbf{v}_T$	Target velocity vector
W_s	Width (m) of the ground swath to be imaged
ξ	Dummy variable used in the matched filter derivation
x	Cross-track distance (m)
y	Along-track distance (m)
$z(t)$	Analytic matched filter impulse response
$Z(\omega)$	Fourier transform of $z(t)$
ZD	Zero-Doppler

CHAPTER 1. INTRODUCTION

Synthetic aperture radar (SAR) is a coherent side-looking imaging radar technology capable of producing near-photographic quality images of a ground scene in any weather or lighting conditions. The radar antenna is typically carried on an airplane or a satellite, scans the ground, and produces an image with resolution much finer than what a real-aperture radar can achieve. Figures 1.1 and 1.2 are examples of modern SAR imagery produced by Sandia National Laboratories.

SAR differs from real-aperture radar by the size of the antenna used and how the data is processed to form an image. To obtain fine image resolution with a real-aperture radar, a single large antenna (or array of antennas) must be used to produce a narrow beamwidth. The difference with SAR is that, due to size and weight limitations for airborne and spaceborne applications, a small antenna is used. By itself, a small antenna is incapable of high-resolution imagery because of its inherently wide beamwidth. But SAR resolves this issue by using the small antenna to take radar measurements from many points in space at regular time intervals along the radar platform's flight path, essentially mimicking the functionality of a long linear phased antenna array.

This method of synthesizing a large radar aperture produces a very narrow synthetic beamwidth [1–5]. By proper signal and data processing, SAR achieves much finer image resolution than the physical antenna size suggests based on conventional antenna theory. The most remarkable and counterintuitive key fact about SAR is that the lower bound on image azimuth resolution is equal to half the physical antenna's azimuth dimension, regardless of the distance to the target [1–4, 6–11].

However, this extreme enhancement in image resolution comes at a price in terms of system complexity and sensitivity to how cooperative the ground scene is during the radar scan. In a real antenna or phased array, all antenna elements record data simultaneously, while a SAR system must sample each element position sequentially in time as the platform moves, and then process the data. Flying the synthetic aperture requires time, sometimes as much as tens of seconds. If any part of the ground scene being imaged changes during the scan time, that part of the image may

defocus in proportion to the severity of the change. For this reason, SAR was originally designed to image stationary ground scenes [1, 2, 12, 13].

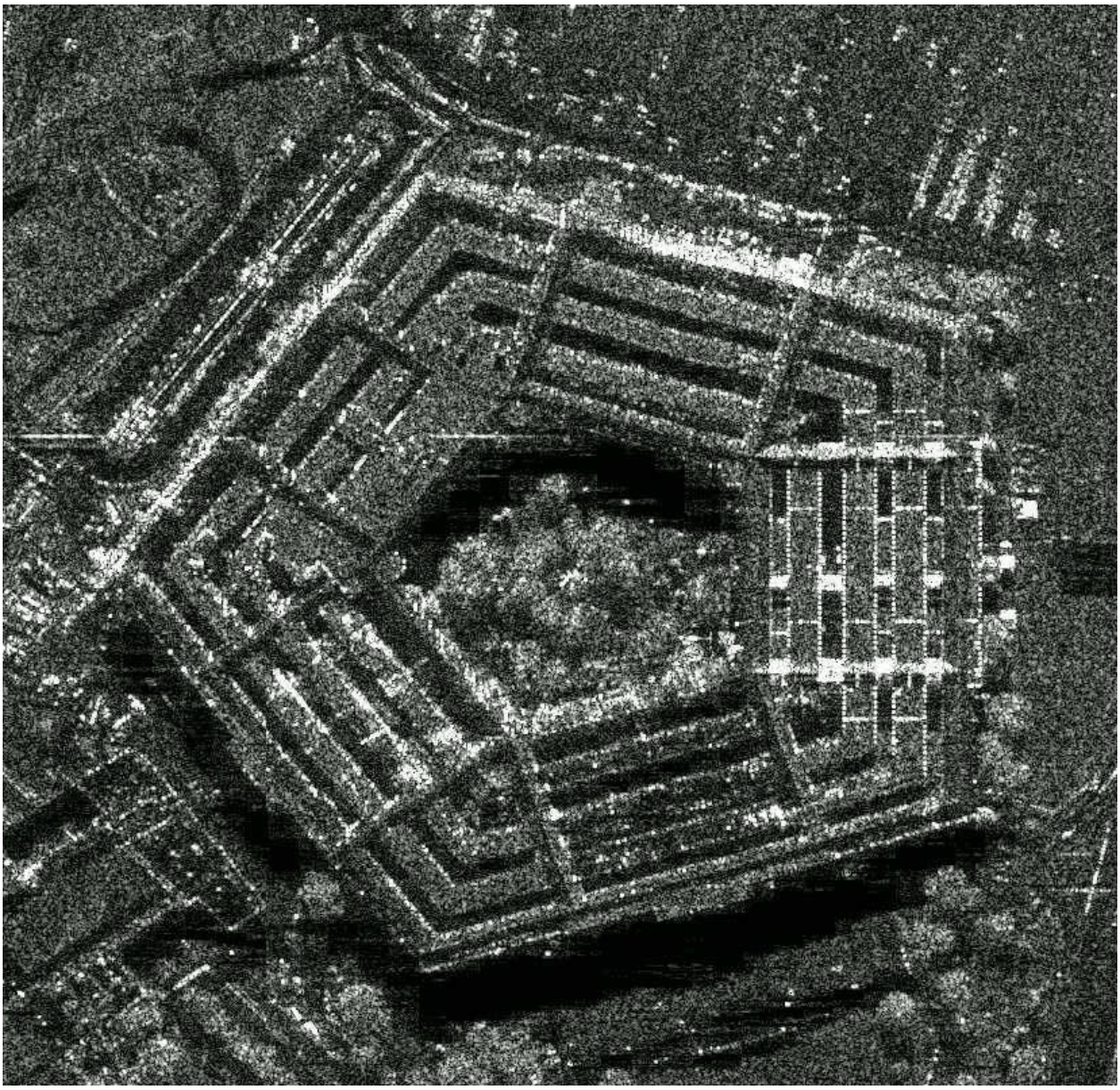

Figure 1.1: Ku-band SAR image of the Pentagon in Washington, D.C. (Courtesy Sandia National Laboratories)

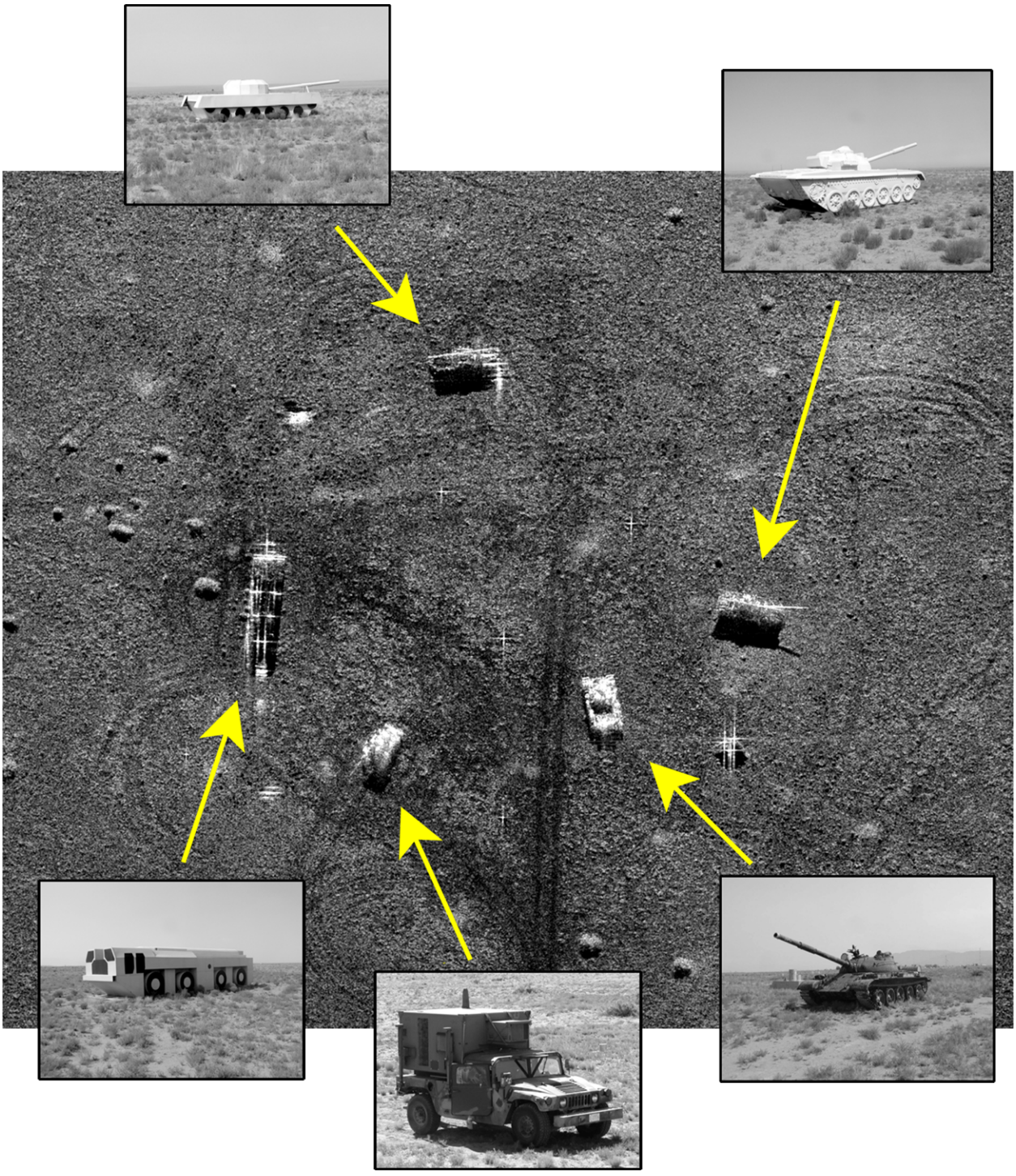

Figure 1.2: Ka-band SAR image of military ground targets. (Courtesy Sandia National Laboratories)

As an all-weather day/night imaging technology, and because of its ability to create high-resolution imagery from a long standoff range, SAR has been widely used for various military purposes, including surveillance and reconnaissance [1]. But the military is understandably interested in also being able to detect, locate, and track moving targets on the ground, a process called ground moving target indication (GMTI).

Normally, specialized multi-channel radars designed for GMTI are used; however, due to lower costs and higher availability, there is a great deal of interest in using conventional single-channel SAR to perform GMTI. The biggest drawback to this desire is that it collides with the fundamental limitation of SAR as described previously in this chapter: the ground scene must remain stationary during the scan time to focus the image correctly. SAR GMTI has been, and still is, an area of intensive research, especially in the past decade or so. In practice, GMTI has been successfully performed with multi-channel SAR systems [13–41].

1.1 Problem Statement

Despite the success with multi-channel SAR systems, there exists a great desire to perform GMTI with single-channel SARs. This is due to reduced cost, simpler hardware and system design, and because so many single-channel SARs already exist. If GMTI can be performed with a single-channel SAR, it would probably be much simpler and less expensive than specialized systems.

1.2 Thesis Statement

This thesis investigates the fundamental feasibility and practicality of performing GMTI on moving point targets using a single-channel widebeam pulsed SAR system in the unsquinted broadside stripmap mode. This thesis assumes the radar platform and ground targets to move in straight lines with constant speeds. All references to radar or target motion assume this ideal simple motion.

I approach the problem by mathematically analyzing the geometry of a broadside stripmap SAR data collection, depicted in Fig. 1.3, with point targets present in the illuminated ground swath. Specifically, I analyze the range history of a point target during a SAR data collection. Range history refers to how the line-of-sight (LOS) distance, or *slant range*, changes over time

between the radar and target. I then use the results of the range history analysis to attempt to solve for the unique target motion that must have produced that range history. I show that this process cannot uniquely identify the target's GMTI solution. Instead, it produces a solution space containing infinitely many GMTI solutions with the identical same range history. This highlights a fundamental need to constrain the target solution when attempting to use a single-channel SAR to perform GMTI. I then develop a limited GMTI method based on applying path constraints to moving targets in the data, and then detecting them and estimating their GMTI solutions using a search scheme based on the backprojection algorithm.

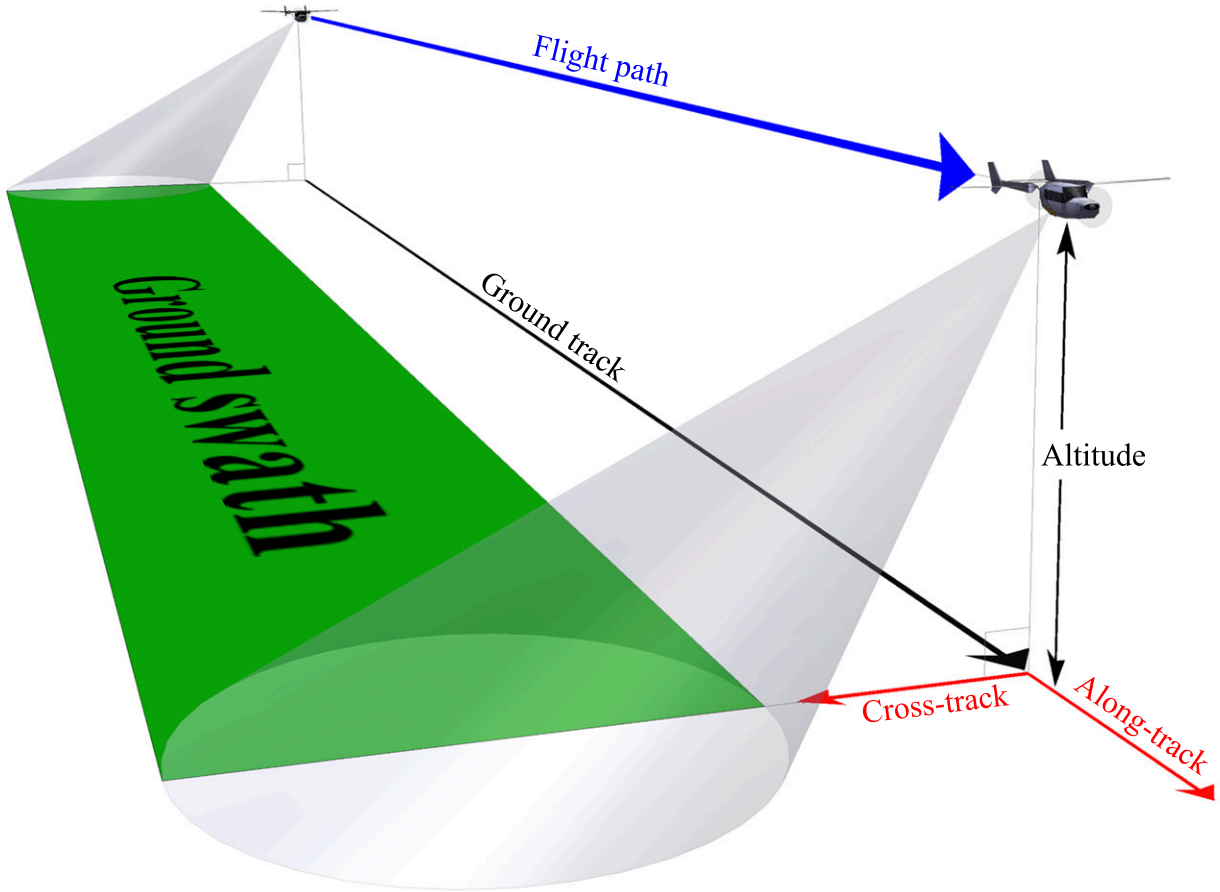

Figure 1.3: A broadside stripmap SAR data collection.

1.3 Results and Conclusions

It is shown that as the radar flies past a ground target, the slant range between them varies as a hyperbolic function of time, for both stationary and moving targets. It is further shown that this hyperbolic range history leads to inherent ambiguities in the SAR data concerning the ability to recover information about the target's initial position and its velocity vector. This leads to the conclusion that without additional outside information about the target, a single-channel SAR system is ill-suited to perform GMTI.

However, in spite of this conclusion, I develop a method that can theoretically enable a single-channel SAR to perform limited GMTI, *if* proper constraints are applied to the target's possible motion. The method works only if the target can be assumed to travel a constrained path within a specified range of speeds. The best way I have found to constrain a target's path is to look for straight roads in the SAR image and use their positions and orientations as the path constraints, with each road searched individually. This method makes use of the backprojection image formation algorithm to perform matched filtering on a set of pixels that move along the constrained path with different speeds and initial positions. It is shown that if the target's path assumption is correct, then the target's true GMTI solution can be found with this method. Without these constraints, it is concluded that a single-channel SAR, by itself, cannot feasibly perform general GMTI in practice based on direct energy returns from a target.

1.4 Thesis Outline

This thesis is organized as follows: Chapter 2 gives technical background on how SAR works and how SAR images are formed. It describes the radar geometry, the pulse waveform, and the signal processing used to collect and store the SAR data. It describes the structure of the stored SAR data, and it describes the backprojection image formation algorithm used in my research. The SAR impulse response is discussed, as well as the unique and important relationship between antenna size and azimuth resolution for SAR

Chapter 3 describes and illustrates he defocusing effects of target motion in SAR imagery using actual and simulated SAR images. It is also shown how backprojection, which is normally

used to image stationary ground scenes, can focus on a moving ground target when the target's motion is known *a priori*.

Chapter 4 derives and presents an ambiguity function for SAR backprojection that I developed. It shows that conventional SAR images of point targets in noise- and clutter-free environments are a subset of the family of BPJ ambiguity functions. The backprojection ambiguity function is the tool I use to perform single-channel SAR (SCS) GMTI according to the method presented in Chapter 6.

Chapter 5 describes the mathematical analysis I did to study the SCS-GMTI problem. It proves that the range history between the SAR and any target, whether moving or stationary, is hyperbolic. It also proves that the hyperbolic range history between the radar and a target causes the SCS-GMTI problem to be underdetermined. This is the fundamental stumbling block that makes a single-channel SAR impractical for GMTI, and highlights a need to constrain the target solution if GMTI performed with a Single-Channel SAR is to have any hope of success.

Chapter 6 describes a method I developed that can potentially resolve the underdetermined nature of the SCS-GMTI problem. This method is based on making informed assumptions about a target's likely path based on roads visible in the SAR imagery, and then searching those roads using the backprojection algorithm in a way slightly different than that for which it was originally developed. Instead of focusing on a collection of stationary pixels in an image with spatial (x, y) coordinates, it focuses on a set of moving pixels along a road in a $(\Delta s, \Delta V)$ position-velocity coordinate system.

Finally, Chapter 7 concludes that SCS-GMTI, based on direct energy returns from point targets, is likely to be infeasible in practice. This is because of not only the ambiguous and underdetermined nature of the problem, but also the restrictive conditions that must be met by the radar platform, the target, and the ground scene in order for my GMTI method to work.

Throughout this thesis, I provide many figures and images to support my explanations of SAR and my research. All simulated SAR images were produced by a SAR simulator I wrote in MatLab for my research. My simulator allows flexibility in the radar design, operational parameters, number of ground targets, target brightness, target behavior, and the location and size of the ground region to be imaged. "Radar design" refers to details such as the radar's frequency band, the signal bandwidth, the pulse length, the antenna size and beamwidth, receiver sampling rate,

transmit power, and the signal processing windows used for pulse shaping and image formation. Operational parameters include the platform altitude, flight speed, radar look angle, pulse repetition frequency, minimum and maximum recorded slant ranges, and the length of the flight track flown during data collection. Table 1.1 lists the SAR parameters I used to create the simulated SAR images in this thesis. Target brightness refers to the amount of radar energy reflected by a point target, determined by its radar cross section in m^2. Target behavior refers to a target's initial position at time zero, and its velocity vector (direction and speed).

Table 1.1: SAR simulator operational parameters and beam radiation pattern used to create the simulated SAR images in this thesis.

Parameter Name:	Value
SAR altitude:	500 m
SAR flight speed:	50 m/s
Boresight look angle:	45°
Nominal incidence angle:	45°
Center frequency:	1.5 GHz (L-band)
Bandwidth:	200 MHz
Pulse length:	2 μs
LFM Frequency ramp rate:	-10^{14} Hz/s
Chirp direction:	down
Pulse shape:	rectangular
Pulse repetition frequency:	2000 pulses/s (Hz)
Receiver sampling rate:	500 Msamples/s
Transmit power:	100 mW
Antenna gain:	15 dB
System loss:	0 dB
Atmospheric loss:	0 dB/km
Elevation beamwidth:	30°
Azimuth beamwidth:	varies from 5° to 50°
RC data interpolation factor:	≥ 16
Backprojection window shape:	rectangular

CHAPTER 2. SAR TECHNICAL BACKGROUND

According to the literature, the idea of SAR was first conceived by Carl A. Wiley [3, 42] in or around 1950 while he was working for the Goodyear Aerospace Corporation. His patent for the SAR concept is shown in Fig. 2.1. Originally, Wiley called the idea "Doppler beam sharpening" (DBS) [1, 42, 43]. In [3], C. W. Sherwin states that the basic DBS concept was to measure the time-changing Doppler shift of the radar signal as the SAR platform flew past the target scene. This enabled the DBS system to locate stationary ground targets or landscape features with azimuth resolution much better than the radar beam itself could provide based on its radiation geometry.

Although the original idea was based on Doppler analysis, it turns out that the entire process can also be described strictly in terms of the situational geometry, without considering Doppler shifting [8, 44]. Doppler analysis uses the conventional definition of a Doppler shift, which refers to the physical change in the echo's frequency as a result of relative radial motion between the radar platform and a target. The geometric interpretation considers only the time-changing distance between them, and how the phase of the echo changes from one pulse to the next as the slant range between them changes. It turns out that if the pulse repetition frequency is high enough, as discussed in Section 2.2.4, then the derivative of the pulse-to-pulse phase measurements for a target is equal to its physical Doppler shift [45]. For pulsed SAR, this enables the stop-and-hop model to be safely used in simulation and produce meaningful results [2, 8, 11, 21].

According to Wiley in [42] and Ulaby et al. in [43, 46], DBS and SAR are the exact same thing, with DBS using a Doppler analysis in the frequency domain, and SAR using a geometric analysis in the time domain. This thesis approaches the SCS-GMTI problem with the purely geometric interpretation of SAR. Unless stated otherwise, any references to Doppler effects are made with respect to the pulse-to-pulse phase change.

In [42], Wiley tells us that Sherwin and his colleagues developed the idea of focusing, which Sherwin himself describes in [3]. In a SAR context, focusing means taking into account the

No. 3,196,436

THE UNITED STATES OF AMERICA

TO ALL TO WHOM THESE PRESENTS SHALL COME:

Whereas Carl A. Wiley, of Phoenix, Arizona, assignor to Goodyear Aerospace Corporation, a corporation of Delaware,

PRESENTED TO THE Commissioner of Patents A PETITION PRAYING FOR THE GRANT OF LETTERS PATENT FOR AN ALLEGED NEW AND USEFUL INVENTION THE TITLE AND A DESCRIPTION OF WHICH ARE CONTAINED IN THE SPECIFICATION OF WHICH A COPY IS HERETO ANNEXED AND MADE A PART HEREOF, AND COMPLIED WITH THE VARIOUS REQUIREMENTS OF LAW IN SUCH CASES MADE AND PROVIDED, AND

Whereas UPON DUE EXAMINATION MADE THE SAID CLAIMANT is ADJUDGED TO BE JUSTLY ENTITLED TO A PATENT UNDER THE LAW.

NOW THEREFORE THESE Letters Patent ARE TO GRANT UNTO THE SAID Goodyear Aerospace Corporation, its successors OR ASSIGNS FOR THE TERM OF SEVENTEEN YEARS FROM THE DATE OF THIS GRANT

THE RIGHT TO EXCLUDE OTHERS FROM MAKING, USING OR SELLING THE SAID INVENTION THROUGHOUT THE UNITED STATES.

In testimony whereof I have hereunto set my hand and caused the seal of the Patent Office to be affixed at the City of Washington this twentieth day of July, in the year of our Lord one thousand nine hundred and sixty-five, and of the Independence of the United States of America the one hundred and ninetieth.

Attest: Ernest W. Swider, Assistant Secretary. Edward J. Brenner, Commissioner of Patents.

Figure 2.1: Carl A. Wiley's patent grant for the concept now known as Synthetic Aperture Radar.

phase of the radar return from a point on the ground based on its slant range from the radar at the time the pulse was emitted. This attention to phase makes SAR a coherent radar system. Focusing allows the system to deal with all ranges in both the near field and the far field [3,6] without making any approximations, and is responsible for the exceptional resolution found in SAR imagery.

The rest of this chapter is organized as follows: Section 2.1 describes the antenna geometry of a SAR system. Section 2.2 discusses the radar equation, the pulse waveform used in my research, the signal processing applied to radar echoes, and the factors that determine a SAR's pulse repetition frequency. Section 2.3 describes how SAR data is range compressed prior to azimuth compression (image formation). Section 2.4 covers the backprojection imaging algorithm, the SAR impulse response, and the advantages of backprojection over other algorithms.

2.1 SAR Antenna Geometry

Unlike conventional forward-looking radars, SAR is a sidelooking radar system as shown in Fig. 1.3. Sherwin tells us in [3] that the primary advantage of the sidelooking configuration is that Doppler shifts pass through zero for targets and landscape features normal to the direction of platform motion, but the rate of change of the Doppler shifts, with respect to the cone angle θ_{cone}, is a maximum at the Zero-Doppler (ZD) line. The ZD line has a cone angle of 90°. Figure 2.2 shows a geometric visualization of a cone angle, which is the angle between a radar platform's velocity vector and an imaginary line connecting the radar phase center to a point on the ground. The cone intersects the ground plane in a hyperbolic curve, and all scatterers on this curve have the same Doppler shift. For this reason, the hyperbolic intersection curve is called an *isodop* [43]. Figure 2.3 shows the cone angle for a ground target in a SAR context.

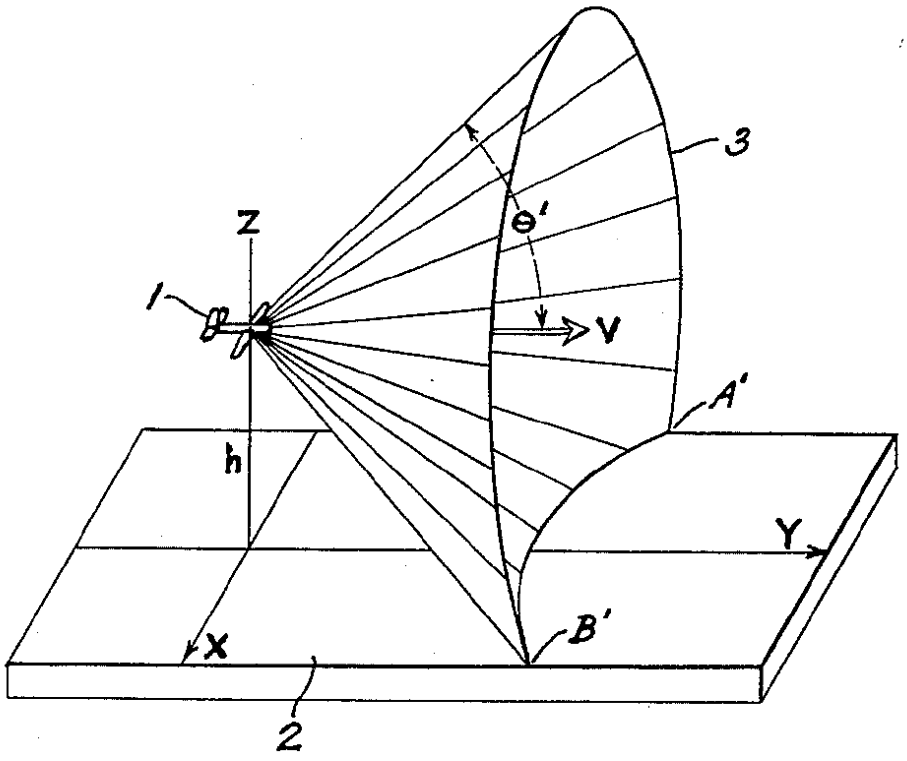

Figure 2.2: The cone angle θ_{cone} is the angle between the platform's velocity vector $\mathbf{v}$ and an imaginary line connecting the antenna phase center to a point on the ground. This image comes from Dr. Wiley's DBS patent [47], and uses θ' for the cone angle. The intersection between the cone and the flat ground forms a hyperbola. All scatterers on this hyperbola produce the same Doppler shift. For this reason, the hyperbolic intersection curve is called an *isodop* [43].

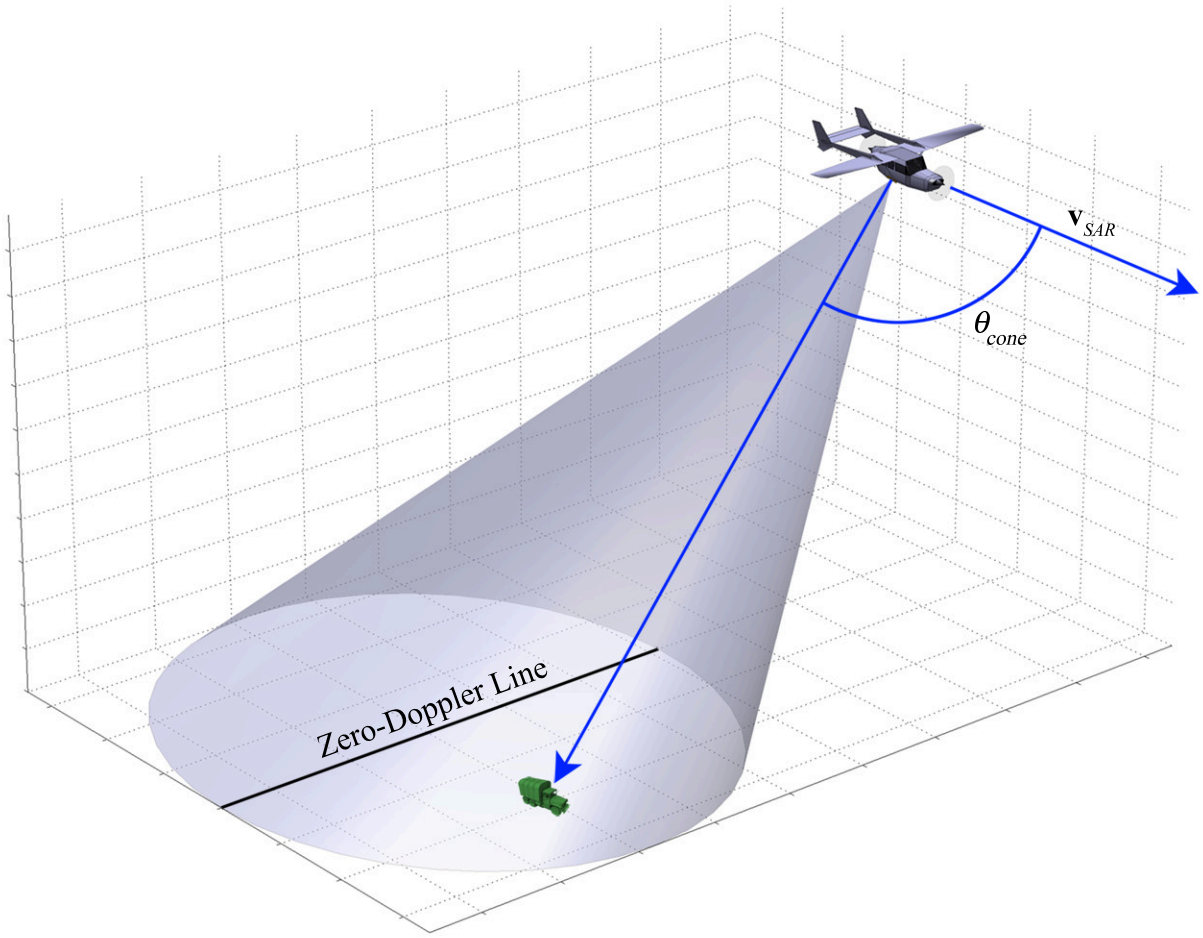

Figure 2.3: The cone angle θ_{cone} for a ground target is the angle between the SAR velocity vector $\mathbf{v}_{SAR}$ and an imaginary line connecting the antenna phase center to the target. All points and targets on the ground with the same cone angle produce the same Doppler shift. The Zero-Doppler (ZD) line has a cone angle of 90°. Targets ahead of the ZD line exhibit a positive Doppler shift, and targets behind it exhibit a negative shift.

2.2 SAR Signal Processing

Radar works by transmitting pulses, recording their echoes, and processing the data to remotely obtain information about a target, or the ground scene in the case of SAR. For this thesis, the radar antenna is assumed to be monostatic, meaning the same antenna is used to both transmit and receive. Also assumed for this thesis is that point scatterers reflect incident radar energy isotropically, or equally in all direcitons.

2.2.1 The Radar Equation

As each radar pulse reflects from the ground scene, different targets and landscape features reflect more or less energy depending on their various radar cross section (RCS) values. As the pulse travels from the antenna out into space, the expanding spherical wavefront causes a *spreading loss*, or a decrease in power flux per unit area, proportional to the inverse square of the distance traveled by the pulse. If a point target is illuminated by the pulse, it reflects some of the energy back to the radar. The amount of radar energy reflected depends on the target's radar reflectivity, or "how bright" it appears from the radar's perspective, as determined by the target's RCS. The energy reflected back from the target also has a spherical wavefront, which induces another inverse-square spreading loss. Therefore the power P_r received in the radar echo from a point target is inversely proportional to the fourth power of the slant range, as given by the *radar equation* [1, 2, 48]:

$$P_r = \frac{P_t G^2 \lambda^2 \sigma}{(4\pi)^3 R^4 L_s L_a(R)}, \tag{2.1}$$

where P_t is the transmit power, G is the antenna gain, λ is the radar wavelength, σ is the target's RCS, R is the slant range to the target, L_s represents system losses, and $L_a(R)$ is the range-dependent atmospheric loss. These two loss factors are ignored for this thesis.

2.2.2 SAR Pulse Waveform

The radar pulse waveform used in this thesis is a linear frequency modulated (LFM) pulse, also called a chirp. This is in contrast to the simple interrupted continuous wave (ICW) used by older radar systems [1]. A "continuous wave" (CW) signal is an always-on signal with a single pure frequency. An "interrupted" CW is a CW signal with a duty cycle less than 100%, and has the appearance of a periodic train of constant-frequency pulses. A rectangular ICW pulse is shown in Fig. 2.4.

A LFM chirp is a sinusoidal waveform whose frequency changes linearly with time [1, 2]. It is swept from an initial frequency to a final frequency as determined by the carrier (or center frequency), the bandwidth, and the chirp direction. The LFM chirp used in this thesis sweeps from a higher frequency down to a lower one, and is called a downchirp. An upchirp sweeps from a lower frequency up to a higher one. The pulse length and bandwidth determine the frequency ramp

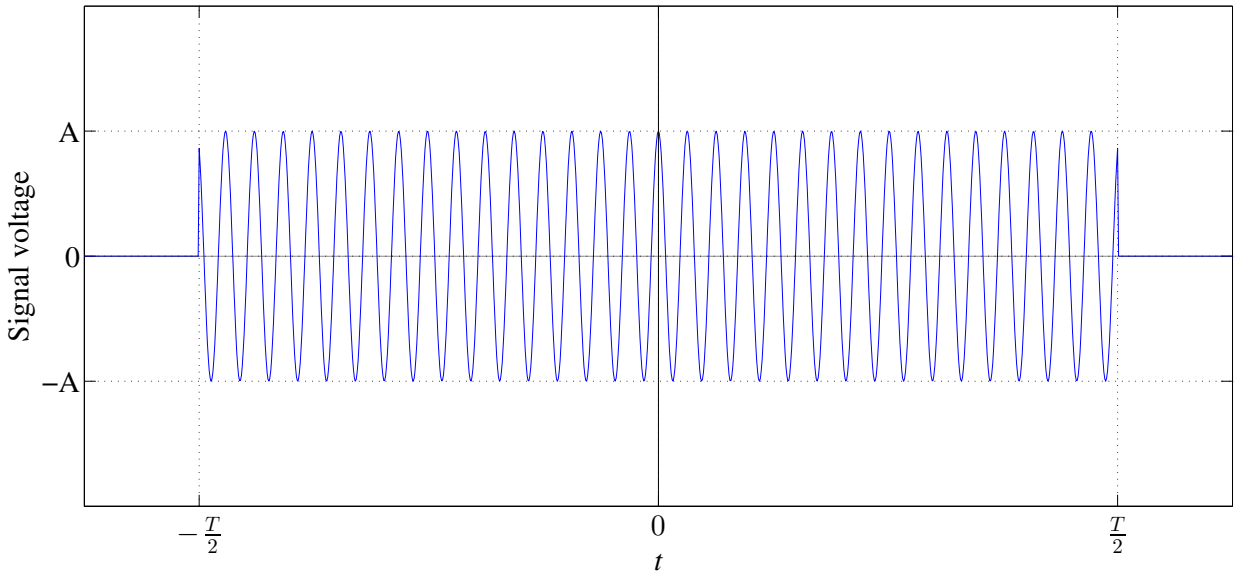

Figure 2.4: A simple rectangular ICW pulse. The quantity A is the pulse amplitude, and T is the pulse length.

rate. The primary reason for preferring a LFM pulse over an ICW is the LFM pulse's mathematical properties which allow its pulse length to be decoupled from its range resolution.

Range resolution and detection performance are two (out of many) important design factors for a radar. Range resolution refers to the radar's ability to distinguish between two different targets at nearly the same distance from the radar. Detection performance refers to the target's signal-to-noise ratio (SNR), which is the amount of energy in a target's radar echo relative to the energy received from noise, clutter, and other interference. For radar systems using an ICW pulse, the range resolution ΔR is directly tied to its pulse length T by the relation [1]

$$\Delta R_{ICW} = \frac{cT}{2}, \tag{2.2}$$

where c is the speed of light. Equation (2.2) shows that better range resolution means shorter pulses. However, improved detection performance requires putting more energy on the target. Since a radar transmitter is typically operated at its maximum power level, putting more energy on the target means lengthening the pulse. Range resolution and detection performance are therefore conflicting metrics for an ICW pulse [1].

The LFM pulse decouples range resolution from its pulse length because of its mathematical auto-correlation properties. Its frequency sweep gives it a wide bandwidth BW, which determines the range resolution according to the equation [1]

$$\Delta R_{LFM} = \frac{c}{2BW}. \tag{2.3}$$

In my research I used a bandwidth of 200 MHz, corresponding to a range resolution of 75 cm.

Since ΔR_{LFM} depends only on the bandwidth, the energy in the pulse can be spread out over a relatively long period of time without compromising the range resolution or detection performance [1]. This relaxes the need for a high power transmitter, which also has the added benefit of reducing the transmitter's size, weight, and cost. An ICW radar, however, must transmit very short, high power pulses to achieve fine range resolution with good detection performance. A LFM pulse does not impose these undesirable needs on a radar designer.

To simplify simulation and the research for this thesis, a complex-valued LFM downchirp centered at baseband is used. This baseband downchirp is illustrated in Fig. 2.5. Although in practice a real-valued signal is transmitted, it is treated as a complex-valued quantity because the coherent nature of SAR requires keeping track of both the magnitude and phase of the transmit signal and its echo. For my research and simulations, I used the following complex exponentials for the LFM transmit $[\psi_{LFM}(t)]$ and received echo $\left[\psi_{LFM,r}(t)\right]$ waveforms:

$$\psi_{LFM}(t) = A \cdot \text{rect}\left(\frac{t}{T}\right) e^{j\left(\frac{1}{2}k_r t^2\right)}, \tag{2.4}$$

$$\psi_{LFM,r}(t) = \alpha A \cdot \text{rect}\left(\frac{t-\tau}{T}\right) e^{j\left[\frac{1}{2}k_r (t-\tau)^2 + \phi\right]}, \tag{2.5}$$

$$\text{where rect}(t) = \begin{cases} 1, & |t| \leq \frac{1}{2} \\ 0, & \text{otherwise,} \end{cases} \tag{2.6}$$

the pulse shape is rectangular, A is the transmit amplitude, t is time, T is the pulse length, k_r is the LFM frequency ramp rate in rad/s^2, α is a scaling constant that absorbs the spreading loss predicted by the radar equation [Eq. (2.1)], τ is the pulse's round trip flight time echo delay, and ϕ is the phase shift imparted to the pulse by its trip to the target and back, defined as $\phi = \omega_0 \tau$.

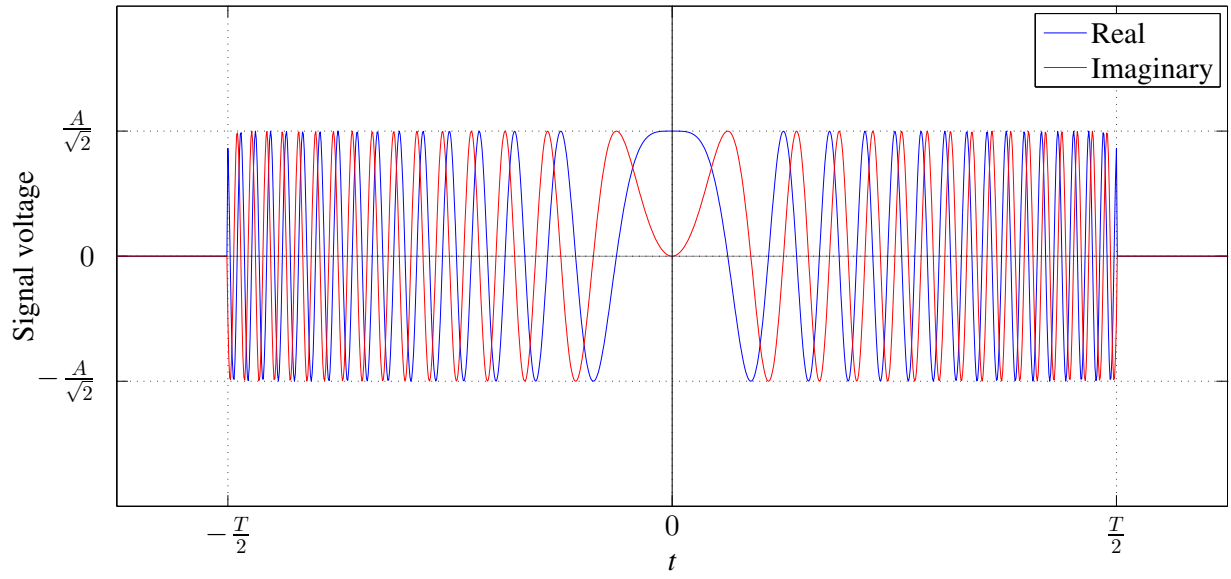

Figure 2.5: A rectangular complex LFM downchirp shifted to baseband. The quantity A is the waveform amplitude, and T is the pulse length.

Even though the LFM waveform in Fig. 2.5 is shown shifted to baseband, the physical phase shift still depends on the radar's actual center frequency ω_0. To be precise, since the LFM chirp is not a single pure frequency, the phase shift for all instants of the echo is not a single value for ϕ. But since the bandwidth is generally small compared to the carrier, the relative difference in frequency is also small from the beginning to the end of the transmitted chirp. Therefore the approximation using only the carrier frequency to compute the entire echo's phase shift introduces negligible error while greatly simplifying computations and simulation.

2.2.3 Echo Signal Processing

The range resolution improvement of a LFM pulse over an ICW pulse becomes apparent when the return echo is processed. After every pulse, the system waits for, records, and processes the radar returns from the ground scene before transmitting the next pulse. The echo from a point target is an attenuated, time-delayed, phase-shifted copy of the transmit waveform. The echo is processed through a matched filter which cross-correlates the return echo with a copy of the transmit signal. The result of this matched filtering operation is a sinc function, shown in Fig. 2.6.

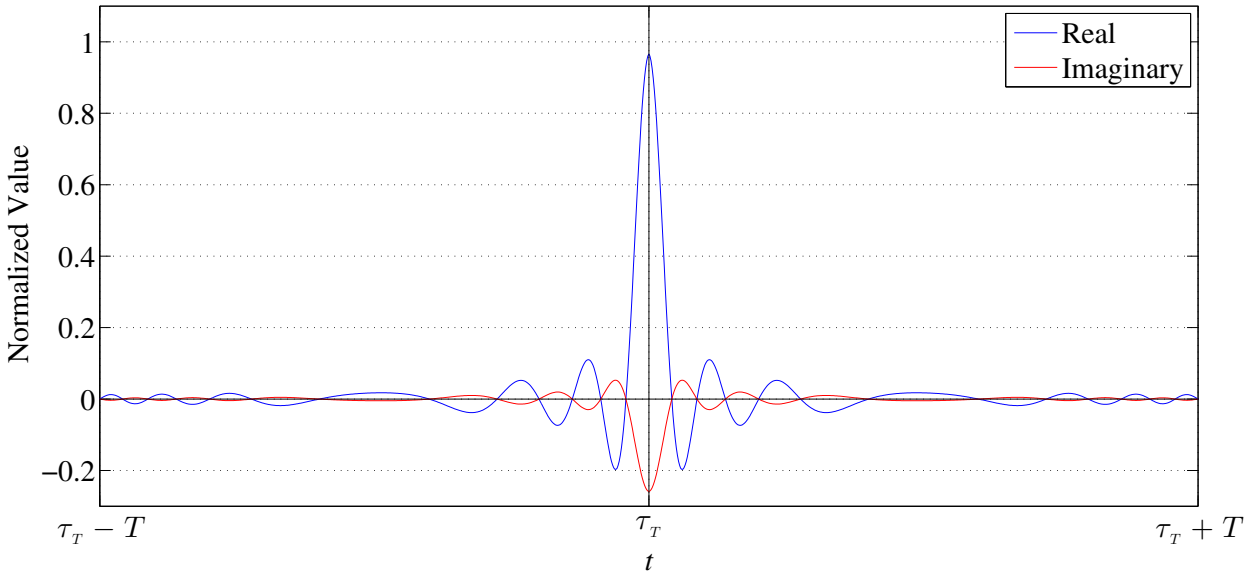

Figure 2.6: Complex sinc function output from the matched filtering (cross-correlation) between a complex LFM transmit signal and its subsequent echo from a point target. The quantity t is time, T is the pulse length, and τ_T is the target's echo delay. The complex phase shift depends on the range to the target. When the pulse's round-trip flight distance is an integer number of wavelengths λ, the matched filter output is purely real. The phase shift shown here is 345°. The width of the mainlobe is a direct measure of the LFM waveform's range resolution.

The width of the sinc mainlobe is a direct measure of the LFM waveform's range resolution. A wider bandwidth BW produces a narrower sinc mainlobe, which means finer range resolution.

2.2.4 SAR PRF Constraints

A radar system transmits pulses at a rate called the pulse repetition frequency (PRF), and the time between the beginning instants of two sequential pulses is called the pulse repetition interval (PRI). The PRF and PRI are inversely related by the equation

$$PRI = \frac{1}{PRF}. \tag{2.7}$$

Radars in practice use PRFs anywhere from several hundred Hz to many tens of kHz, depending on the application, and sometimes as high as several hundred kHz [1]. For SAR, there are two factors that determine the upper and lower bounds on the PRF.

PRF Lower Bound

The PRF lower bound is equal to the Doppler bandwidth of the SAR system [1, 7, 14, 15]. The Doppler bandwidth is the range of Doppler shifts observed by the SAR system as ground targets and ground clutter traverse the mainlobe as the SAR platform flies. The PRF must match or exceed the Doppler bandwidth to prevent aliasing. The Doppler bandwidth BW_D is determined by the platform velocity v_{SAR}, the radar's carrier wavelength λ, and the azimuth beamwidth θ_{3dB}. These relationships are given by

$$PRF \geq BW_D = \frac{4v_{SAR}}{\lambda} \sin\left(\frac{1}{2}\theta_{3dB}\right). \tag{2.8}$$

When the small angle approximation is used for narrow beamwidths, as Richards does in [1], the math reduces in such a way that an equivalent condition emerges: the spatial separation along the flight track between two adjacent pulses must be no greater than half the along-track dimension of the physical antenna. Since this thesis covers widebeam SAR, the Doppler bandwidth given by Eq. (2.8) is used to determine the PRF's lower bound.

PRF Upper Bound

The PRF's upper bound is determined by the width of the desired stripmap region to be imaged. Specifically, 'width' in this context refers to the cross-track dimension of the ground swath depicted in Fig. 1.3. In [1], Richards calls this dimension the 'swath length', but I call it the swath width instead.

Figure 2.7 depicts the situational geometry that determines the PRF's upper bound. The primary concern is to avoid having successive pulses overlap at the receiver [1, 15]. This is done by allowing enough time between pulses for the radar echo from the far edge of the ground swath to arrive back at the receiver before the echo from the next pulse arrives from the near edge. This spacing also enables unambiguous range measurement within the swath. In Fig. 2.7, the imaged swath width W_s is equal to the size of the mainlobe's ground footprint in the cross-track direction due to the mainlobe elevation beamwidth. But the swath width can be made smaller by restricting the time span over which the return echo is sampled. If this is done, the maximum allowable PRF is increased. The minimum time separation between pulse transmissions, i.e. the PRI, is determined

by the desired swath W_s and the nominal incidence angle δ according to the constraint

$$PRI_{min} \geq \frac{2}{c} W_s \cos(\delta) \Rightarrow PRF_{max} \leq \frac{c}{2W_s \cos(\delta)}. \tag{2.9}$$

Equation (2.9) assumes a plane wave approximation, whereas Fig. 2.7 emphasizes the spherical wavefront of the radar signal. Therefore, Eq. (2.9) is not exact, but is close enough for design purposes. It turns out that if the desired swath width is to be limited by the the full mainlobe elevation beamwidth, other issues arise which must be addressed, but they are beyond the scope of this thesis. The interested reader is referred to Section 8.1.4 of the Richards radar textbook [1]. The constraints imposed by Eqs. (2.8) and (2.9) limit a SAR system to a relatively low PRF [1]. In my simulations during the course of my research, I used a PRF of 2000 Hz.

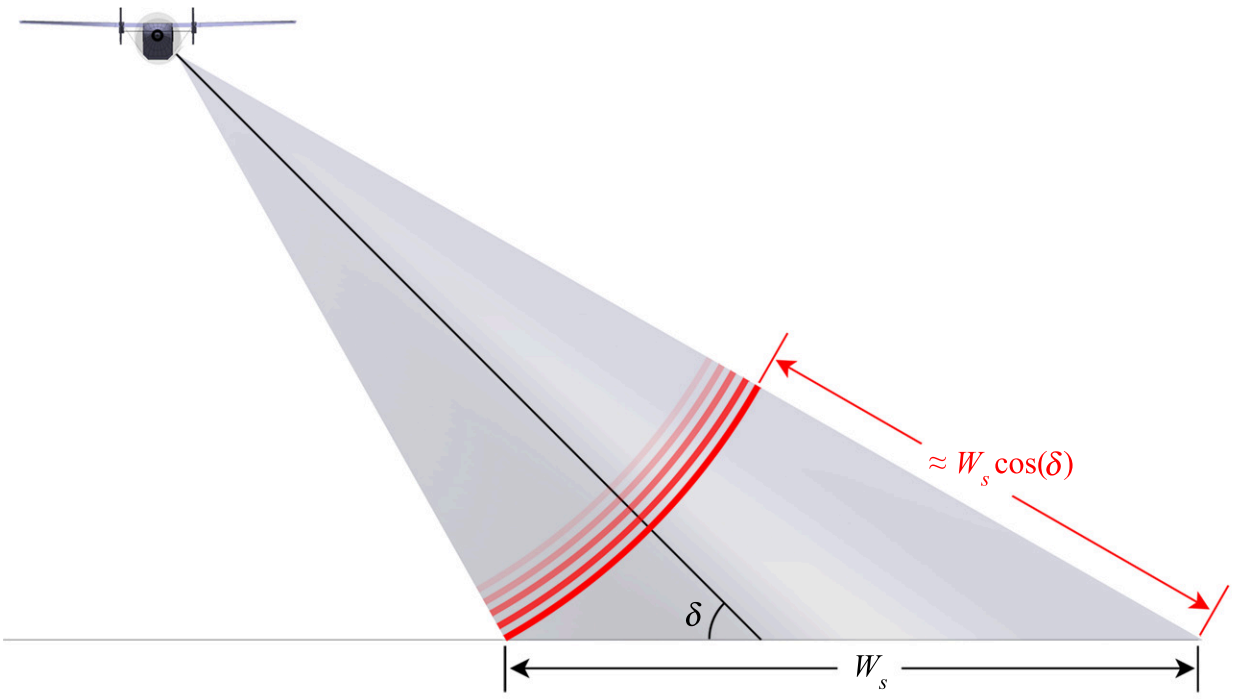

Figure 2.7: The upper bound on the SAR PRF is determined by the swath width W_s. Although W_s here is shown as limited by the elevation beamwidth, it can be made smaller by restricting the time interval over which the return echo is sampled, which increases the maximum PRF. In this figure, the airplane and radar beam are viewed from behind the airplane looking in the along-track direction, with the airplane flying into the page. The quantity δ is the nominal incidence angle, determined by the radar boresight look angle.

2.3 Range Compressed Data

Range compressed (RC) data is stored prior to image formation when using backprojection, which is explained in Section 2.4. In my research, I simulated LFM pulses and their return echoes, but after cross-correlating them to synthesize the RC data, I discarded the raw radar echo signal due to RAM limitations, and saved the RC data.

The sinc function shown in Fig. 2.6 is a mathematically ideal example of a single pulse's RC data for a point target. The sinc function's mainlobe position on the time axis directly indicates the pulse's light-speed echo delay for a target, and therefore the target's slant range for a particular pulse. This is the reason the data is called "range compressed". The echo signal is also phase-shifted in relation to the wavelength λ and the slant range R to the target, as given by

$$\phi = \frac{4\pi R}{\lambda}, \tag{2.10}$$

where ϕ is the echo's phase shift.

RC data is complex-valued because it contains information about both the intensity and phase of the of the radar echo samples. Although the entire pulse is transmitted in the short timespan of a single pulse length, the received echo is spread out in time because of the varying distances to the different parts of the landscape illuminated by the radar beam, as depicted in Fig. 2.7. This "smeared out" echo is processed through a matched filter as described previously in Section 2.2.3, producing the RC data for a given pulse. In practice, RC data is a superposition of many sinc functions, one from each point on the ground illuminated by the radar pulse.

The signature of a particularly bright point-like target, such as a vehicle or a corner reflector, might show up as a narrow spike in RC data, indicating that the target reflected much more radar energy than the surrounding landscape. However, because of the radar's wide beamwidth, the RC data contains little information about the direction to the target, only that it is within the radar beam's mainlobe, or possibly a sidelobe. Figure 2.8 shows RC data for a single simulated pulse reflecting from four ground targets, with no ground clutter or other interference. Ground clutter includes grass, bushes, trees, rocks, signs, buildings, and any other landscape feature or man-made object that is not a target of interest. Figure 2.9 shows the RC data for the same radar pulse as Fig. 2.8, except the targets are now immersed in uniformly distributed ground clutter.

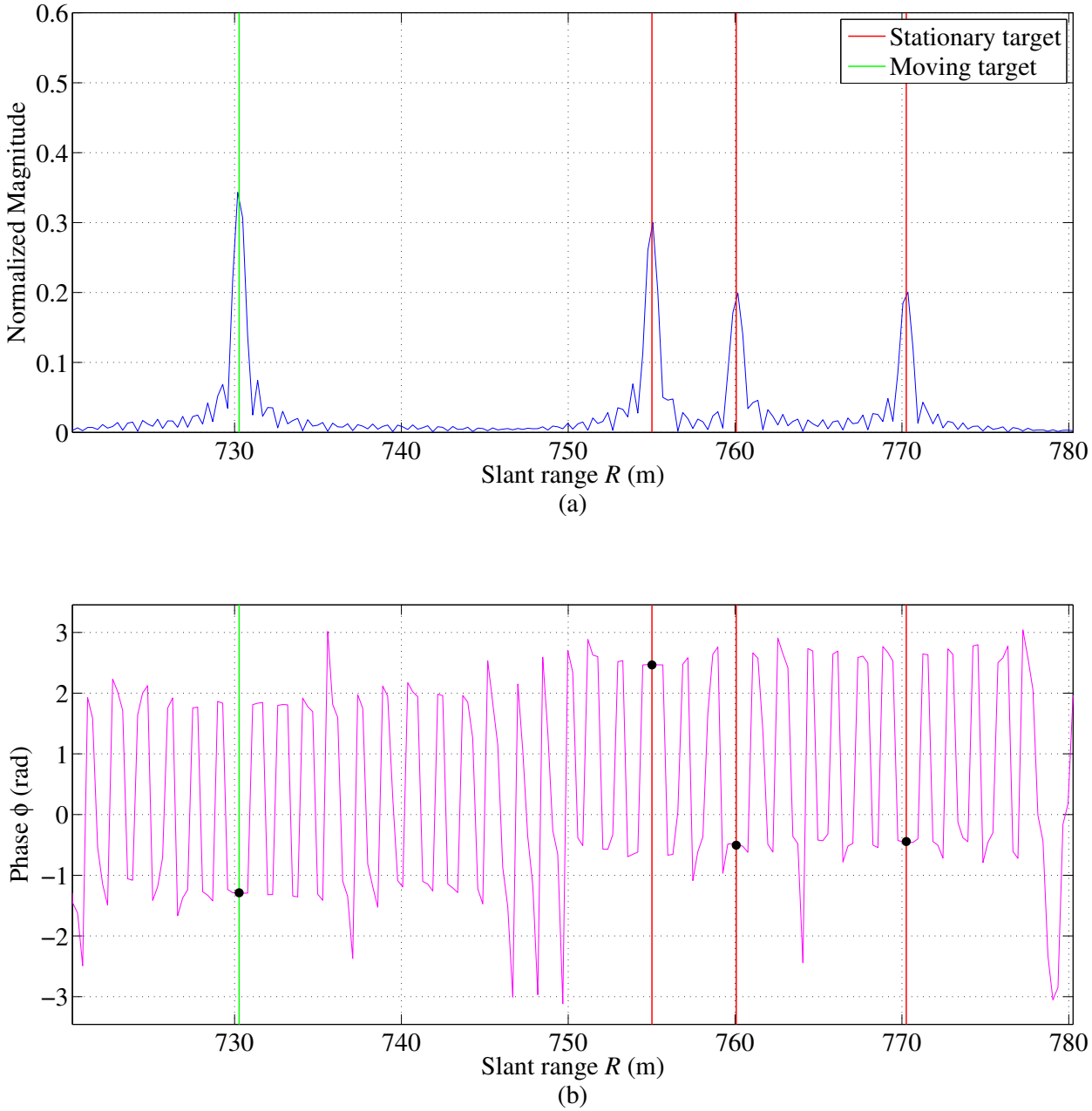

Figure 2.8: Magnitude (a) and phase (b) of the RC data for a single simulated pulse reflected from one moving target and three stationary targets in a flat, sterile environment free of noise, ground clutter, or any other interference. Magnitude is normalized relative to the peak echo magnitude for the entire time the SAR collected data. The red and green vertical lines indicate the targets' true slant ranges for this particular pulse based on complete knowledge of the target positions and velocity vectors. The black dots in the phase plot indicate the true echo phases from each target based on the wavelength and round trip distance traveled by the pulse.

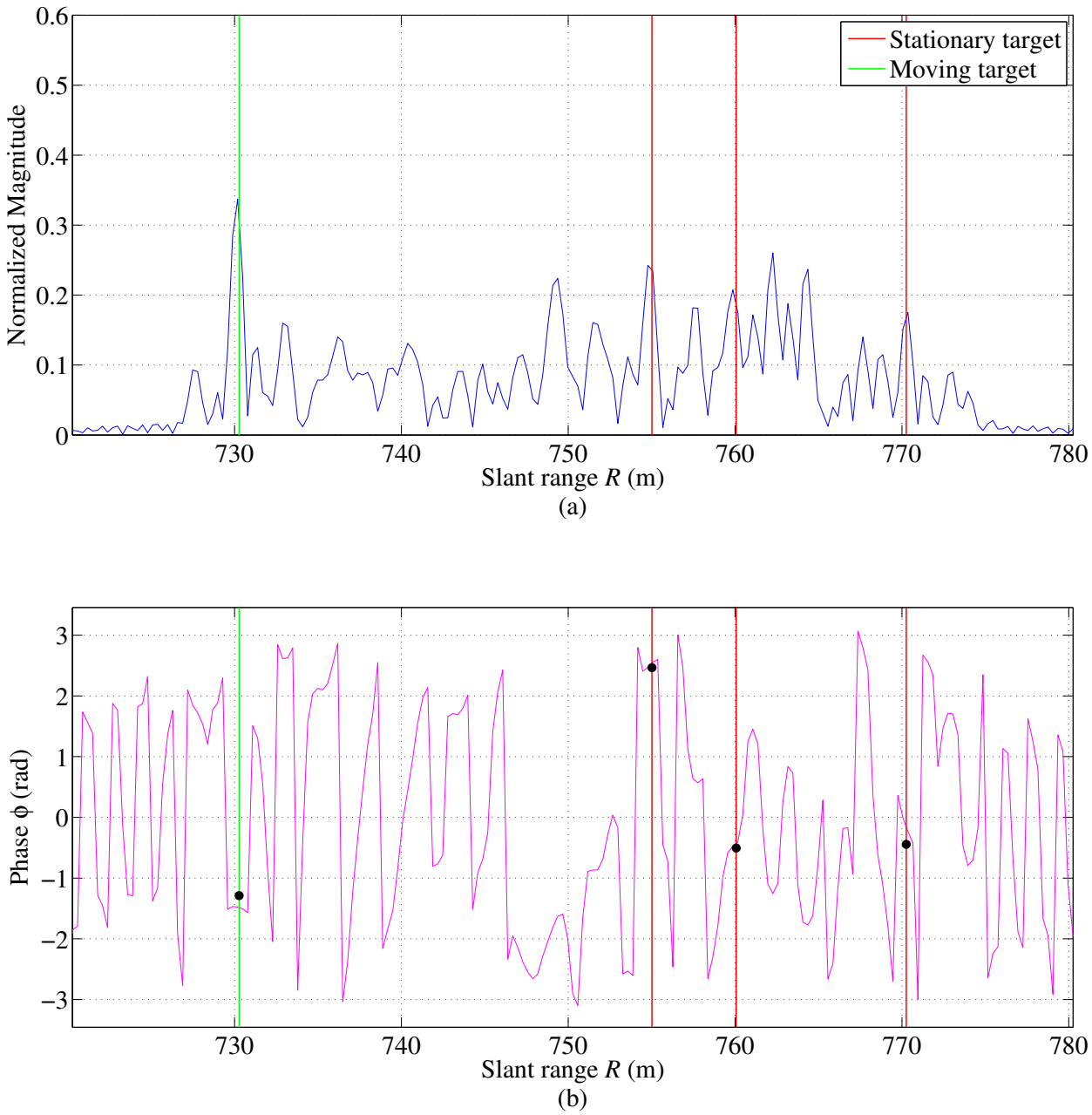

Figure 2.9: The same simulated RC data as in Fig. 2.8, except with ground clutter included. Note that some target peaks in the magnitude plot are lower than some clutter peaks. Also note that due to wave interference, some of the black dots in the phase plot, which indicate the true target phases, do not match up exactly with the data as they do in Fig. 2.8.

Figure 2.10 shows magnitude plots of the RC data for an entire simulated SAR data collection plotted in two dimensions, both with and without ground clutter, using the same target data in both cases. Each column of pixels in Figure 2.10 corresponds to the RC data for a single pulse, with magnitude indicated by the color bars to the right of each plot. The single-pulse RC data in Fig. 2.8a corresponds to the leftmost column of pixels in Fig. 2.10a, and Fig. 2.9a corresponds to the leftmost column of pixels in Fig. 2.10b. In Figs. 2.8 and 2.9, the horizontal axes correspond to the vertical axis in Fig. 2.10. Note that in Figs. 2.8 and 2.9, the horizontal axis is slant range (m), while in Fig. 2.10, the corresponding vertical axis is time (μs). This is because for the single-pulse RC data plots in Figs. 2.8 and 2.9, the intent is to demonstrate how RC data depends on the slant ranges to scatterers on the ground. But for two-dimensional RC data plots, is it customary to use time for both axes.

To fully understand Fig. 2.10, it is necessary to understand the time axes used in each dimension. The vertical axis is called *fast time* and the horizontal axis is *slow time*. Fast time is a time scale comparable to the round-trip flight time of a single pulse. Because a pulse travels to the ground and back at the speed of light, operations on this time scale must be performed at a sampling rate much faster than those that take place from one pulse to the next. These fast-time operations include transmitting a pulse, sampling its return echo, and performing matched filtering on it. Slow-time refers to the much longer time scale between pulses, or the PRI. Operations on this time scale span one or more PRIs, and include writing the RC data to storage and performing SAR image formation [1, 2].

As the flight progresses and data continues to be collected, the slant ranges to all the various ground targets and landscape features change as the platform first approaches, reaches a point of closest approach as it flies past, and then recedes as it flies away. This behavior is observable as a *range migration curve* (RMC) in the RC data, sometimes informally called range history or a range smile. Figure 2.10a shows four RMCs: three for stationary targets and one for a moving target. The moving target's RMC is the one seen to cut across the other RMCs. For the ideal radar and target motions assumed in this thesis, these RMCs are hyperbolic, which will be proved in Chapter 5.

Figure 2.10b shows the same four RMCs, but includes ground clutter. Because ground clutter is computationally intensive to simulate, I only simulated clutter for a 50m x 50m patch of

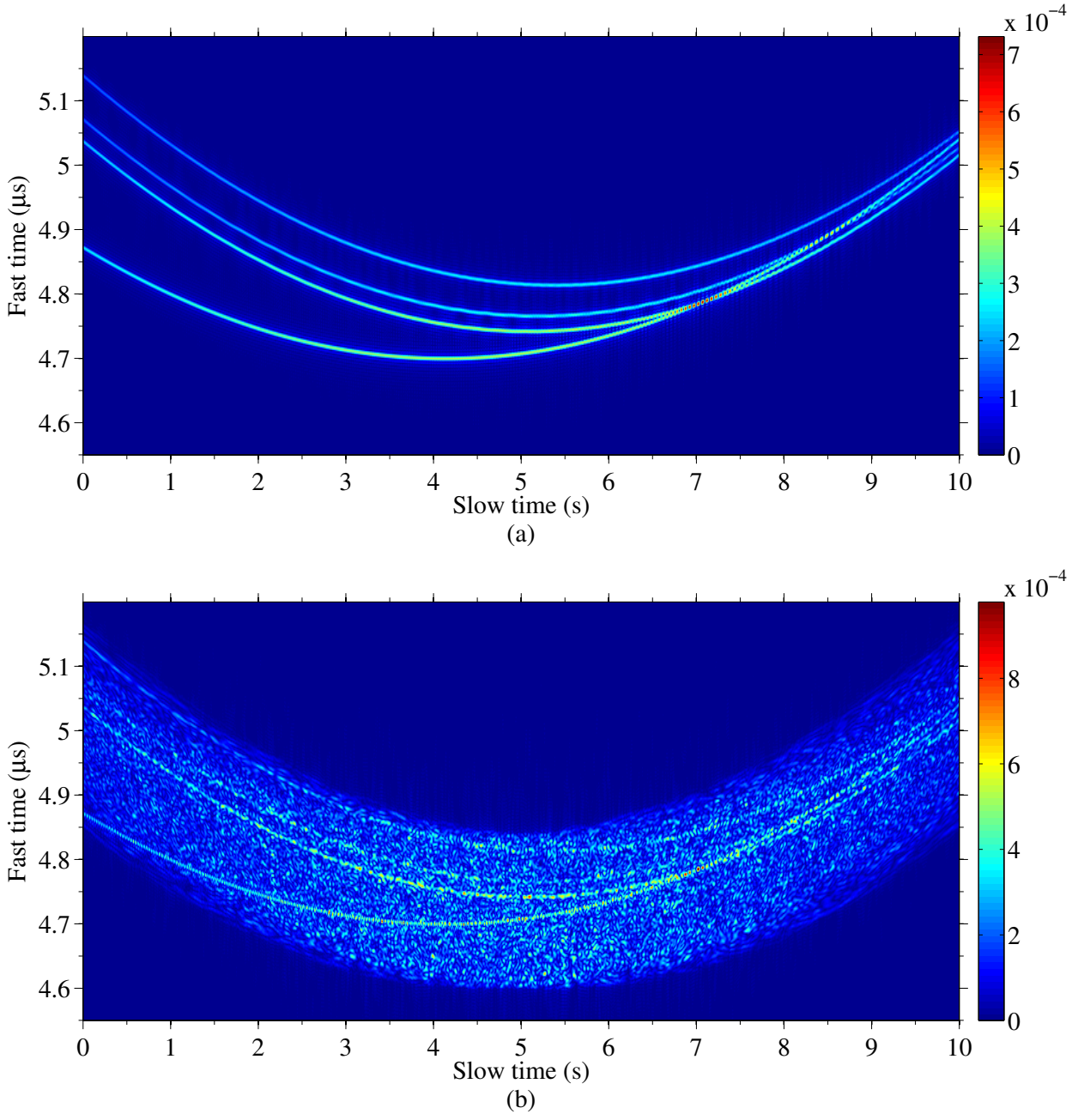

Figure 2.10: Two-dimensional RC data from a simulated SAR data collection. In panel (a), RMCs for four targets are easily visible. Three of the targets are stationary, and one is moving. The moving target's RMC is the one that starts out below the others and then cuts across them toward the end. When radar and target motion are rectilinear with constant speeds, RMCs are always hyperbolic. Panel (b) shows the effect of including a patch of ground clutter big enough to fully contain the targets during the data collection.

ground, and limited my target simulations to locations and movements which kept them within the clutter patch during data collection. It is apparent that the presence of ground clutter obscures the radar signatures of the targets of interest, and is a universal problem in GMTI.

2.4 Image Formation: the Backprojection Algorithm

SAR image formation has an interesting history. When SAR was first developed, SAR data was recorded on film, and images were made from the radar data using elegant optical systems [4, 7, 42, 43]. Modern advances in computing power have rendered the optical processing method obsolete, and SAR data processing and image formation are now done digitally. Many image formation algorithms have been invented and used during SAR's approximately 60 year history, but this thesis considers only the backprojection (BPJ) algorithm. BPJ creates a radar image which is essentially a map of backscatter intensity at each pixel location. Backscatter intensity is characterized by the quantity σ^0, which represents a pixel's normalized RCS.

The most apparent difference between an optical image and a SAR image is the final image geometry. A human eye or a camera sees a perspective view based on the viewing position in 3-space. For SAR, regardless of the radar viewing geometry, the image produced is always an overhead 2-D map view of the ground scene.

Forming a SAR image requires an accurate record of the platform's motion history, regardless of the image formation algorithm used [10, 15, 21, 43, 49–51]. For reasons which are clarified later in Section 2.4.3, BPJ is an optimal image formation algorithm [11, 52], able to robustly handle any linear or nonlinear flight track [2, 52–55]. BPJ is the most general and exact algorithm for forming SAR images, because it works by applying the principle of focusing [2] as discussed at the beginning of this chapter. Image focus refers to and depends on the radar's ability to compensate for all relative motion between the antenna phase center and each image pixel [56]. The need to account for the relative motion between the radar and the image pixels is the reason SAR image formation requires an accurate motion history record. Unfortunately, accurately recording the radar's position during the flight is one of the biggest challenges in SAR imaging [10]. Older SAR systems accomplished this primarily with inertial measurement units (IMUs), but modern SARs include Global Positioning System (GPS) information. In this thesis, all simulated SAR images are formed with BJP, and the SAR platform is assumed to have a perfect motion history record.

Besides requiring an accurate flight path record, BPJ also requires the RC data for each pulse [55]. Each pixel in the image receives sample contributions from the RC data based on its range/phase history during the time it was illuminated by the radar. The RC data used to compute the pixel's final complex image value are only from the pulses for which the pixel was illuminated by the radar beam's mainlobe. This is illustrated in Fig. 2.11.

Azimuth (or cross-range) resolution depends on the *integration angle*. The integration angle ϑ is the angle through which the SAR moves relative to a pixel as the pixel's backscatter values are coherently summed during image formation. Azimuth resolution improves as ϑ increases, up to the limit imposed by the radar's azimuth beamwidth.

The finest achievable azimuth resolution is realized if the integration angle ϑ is equal to the mainlobe azimuth beamwidth θ_{3dB}. In this scenario, illustrated in Fig. 2.12, the SAR takes advantage of the full extent of the mainlobe's geometry as it passes over a target or pixel, and illuminates it from the widest possible angular extent. When $\vartheta = \theta_{3dB}$, the best case azimuth

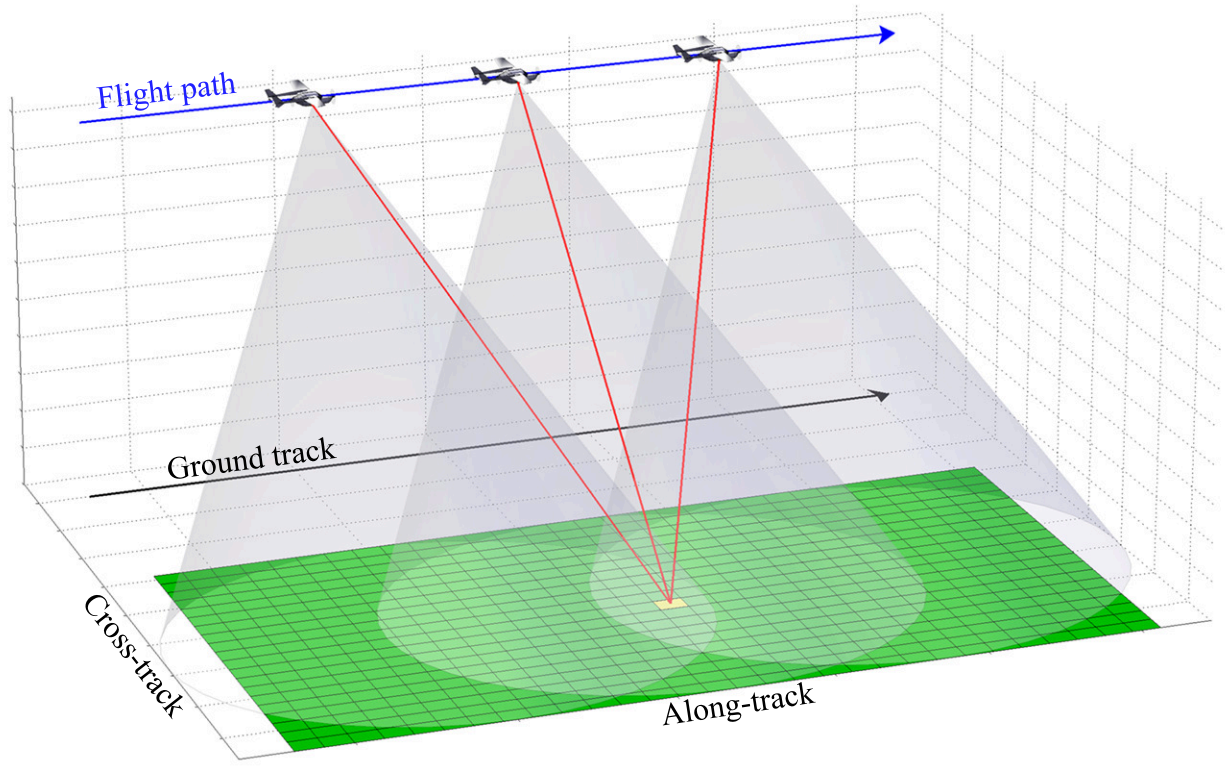

Figure 2.11: In SAR image formation, only the pulses that illuminate a pixel (yellow) are able to contribute to its final image value.

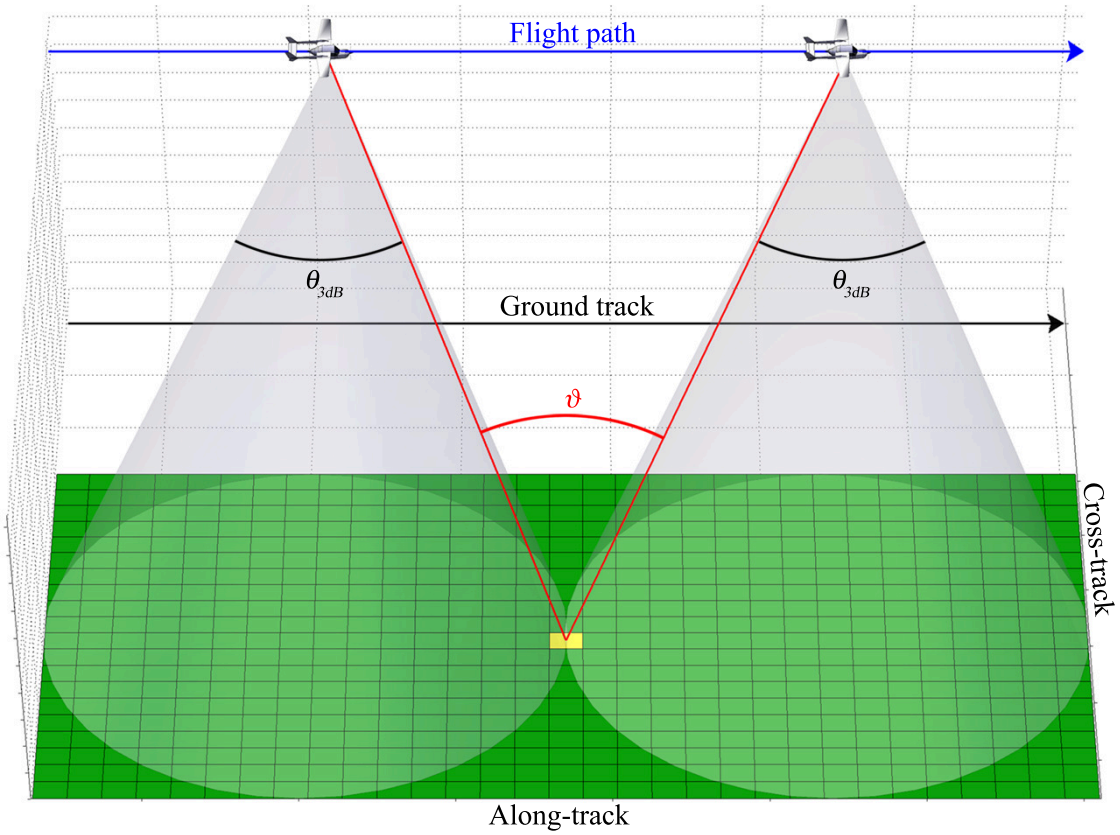

Figure 2.12: The integration angle ϑ is the angle through which the SAR moves relative to a pixel as the pixel's backscatter values are coherently summed during image formation. When ϑ is equal to the mainlobe azimuth beamwidth as shown here, the best achievable azimuth resolution is realized, and is on the order of the physical antenna's along-track dimension.

resolution is comparable to the along-track dimension of the physical radar antenna. In theory, the lower bound on azimuth resolution is half the antenna's along-track dimension. In practice however, signal processing nonidealities, such as windowing for sidelobe control, degrade the best-case azimuth resolution approximately 50% to 100% away from this ideal [1].

The relationship between azimuth resolution and integration angle leads to the interesting observation that if azimuth resolution for SAR is to be independent of slant range, as stated as the beginning of Chapter 1, then the synthetic aperture length for each pixel must be directly proportional to the slant range of closest approach [11, 43]. This ensures that the same integration angle is used for all pixels in the image during their respective *dwell times*. Dwell time refers to the time the radar spent illuminating the target or a pixel as it flew past, and is directly related to the synthetic aperture length for that target or pixel.

Because the relationship between the antenna's azimuth dimension and the best-case azimuth resolution is so centrally important in SAR imaging, the antenna's azimuth dimension is referred to as simply the "antenna size" for the rest of this thesis.

2.4.1 The Backprojection Equation and Visualization

The backprojection equation [46, 57] used in this thesis is

$$P(x,y,z) = \sum_{n=1}^{N} RC[\tau(x,y,z,n)] \cdot e^{-j\phi(x,y,z,n)}, \tag{2.11}$$

where x, y, and z are the spatial coordinates of a given pixel, $P(\cdot)$ is the final complex image value of the pixel after BPJ is performed, n is the pulse number, N is the number of pulses in the integration angle for the pixel, $RC(\cdot)$ is the RC data for a given pulse number n, $\tau(\cdot)$ and $\phi(\cdot)$ are the echo delay and echo phase shift, respectively, both of which depend on the pixel location (x,y,z) and the pulse number n. Even though Eq. (2.11) shows the pulse index n starting at 1, it must be understood that pulse number $n = 1$ refers to the first pulse that illuminates the pixel, not necessarily the first pulse of the SAR flight. For this thesis, Eq. (2.11) is referred to as "the BPJ equation".

The conceptual implementation of the BPJ process for a single pixel is as follows [2, 52, 54, 55]. Let the pixel value $P(\cdot)$ start out at zero, and consider the first pulse for which the pixel was illuminated. First, the digital RC data for that pulse is interpolated. In my simulations I interpolated the RC data by a factor of at least 16, but in practice, as long as the Nyquist sampling constraint has been satisfied, the RC data may be interpolated to arbitrary precision [52, 53]. Next, the slant range R between the pixel center and the radar phase center is computed using the Pythagorean Theorem, based on their known positions in 3-space. The slant range is then used to compute the pulse's light-speed echo delay τ, and its round-trip phase shift ϕ. The echo delay τ is defined as

$$\tau = \frac{2R}{c}, \tag{2.12}$$

and ϕ is found with Eq. (2.10). The echo delay, the known receiver sampling rate, and the interpolation factor for the RC data are then used to determine which digital sample index of the interpolated RC data best corresponds to the pixel's slant range for that pulse. The complex value

of this RC data sample is then multiplied by $e^{-j\phi}$ to remove the round-trip phase shift. The final result of all these computations yields a complex value, which is then added to the image pixel. The process is then repeated for every pulse, with each result added to the pixel's accumulating running sum. The magnitude of the pixel's final complex value represents the pixel's brightness in the SAR image.

The BPJ equation [Eq. (2.11)] itself is deceptively simple. While the mathematical computations described in the previous paragraph are each individually straightforward, BPJ is a very computationally intensive algorithm. This is due to the sheer number of pixel computations that must be performed to form an image with BPJ. In computer science terminology, the BPJ algorithm has $O(N^3)$. This prevented its widespread use in the early days of SAR [52–54] because computers did not yet have the necessary processing power to form images in a timely manner using BPJ. BPJ's computational expense is the tradeoff for the optimality, robustness, generality, flexibility, mathematical simplicity, and extremely high quality images produced by the algorithm. Fortunately, BPJ lends itself well to the parallel processing capabilities of modern computers. Parallel processing, coupled with the exponential growth trends of computing power in recent decades, has made the computational expense of BPJ a much smaller problem.

The previous mathematical description of BPJ was explained in terms of pixel-by-pixel computations, but in practice it makes much more sense to do the BPJ computations on a pulse-by-pulse basis [55]. The pixel-by-pixel approach requires every pulse's RC data record to be accessed and interpolated once for every pixel. The pulse-by-pulse approach needs to access and interpolate each pulse's RC data only once for the entire image. Each pulse then contributes to every pixel in the scene. This saves an enormous amount of time on the memory-read and interpolation operations. For the rest of this thesis, BPJ is treated as a pulse-by-pulse operation.

The pulse-by-pulse implementation of BPJ enables an interesting visualization of the BPJ image formation process. For a sterile, flat ground scene containing only a stationary point target and no ground clutter, the BPJ operation on the first pulse contributes the same complex value to every pixel with the same slant range as the point target. The target's circular iso-range is back-projected, or essentially "painted", onto the blank image with the first pulse's contribution from its RC data, with the iso-range arc centered on the SAR platform's nadir point on the ground directly below it. As each pulse back-projects its own iso-range onto the image, all the iso-range arcs

intersect at the true target position. This process is illustrated for three stationary point targets in Figs. 2.13 through 2.22. The platform speed is 50 m/s. These figures demonstrate BPJ by showing sequential image contributions from five pulses in a ten-second data collection, with each pulse separated in time by 2.5 seconds, which is this case equates to 125 meters between pulses. For each BPJ image frame, the iso-range circles contributed by the their respective pulses are highlighted by being brighter than the iso-range circles from previous pulses. Each BPJ image frame is accompanied by the corresponding RC data for the contributing pulse. Figure 2.23 shows the final BPJ image for the sequence of frames in Figs. 2.13 through 2.22.

As stated previously, each BPJ contribution is reverse-phase-shifted based on each pixel's slant range. This is how BPJ applies the principle of SAR focusing as described earlier. The result in the final image is a coherent gain at the true target position due to constructive interference. All the other pixels experience destructive interference, except for pixels in the immediate proximity of the true target location. Pixels far from the target end up with negligible complex values, while pixels near the target undergo only partially destructive interference, producing the characteristic sidelobe patterns seen for point targets in BPJ images, shown in Figs. 2.24 and 2.25.

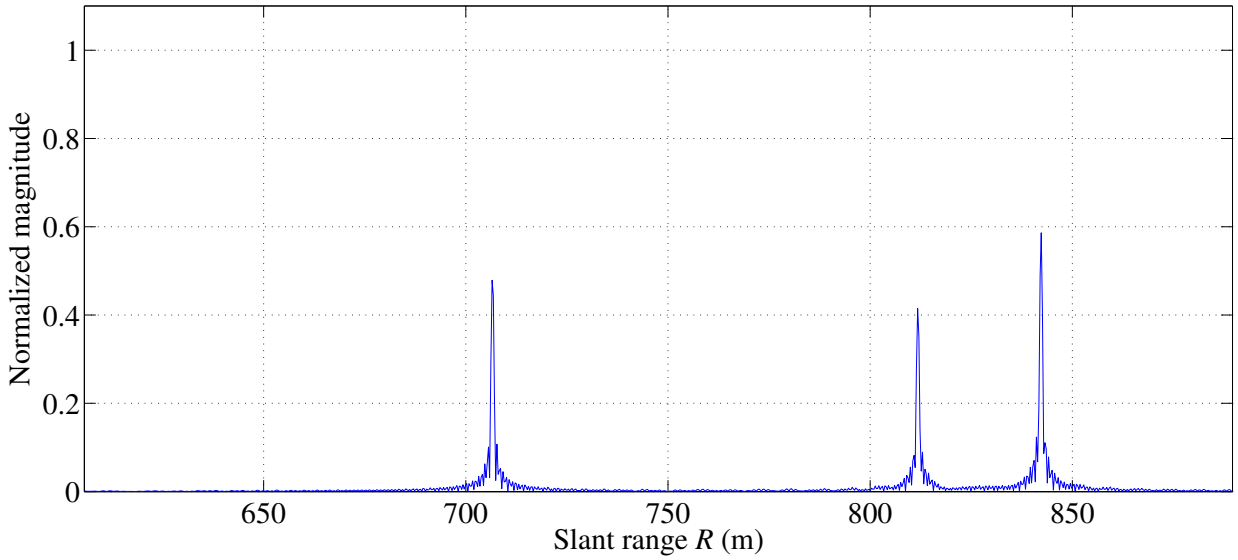

Figure 2.13: RC data magnitude, frame 1 of 5. This simulated RC data is for the first pulse used to form the image of the three point targets whose single-pulse responses are shown here. The three peaks indicate only the slant ranges to each target for the first pulse, and give no information about the directions to the targets, except that they are within the mainlobe azimuth beamwidth.

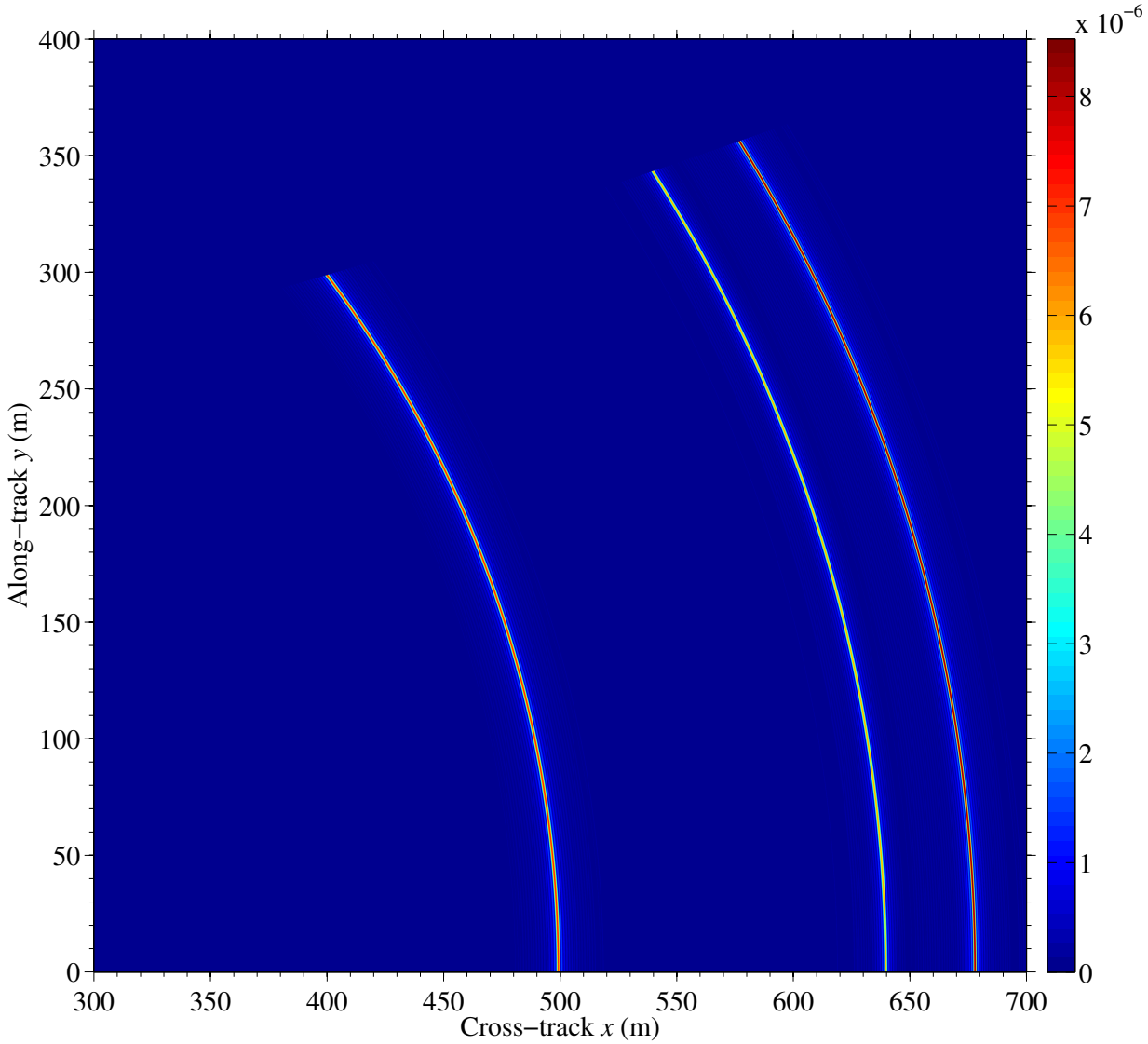

Figure 2.14: BPJ frame 1 of 5. This is the BPJ image formation in progress for three stationary point targets, showing the first pulse's contribution (magnitude only). North is up, and the SAR platform is off-image to the left, flying north and looking to the right. The corresponding RC data for this frame is shown in Fig. 2.13. The targets' concentric iso-range arcs are centered on the platform's nadir ground point for the first pulse. They are truncated at the top because the BPJ image contributions for each pulse are limited to pixels visible within the azimuth beamwidth for that pulse. This illustrates the poor angular resolution of a real-aperture beam, because based on this first pulse alone, the targets cannot be precisely located beyond knowing they are within the radar's mainlobe. Not until more pulses contribute to the image will the target locations become clear. Note that the relative spacing of the target peaks in Fig. 2.13 nearly matches the relative radii of the iso-range arcs here. The slight difference is because the image plane, onto which RC data is backprojected, is the flat-Earth ground plane, which does not contain the airborne radar.

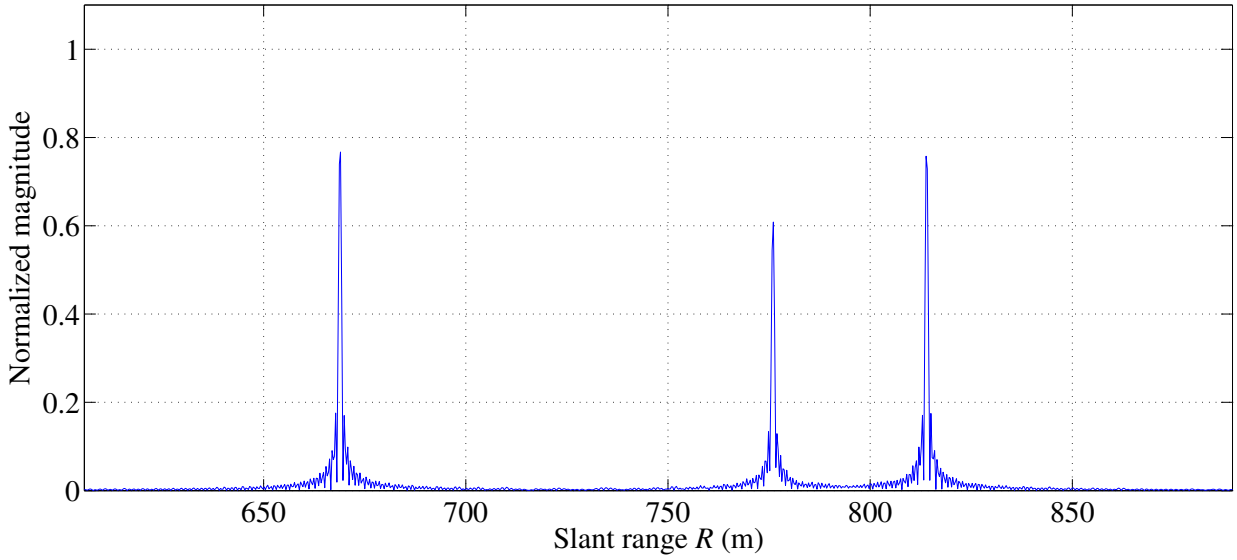

Figure 2.15: RC data magnitude, frame 2 of 5. This data is from a pulse located 125 meters further along the flight path than the previous pulse whose RC data is shown in Fig. 2.13. The peaks have shifted to the left because the radar is now closer to the targets. This RC data makes the BPJ contribution shown in Fig. 2.16.

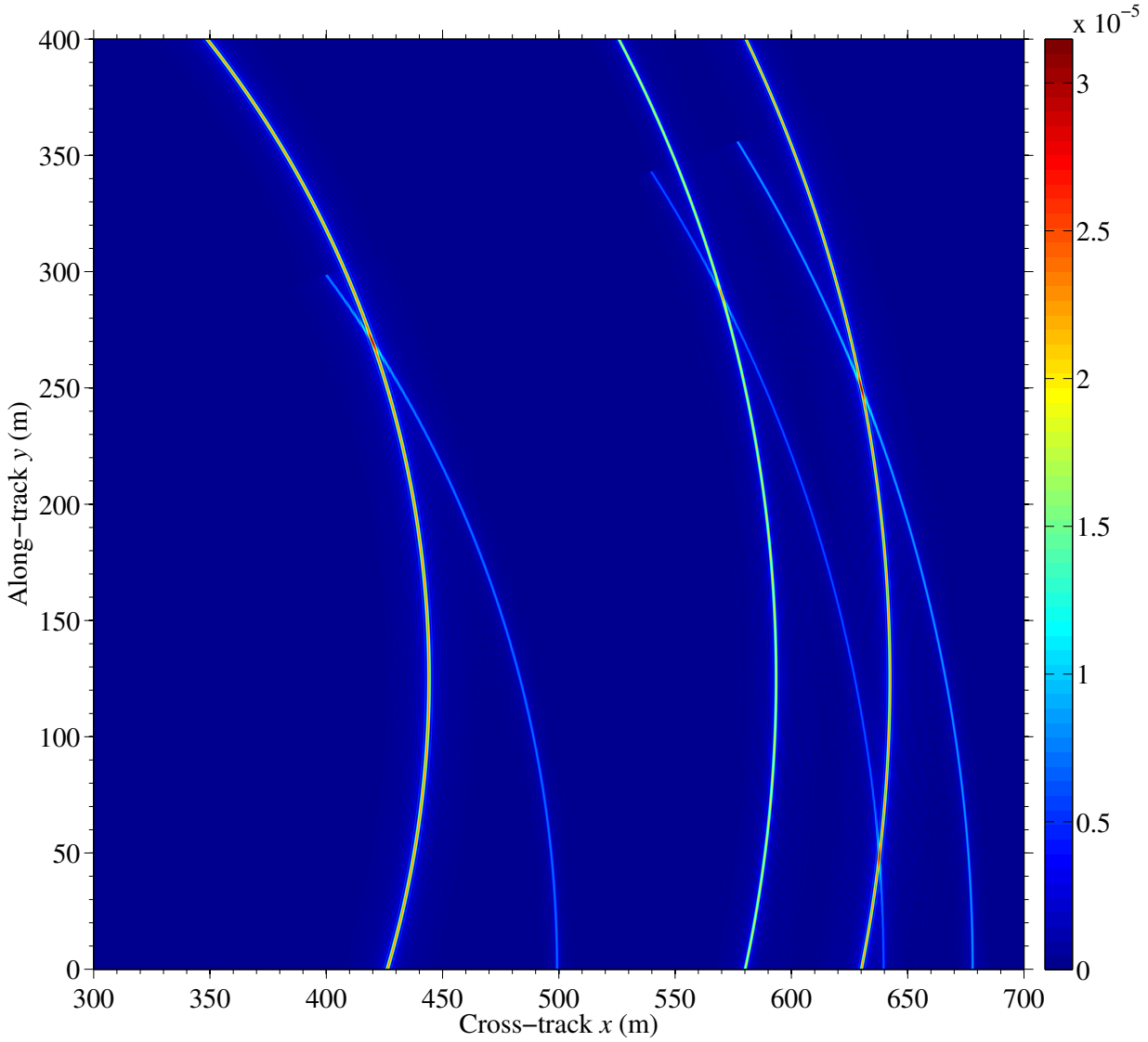

Figure 2.16: BPJ frame 2 of 5. The brighter concentric circular arcs are the backprojected contribution from the RC data shown in Fig. 2.15. The intersection points in the top half of this image indicate the targets' true positions. Note that the new iso-range arcs in this frame are centered on the new spatial position from which the pulse was transmitted.

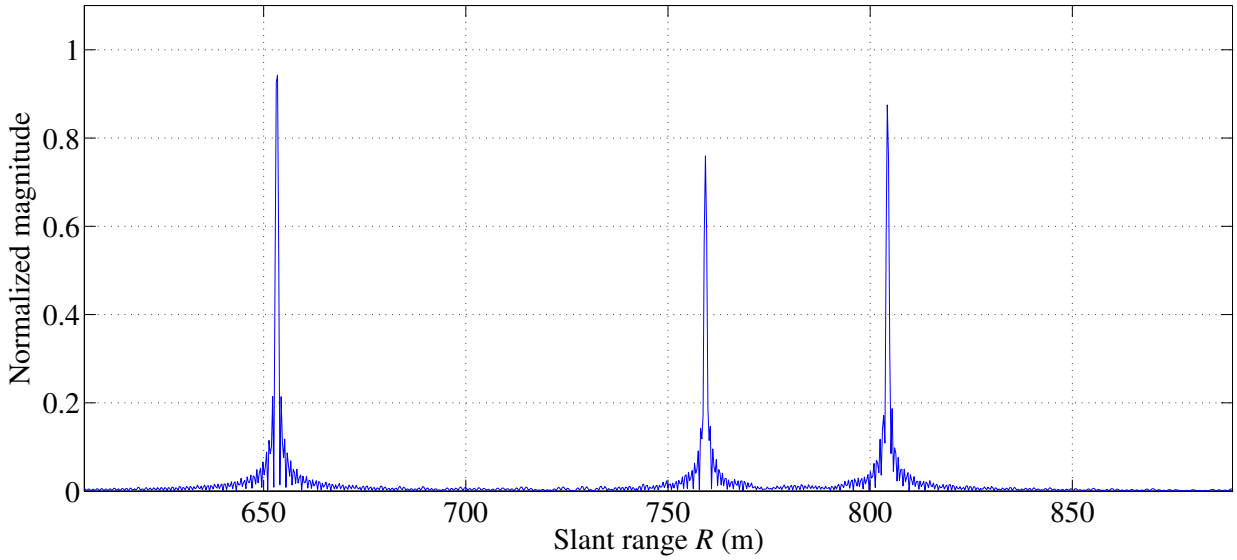

Figure 2.17: RC data magnitude, frame 3 of 5. This RC data makes the BPJ contribution shown in Fig. 2.18.

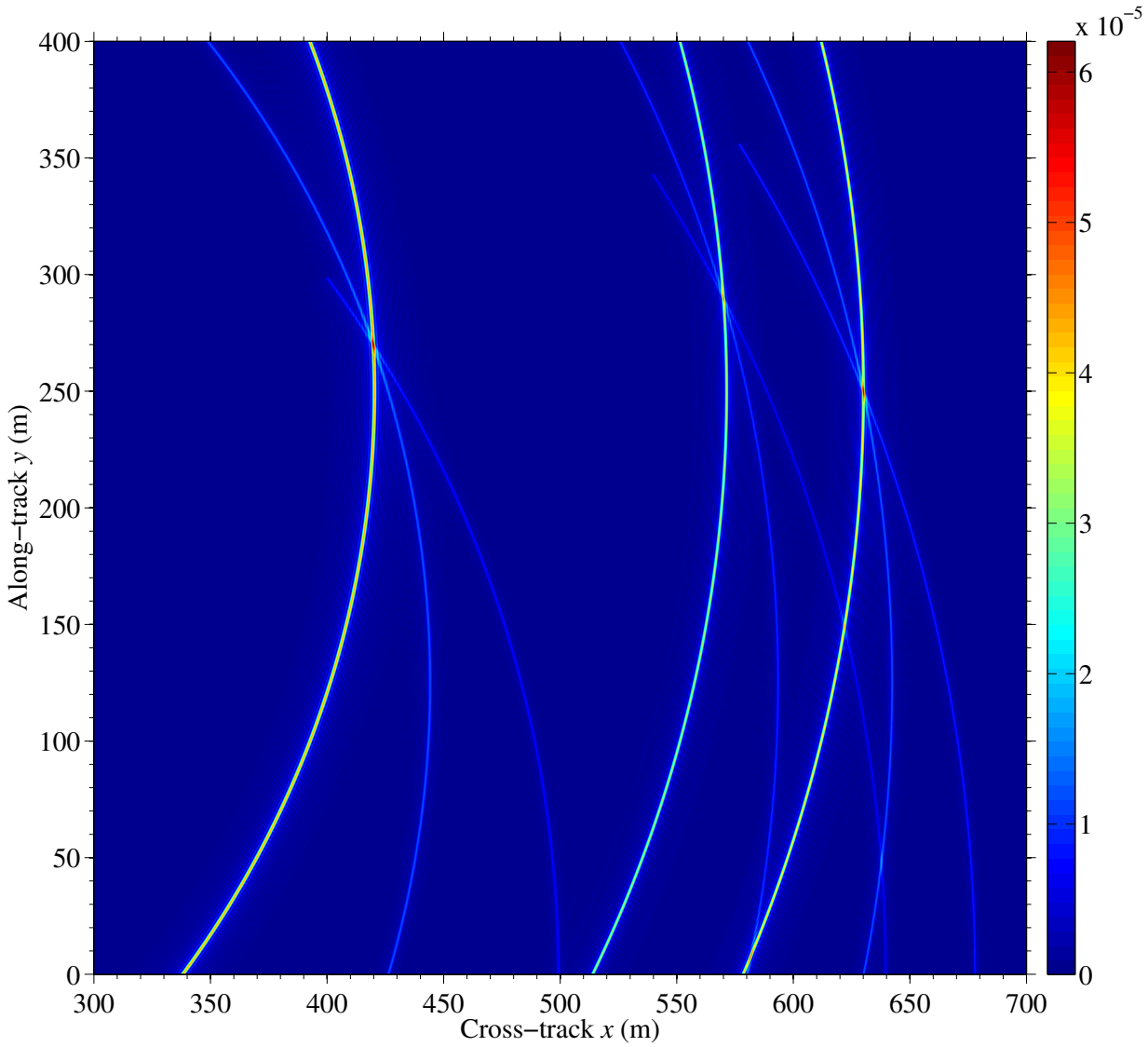

Figure 2.18: BPJ frame 3 of 5. The brighter concentric circular arcs are the backprojected contribution from the RC data shown in Fig. 2.17. The intersection points in the top half of this image indicate the targets' true positions.

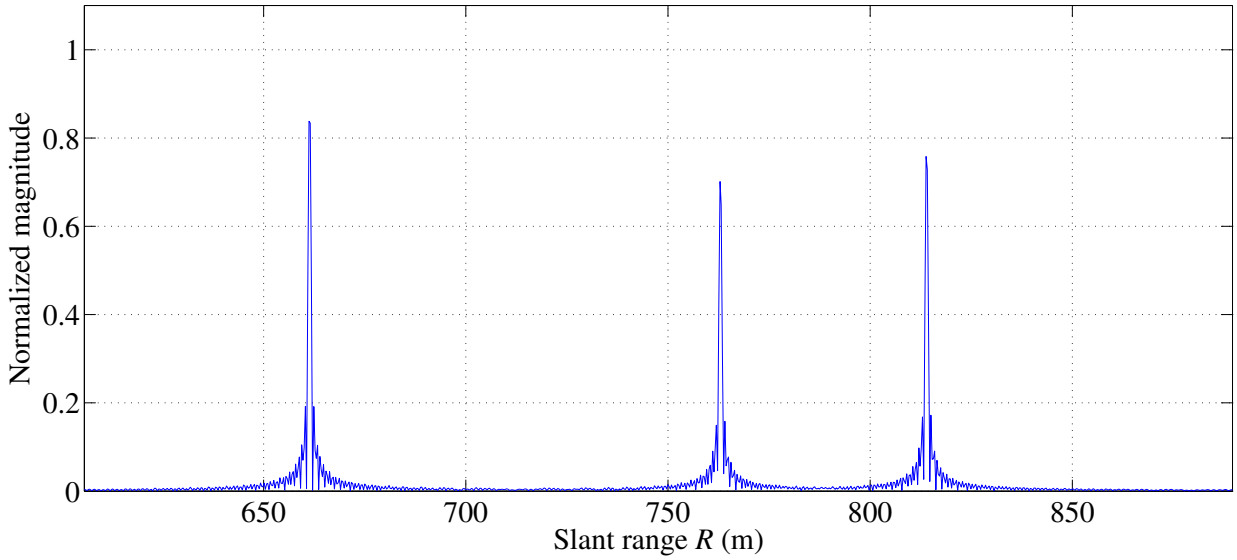

Figure 2.19: RC data magnitude, frame 4 of 5. This RC data makes the BPJ contribution shown in Fig. 2.20.

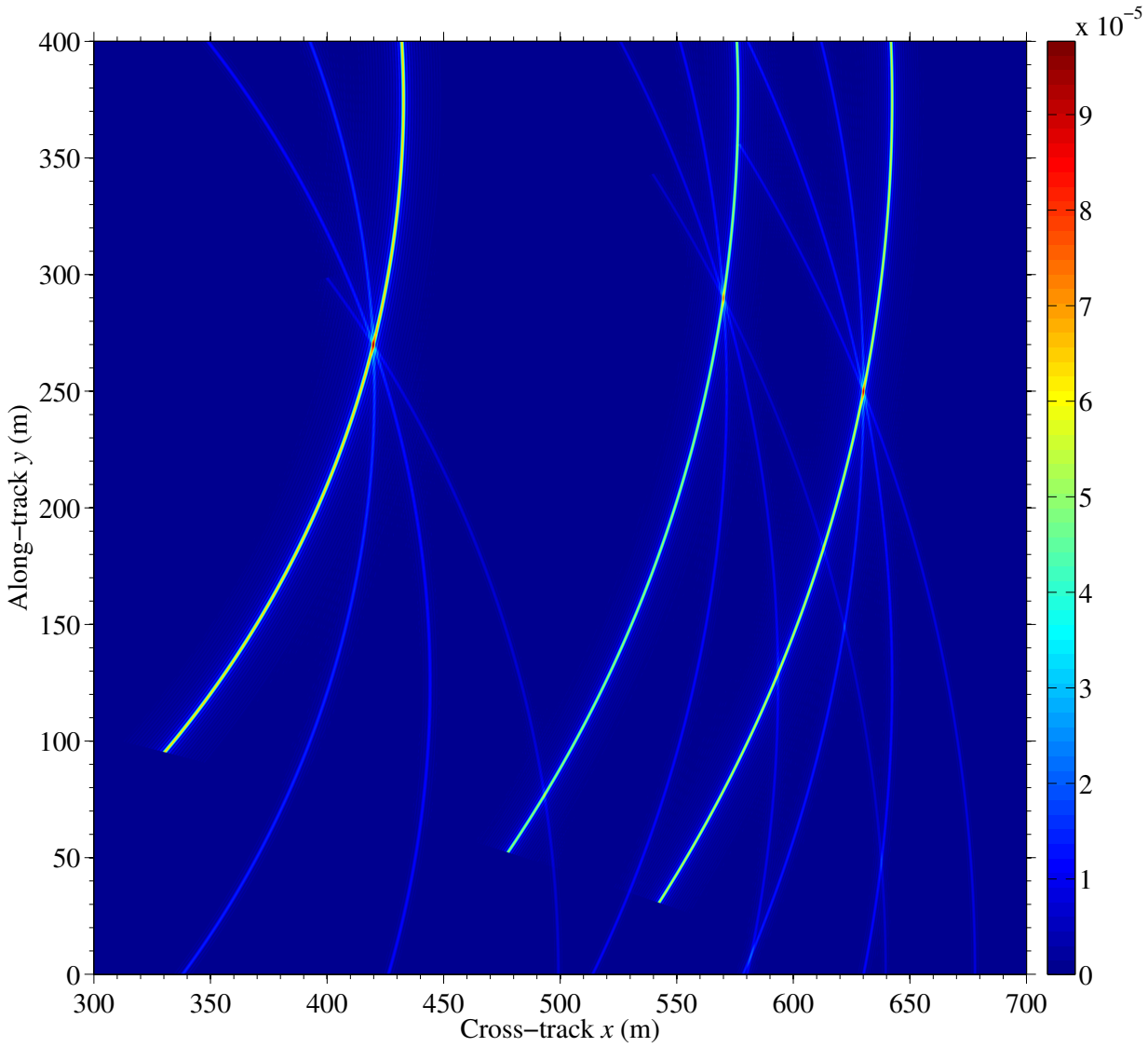

Figure 2.20: BPJ frame 4 of 5. The brighter concentric circular arcs are the backprojected contribution from the RC data shown in Fig. 2.19. The intersection points in the top half of this image indicate the targets' true positions.

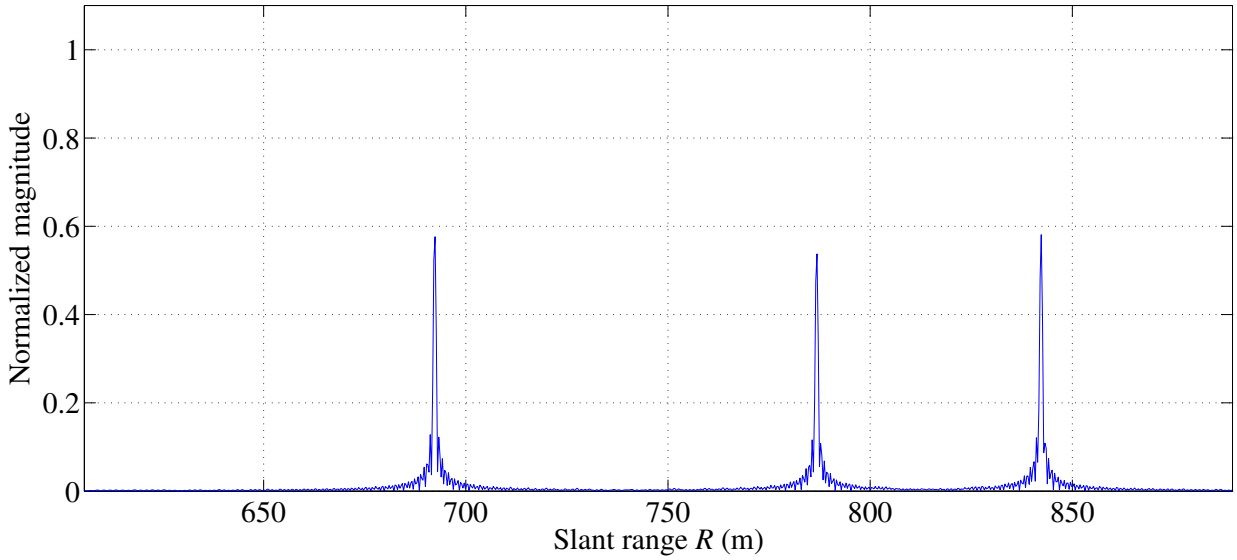

Figure 2.21: RC data magnitude, frame 5 of 5. This RC data makes the BPJ contribution shown in Fig. 2.22.

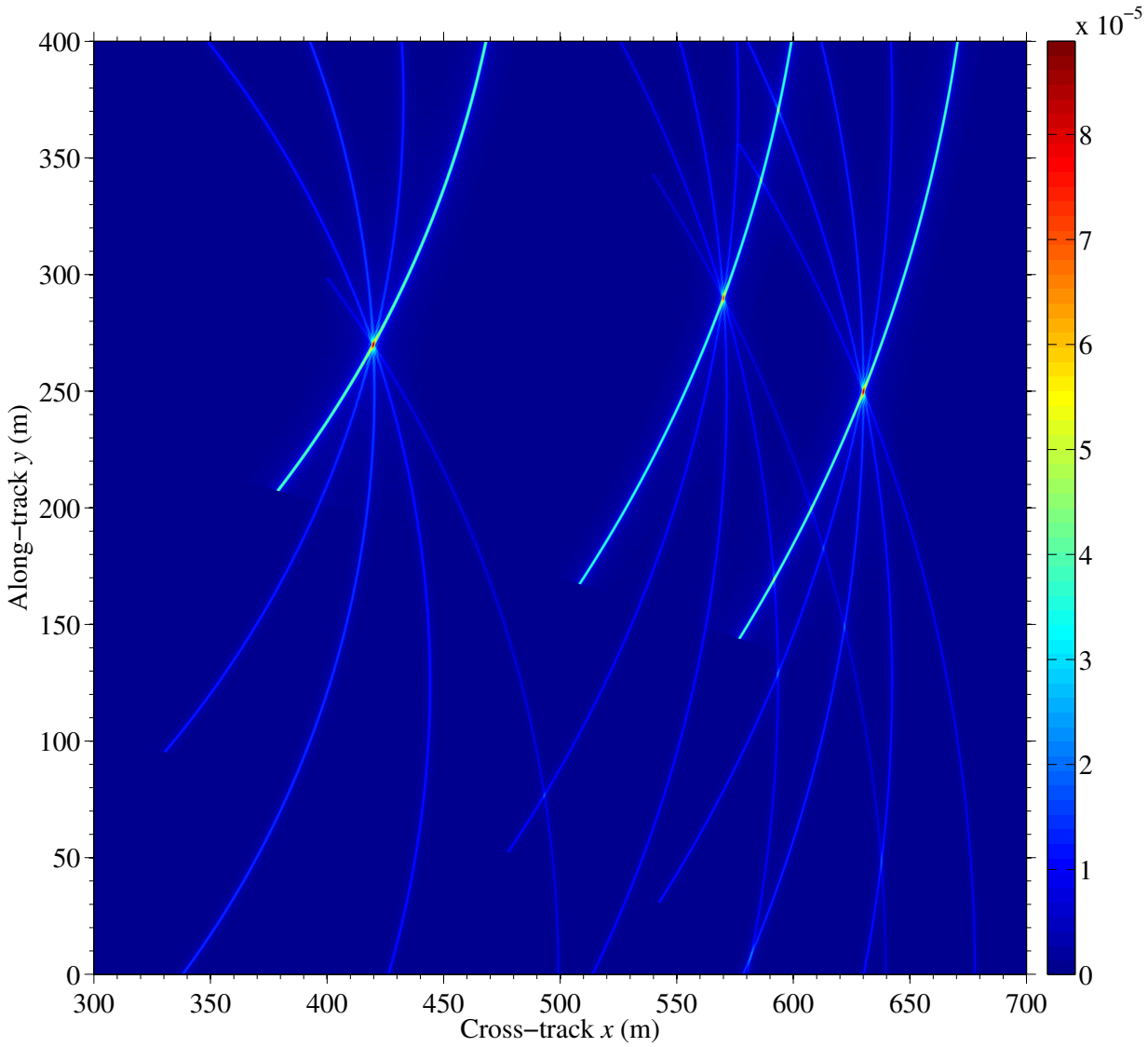

Figure 2.22: BPJ frame 5 of 5. The brighter concentric circular arcs are the backprojected contribution from the RC data shown in Fig. 2.21. The intersection points in the top half of this image indicate the targets' true positions.

2.4.2 The SAR Impulse Response

From a SAR perspective, a point target represents an impulse to the SAR processing chain. The SAR impulse response (IPR) includes both the target's phase history and its appearance in the final output image, and either one or both together can be considered to be the SAR IPR. Figure 2.23 shows the SAR IPRs for the three point targets whose image formation process was demonstrated in Figs. 2.13 through 2.22.

Figure 2.24 shows spatially oversampled (1cm x 1 cm pixels) close-ups of the SAR IPR for the center target in Fig. 2.23 for three different integration angles, and is representative of all point target images. Table 2.1 lists the relevant details for the three antenna geometries used for the IPR images in Fig. 2.24. Different antenna sizes produce different beamwidths, which in turn allow different maximum synthetic aperture lengths and integration angles for a pixel in stripmap SAR, which ultimately determines the best achievable azimuth resolution in a SAR image [1]. The purpose of Fig. 2.24 is to illustrate the direct relationship between antenna size and azimuth resolution, as well as to show the fine structure of the SAR IPR for a point target, and its sidelobes in the range and azimuth directions. In actual SAR imagery, this sidelobe phenomenon is observable in images of corner reflectors, which very accurately model true point targets. Figure 2.25 shows an actual SAR image of corner reflectors and an optical photograph of the same target scene.

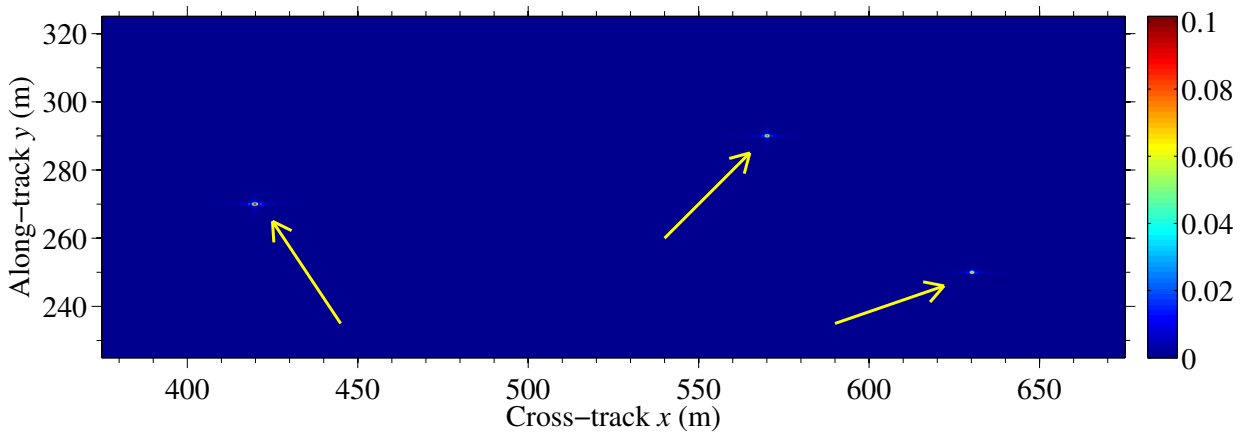

Figure 2.23: Final image of three stationary point targets, formed from the BPJ algorithm demonstrated in Figs. 2.13 through 2.22. North is up.

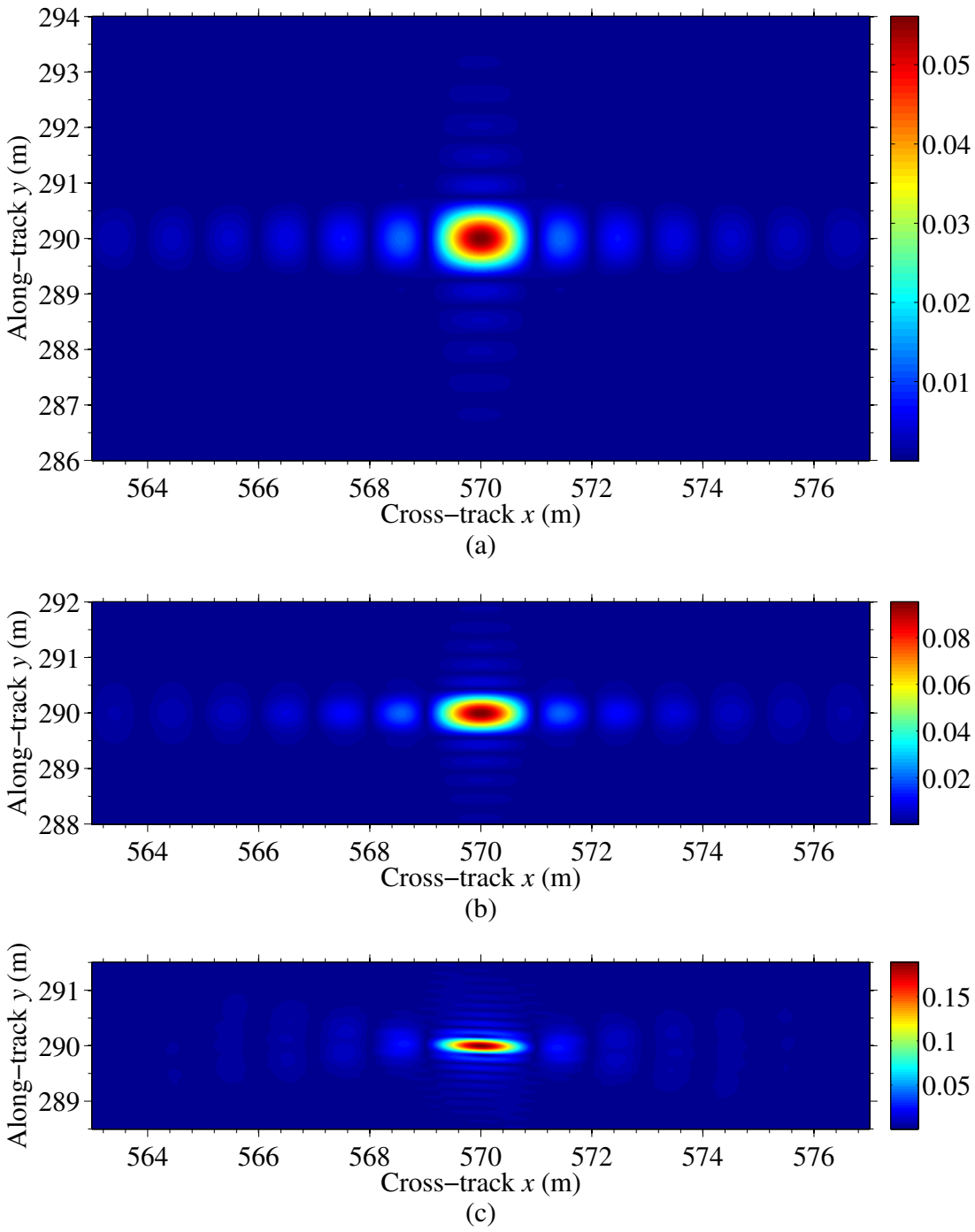

Figure 2.24: Close-ups of the center target in Fig. 2.23 for three different antenna sizes. North is up. These images, which are all on the same physical scale, were made with the BPJ algorithm. These images use 1cm x 1cm pixels to oversample and show the fine structure of the SAR IPR for a point target, and its sidelobes in range and azimuth. The same target is imaged with three different antenna sizes, producing three different beamwidths, and therefore three different maximum integration angles. Table 2.1 lists the relevant details for the three antenna sizes and beam geometries. This figure and Table 2.1 together illustrate the direct relationship between antenna size and SAR azimuth resolution. The ground range resolution is the same in all three images, because the target position and the LFM bandwidth are the same in all three images.

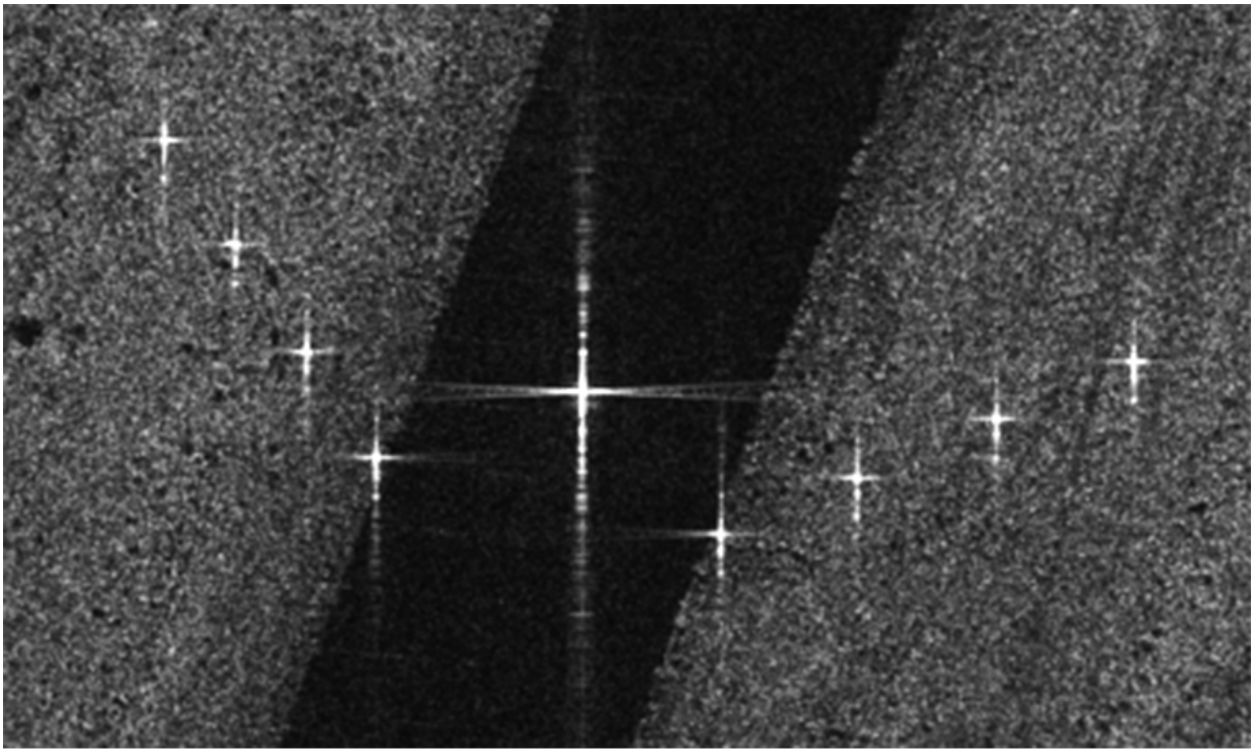

(a)

(b)

Figure 2.25: Corner reflectors on and next to a runway. Panel (a) is a SAR image of the target scene, and panel (b) is an optical photograph of the same area. In the SAR image, note the sidelobe structures of the corner reflector, similar to the simulated SAR IPRs for the point target in Fig. 2.24. (Courtesy Sandia National Laboratories)

Table 2.1: Antenna and beam geometries
for the IPR images in Fig. 2.24.

IPR image	Antenna size	Beamwidth
Figure 2.24a	1 m	10 deg
Figure 2.24b	60 cm	17 deg
Figure 2.24c	21 cm	50 deg

As Table 2.1 and Fig. 2.24 indicate, and as stated previously, azimuth resolution and antenna size are directly related for SAR, and do not depend on the range to the pixel or target. Such a relationship is remarkable, given that the azimuth resolution of a real-aperture radar (RAR) depends on both the physical beamwidth θ_{3dB} and the target range R. The physical beamwidth in turn has an inverse relationship to the aperture size D, given by the equation

$$\theta_{3dB} = a\frac{\lambda}{D} \text{ rad}, \tag{2.13}$$

where a is a scale factor that depends on the physical aperture shape and the amplitude and phase illumination windows used [43]. For a uniformly illuminated rectangular aperture, a is approximately 0.88, while for a uniformly illuminated circular aperture, a is approximately 1. For the sake of convenience, a is set to 1 for this thesis.

Equation (2.13) applies to all passive and active remote sensing instruments, including the human eye, telescopes, and radar antennas. For example, if the wavelength λ is 630 nm (red light), and the aperture size is 3 mm (pupil of a human eye on a sunny day), Eq. (2.13) predicts a beamwidth of 0.012°. This means that in theory, from a kilometer away a human eye can resolve two objects 21 cm apart in azimuth. In contrast, typical parameters for a radar system might be a 30 cm wavelength (L-band) and a 1 meter antenna size for airborne applications. Eq. (2.13) predicts a radar beamwidth of 17°, which has an azimuth resolution of 300 m for a target range of 1 km.

The equations for RAR and SAR azimuth resolutions ΔAZ [1] are

$$\Delta AZ_{RAR} = 2R\sin\left(\frac{1}{2}\theta_{3dB}\right) \approx \theta_{3dB}R = \frac{\lambda R}{D}, \tag{2.14}$$

$$\Delta AZ_{SAR} = \frac{D}{2}. \tag{2.15}$$

The approximation made in Eq. 2.14 is the small-angle approximation, which applies when a narrow beamwidth is used. Note the opposing dependencies of azimuth resolution ΔAZ on the physical antenna size D in Eqs. (2.14) and (2.15). This is the fundamental difference between SAR and RAR.

A basic truth for any engineering aspect of a technical system, such as radar, is that performance improvements in any area nearly always carry a cost in terms of unavoidable tradeoffs in other areas. For SAR and the azimuth resolution improvement obtained by decreasing the antenna size, the tradeoff comes in the form of several penalties imposed by the wider physical beam that radiates from the smaller antenna. First, the SNR is severely reduced [1,58] because a fixed amount of signal energy is spread over a wider area, essentially "diluting" the radar beam intensity. This penalty can be paid in the form of either accepting the lower SNR and the subsequent image quality degradation, or using a higher power transmitter to compensate. The Doppler bandwidth also increases for a wider beam, which raises the lower bound on the PRF [see Eq. (2.8) in Section 2.2.4]. The higher minimum PRF and the wider beam both increase the data processing load [58]. This is just one example of the classic problem of engineering tradeoffs, and is characteristic of the challenges involved in designing a radar or any other advanced technical system.

2.4.3 Advantages of Backprojection

So far this section (2.4) has outlined the technical details of how BPJ works, the computational expense of BPJ, and the benefits and tradeoffs involved in decreasing the antenna size for better azimuth resolution. Some advantages are now discussed that make the BPJ imaging algorithm superior to other imaging techniques. The most important advantages of BPJ include automatically accounting for range migration, nearly perfect motion compensation for any linear or nonlinear flight path, excellent focus for any integration angle as described previously, its mathematical simplicity, and its conduciveness to parallel processing.

The mathematical simplicity and parallel nature of BPJ have already been covered. The other three advantages listed all depend on having an accurate platform motion history. This thesis assumes an exact flight path record, which allows the BPJ algorithm to accurately compute the slant range from each pulse position in the sky to every pixel on the ground. This in turn enables accurate echo phase-shift computations between each pulse and every pixel. With this phase information,

BPJ achieves its excellent focus over the entire integration angle for all pixels. Range migration and motion compensation, however, each deserve a more detailed discussion to put BPJ's strengths in these areas into context.

Range Migration

One of the oldest problems in SAR image formation is the issue of *range migration*, or the apparent motion of a target through one or more range resolution cells during image formation. A range resolution cell is a slant range difference equal to the radar's range resolution ΔR. For older SAR image formation algorithms, proper image focus requires the target or pixel to remain within the same range resolution cell during the coherent processing interval (CPI).

A CPI in conventional radars is the number of pulses used to make a detection decision. A detection decision made on the basis of a single pulse may not be reliable, especially if the target's SNR is low. Because of this, multiple pulses are coherently integrated to boost the SNR by a factor equal to the number of pulses used. The coherently integrated sum of these pulses is then used to make a much more reliable detection decision [1, 2]. For SAR, a CPI is the number of pulses, or the synthetic aperture length, used to compute an image pixel [14].

During SAR image formation using older algorithms, if the slant range to a target or pixel changes by more than the radar's range resolution during a CPI, it causes focusing problems that require corrective action to compensate [8, 10, 14, 15, 59, 60]. BPJ does not suffer from the range migration problem. As described in the previous discussion on the BPJ equation (Section 2.4.1), each pulse's RC data record makes contributions to the SAR image by computing the slant range from that pulse position to each illuminated pixel. The computed slant range for a given pixel is then used to sample that pulse's RC data at the appropriate timing index, and then reverse-phase-shift the RC data sample before adding it to the image pixel value. As the pixel traverses multiple range resolution cells, the BPJ algorithm automatically accounts for it by sampling the RC data at the correct timing index, based on the pixel's current slant range for a given pulse. In other words, BPJ's inherently optimal focus eliminates the range migration issue.

Motion Compensation: Deviations from a Straight Flight Path

Older SAR image formation algorithms require the use of a "reference function", or an expected flight path, to perform the necessary image formation computations. For these older algorithms, proper image focus depends on the SAR platform's adherence to the assumed flight path, which is typically a straight line. Any deviations from this ideal trajectory require phase adjustments to bring the radar data back into compliance with the reference function flight path [10, 42, 54, 58, 61–67]. This process is called *motion compensation*.

BPJ inherently can achieve perfect motion compensation because it makes no assumptions about its flight path. Instead, it relies on the flight path data as recorded by the GPS and IMU equipment on the SAR platform. Even if high-speed fluctuating cross winds make the SAR's path through the sky resemble a noisy sine wave, BPJ still makes accurate slant range computations to the pixels as long as the motion history is accurately recorded. No phase adjustments to the data are needed to correct for unanticipated variations in the SAR platform's path. Other factors however, such as cable delays, may require corrective data manipulation.

The ability of BPJ to inherently handle any arbitrary flight path and antenna pointing direction is sufficiently noteworthy to merit an example of such imagery. In [54], Othmar Frey does a detailed comparison between SAR imagery made using BPJ, and another imaging algorithm called "Patchwise frequency-domain processing and mosaicking". Both algorithms use the same experimental SAR data sets to form their respective images. The SAR data was collected over four different flight tracks over a military airfield at Emmen, Switzerland. One was a quasi-linear flight path to be used as a reference, and the other three flight tracks were designed to push the limits of SAR image formation. The other three flight tracks respectively included a double bend, a dive, and a 90° curve during data collection. Figure 2.26 shows two orthogonal views of the four flight tracks, Fig. 2.27 shows the BPJ images from the four flight paths, and Fig. 2.28 shows an optical satellite image of the airfield. Figures 2.26 and 2.27 both come from [54], and Fig. 2.28 comes from Google Earth.

Only the BPJ imagery from Frey's analysis is shown here. The imagery from the other algorithm suffered from severe defocusing and image ghosting for the three nonlinear flight tracks, whereas the BPJ images in Fig. 2.27 focused extremely well in all cases. The interested reader is referred to [54] for more information about the study.

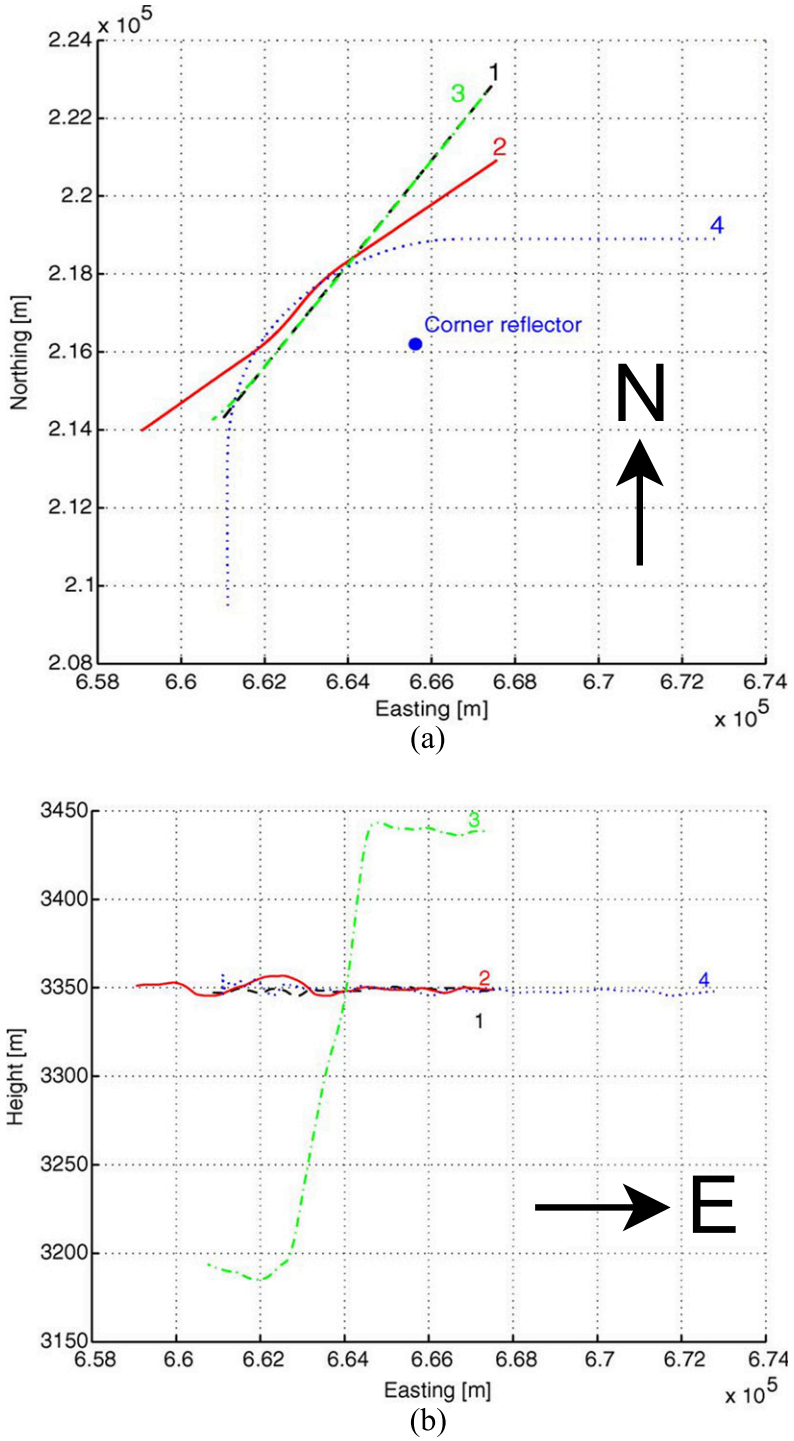

Figure 2.26: The four flight tracks used in Frey's analysis of BPJ's ability to handle SAR data from atypical flight paths. Panel (a) is a top-down view with north up, and panel (b) is a horizontal view looking north, with east to the right. Flight track 1 is a quasi-linear reference track, track 2 has a double bend, track 3 has a dive, and track 4 has a 90° curve. For the dive in track 3, an analysis of the figures here appears to indicate a dive angle of approximately 4.4° below the horizon. The images formed from these flight tracks are in Fig. 2.27. (Source: [54])

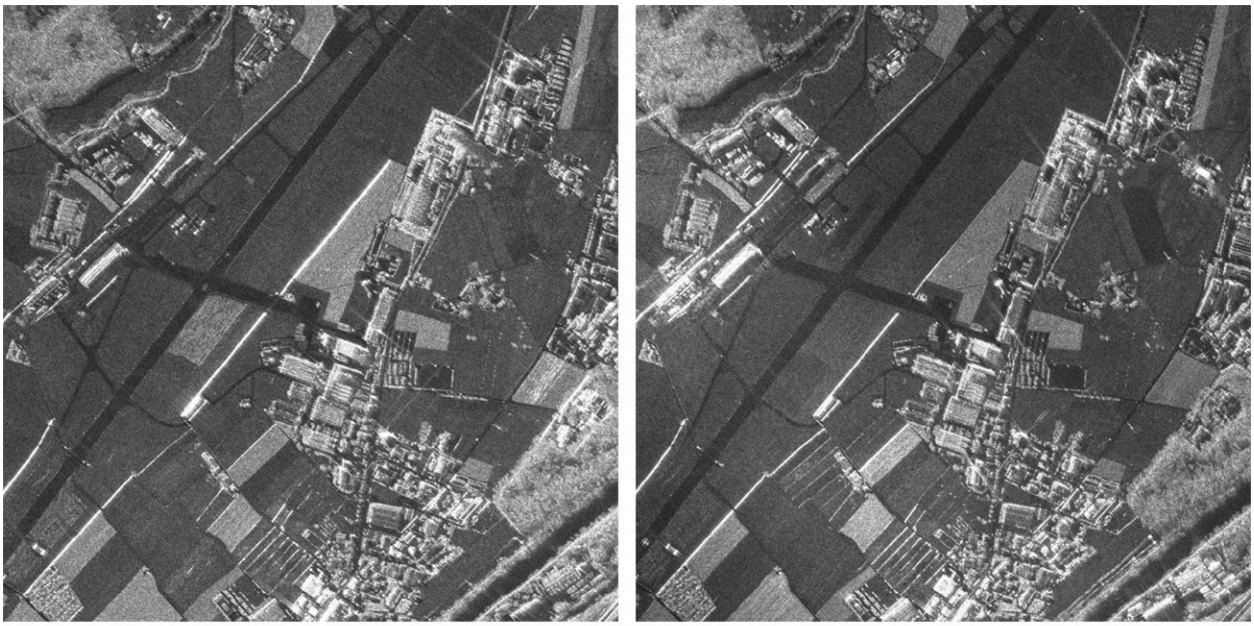

(a) - Quasi-linear reference track

(b) - Double bend

(c) - Dive

(d) - 90° curve

Figure 2.27: BPJ images from Frey's SAR experiment with the nonlinear flight tracks in Fig. 2.26. North is up. The label under each image respectively indicates the relevant atypical geometry of the path flown to collect the SAR data for that image. Note the excellent focus in all cases. (Source: [54])

Figure 2.28: Optical satellite image of the airfield at Emmen, Switzerland, shown in the BPJ images of Fig. 2.27. North is up. (Source: Google Earth)

CHAPTER 3. HOW MOVING TARGETS APPEAR IN SAR IMAGES

Since this thesis is a study on GMTI, it is helpful for the reader to understand how target motion effects in optical photography differ from how SAR imagery is affected by moving targets. As stated in Chapter 1, SAR image focus requires the ground scene to remain stationary while the data is collected. If a target moves during data collection, its phase history differs from that of the stationary landscape features around it [13], and the target's appearance in the SAR image defocuses in proportion to the severity of its motion. The visual defocusing effect of a moving target's image in SAR can be very different from that of excessive target speed in optical photography. An example of this in optical imagery is a picture of a tracer round fired from a rifle. A tracer round is essentially a bullet that glows very brightly after being fired so its path can be followed visually. Figure 3.1 shows an example of this.

When a camera takes a picture, it opens its shutter to allow light in through a lens and onto the film (older cameras) or pixel array (digital cameras), where the image focuses. During the time the shutter is open (the exposure time), if anything in the scene moves fast enough, it appears blurred in the image. A fast shutter speed means the exposure time is very short, and a slow shutter speed means the exposure time is longer. When photographing a tracer round fired from a rifle, the round travels so fast that the shutter speed on most cameras is too slow to capture a sharp image of it. Instead, the brightly glowing tracer leaves a well-defined streak in the image because of its motion during the exposure.

In the optical photograph in Fig. 3.1, the bright streak left by the fast-moving tracer round clearly indicates its initial position and its direction of travel, especially in the context of the rest of the photo. This is because optical photography is noncoherent and has fine angular resolution. But due to SAR's wider beamwidth and coherent nature, a moving target's image can defocus in a way completely different than for optical photography.

Figure 3.1: A tracer round fired from a rifle. (Courtesy Department of Defense)

In SAR imagery, the particular way in which a moving target's image defocuses depends on exactly how the target moves relative to the SAR. Along-track and cross-track target motion each affect the target's image differently [13, 68]. Along-track motion smears the target image in a manner similar to the tracer photo in Fig. 3.1, while cross-track motion shifts the target image to a new position in the SAR image while generally preserving its focused appearance. These effects are explained in greater detail in the next two sections, and are illustrated with examples of simulated and actual SAR images (Figs. 3.2 through 3.15).

The rest of this chapter is organized as follows: Section 3.1 describes the effects of along-track target motion in SAR imagery, and Section 3.2 describes cross-track target motion effects. Section 3.3 then describes how to focus a moving target in SAR data using a slightly modified BPJ algorithm and *a priori* knowledge about the target.

The simulated SAR images in this chapter need some prior clarification to be fully understood. In Figs. 3.2 through 3.15, some of the simulated images include green arrows that indicate the true path traveled by the target while radar data was collected. Depending on the radar beamwidth and initial target position, the moving target(s) may or may or may not be visible to the radar beam when the radar is turned on at time zero. Clearly, a target produces a radar response only while it is illuminated by the radar. A target may move away from its initial time-zero position by the time the SAR platform flies forward far enough to illuminate it, and as the SAR flies past, the target may leave the mainlobe before the data collection finishes. Therefore, a target may be visible for only part of the radar scan, especially for narrow beamwidths. In the following simulated SAR images of moving targets, green arrows indicate the true target paths. Dark green arrows indicate the total path traveled by the target during data collection, and lighter green arrows indicate the part of the path traveled while the target was illuminated by the radar. Green and red squares at the tail and head of each arrow respectively indicate the target's initial and final positions. Dark green and red squares correspond to the entire data collection, and lighter green and red squares correspond to the time the target was illuminated by the radar beam.

3.1 Along-Track Target Motion

For a target whose motion includes an along-track component, its SAR IPR smears out in the along-track direction [13, 68, 69]. For small integration angles, the smeared image resembles

a linear blur, an effect roughly comparable to that of the tracer round photo in Fig. 3.1. For wide integration angles, the smeared-out target image curves visibly. These effects are shown in Figs. 3.2 through 3.6. Figures 3.2 and 3.3 show this smearing effect in simulated SAR imagery, and Figs. 3.4 through 3.6 show the effect in actual SAR imagery.

For a target moving in the along-track direction, the integration angle used during image formation determines how much the target's smeared image curves, and the target's direction of travel determines the direction in which the image curves. If the target moves in the same direction as the SAR platform, its image curves hyperbolically and concave outward, away from the radar. For along-track motion in the opposite direction, the smeared target image is elliptically curved and concave inward toward the radar [13]. The mathematical proof of these statements is beyond the scope of this thesis, but the interested reader is referred to Jao's paper [13]. The simulated SAR image in Fig. 3.2 shows the effect of various target speeds for targets moving in both opposing along-track directions. Figure 3.3 illustrates the different curvatures that result from using different integration angles when the target moves in the same direction as the SAR platform. For target motion in the opposite direction, the results are the same except for the direction of curvature as described previously.

In Figs. 3.2 and 3.3, which depict strictly along-track target motion, each smeared target image is centered in azimuth about the illuminated portion of the target's motion as indicated by the lighter green arrow. Also note that where the target image is visibly curved, the centerpoint of the target's illuminated path is tangent to the apex of the target image's curved smear. This effect is present for all cases of along-track target motion, but is especially noticeable when the smeared image curves more due to a wider integration angle. The BPJ integration angle is generally chosen to be equal to the radar's half-power (-3dB) azimuth beamwidth, because a target is most visible to the radar when it is illuminated by the radar beam's mainlobe. For this reason, and to simplify the following discussion, the target's path traveled while illuminated within the mainlobe's half-power beamwidth is referred to as the target's *radar-visible path*.

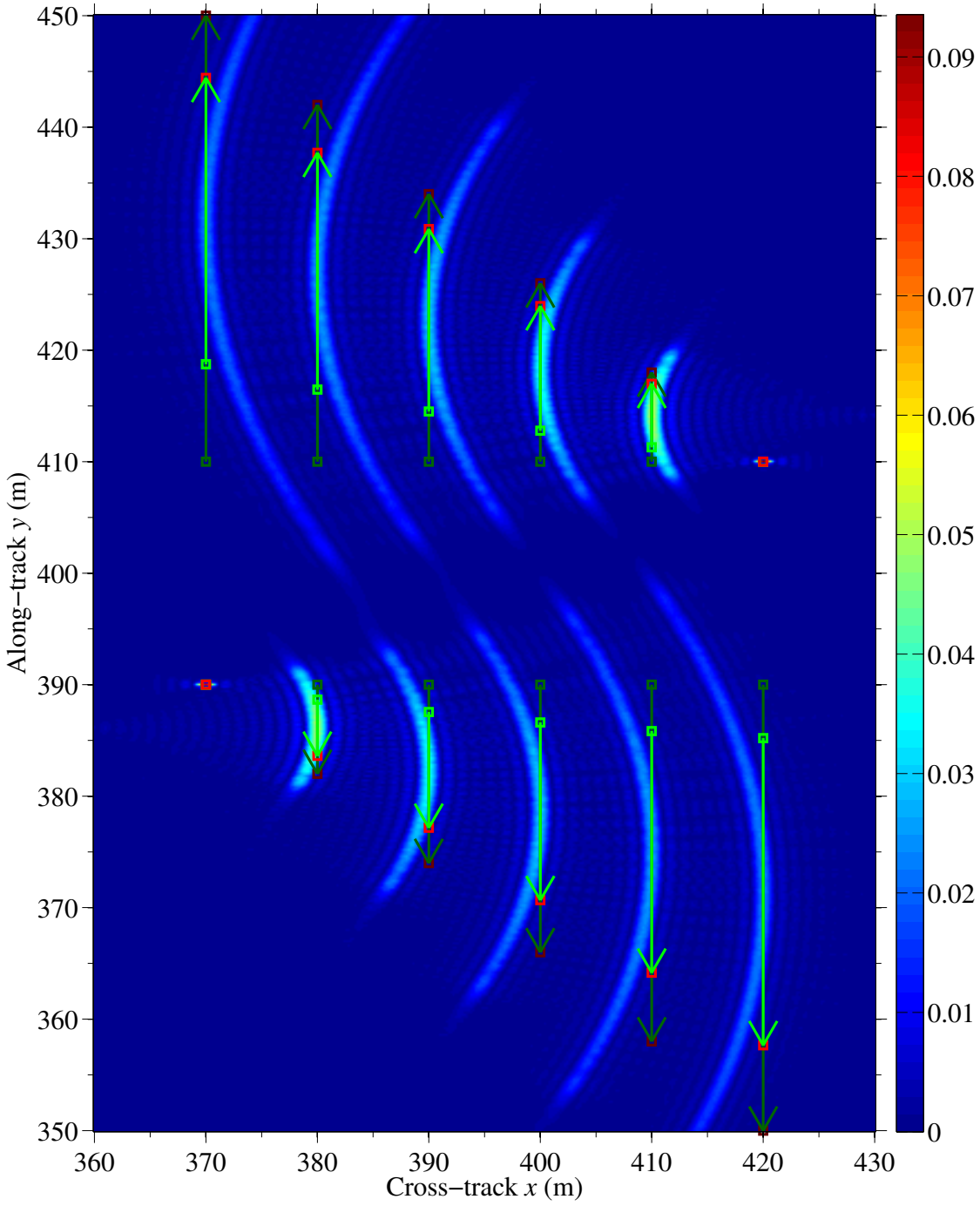

Figure 3.2: Simulated SAR image of 12 targets showing the effects of along-track target motion. North is up. The SAR platform is off-image to the left, looking to the right and flying north at 50 m/s, and the integration angle is 50°. The six targets in the top half travel in the same direction as the SAR platform, and their images smear in the along-track direction with hyperbolic curvatures that are concave outward away from the radar. In the bottom half, the targets move in the opposite direction as the SAR and exhibit the same along-track image smearing, except with curvatures that are elliptical and concave inward toward the radar [13]. Increasing target speed produces a longer smear. The target speeds range from stationary to 2.5 m/s, in 0.5 m/s increments.

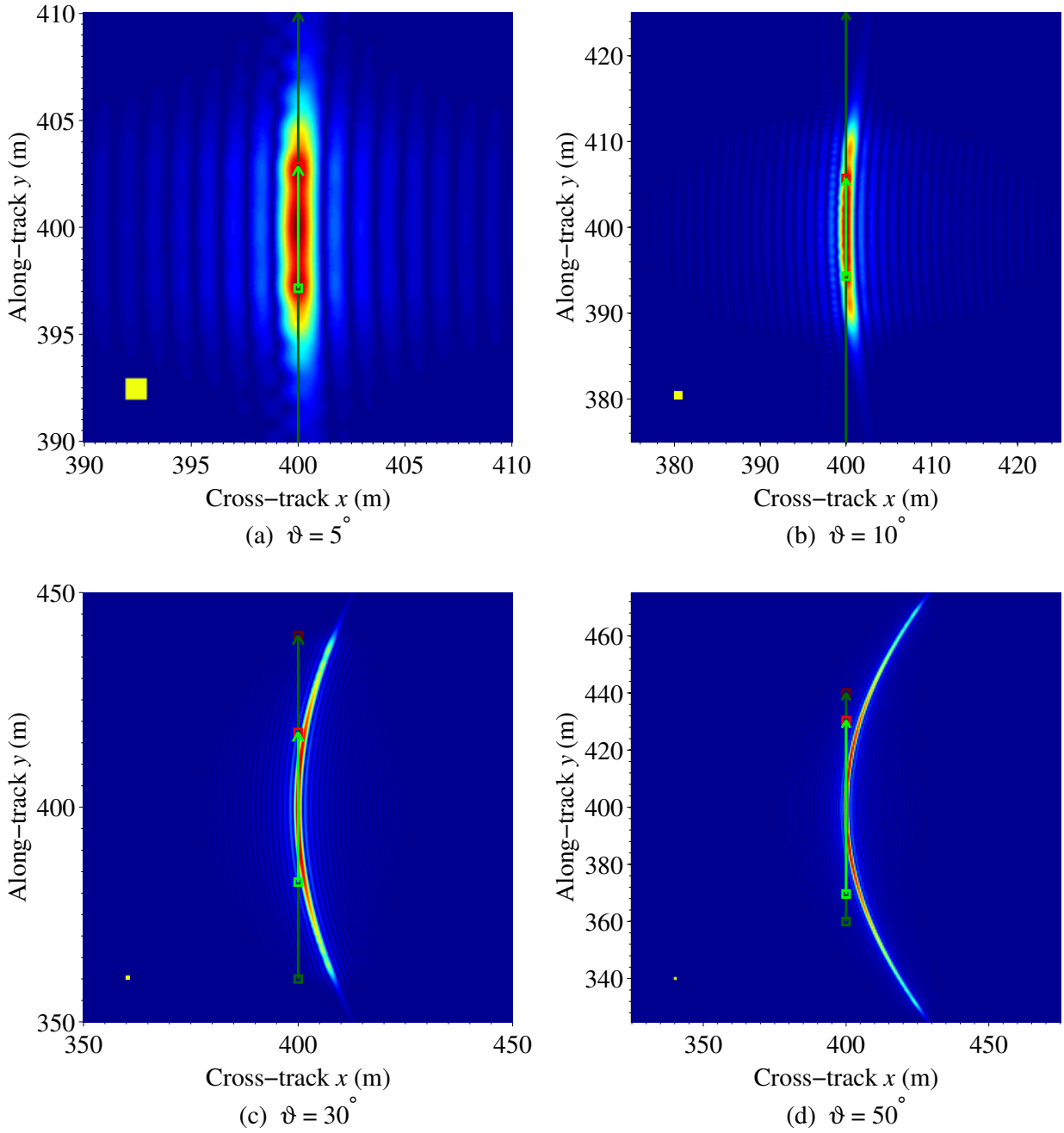

Figure 3.3: A simulated comparison of various integration angles used to image the same target on the same trajectory each time, moving in the same along-track direction as the SAR. North is up. The SAR platform is off-image to the left, looking to the right and flying north at 50 m/s. The integration angles range from 5° to 50°, and are given below each image. The wider the integration angle ϑ, the more curved the target's IPR image appears. The smeared target image appears to trace out the same hyperbolic curve in all cases, with wider values of ϑ smearing the image out further along the curve. For a narrow integration angle, the smearing effect appears almost linear. In addition to the axis scales, each image contains a yellow square in the lower left indicating a 1 m^2 patch of ground, showing how the size of the smeared image increases with increasing ϑ. The target's velocity is 5 m/s traveling toward the top of the page, as indicated by the light green arrow in each image.

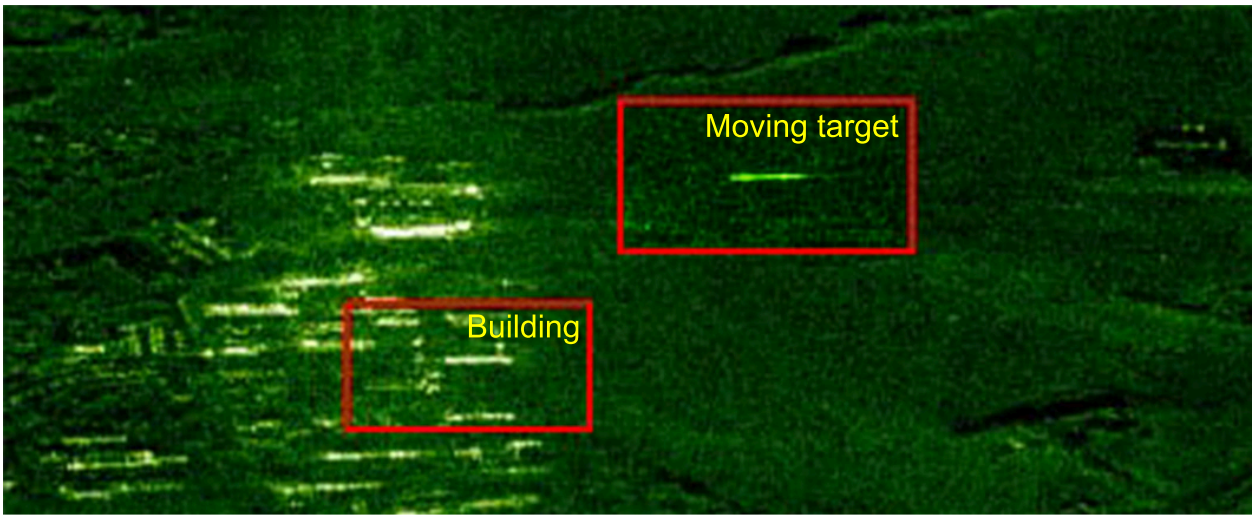

(a)

(b)

Figure 3.4: Panel (a) is an actual SAR image showing the effect of along-track target motion. The flight track is horizontal with respect to the image orientation. The red boxes show the similarity between an along-track moving target signature and a stationary building with a similar appearance due to its shape. The illumination direction is not given in the source paper, but based on the shadows in the image, the illumination angle appears to be from below the image looking toward the top. The integration angle is not given either, but based on the apparent lack of curvature for the moving target's image, it is possible the integration angle is small. Panel (b) is a photo of the moving target, a car with a roof-mounted corner reflector aimed in the SAR's general direction. (Source: [70])

Figure 3.5: SAR BPJ image of the coastal town of Simrishamn in southern Sweden, with south up. The SAR platform is off-image to the left, looking to the right and flying toward the top of the page, with an integration angle of 110°. In the upper left part of the image in the black box, a sea vessel moving in the same along-track direction as the SAR leaves an outward-curved hyperbolically smeared image. (Source: [33])

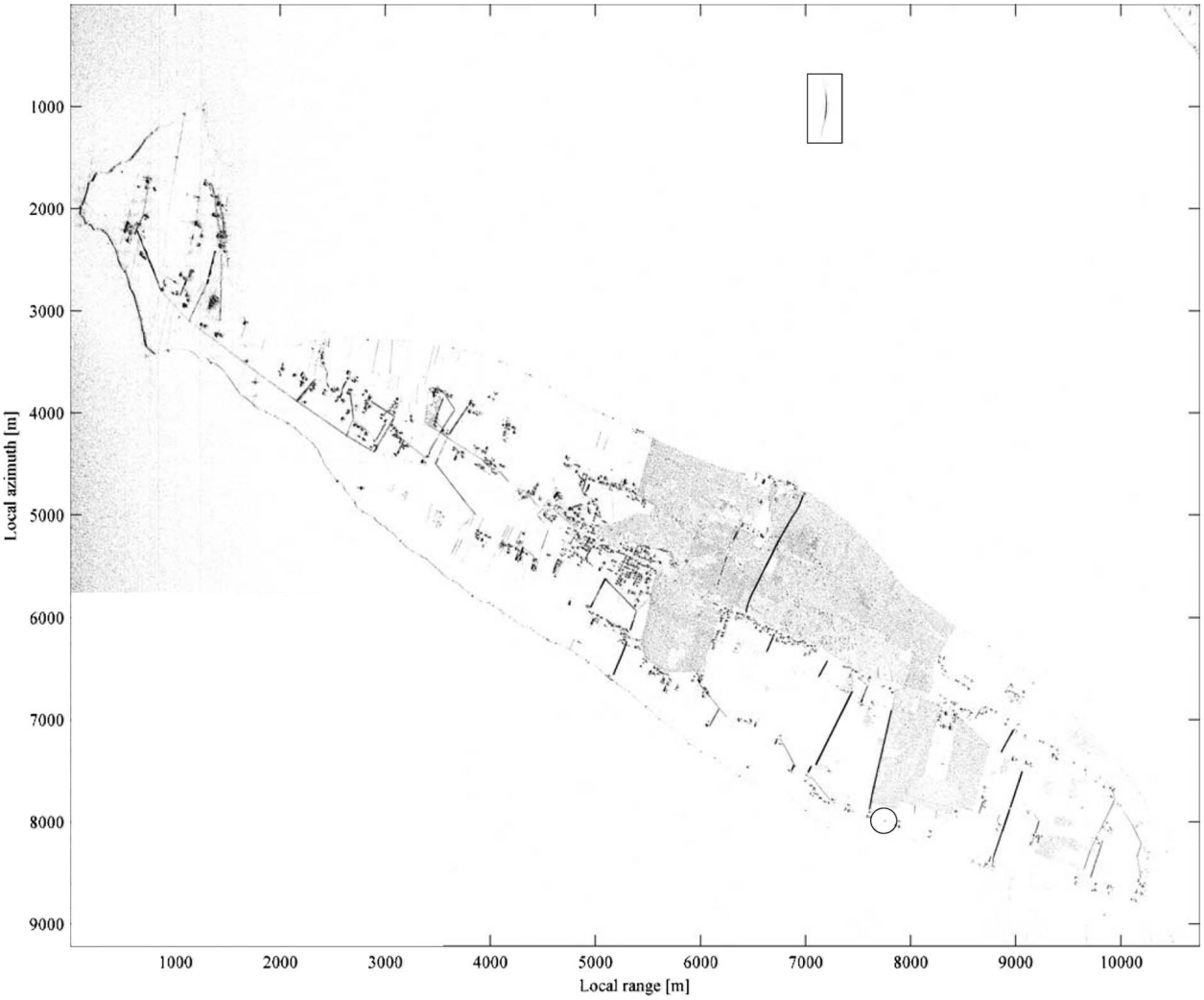

Figure 3.6: SAR BPJ image of the island Visingsö in southern Sweden, with north to the left. The SAR platform is off-image to the left, looking to the right and flying toward the top of the page, with an integration angle of 110°. In the upper right part of the image in the black box, a sea vessel moving in the along-track direction opposite the SAR leaves an inward-curved elliptically smeared image. (Source: [33])

3.2 Cross-Track Target Motion

A moving target's cross-track motion affects its SAR IPR completely differently than its along-track motion does. If a target moves strictly in the along-track direction, its image smears out and possibly curves, but still approximately indicates the target's general location and path traveled during the target's dwell time. In contrast, strictly cross-track target motion induces relatively little image blurring, but instead shifts the target's image position in the azimuth direction. The moving target's SAR image appears as a stationary target in a different location. For an outbound target moving away from the SAR, the target image is displaced in azimuth backward in the direction opposite the SAR's flight heading, while an inbound target moving toward the SAR has its image displaced forward in the same direction as the SAR motion.

For cross-track target motion, the amount of azimuth shift is directly proportional to the target's radial velocity [13–16, 68, 69, 71, 72]. Chen [69] expounds in his paper that the amount of shift is directly proportional to both the target's radial velocity and its ground range from the SAR, and inversely proportional to the SAR platform speed. I have verified these relationships in simulation. One interesting potential result of these image-shifting effects is that for a long standoff range, sufficiently fast target motion, or sufficiently slow SAR motion, the azimuth shift for a cross-track moving target may be sufficiently large to cause the target to disappear entirely from the SAR image. Figures 3.7 through 3.15 show cross-track target motion effects in simulated and actual SAR images, and also illustrate the different specific shifting effects described by Chen in [69]. A full mathematical treatment of the azimuth-shifting effect on cross-track moving target images is not given here, but the interested reader is referred to the literature cited at the beginning of this paragraph. This thesis only describes and illustrates the effect.

The statement that a target's image is shifted in one direction or the other calls for some clarification. The literature cited in the previous paragraph says the target image remains well-focused but shifted in azimuth. But shifted relative to what? The target is moving, and does not have a single "true position" from which its image can shift. As it turns out, simulation results show that the image is shifted in azimuth relative to the approximate centerpoint of the target's radar-visible path. The distance by which the image shifts appears to be approximately proportional to the distance the target covered on its radar-visible path during the BPJ integration time. This is illustrated in Fig. 3.7.

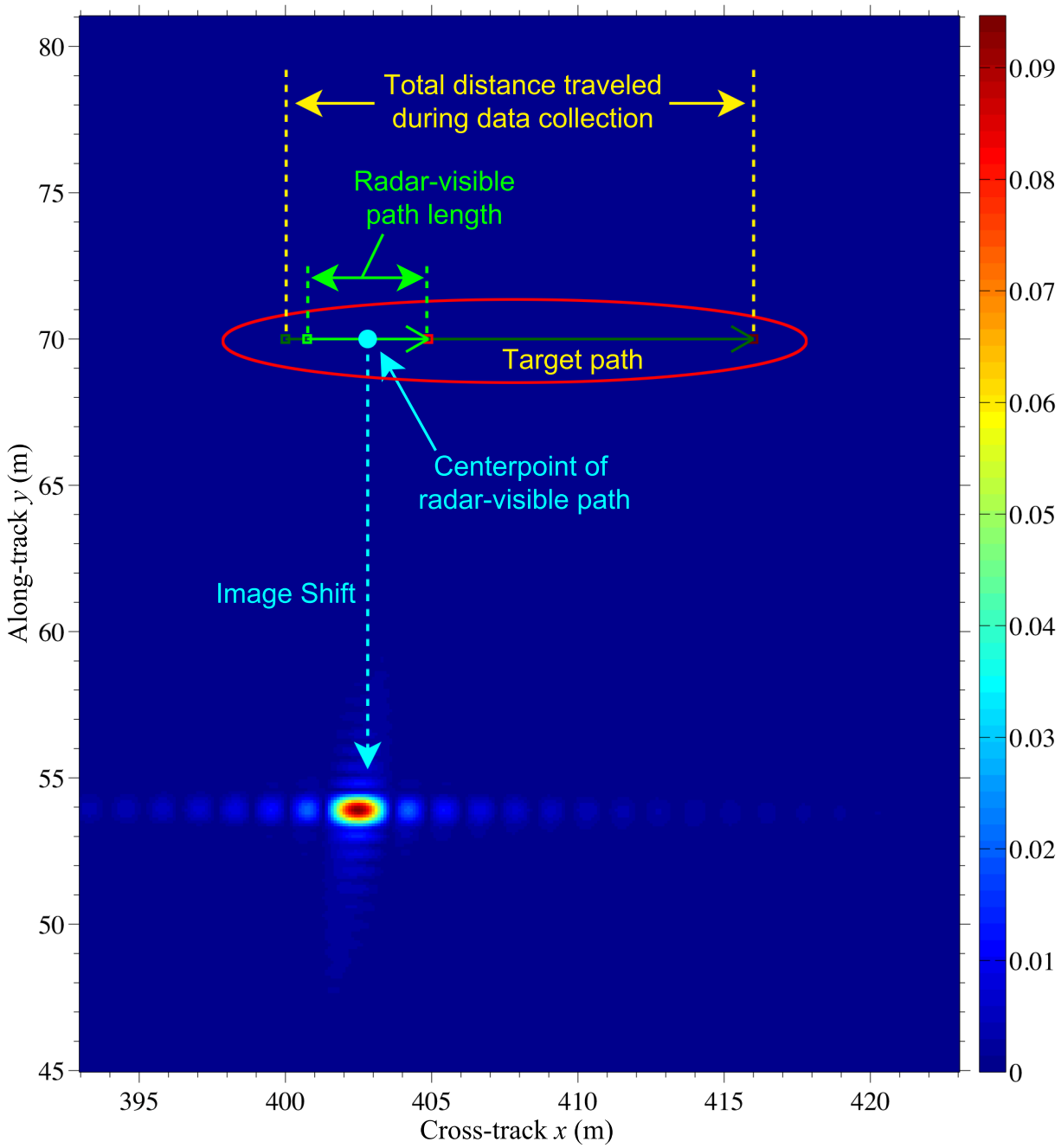

Figure 3.7: A simulated SAR image of a cross-track moving target. North is up. The SAR platform is off-image to the left, looking to the right and flying north at 50 m/s, and the integration angle is 10°. The target is outbound moving away from the SAR, and its image is shifted in azimuth in the direction opposite the SAR's flight heading. The target's radar-visible path is indicated by the light green arrow, and the target's shifted image is located approximately below the centerpoint of the radar-visible target path.

Because it was not the main focus of my research, the relationship between the radar-visible path length and the amount of the target image's azimuth shift was only briefly studied. All the effects described by Chen in [69] affect the target's radar-visible path length, producing the corresponding azimuth shifts. Simulation results (Figs. 3.9 through 3.12) show that the relationship between a target's radar-visible path length and the target image's azimuth shift distance appears to be approximately linear, but is not exactly linear. It is possible that this nonlinearity results from the constant integration angle used during SAR image formation. A constant integration angle gives the imaging threshold's ground footprint a hyperbolic shape at the leading and trailing edges, as illustrated in Fig. 3.8. A hyperbola is asymptotically linear at positions far from its apex, but very nonlinear near the apex. The apex of the hyperbolic imaging threshold is directly below the SAR's flight path, as shown in both Figs. 2.2 and 3.8. For a cross-track moving target far away from the SAR platform in range, its azimuth shift may be more linearly dependent on its visible path length. But if the target's ground range from the radar puts it close to the near edge of the radar's ground swath, as is true for all the simulated SAR images in this thesis, then the target is closer to the nonlinear region near the apex of the hyperbolic imaging threshold. This may possibly cause the observed small nonlinearity between target's visible path length and the target image's azimuth shift distance.

The simplest explanation for the azimuth IPR-shifting phenomenon is the Doppler effect. As stated at the beginning of Chapter 2, SAR was originally invented under the name Doppler beam sharpening. DBS approaches the radar imaging problem from the perspective of Doppler analysis in the frequency domain, using the time-changing Doppler shifts of landscape features to achieve fine azimuth resolution with the "Doppler-sharpened" synthetic beam [73]. Basically, DBS relies on the Doppler effect induced by radar platform motion to image and locate stationary targets with fine azimuth resolution. When a target has a cross-track component to its motion, its Doppler shift differs from that of the stationary landscape around it, causing the target to be azimuth-shifted and mislocated in the SAR image. This is the frequency-domain Doppler explanation for why a target's azimuth motion affects its SAR image the way it does.

The time-domain geometric SAR explanation for this phenomenon is slightly more complicated. Figures 2.13 through 2.22 illustrate the BPJ process for imaging stationary targets. In the BPJ frames, the circular iso-range arcs represent each respective radar pulse's RC data contri-

bution to the SAR image. In each successive BPJ image frame, the arcs intersect at the stationary targets' true positions. When a target moves strictly in the cross-track direction, the radius of its iso-range arc progressively changes in time relative to those of nearby fixed landscape features. The radius's rate of change is just right to make the back-projected arcs intersect almost perfectly at a mislocated azimuth position, producing a very well-focused target image in the wrong place.

Figure 3.9 illustrates the general effect of cross-track target motion in SAR images, with different target speeds directly affecting the azimuth shift of the target image. Figure 3.10 shows how different integration angles affect shifted target images, and the slight blurring effect that wider angles impart. Figure 3.11 shows how target range directly and proportionately affects the target image azimuth shift. Figure 3.12 shows the inverse relationship between SAR platform speed and image shift. Figures 3.14 and 3.15 show actual SAR images containing cross-track moving targets (a train and a boat) whose images are azimuth-shifted from their true positions.

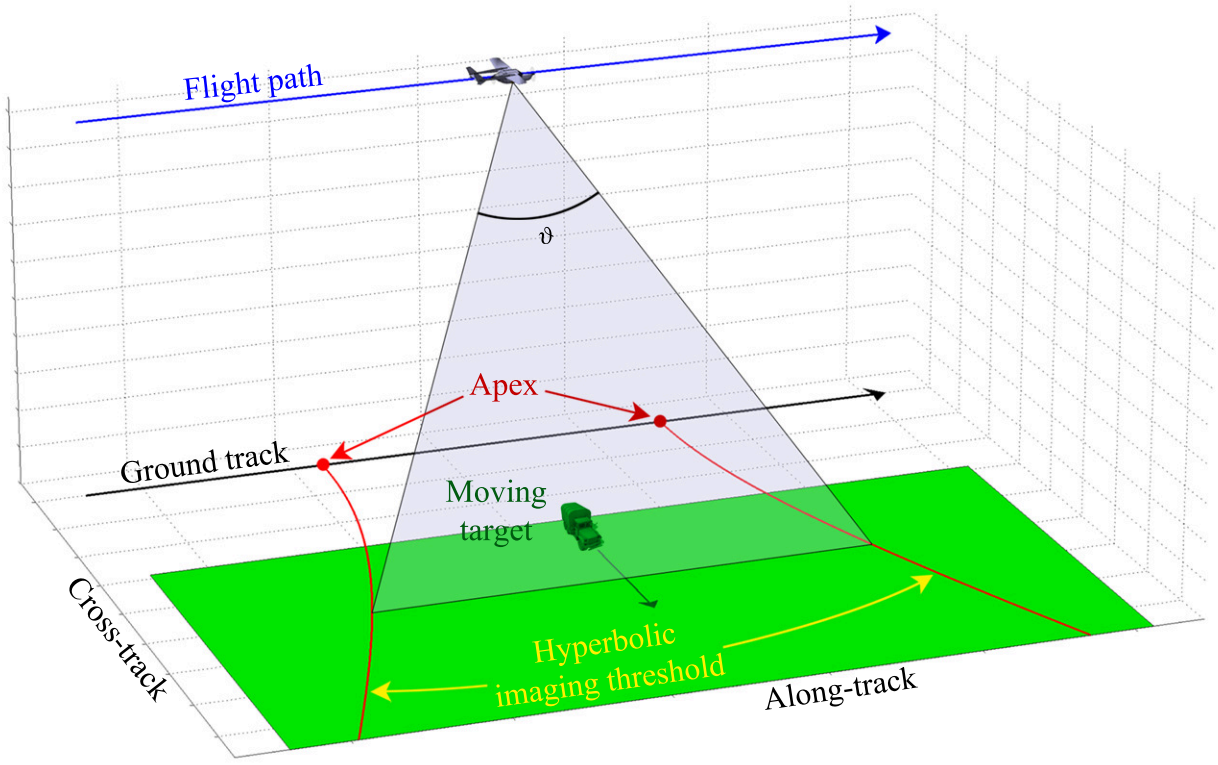

Figure 3.8: If the same integration angle is used for all image pixels, the imaging threshold on the ground is hyperbolic at the leading and trailing edges. This figure shows a cross-track moving target close to the near edge of the ground swath, in the hyperbola's nonlinear region near its apex. The integration angle ϑ shown here is 50°

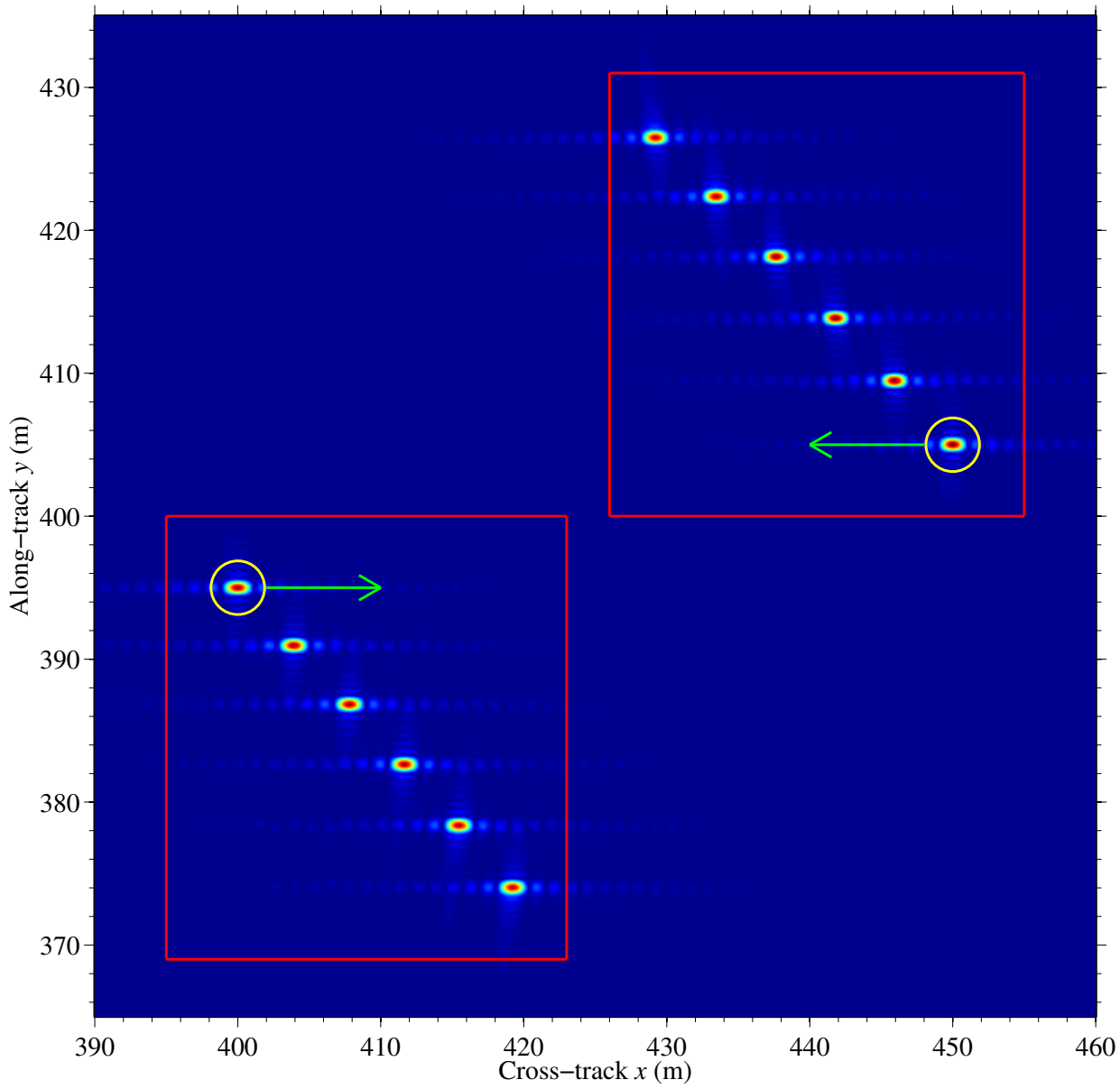

Figure 3.9: A simulated SAR image showing the general effect of cross-track target motion. North is up. The SAR platform is off-image to the left, looking to the right and flying north at 50 m/s, with an integration angle of 10°. Outbound moving targets have their images shifted backward in azimuth relative to the SAR's direction of travel, while inbound targets have their images shifted farther ahead in azimuth relative to the SAR's heading. In each red box, six targets start from the same position at time zero, with speeds ranging from stationary to 2.5 m/s, in 0.5 m/s increments. The initial position is indicated by the yellow circle, with the green arrow showing the direction of travel. The targets' complete paths are not shown here because they would clutter the image beyond usefulness. Each target image is shifted in azimuth in direct proportion to its speed.

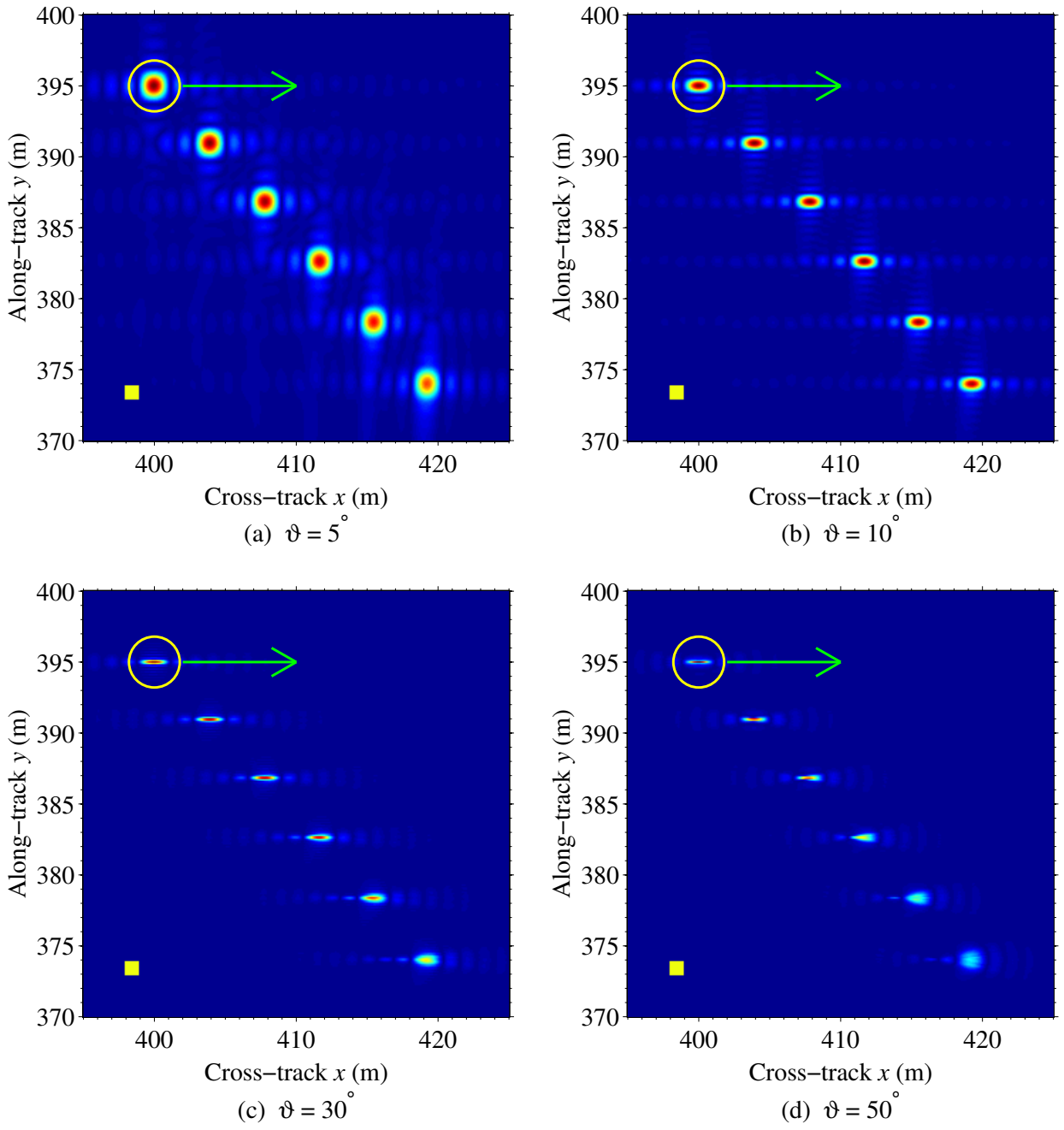

Figure 3.10: Simulated SAR images showing the appearance of cross-track moving targets for different integration angles. North is up. The SAR platform is off-image to the left, looking to the right and flying north at 50 m/s. In each image, six targets start from the same position at time zero, with speeds ranging from stationary to 2.5 m/s, in 0.5 m/s increments. The integration angles ϑ range from 5° to 50°, and are given below each image. The initial position is indicated by the yellow circle, with the green arrow showing the direction of travel. The targets' complete paths are not shown here because they would clutter the image beyond usefulness. A yellow square in the lower left of each image provides a simple 1 m^2 scale. A slight blurring effect appears for wider integration angles.

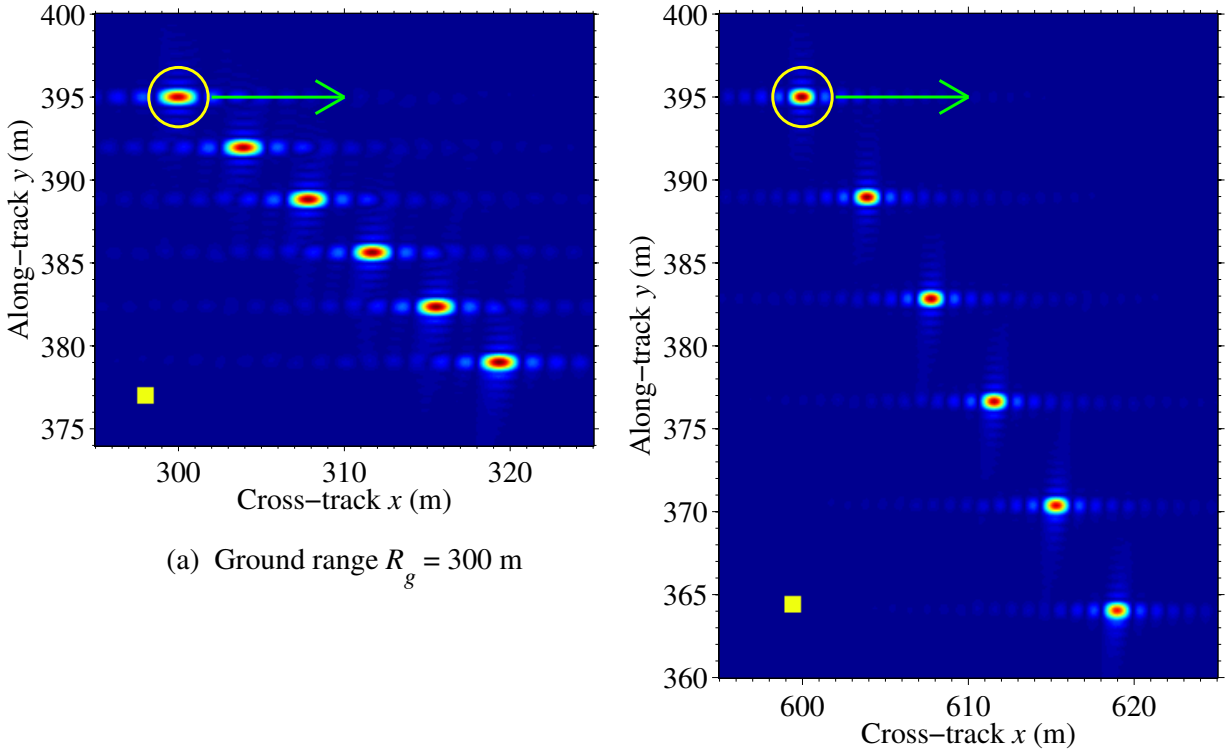

(a) Ground range R_g = 300 m

(b) Ground range R_g = 600 m

Figure 3.11: Simulated SAR images showing the effect of cross-track target motion for different target ranges. A change in the target's ground range at time zero affects the azimuth shift of its image. North is up. The SAR platform is off-image to the left, looking to the right and flying north at 50 m/s, with an integration angle of 10°. In each image, six targets start from the same position with speeds ranging from stationary to 2.5 m/s, in 0.5 m/s increments. The initial position is indicated by the yellow circle, with the green arrow showing the direction of travel. The targets' complete paths are not shown here because they would clutter the image beyond usefulness. A yellow square in the lower left of each image provides a simple 1 m^2 scale. In image (a), the initial target position is 300 meters away from the SAR's ground track, and in image (b) the initial target position is twice as far out, at 600 meters away. The target images in image (b) are shifted in azimuth twice as much as the targets in image (a), in direct proportion to their different ground ranges.

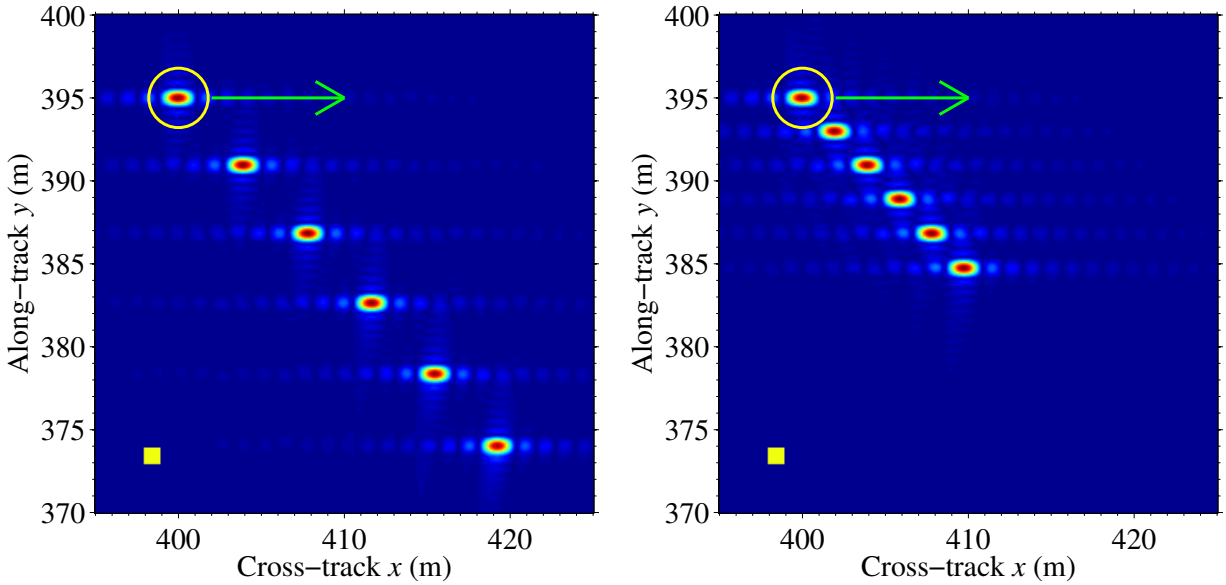

(a) V_{SAR} = 50 m/s

(a) V_{SAR} = 100 m/s

Figure 3.12: Simulated SAR images showing the effect of cross-track target motion for different SAR platform speeds. A change in the SAR airspeed inversely affects the azimuth shift of the target image. North is up. The SAR platform is off-image to the left, looking to the right and flying north, with an integration angle of 10°. In each image, six targets start from the same position with speeds ranging from stationary to 2.5 m/s, in 0.5 m/s increments. The initial position is indicated by the yellow circle, with the green arrow showing the direction of travel. The targets' complete paths are not shown here because they would clutter the image beyond usefulness. A yellow square in the lower left of each image provides a simple 1 m^2 scale. In image (a), the SAR flies at 50 m/s, and in image (b) the SAR flies twice as fast at 100 m/s. The target images in image (b) are shifted in azimuth half as much as the targets in image (a), inversely proportional to the change in the SAR airspeed.

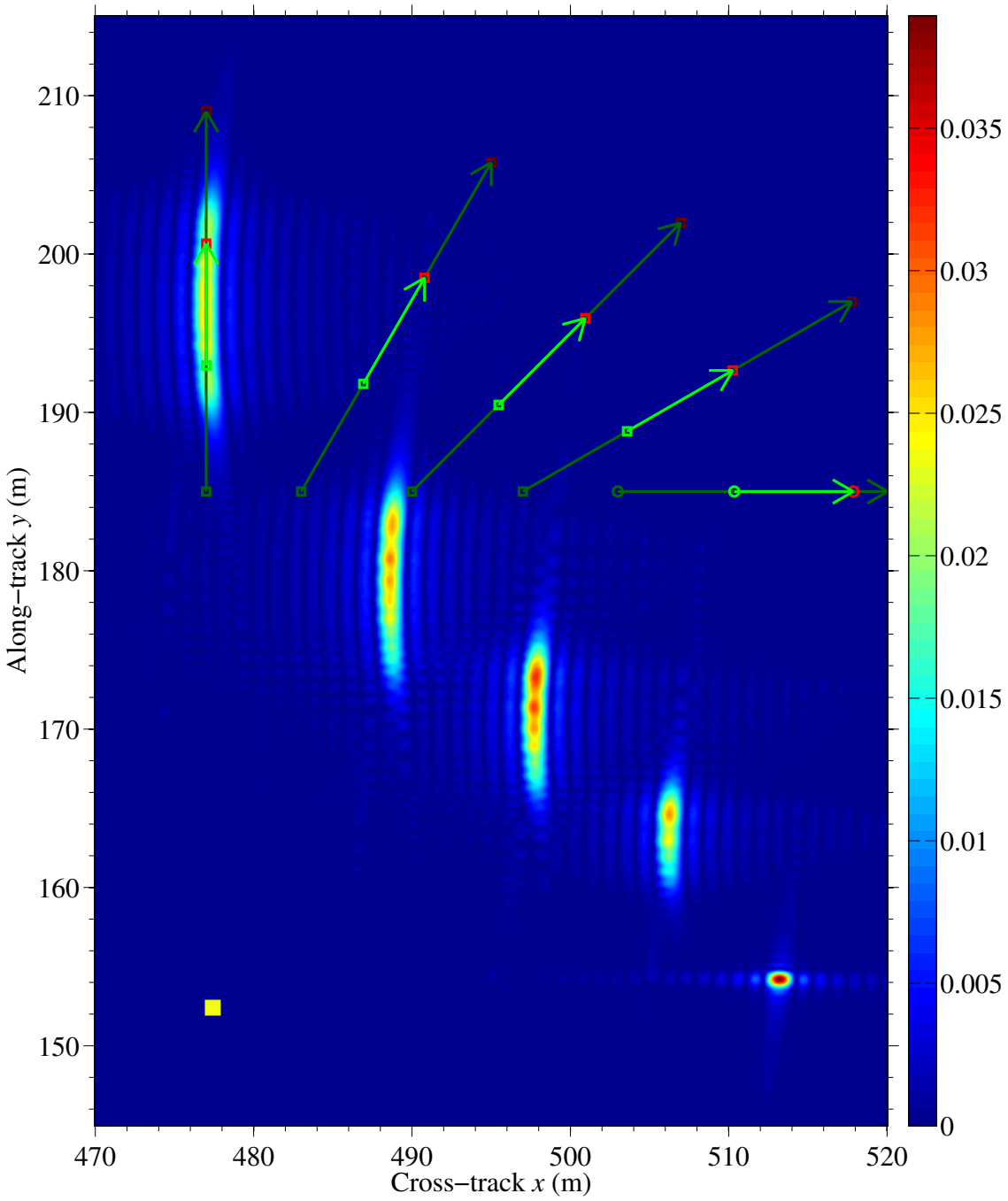

Figure 3.13: Simulated SAR image of five moving targets. The brighter green arrows show the targets' true radar-visible paths during their dwell time. North is up. The SAR platform is off-image to the left, looking to the right and flying north at 50 m/s, with an integration angle of 10°. From left to right for the green arrows in the image, the target headings are 0° (due north), 30°, 45°, 60°, and 90° (due east). The targets' corresponding SAR images appear in order from upper left to lower right. All targets move at 3 m/s. A yellow square in the lower left provides a simple 1 m^2 scale. The moving target images smear and shift in azimuth according the SAR target motion effects described in this chapter.

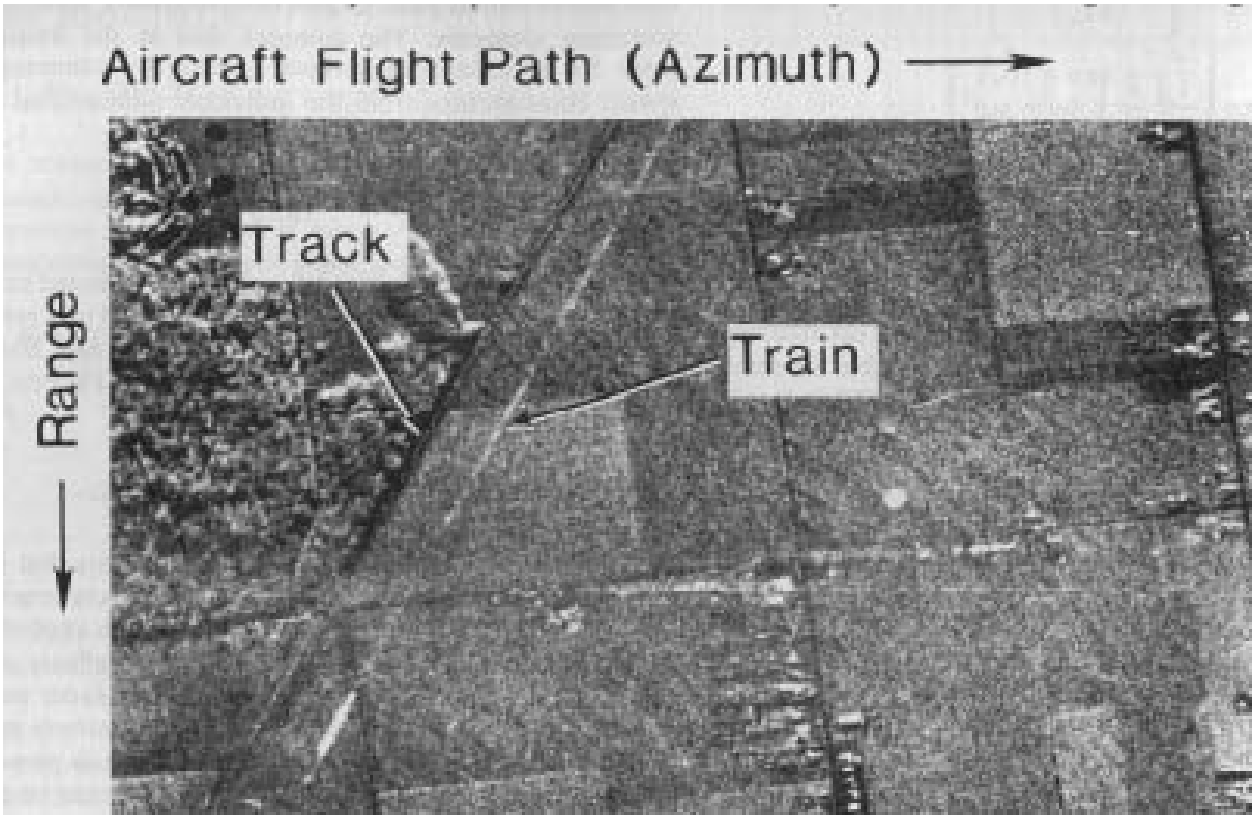

Figure 3.14: Actual SAR image of a train moving mostly in the cross-track direction, shifted off its tracks due to the cross-track component of its motion. (Source: [74])

Figure 3.15: Actual SAR image of a boat moving in the cross-track direction toward the bottom of the image. The long dark line is the boat's wake, and the bright spot near the center is the boat, which is clearly mislocated from its expected position at the head of the wake. (Source: [74])

An interesting observation about target motion in SAR images is that the effect on the target's image, whether smearing or position shifting, is always in the azimuth direction. If a moving target has both along-track and cross-track components to its velocity vector, each motion type independently imparts its own effect to the target image. The along-track motion smears the target image in azimuth, and the cross-track motion shifts the smeared image in azimuth. Generally, moving targets exhibit a combination of along-track and cross-track motions. Figure 3.13 is a simulated SAR image illustrating this effect for multiple targets moving in various directions between due north and due east, with green arrows indicating their true paths traveled during the data collection. Regardless of a target's heading, as long as it moves with a constant speed in a straight line, both the along-track and cross-track motion components each produce a completely different effect, but always in the azimuth direction from the SAR's perspective.

3.3 Focusing Moving Targets with Backprojection

SAR was invented to image stationary ground scenes. As a SAR image formation algorithm, BPJ also was originally developed for the same purpose. BPJ reconstructs the phase history of every pixel center relative to the SAR's path through the sky. As stated at the beginning of Section 2.4.2, a pixel's phase history is the IPR of a SAR system. This use of the SAR IPR makes BPJ a two-dimensional spatial matched filter (MF) [2], which makes BPJ the most general and exact image formation algorithm for a single-channel SAR.

Part of the BPJ processing chain is to compute the slant ranges from each pulse to every pixel on the ground, so the digital RC data for any given pulse can be sampled at the correct time index for each pixel range. When this process is completed for every pixel relative to one pulse, BPJ moves on to the next pulse and repeats the process. New slant ranges are computed based only on the SAR platform motion, and the image pixels are assumed to remain stationary. This process is illustrated for a single pixel in Fig. 3.16. In this scenario, the pixels are matched to the stationary ground scene, and fixed targets and landscape features come into focus in the final image. An excellent example of such imagery is Fig. 2.27 in Section 2.4.3, which was used in the discussion on motion compensation and Frey's BPJ experiment with nonlinear flight paths [54].

If a target moves during the data collection, its appearance defocuses in the SAR image as described in this chapter. This is because the pixels are not matched to the target's motion. If

the target's motion is known *a priori*, the BPJ algorithm can be modified to to account for it. If the image pixel positions are incrementally updated from one pulse to the next to maintain their positions relative to the moving target, the moving pixels' phase histories and IPRs now match that of the moving target, and the target comes into focus [21,45]. With the same SAR data, BPJ is now matched to the moving target. This process is illustrated in Fig. 3.17. The tradeoff for matching the SAR to a moving target is that the rest of the stationary ground scene defocuses.

Figures 3.5 and 3.6 are actual SAR BPJ images of two different regions, each containing a moving sea vessel, and are repeated for convenience in Figs. 3.18 and 3.20. Figures 3.19 and 3.21 show the same scenes, except they are refocused to match the target's motion. In each case, the target image comes into sharp focus while the rest of the scene smears out and defocuses. Figures 3.22 through 3.24 show this effect in simulated SAR images for multiple targets moving simultaneously with different velocity vectors, and how focusing on each target individually affects the other mismatched target images.

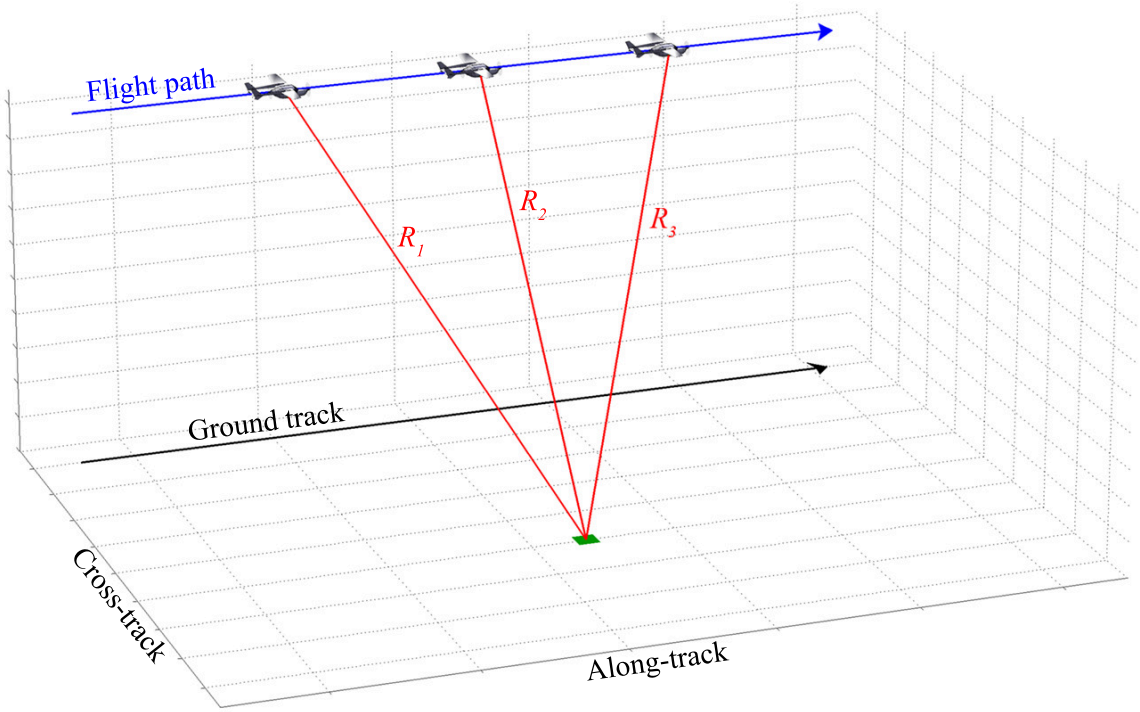

Figure 3.16: BPJ slant range computations for a single stationary image pixel. The BPJ processing chain includes a step for computing the slant ranges from each pulse in the sky to every pixel on the ground. Conventional BPJ computes these slant ranges based on a moving SAR platform and stationary pixels.

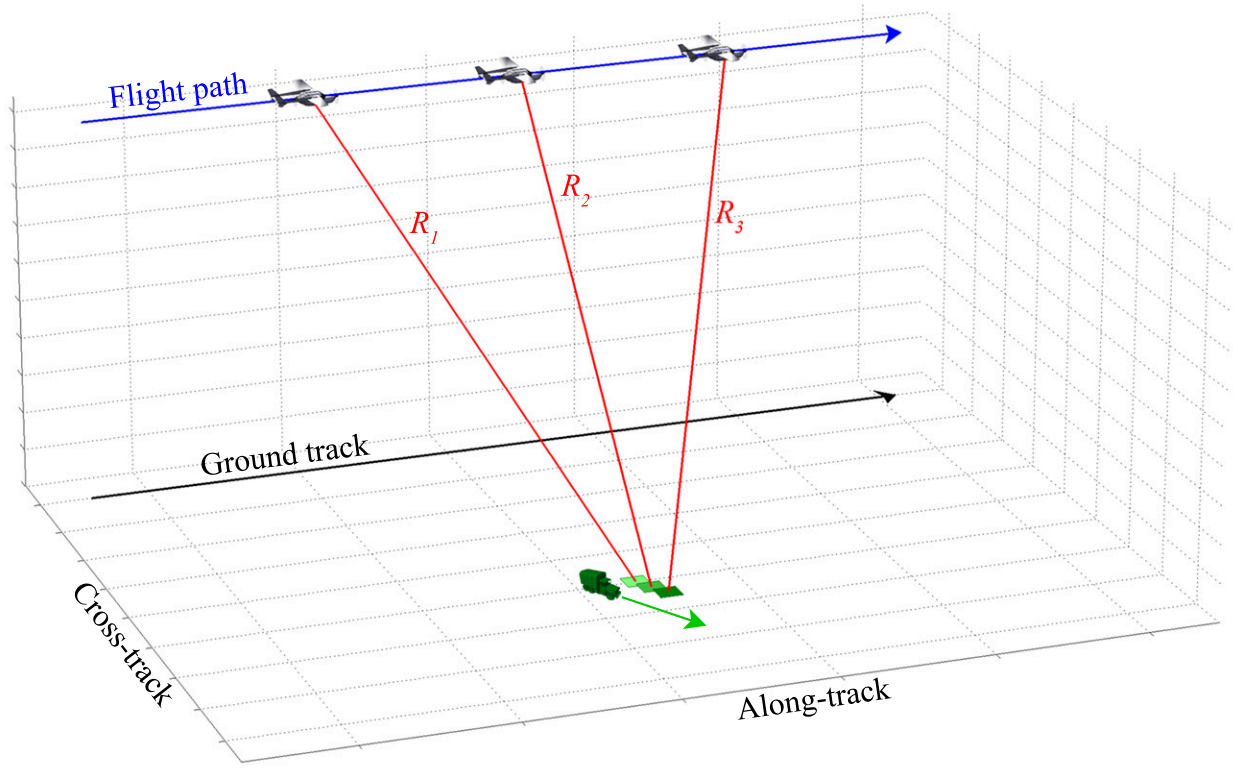

Figure 3.17: BPJ slant range computations for a single image pixel matched to a moving target. By incrementally changing the pixel positions from one pulse to the next to keep pace with the target, the slant range computations for BPJ can factor in the time-changing positions of both the SAR platform *and* the moving pixels. When the pixel motion matches the velocity vector of a moving target, their phase histories and IPRs match, and the target comes into focus in the SAR image. The rest of the stationary ground scene defocuses in response.

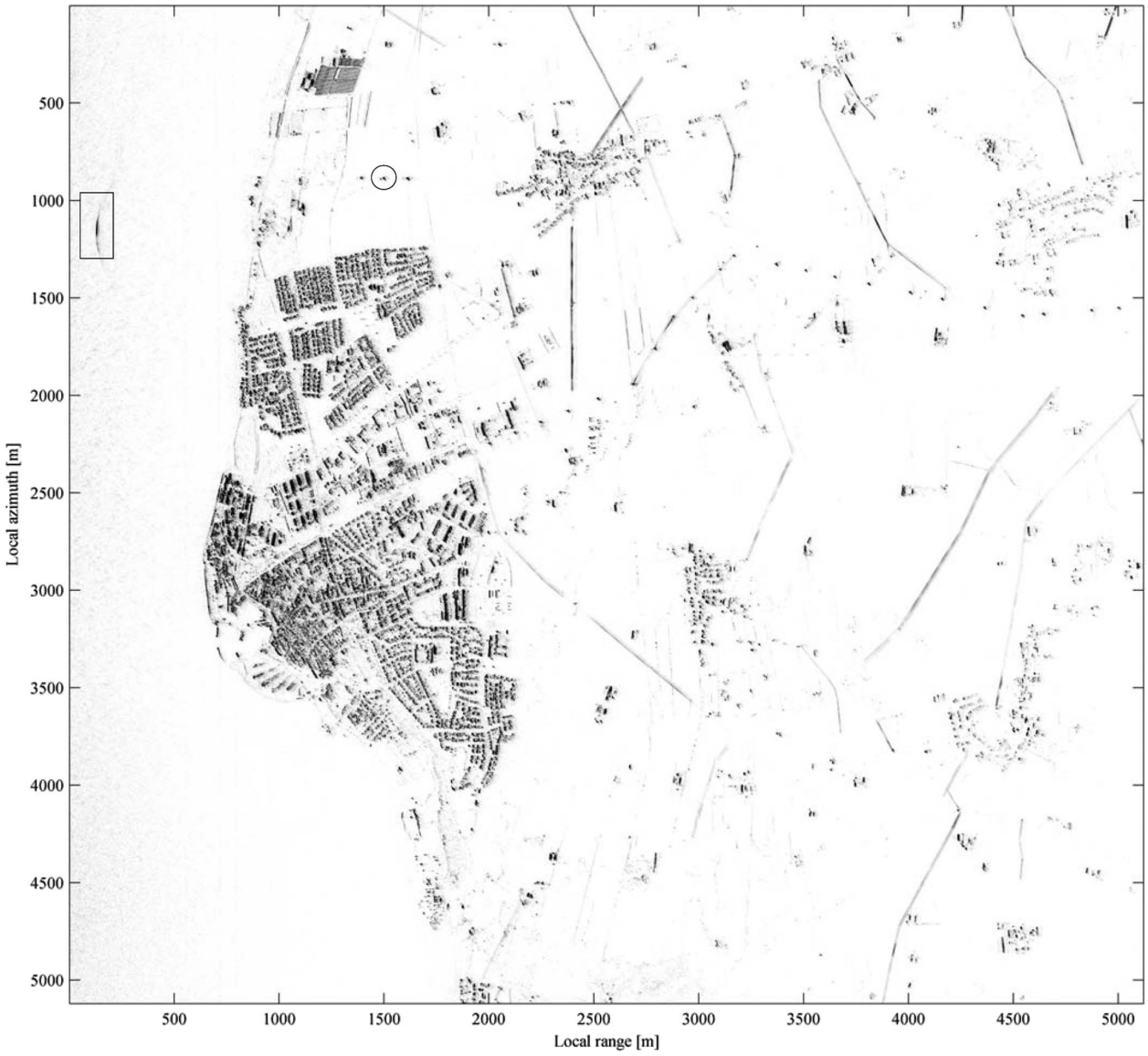

Figure 3.18: SAR BPJ image of the coastal town of Simrishamn in southern Sweden, with south up. The SAR platform is off-image to the left, looking to the right and flying toward the top of the page, with an integration angle of 110°. In the upper left part of the image in the black box, a sea vessel moving in the same along-track direction as the SAR leaves an outward-curved hyperbolically smeared image. (Source: [33])

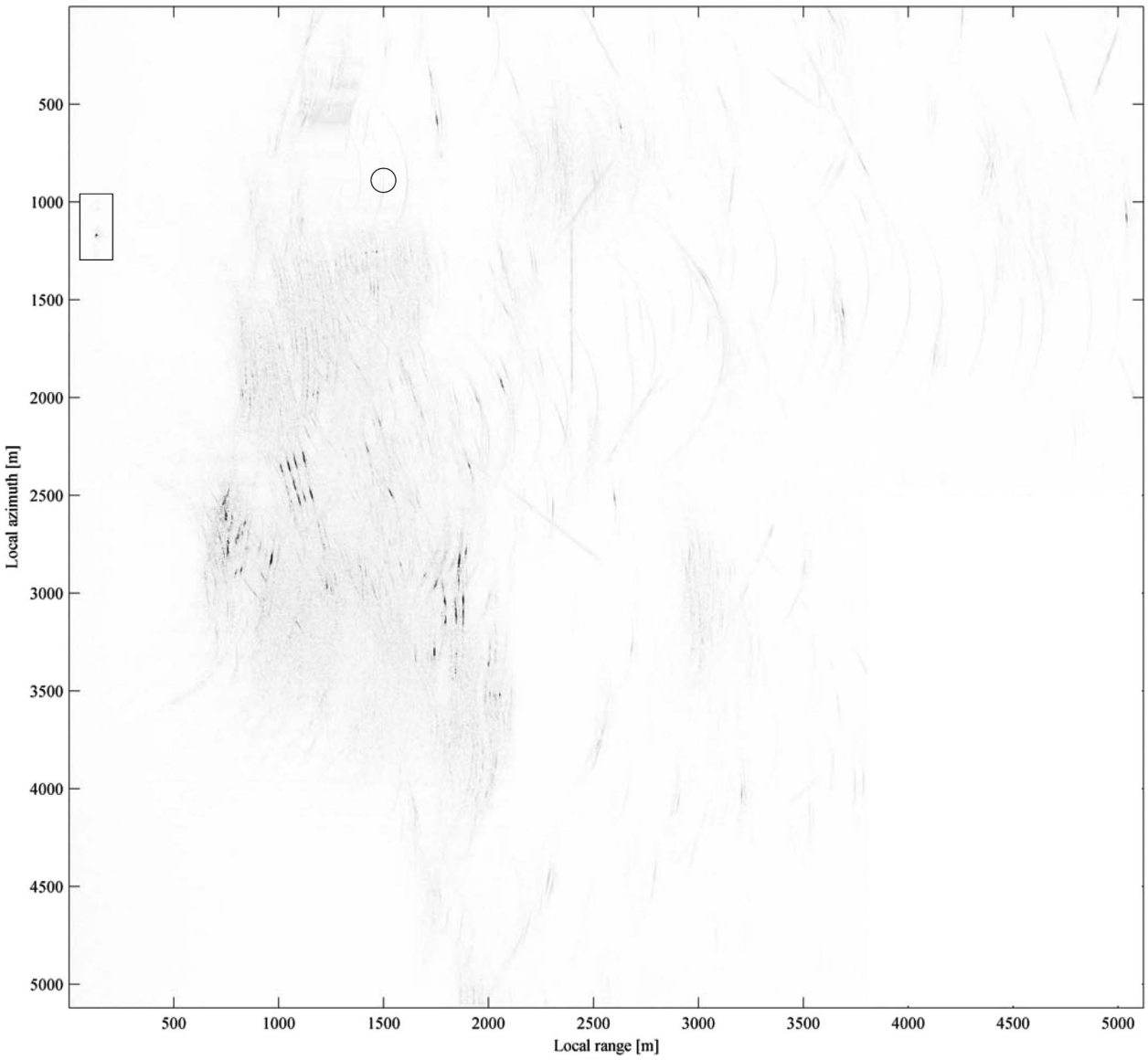

Figure 3.19: The same image scene as Figs. 3.5 and 3.18, except the SAR focus is now matched to the sea vessel's motion. In the upper left in the black box, the vessel is focused, while the rest of the scene defocuses in response. (Source: [33])

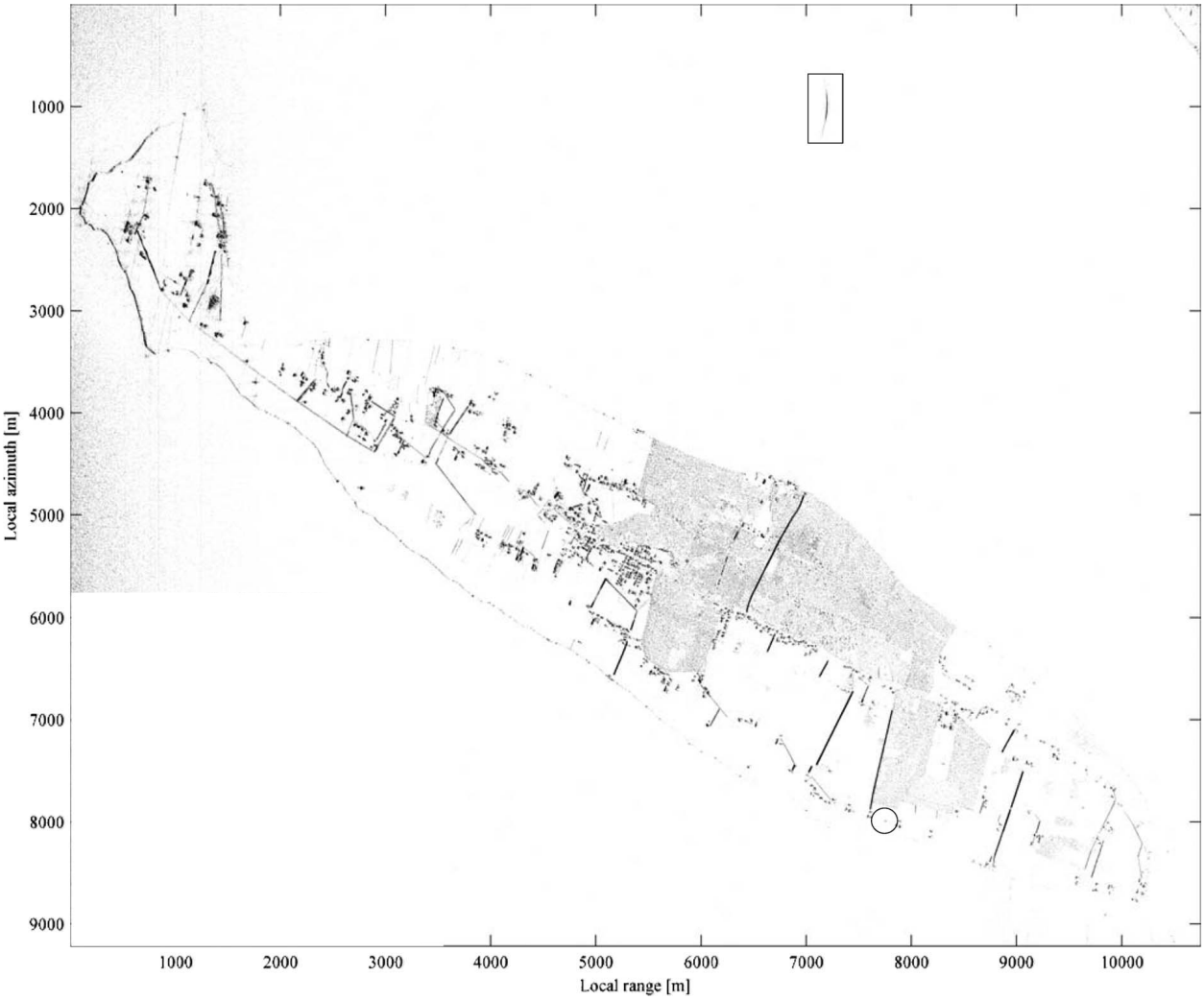

Figure 3.20: SAR BPJ image of the island Visingsö in southern Sweden, with north to the left. The SAR platform is off-image to the left, looking to the right and flying toward the top of the page, with an integration angle of 110°. In the upper right part of the image in the black box, a sea vessel moving in the along-track direction opposite the SAR leaves an inward-curved elliptically smeared image. (Source: [33])

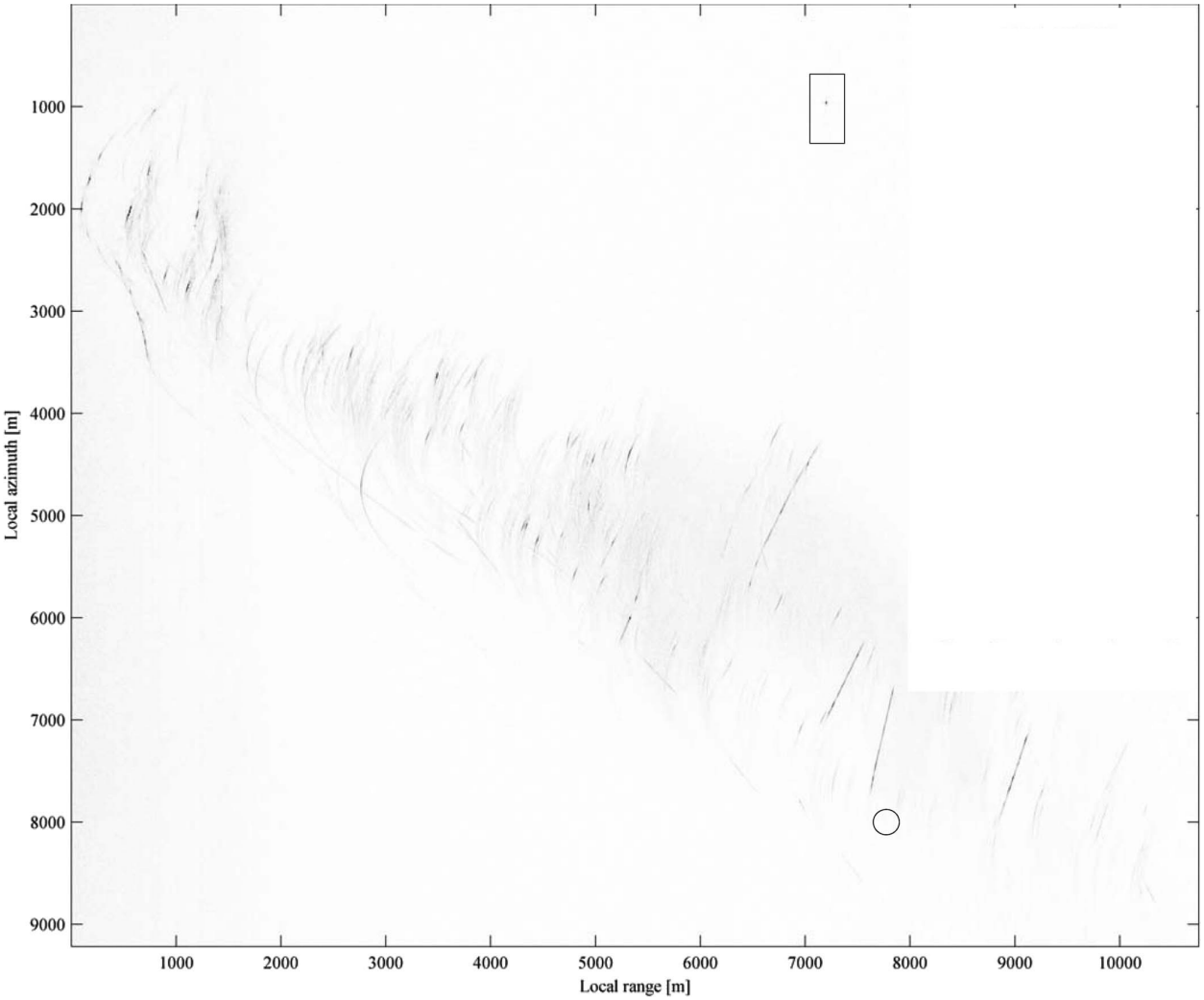

Figure 3.21: The same image scene as Figs. 3.6 and 3.20, except the SAR focus is now matched to the sea vessel's motion. In the upper right in the black box, the vessel is focused, while the rest of the scene defocuses in response. (Source: [33])

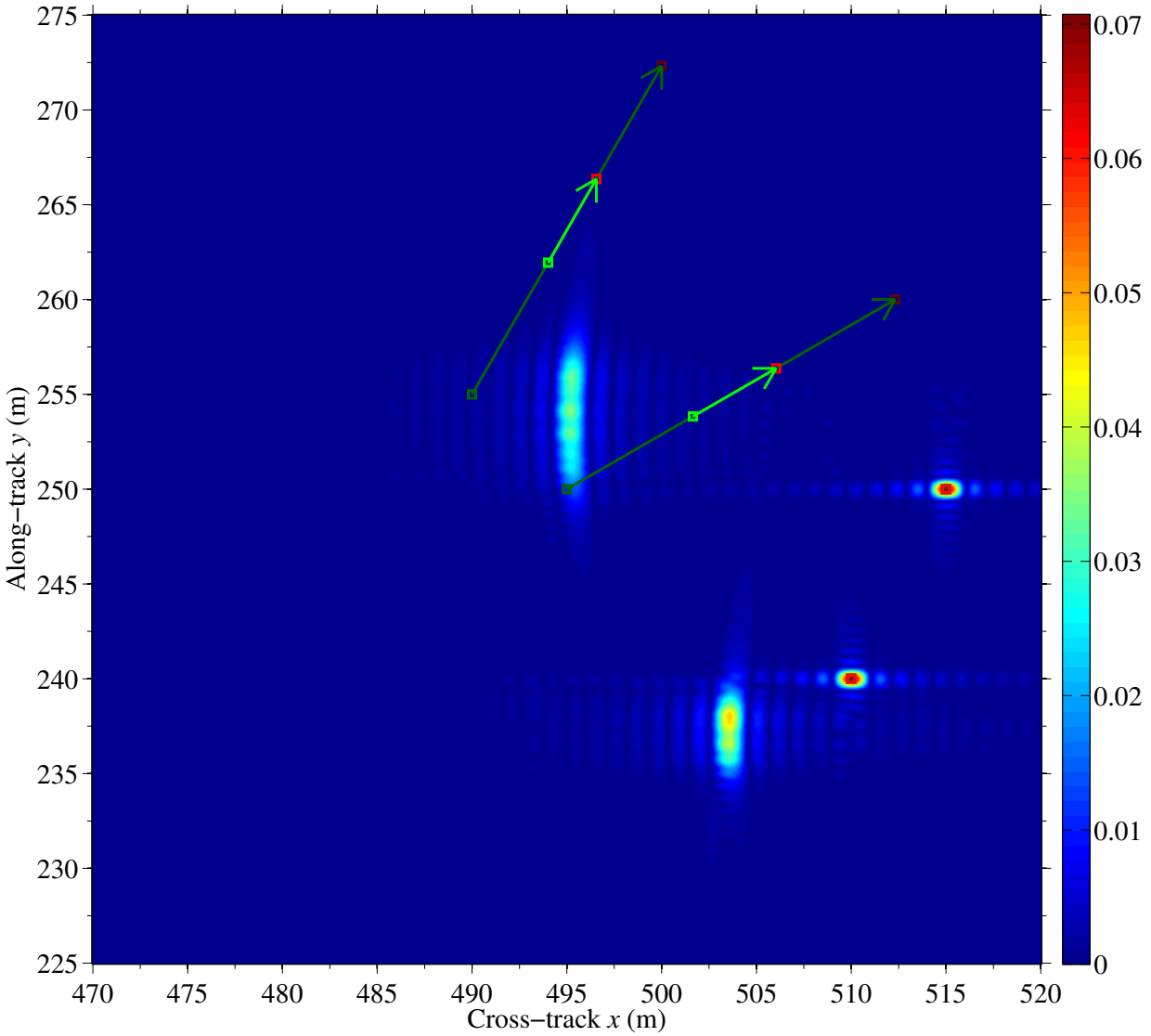

Figure 3.22: A simulated SAR image of four point targets, with two targets stationary and two moving. North is up. The SAR platform is off-image to the left, looking to the right and flying north at 50 m/s, with an integration angle of 10°. The stationary targets on the right are focused, and the other two defocused images are the moving targets. The lighter green arrows indicate the targets' radar-visible paths. The moving target velocities are both 2 m/s, with headings of 30° and 60° as indicated by the green arrows. This image and Figs. 3.23 and 3.24 all use the same RC data, but this one is matched to the stationary ground as a reference, while the other two figures are each matched to one of the two moving targets.

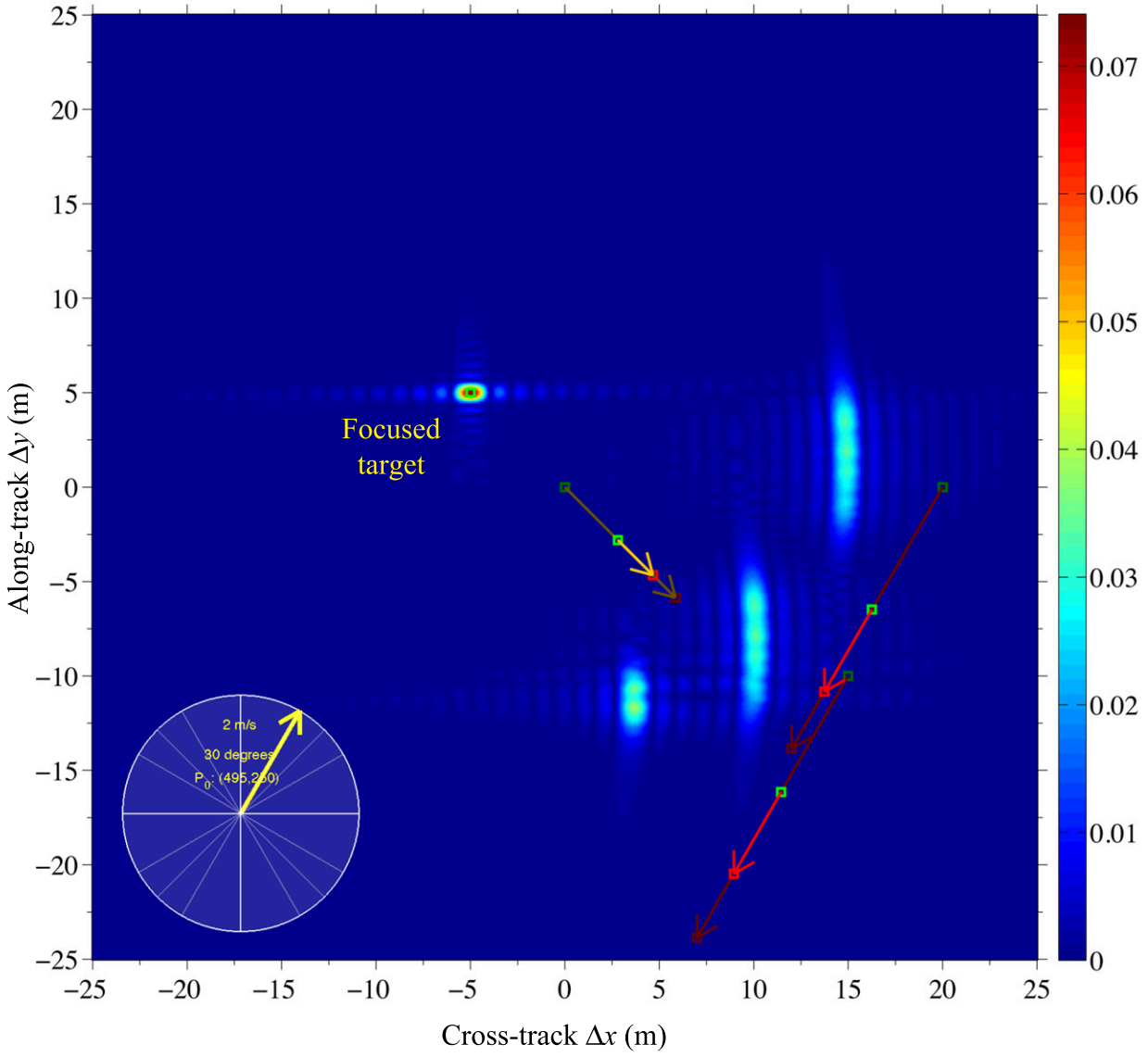

Figure 3.23: The same target scene as in Fig. 3.22, except the focus is now matched to the leftmost target, which is moving. The compass in the lower left shows the velocity vector of the moving focus. Because the image pixels match the velocity vector of the leftmost target, that target comes into focus, while the other targets defocus. In the reference frame of the moving image pixels, the red arrows show the apparent paths of the stationary targets, and the orange arrow shows the apparent path of the other mismatched moving target. The lighter red and orange arrows indicate the radar-visible portions of the apparent target motion relative to the moving reference frame. The moving image pixels started out in the same position as those of Fig. 3.22, but because they are matched to a nonstationary velocity vector, the axes are marked relative to the image center, and not absolute ground positions. The initial centerpoint of the moving image is given on the compass.

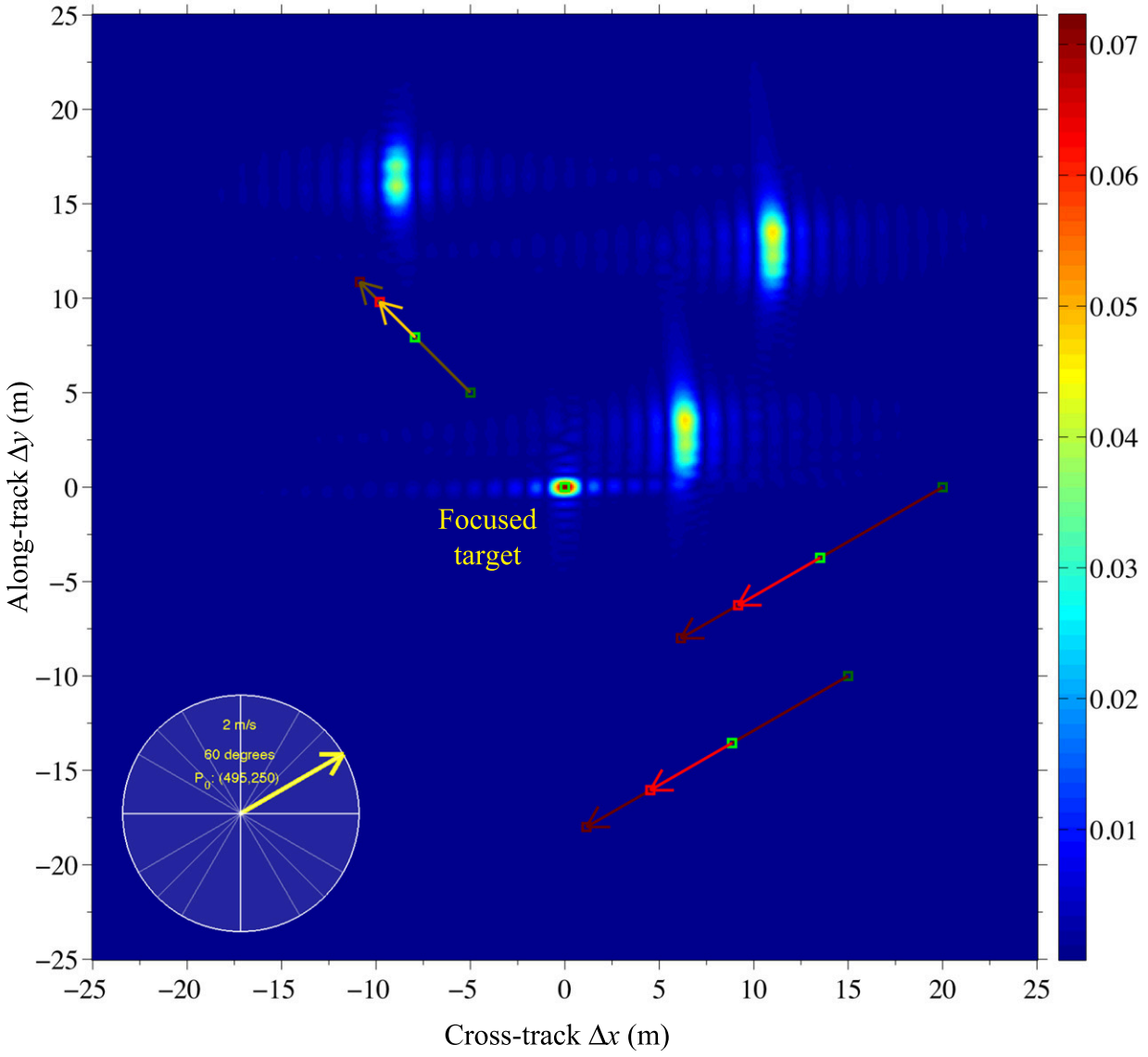

Figure 3.24: The same target scene as in Fig. 3.22, except the focus is now matched to the moving target second from left. The compass in the lower left shows the velocity vector of the moving focus. Because the image pixels match the velocity vector of the second-from-left target, that target comes into focus, while the other targets defocus. In the reference frame of the moving image pixels, the red arrows show the apparent paths of the stationary targets, and the orange arrow shows the apparent path of the other mismatched moving target. The lighter red and orange arrows indicate the radar-visible portions of the apparent target motion relative to the moving reference frame. The moving image pixels started out in the same position as those of Fig. 3.22, but because they are matched to a nonstationary velocity vector, the axes are marked relative to the image center, and not absolute ground positions. The initial centerpoint of the moving image is given on the compass.

CHAPTER 4. A SAR BACKPROJECTION AMBIGUITY FUNCTION

An ambiguity function (AF) is a mathematical expression that predicts the output from a matched filter (MF) when the input signal is mismatched to the filter design. For example, a receiver on a conventional radar may have a MF matched to an expected echo from a stationary target. If the radar is stationary, then it expects the received echo to have the same frequency content as the transmitted pulse. But if the target is actually moving with a radial component along the radar's LOS, then its echo is Doppler-shifted. For any MF, the filter output SNR is maximized when the received signal is matched to the filter design [14, 48]. A mismatch in Doppler shift causes the MF output to be less than when the filter is correctly matched to the target echo. As Chen states in [14], a MF is equivalent to a correlator, which is why a SAR receiver cross-correlates each radar echo with a copy of the transmit waveform. A thorough treatment of matched filtering is not given here, but the interested reader is referred to virtually any textbook on radar or digital communications. By predicting the output from a MF for a mismatched input, an AF also predicts how much signal mismatch can be tolerated before a target's detectability diminishes below a given threshold.

This chapter derives and presents an AF I developed for SAR BPJ, and is organized as follows: Section 4.1 describes the derivation of AFs in general. Section 4.2 derives the AF for a simple ICW waveform, and Section 4.3 derives the AF for a LFM chirp waveform. These are two important AFs, and can be found discussed and derived in many radar textbooks. Peebles does an excellent job in [48] of deriving the AF in general, as well as for the ICW and LFM waveforms, and I include these derivations in Sections 4.1 through 4.3. I include them to give background and show what can be learned from an AF. They are also intended to help the reader understand the derivation process and final result for the AF I developed for SAR BPJ, presented in Section 4.4. I then give three examples of BPJ AFs. The derivations given in Sections 4.1 through 4.3 are paraphrased from Peebles in [48], and the AF for SAR BPJ in Section 4.4 is my original work.

4.1 General Ambiguity Function Derivation

Deriving an ambiguity function starts with the general expressions for a real radar transmit signal and its echo:

• Real radar transmit signal

$$s(t) = a(t)\cos[\omega_0 t + \theta(t) + \phi_0], \tag{4.1}$$

• Real radar echo received

$$s_r(t) = \alpha a(t-\tau)\cos[(\omega_0 + \omega_d)\cdot(t-\tau) + \theta(t-\tau)], \tag{4.2}$$

where α is a scaling constant that absorbs the spreading loss attenuation predicted by the radar range equation [Eq. (2.1)], $a(t)$ is the amplitude modulation (pulse shape), $\theta(t)$ is the frequency modulation, ω_0 is the carrier frequency, τ is the target's echo delay, ω_d is the echo's Doppler shift, and ϕ_0 is the initial phase, which can be safely set to zero and ignored with no loss of generality.

To simplify the math involved in deriving an ambiguity function, some mathematical substitutions are made. The real radar transmit signal, the subsequent echo, and the MF are represented by their *analytic* counterparts. An analytic signal or filter is a complex representation of the real signal or filter, but has only positive frequency content (signals) or frequency response (filters).

The analytic signal and filter are constructed by exploiting the following two facts:
1) the complex exponential $e^{j\theta} = \cos\theta + j\sin\theta$ has only a positive frequency component, and
2) the cosine function used in Eq. (4.1) to model the physical signal is the real part of such a complex exponential, and therefore the analytic signal contains all the information about the actual signal.

The analytic versions of the real signals in Eqs. (4.1) and (4.2) are given as follows:

• Analytic radar transmit signal

$$\psi(t) = a(t)e^{j[\omega_0 t + \theta(t)]}, \tag{4.3}$$

• Analytic radar echo received

$$\psi_r(t) = \alpha a(t-\tau)e^{j[(\omega_0+\omega_d)\cdot(t-\tau)+\theta(t-\tau)]}. \tag{4.4}$$

The analytic radar echo received is especially important, and can be rewritten as

$$\psi_r(t) = \alpha \underbrace{a(t-\tau)}_{\substack{\text{Amplitude} \\ \text{modulation}}} \overbrace{e^{j\omega_0 \cdot (t-\tau)}}^{\substack{\text{Carrier} \\ \text{component}}} \underbrace{e^{j\theta(t-\tau)}}_{\substack{\text{Frequency} \\ \text{modulation}}} \overbrace{e^{j\omega_d \cdot (t-\tau)}}^{\substack{\text{Doppler} \\ \text{shift}}}. \tag{4.5}$$

To aid in constructing the ambiguity function, the following two assignments are made:

$$g(t-\tau) = a(t-\tau)e^{j\theta(t-\tau)}, \tag{4.6}$$

which contains only the amplitude and frequency modulations, and

$$\psi(t-\tau) = g(t-\tau)e^{j\omega_0 \cdot (t-\tau)}, \tag{4.7}$$

which adds the carrier component. In terms of these two assignments, the analytic version of the received radar echo can be written in either of two equivalent forms:

$$\psi_r(t) = \alpha \psi(t-\tau)e^{j\omega_d \cdot (t-\tau)} \tag{4.8}$$

$$= \alpha g(t-\tau)e^{j(\omega_0+\omega_d) \cdot (t-\tau)}. \tag{4.9}$$

Next, consider the matched filter in the receiver, and an isolated point target reflecting a radar pulse. When the return echo passes through the MF, the MF response has a peak value at an instant in time I call t_{MF}. As stated previously, the time τ represents the echo delay. Specifically, it represents the instant in time when the leading edge of the signal's echo first arrives back at the receiver. Since all physical systems are causal (i.e., they cannot respond until *after* being stimulated), the MF's peak response at time $t = t_{MF}$ cannot happen until the entire echo has been received into the MF. Since the length of the echo is just the pulse length T, this means the peak response time t_{MF} can occur no sooner than the echo delay τ plus the time T required for the entire echo to pass into the MF:

$$t_{MF} \geq \tau + T. \tag{4.10}$$

The optimal MF's IPR is proportional to the time-reversed complex conjugate of the signal to which it is matched, which for radar is a copy of the transmit signal. It can be shown [48] that the optimal radar MF has the following IPR:

$$h(t) = \frac{2C\alpha}{N_0} s(t_{MF} - \tau - t), \tag{4.11}$$

where C is an arbitrary nonzero scale factor that comes out of the MF derivation (not covered in this thesis), and N_0 is the noise power in the filter. Note that $h(t)$ has no complex conjugation operator in it because $s(t)$ is real-valued.

The analytic version of the real MF in Eq. (4.11) is

$$z(t) = \frac{2C\alpha}{N_0} \psi^*(t_{MF} - \tau - t), \tag{4.12}$$

where $\psi(\cdot)$ has the same structure as Eq. (4.3), and the '*' superscript is the complex conjugation operator. The Fourier transform (FT) of the analytic MF is

$$Z(\omega) = 2U(\omega)H(\omega), \tag{4.13}$$

where ω is frequency in rad/s, $U(\omega)$ is the unit step function and $H(\omega)$ is the FT of $h(t)$. The factor of 2 appears because the FT of an analytic function has twice the value of the corresponding real function's FT. For this reason, a factor of ½ is artificially introduced into the analytic MF output expression [Eq. (4.14)] when the analytic radar echo $\psi_r(t)$ is applied to the analytic MF $z(t)$, so that its real part is equal to the real filter's output:

$$\psi_0(t) = \frac{1}{2} \psi_r(t) \star z(t), \tag{4.14}$$

where the '$\star$' between $\psi_r(t)$ and $z(t)$ is the cross-correlation operator. Skipping the mathematical details of setting up the convolution integral, performing variable substitution, and simplifying,

Eq. (4.14) becomes

$$\psi_0(t_{MF}+\Delta t) = \frac{C\alpha^2}{N_0} e^{j(\omega_0+\omega_d)\Delta t} \underbrace{\int_{-\infty}^{\infty} g^*(\xi)g(\xi+\Delta t)e^{j\omega_d\xi}d\xi}_{\chi(\Delta t,\omega_d)}, \tag{4.15}$$

where Δt is the time difference relative to the MF's peak output instant t_{MF}, and is defined as

$$\Delta t = t - t_{MF}. \tag{4.16}$$

The quantity ξ is a dummy variable for integration, and the integral labelled $\chi(\Delta t,\omega_d)$ represents the *matched filter response* [48] over time Δt to a radar echo whose Doppler shift differs by a frequency difference ω_d from the expected Doppler shift to which the MF is matched. Note that $\chi(\Delta t,\omega_d)$ has no dependence on the carrier frequency.

The key result is that the ambiguity function is the magnitude of the matched filter response:

$$AF(\Delta t,\omega_d) = |\chi(\Delta t,\omega_d)| = \boxed{\left|\int_{-\infty}^{\infty} g^*(\xi)g(\xi+\Delta t)e^{j\omega_d\xi}d\xi\right|}. \tag{4.17}$$

This result is used to compute the AFs for the ICW and LFM waveforms in Sections 4.2 and 4.3. It should be noted the even though the AF is defined in terms of the matched filter response, there is no universally accepted definition for the AF. Some authors define the AF as $|\chi(\Delta t,\omega_d)|^2$ [48], while others use the direct magnitude $|\chi(\Delta t,\omega_d)|$ [1,2]. Others still do not even take the magnitude, but leave it in its complex form of $\chi(\Delta t,\omega_d)$ [14,43]. This thesis uses the direct magnitude.

An AF for a single radar pulse has two independent variables (Δt and ω_d), and is plotted as a 3-D surface plot. All AFs have the following three properties [1,48]:

1) The maximum possible value of an AF depends only on the energy in the received echo, and occurs at time t_{MF} when there is no Doppler mismatch between the MF and the echo signal. In other words, an AF has a central peak at $|\chi(0,0)|$.

2) The total energy under the AF surface is constant, and also depends only on the energy in the received echo. If the waveform is changed, the energy under the AF surface is redistributed, but cannot be removed unless a weaker echo is received.

3) An AF has odd (180° rotational) symmetry about its central peak.

4.2 Ambiguity Function for a Simple ICW Pulse

The ICW pulse whose AF is derived in this section is shown in Fig. 2.4, which is repeated for convenience as Fig. 4.1. As shown by Eqs. (4.6) and (4.17), the AF computation needs only the pulse's amplitude and frequency modulations. The ICW amplitude modulation is rectangular, and it has no frequency modulation. This is expressed mathematically as follows:

$$\begin{aligned} & a_{ICW}(t) = A \cdot \text{rect}\left(\frac{t}{T}\right), \\ & \theta_{ICW}(t) = 0, \\ \therefore \quad & g_{ICW}(t) = a_{ICW}(t) \cdot e^{j\theta_{ICW}(t)} \\ & \qquad = A \cdot \text{rect}\left(\frac{t}{T}\right). \end{aligned} \tag{4.18}$$

Without the carrier component, Eq. (4.18) is the ICW transmit waveform shifted to baseband. Applying Eq. (4.18) to Eq. (4.17), the AF of a rectangular ICW pulse can be shown to be

$$\begin{aligned} AF_{ICW}(\Delta t, \omega_d) &= \left| \int_{-\infty}^{\infty} A \cdot \text{rect}\left(\frac{\xi}{T}\right) A \cdot \text{rect}\left(\frac{\xi + \Delta t}{T}\right) e^{j\omega_d \xi} d\xi \right| \\ &= A^2 \left| \int_{\frac{-T}{2}}^{\frac{T}{2}} \text{rect}\left(\frac{\xi + \Delta t}{T}\right) e^{j\omega_d \xi} d\xi \right| \\ &= A^2 T \left(1 - \frac{|\Delta t|}{T}\right) \text{sinc}\left[\frac{\omega_d T}{2}\left(1 - \frac{|\Delta t|}{T}\right)\right] \end{aligned} \tag{4.19}$$

for $|\Delta t| \leq T$, and 0 otherwise. This thesis uses the definition

$$\text{sinc}(x) = \frac{\sin(x)}{x}. \tag{4.20}$$

The ambiguity function for a rectangular ICW pulse is shown plotted in Figs. 4.2 and 4.3.

Useful features of an AF are its cuts across the zero-valued center of each axis. For an individual radar pulse, the zero-Doppler and zero-time-difference cuts are used to determine how much echo Doppler mismatch and sample timing error the MF can tolerate before detection performance is degraded beyond usefulness. The zero-Doppler and zero-time-difference cuts for an ICW AF are shown in Figs. 4.4 and 4.5.

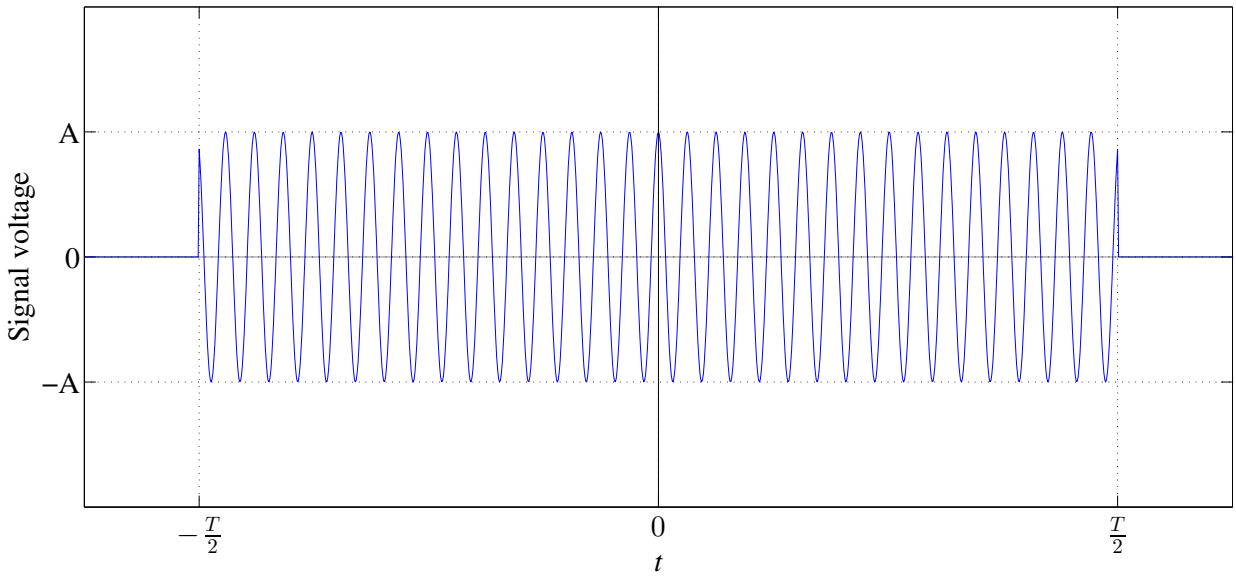

Figure 4.1: A simple rectangular ICW pulse. The quantity A is the pulse amplitude, and T is the pulse length.

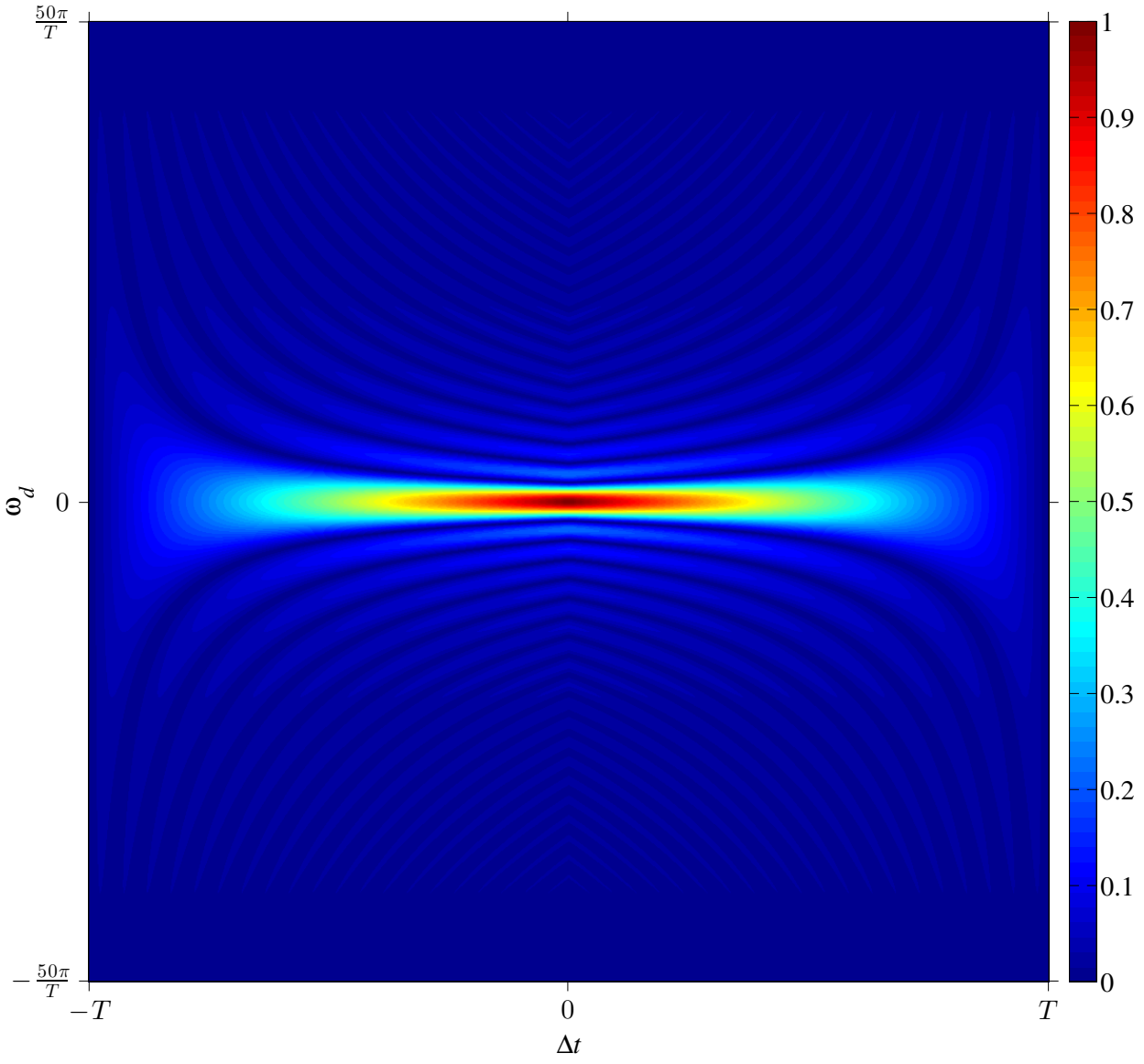

Figure 4.2: The ambiguity function for a simple rectangular ICW pulse. The normalized MF output magnitude for each $(\Delta t, \omega_d)$ pair is given by the color scale to the right. The quantity ω_d is the Doppler mismatch, and Δt is the time difference from the MF peak response time t_{MF}.

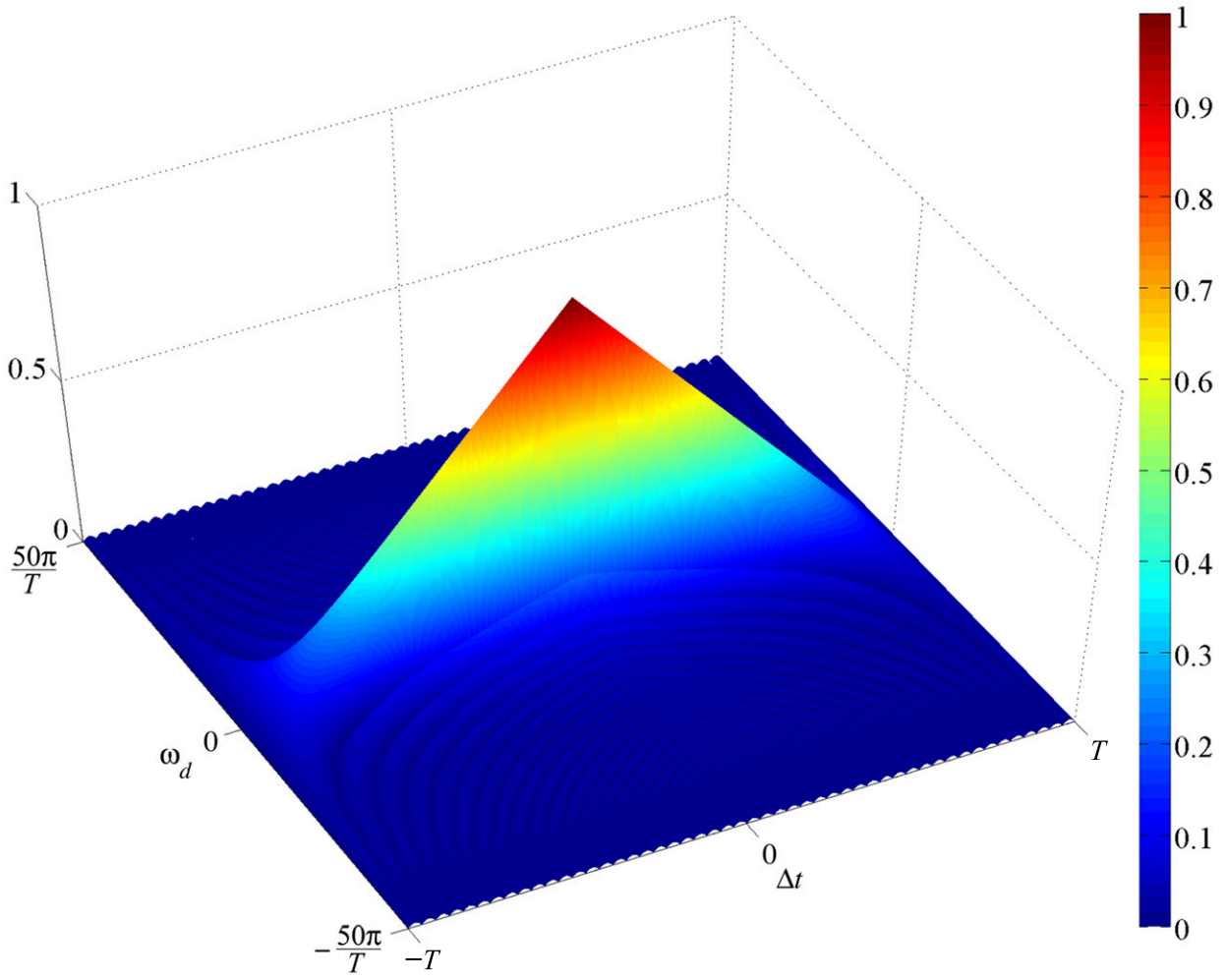

Figure 4.3: The ambiguity function in 3-D for a simple rectangular ICW pulse. The normalized MF output magnitude for each $(\Delta t, \omega_d)$ pair is given by the color scale to the right. The quantity ω_d is the Doppler mismatch, and Δt is the time difference from the MF peak response time t_{MF}.

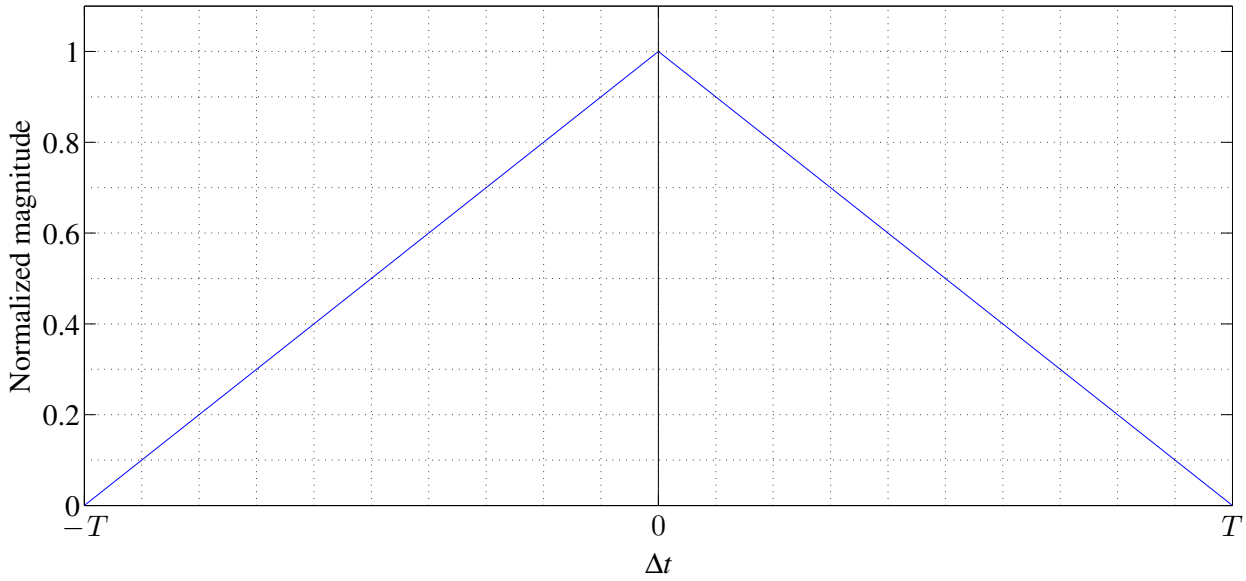

Figure 4.4: Zero-Doppler ($\omega_d = 0$) cut from the ICW ambiguity function of Fig. 4.3.

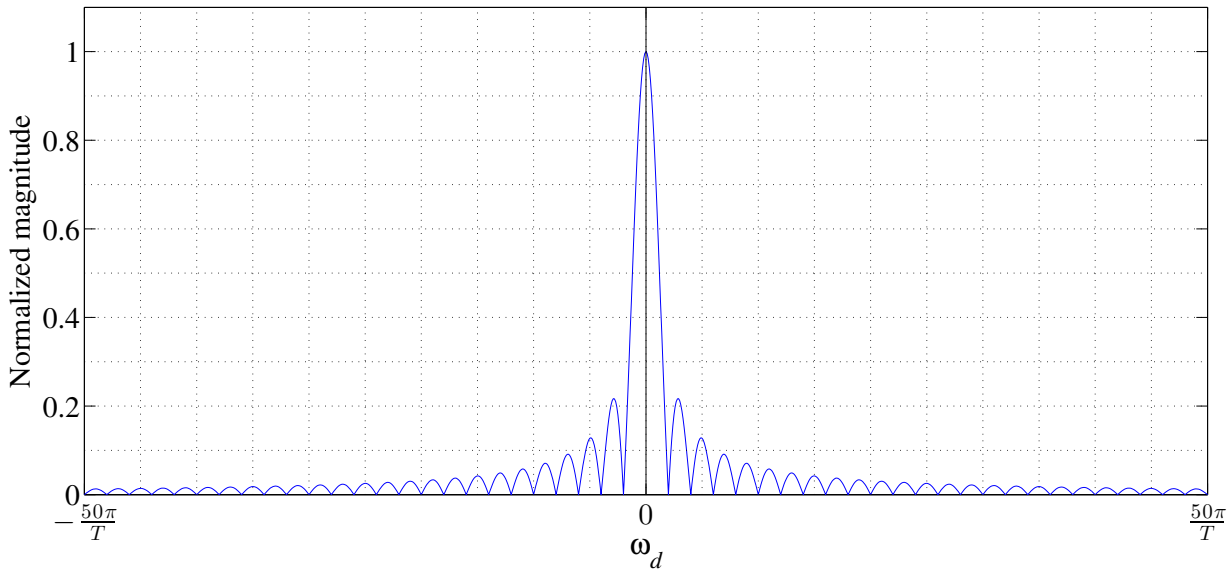

Figure 4.5: Zero-time-difference ($\Delta t = 0$) cut from the ICW ambiguity function of Fig. 4.3.

If the detection threshold is -3dB, or half of the peak output of a MF, then the ICW AF of Fig. 4.3 shows that in the absence of Doppler error, a sample timing error of up to half the pulse length still allows the target to be detected. For a 1 μs pulse, this allows a sample timing error of ± 0.5 μs. However, this large sample timing error tolerance comes at the expense of range resolution, which is observable in the width of the AF's triangular "blade" along the zero-Doppler cut in Figs. 4.3 and 4.4. According to Eq. (2.2), a 1 μs ICW pulse has a range resolution of 150 m.

The Doppler resolution ΔF_D of an ICW pulse is given by the blade's thickness along the Doppler axis at $\Delta t = 0$, as shown in Fig. 4.5, and is defined [1] as

$$\Delta F_D = \frac{1}{T}. \tag{4.21}$$

It turns out that for target detection, an ICW pulse is very robust against Doppler mismatch. A Doppler shift F_D that would prevent detection requires speeds faster than the capabilities of almost any conceivable man-made target of interest, except possibly missiles or spacecraft. The Doppler shift formula [1] is

$$F_D = \frac{2v_{LOS}}{\lambda} = \frac{2v_{LOS}f_0}{c}, \tag{4.22}$$

where v_{LOS} is a target's relative radial velocity (its closing speed), λ is the radar wavelength, and f_0 is the radar frequency in Hz. Echos from inbound targets exhibit positive Doppler shifts, and outbound targets produce negative shifts. For an ICW pulse to suffer enough Doppler shift to prevent detection with a MF requires abnormally high radar frequencies, a very long pulse length, high supersonic target speeds, or an appropriate combination of these three factors. For example, assuming a 1 μs pulse and no sample timing error, the MF can tolerate over 600 kHz of Doppler mismatch before its output drops below the -3dB detection threshold. Such an extreme Doppler shift for a 1 μs pulse requires radial target speeds of at least 40 km/s for L-band, at least 7.5 km/s for X-band, and at least 2.2 km/s for Ka-band.

4.3 Ambiguity Function for a LFM Pulse

A rectangular LFM pulse waveform is shown in Fig. 2.5, and is repeated for convenience in Fig. 4.6. Following the same procedure for deriving the ICW AF, the mathematical starting point

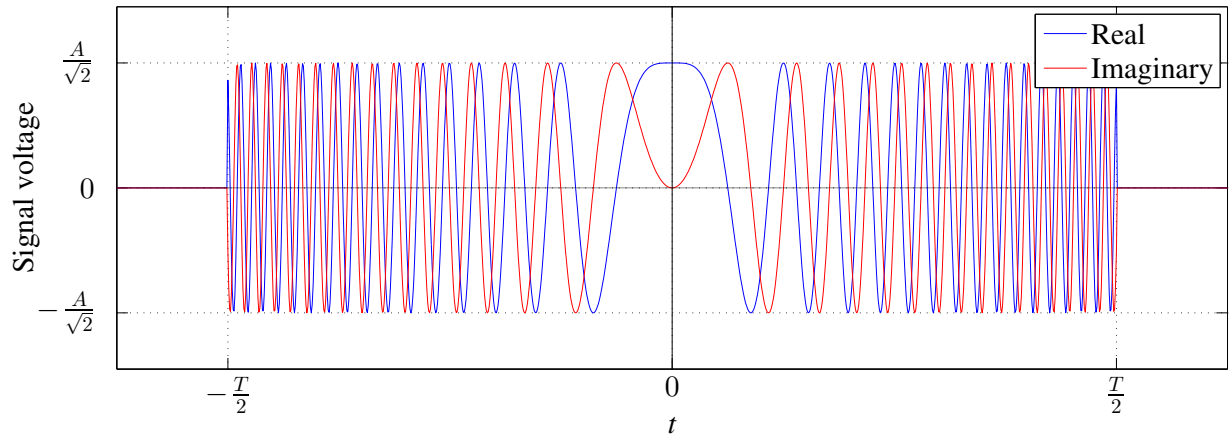

Figure 4.6: A rectangular complex LFM downchirp shifted to baseband. The quantity A is the waveform amplitude, and T is the pulse length.

for the LFM pulse's ambiguity function is as follows:

$$\begin{aligned} a_{LFM}(t) &= A \cdot \text{rect}\left(\frac{t}{T}\right), \\ \theta_{LFM}(t) &= \frac{1}{2} k_r t^2, \\ \therefore \quad g_{LFM}(t) &= a_{LFM}(t) \cdot e^{j\theta_{LFM}(t)} \\ &= A \cdot \text{rect}\left(\frac{t}{T}\right) e^{j\left(\frac{1}{2}k_r t^2\right)}, \end{aligned} \tag{4.23}$$

where k_r is the LFM frequency ramp rate, and $g_{LFM}(t)$ is the same baseband-shifted transmit waveform used in my simulations and research [Eq. (2.4)]. Applying Eq. (4.23) to Eq. (4.17), the ambiguity function for a LFM pulse can be shown to be

$$\begin{aligned} AF_{LFM}(\Delta t, \omega_d) &= \left| \int_{-\infty}^{\infty} A \cdot \text{rect}\left(\frac{\xi}{T}\right) e^{-j\left(\frac{1}{2}k_r \xi^2\right)} A \cdot \text{rect}\left(\frac{\xi + \Delta t}{T}\right) e^{j\frac{1}{2}k_r(\xi+\Delta t)^2} e^{j\omega_d \xi} d\xi \right| \\ &= A^2 \left| e^{j\left(\frac{1}{2}k_r \Delta t^2\right)} \int_{\frac{-T}{2}}^{\frac{T}{2}} \text{rect}\left(\frac{\xi + \Delta t}{T}\right) e^{j(k_r \Delta t + \omega_d)\xi} d\xi \right| \\ &= A^2 T \left(1 - \frac{|\Delta t|}{T}\right) \text{sinc}\left[\frac{(k_r \Delta t + \omega_d)T}{2}\left(1 - \frac{|\Delta t|}{T}\right)\right] \end{aligned} \tag{4.24}$$

for $|\Delta t| \leq T$, and 0 otherwise. This ambiguity function for a LFM pulse is shown plotted in Figs. 4.7 (2-D) and 4.8 (3-D) for a time-bandwidth product $T \cdot BW$ of 25. The zero-Doppler and zero-time-difference cuts are respectively shown in Figs. 4.9 and 4.10.

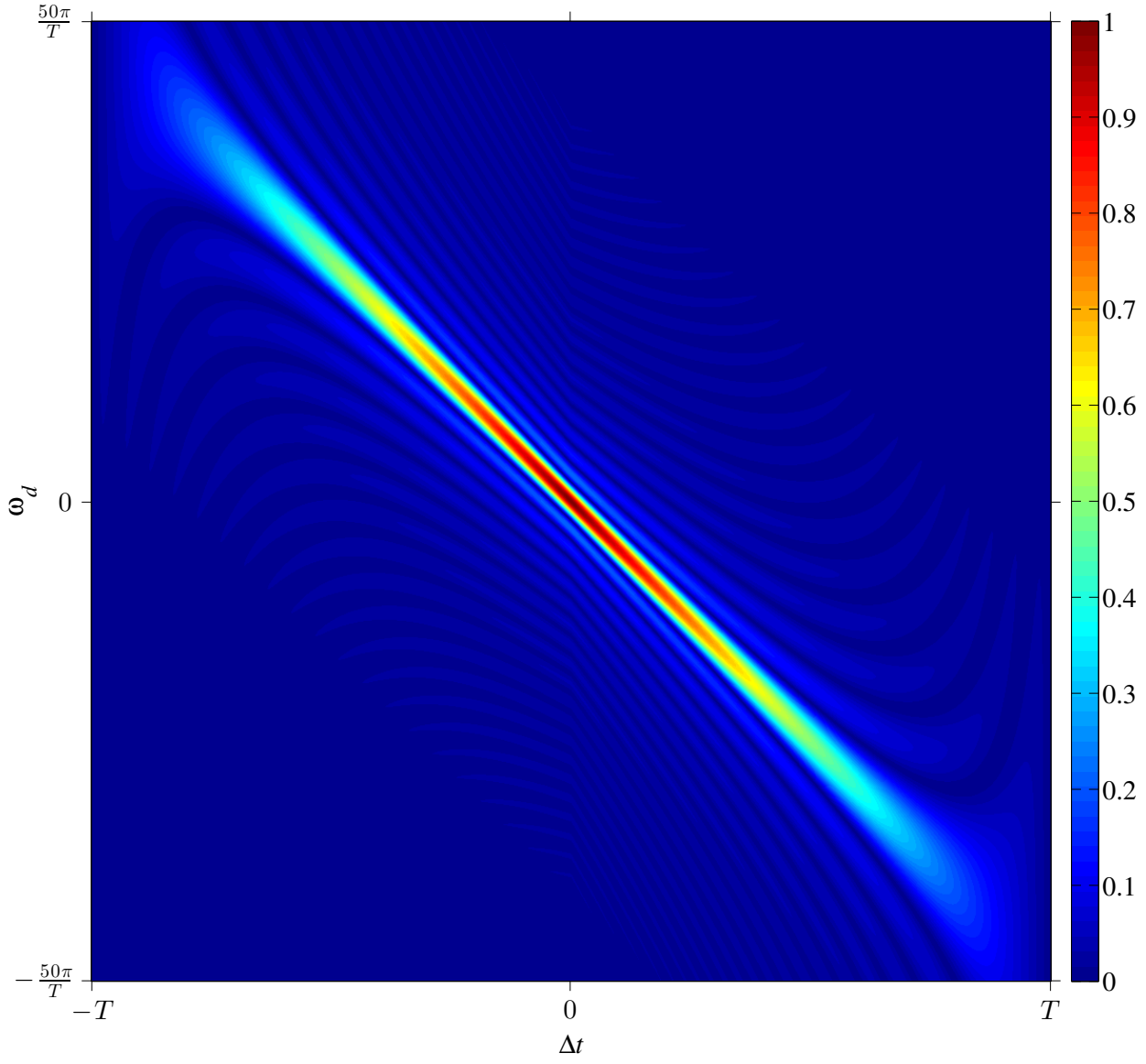

Figure 4.7: The ambiguity function for a rectangular LFM pulse with time-bandwidth product $T \cdot BW = 25$. The normalized MF output magnitude for each $(\Delta t, \omega_d)$ pair is given by the color scale to the right. The quantity ω_d is the Doppler mismatch, and Δt is the time difference from the MF peak response time t_{MF}.

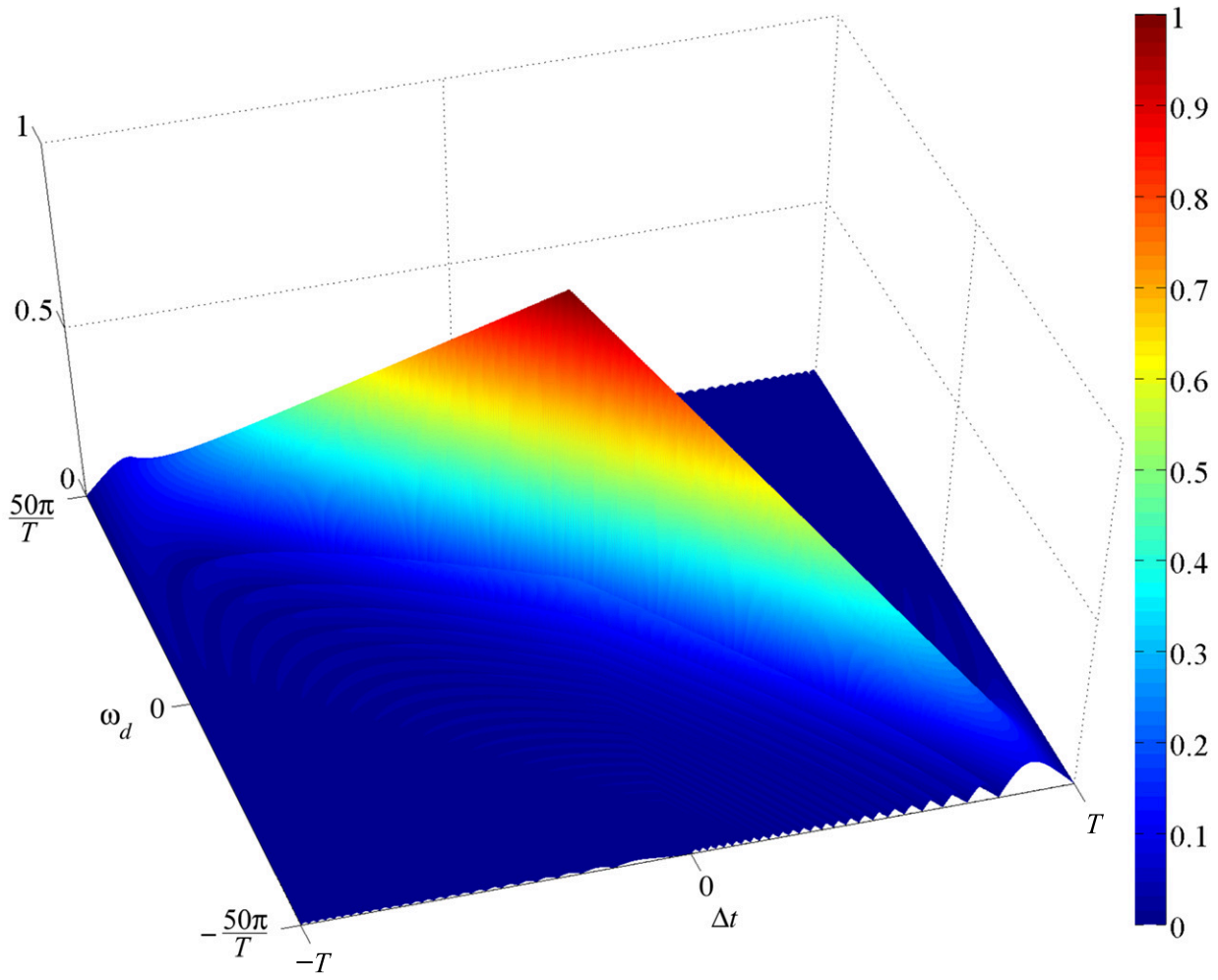

Figure 4.8: The ambiguity function in 3-D for a rectangular LFM pulse with time-bandwidth product $T \cdot BW = 25$. The normalized MF output magnitude for each $(\Delta t, \omega_d)$ pair is given by the color scale to the right. The quantity ω_d is the Doppler mismatch, and Δt is the time difference from the MF peak response time t_{MF}.

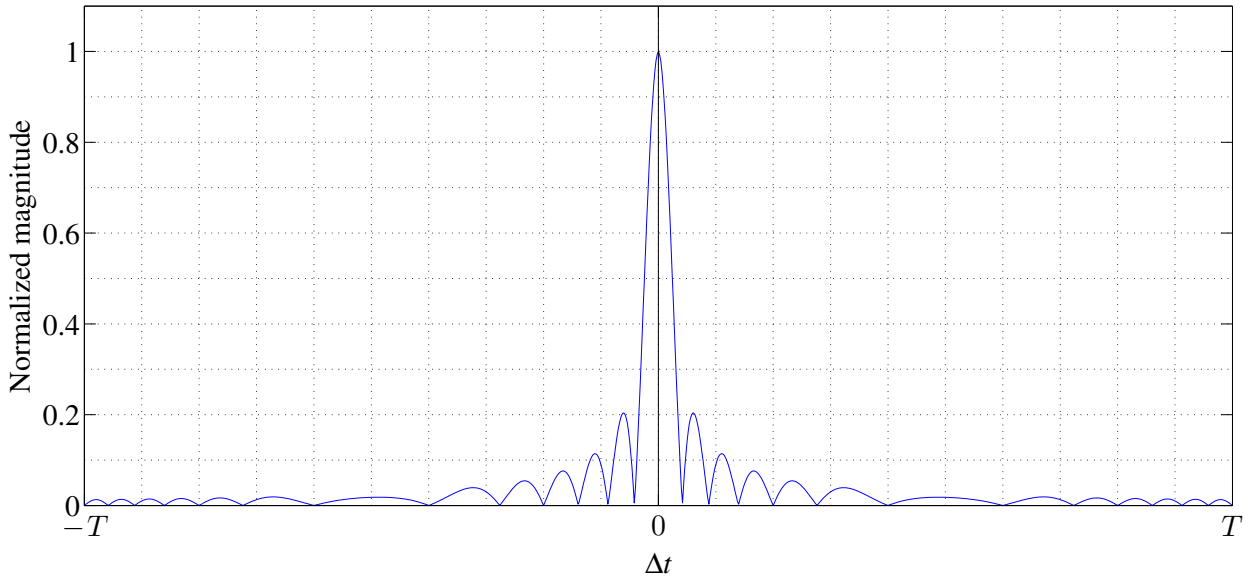

Figure 4.9: Zero-Doppler ($\omega_d = 0$) cut from the LFM ambiguity function of Fig. 4.8.

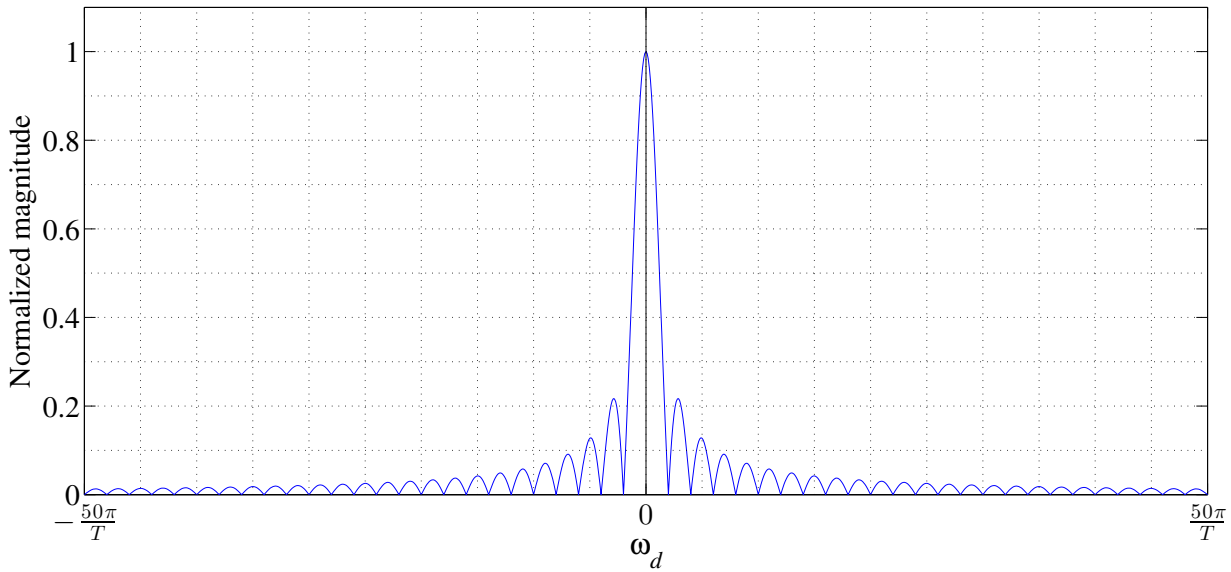

Figure 4.10: Zero-time-difference ($\Delta t = 0$) cut from the LFM ambiguity function of Fig. 4.8.

In Figs. 4.7 and 4.8, the LFM AF has a blade like the ICW AF in Figs. 4.2 and 4.3, but the blade is rotated in (Δt, ω_d) space due to the LFM frequency sweep. This illustrates the second property of AFs listed at the end of Section 4.1. When the frequency sweep is reduced to 0 Hz/s, the LFM pulse becomes an ICW pulse, and the LFM AF becomes an ICW AF. This is easily verified by comparing the baseband ICW and LFM waveforms in Eqs. (4.18) and (4.23), as well as the ICW and LFM AF expressions in Eqs. (4.19) and (4.24). When the frequency ramp rate variable k_r in the LFM equations is set to zero, they become the ICW equations. When k_r is nonzero, the blade rotates. All points on the blade's "edge" correspond to the sinc function's central peak in Eq. (4.24), which happens when the sinc's argument is set to zero:

$$\begin{aligned} k_r\Delta\tau + \omega_d &= 0 \\ \Rightarrow \omega_d &= -k_r\Delta\tau. \end{aligned} \tag{4.25}$$

This result shows that the slope of the AF blade is $-k_r$. For an upchirp, where k_r is positive, the AF blade's edge has a negative slope when viewed from above, as Fig. 4.7 shows, and vice versa for a downchirp.

This rotated blade indicates some important functional differences between ICW and LFM pulses. The only thing not changed is the zero-time-difference cut. This cut in Fig. 4.10 for the LFM AF is identical to the zero-time-difference cut in Fig. 4.5 for the ICW AF, which means the LFM pulse has the same Doppler resolution as an ICW pulse [1].

The LFM AF zero-Doppler cut in Fig. 4.9, however, is very different than from the ICW case in Fig. 4.4. For the LFM AF, the zero-Doppler cut is very sinc-like, with a main lobe much narrower than the the triangular zero-Doppler cut for the ICW case. This indicates, as covered in Sections 2.2.2 and 2.2.3, that the LFM pulse has much better range resolution than the ICW pulse. The un-sinc-like sidelobes are due to the quadratic phase term in the LFM transmit waveform [Eqs. (2.4) and (4.23)], which is the source of the linear frequency modulation.

The LFM AF's rotated blade also produces another significant effect worth mentioning. As stated earlier, at the end of Section 2.4.2, nearly every engineering benefit gained in some aspect of a system must be paid for elsewhere in the form of some tradeoff. For a LFM pulse, the benefit is greatly improved range resolution. One tradeoff, however, is not so obvious until its AF

is visualized in Figs. 4.7 and 4.8. The LFM AF shows that a nonzero Doppler shift changes the timing of the peak output from the matched filter, causing the target to appear at a different range than where it actually is [1, 2].

However, even though this is technically a tradeoff against the LFM pulse's improved range resolution, it turns out to not be a significant penalty at all. There are two reasons for this: first, this phenomenon actually makes the LFM pulse more Doppler tolerant than the ICW pulse, which is already very Doppler tolerant as discussed in Section 4.2. If a target's Doppler shift is high enough to shift the timing peak significantly for a LFM pulse, the peak is still very discernible according to the LFM AF, which means the target can still be detected. The same cannot be said for an ICW pulse with a high Doppler shift.

Second, the speeds required to noticeably shift the MF's peak response time are still prohibitively high for many targets of interest. Starting from Eq. (4.25) and using the substitutions $\omega_d = 2\pi F_D$, $k_r = \frac{BW}{T}$, and $\Delta\tau = \frac{2\delta R}{c}$, where δR is the apparent range error, it can be shown that the relationship between Doppler shift and δR for a LFM pulse is

$$\delta R = -\frac{\pi c T F_D}{BW}. \tag{4.26}$$

Solving Eq. (4.26) for the Doppler shift F_D and substituting it into the Doppler shift formula of Eq. (4.22), a direction relationship between the apparent range error δR and relative radial target speed v_{LOS} can be found:

$$v_{LOS} = -\frac{\delta R \cdot BW}{2\pi T f_0}. \tag{4.27}$$

For a pulse length T of 1 μs, a radar frequency f_0 of 1.5 GHz (L-band), a bandwidth BW of 200 MHz, and a MF matched to a stationary target, the radial target speed required to produce an apparent range error of ± 1 m is $\approx$21 km/s. For 10 GHz (X-band), the required target speed reduces to $\approx$3 km/s. Unless the radar uses a high frequency, a small bandwidth, a long pulse length, or a combination of these factors, this tradeoff is not a significant problem. Even if the radar is designed in such a way that this tradeoff does pose a problem, it turns out that this problem can be overcome rather easily. For an LFM upchirp, whose AF is shown in Figs. 4.7 and 4.8, a receding target with a negative Doppler shift appears to be farther away than it actually is by a range error δR. For a downchirp, the same target appears closer by the same δR. If the radar transmits an upchirp

followed by a downchirp (or vice versa), and averages the two range measurements, the target's true range can be determined [1]. Also, comparing the true range to the measured range gives the range error δR, which when applied to Eq. (4.27), determines the target's true radial speed v_{LOS}. The technical complexity increase required to use an LFM pulse over an ICW pulse appears to be a small price to pay for the benefits received, and is well worth doing.

4.4 Ambiguity Function for SAR Backprojection

The AFs derived in the previous two sections are for single radar pulses. Note that they are based on the MF output as a function of Doppler shifts and time differences relative to the peak MF response. As stated at the beginning of Chapter 2, Doppler shifting in the physical sense can be equivalently interpreted as pulse-to-pulse phase changes in successive radar echos for a sufficiently high PRF. This allows the stop-and-hop model to be used, which makes simulation easier while still producing valid results. The geometric phase interpretation of Doppler is also important for the BPJ AF because the BPJ algorithm deals with the phase of the data based only on the situational geometry. If the SAR PRF satisfies the Nyquist criteria based on the SAR's Doppler bandwidth, then any Doppler effects due to target motion are inherently embedded in the data. But unlike the single-pulse AF, where timing and Doppler mismatches are independent of each other, they are coupled together in the BPJ AF computation, which is explained later in this section.

Backprojection is a two-dimensional spatial matched filter. Unlike a physical MF found in a radar receiver, BPJ is a mathematical MF implemented in software. The BPJ filter design is based not only on the waveform of a single transmitted pulse, but also on the SAR IPR, which is the phase history between the SAR and the pixels used to form the SAR image. Phase history for pixels is equivalently stated as the relative motion between the SAR and the image pixels during image formation. If the pixels are matched to a moving target, the BPJ image is matched to that target in the same sense as a traditional MF correctly matched to a signal.

Range Compressed Data Expression for a Single Pulse

To start the BPJ AF derivation, I compute a mathematical expression for a single pulse's RC data in response to backscattering from only a single point target. For this I use the LFM

transmit and echo waveforms of Eqs. (2.4) and (2.5), repeated here for convenience:

$$\psi_{LFM}(t) = A \cdot \text{rect}\left(\frac{t}{T}\right) e^{j\left(\frac{1}{2}k_r t^2\right)}, \tag{4.28}$$

$$\psi_{LFM,r}(t) = \alpha A \cdot \text{rect}\left(\frac{t-\tau}{T}\right) e^{j\left[\frac{1}{2}k_r(t-\tau)^2+\phi\right]}. \tag{4.29}$$

Note that Eq. (4.29) uses the echo's phase shift ϕ instead of the physical Doppler shift ω_d. In computing the RC data for one pulse, I assume the SAR receiver uses an optimal MF, as given by Eq. (4.12), matched to a copy of the LFM transmit pulse. Applying Eq. (4.28) to Eq. (4.12), the optimal LFM MF is found to be

$$z_{LFM}(t) = \frac{2C\alpha A}{N_0}\text{rect}\left(\frac{t_{MF}-\tau-t}{T}\right) e^{-j\frac{1}{2}k_r(t_{MF}-\tau-t)^2}. \tag{4.30}$$

Next I cross-correlate the received echo signal with the matched filter by applying Eqs. (4.29) and (4.30) to Eq. (4.14) to compute the RC data expression:

$$\begin{aligned} RC(t) &= \psi_{0,LFM}(t) \\ &= \frac{1}{2}\psi_{LFM,r}(t) \star z_{LFM}(t) \\ &= \frac{1}{2}\int_{-\infty}^{\infty} \alpha\psi_{LFM,r}(x-\tau)\frac{2C\alpha}{N_0}\psi^*_{LFM,r}(t_{MF}-\tau-t+x)dx. \end{aligned} \tag{4.31}$$

Making the substitution $\xi = t_{MF} - \tau - t + x$ and moving constant factors out of the integral, Eq. (4.31) becomes

$$RC(t) = \frac{C\alpha^2}{N_0}\int_{-\infty}^{\infty} \psi^*_{LFM,r}(\xi)\psi_{LFM,r}(\xi + t - t_{MF})d\xi. \tag{4.32}$$

Now making the substitution $\Delta t = t - t_{MF}$, Eq. (4.32) becomes

$$\begin{aligned} RC(t) &= \frac{C\alpha^2}{N_0}\int_{-\infty}^{\infty} \psi^*_{LFM,r}(\xi)\psi_{LFM,r}(\xi+\Delta t)d\xi \\ &= \frac{C\alpha^2}{N_0}\int_{-\infty}^{\infty} A\cdot\text{rect}\left(\frac{\xi}{T}\right)e^{-j\frac{1}{2}k_r\xi^2} A\cdot\text{rect}\left(\frac{\xi+\Delta t}{T}\right)e^{j[\frac{1}{2}k_r(\xi+\Delta t)^2+\phi]}d\xi \\ &= \frac{C\alpha^2A^2}{N_0}e^{j(\frac{1}{2}k_r\Delta t^2+\phi)}\int_{-\frac{T}{2}}^{\frac{T}{2}}\text{rect}\left(\frac{\xi+\Delta t}{T}\right)e^{jk_r\Delta t\xi}d\xi. \end{aligned} \tag{4.33}$$

At this point it makes more sense to call it $RC(\Delta t)$ rather than $RC(t)$. I also simplify Eq. (4.33) by dropping the constant factor $\frac{C\alpha^2}{N_0}$ that came from the MF derivation. After making these changes to Eq. (4.33), the RC data for a single pulse can be shown to have the following form:

$$RC(\Delta t) = A^2 T \left(1 - \frac{|\Delta t|}{T}\right) e^{j\phi} \cdot \text{sinc}\left[\frac{k_r T \Delta t}{2}\left(1 - \frac{|\Delta t|}{T}\right)\right]. \tag{4.34}$$

A comparison between Eqs.(4.34) and (4.24) shows that the RC data for one LFM pulse, as used in the stop-and-hop model, is the same as the expression for the LFM AF, except the effect of the Doppler shift ω_d has been replaced by the phase shift ϕ.

The BPJ AF, as I derive it, is based on how mismatches between the velocity vectors of the target and the BPJ focus affect the final pixel values in the image. A pixel's final value depends on how well its IPR (phase history) matches that of the target. When BPJ computes the complex value of an image pixel, it samples each pulse's RC data at the discrete time index best corresponding to the slant range between the SAR and the pixel for that pulse. The location of the sinc's central peak in a given pulse's RC data depends on the current slant range to the target. If a pixel being computed is not in the same location as the target, the sampled index of the RC data most likely is not at the central peak, unless the pixel happens to be at the same range as the target. This means that for most pixels, the phase shift removal factor $e^{-j\phi}$ essentially removes the "wrong" phase because no backscattering target exists at that pixel range. By design, removing the wrong phase causes destructive interference over the course of the BPJ integration for that pixel, and no target appears in that pixel after image formation is complete.

When the RC data is sampled at its central peak, the phase shift removal factor $e^{-j\phi}$ turns the complex RC data point into a purely real number, as illustrated in Fig. 4.11. This is because the echo's physical phase shift $e^{j\phi}$ is directly tied to the target's slant range, and when the computed slant range correctly matches that of the target, the corresponding reverse phase shift computation is also correct. During the BPJ integration process, the maximum possible final pixel value is realized when the pixel is initially matched to the target's initial position, and then matches the target's velocity vector for the rest of the integration time. This ideal matched scenario causes all the BPJ contributions to that pixel to be purely real, which represents the constructive interference

that maximizes the pixel's final BPJ value. This is seen as a bright point in the SAR image, revealing the target's presence and location.

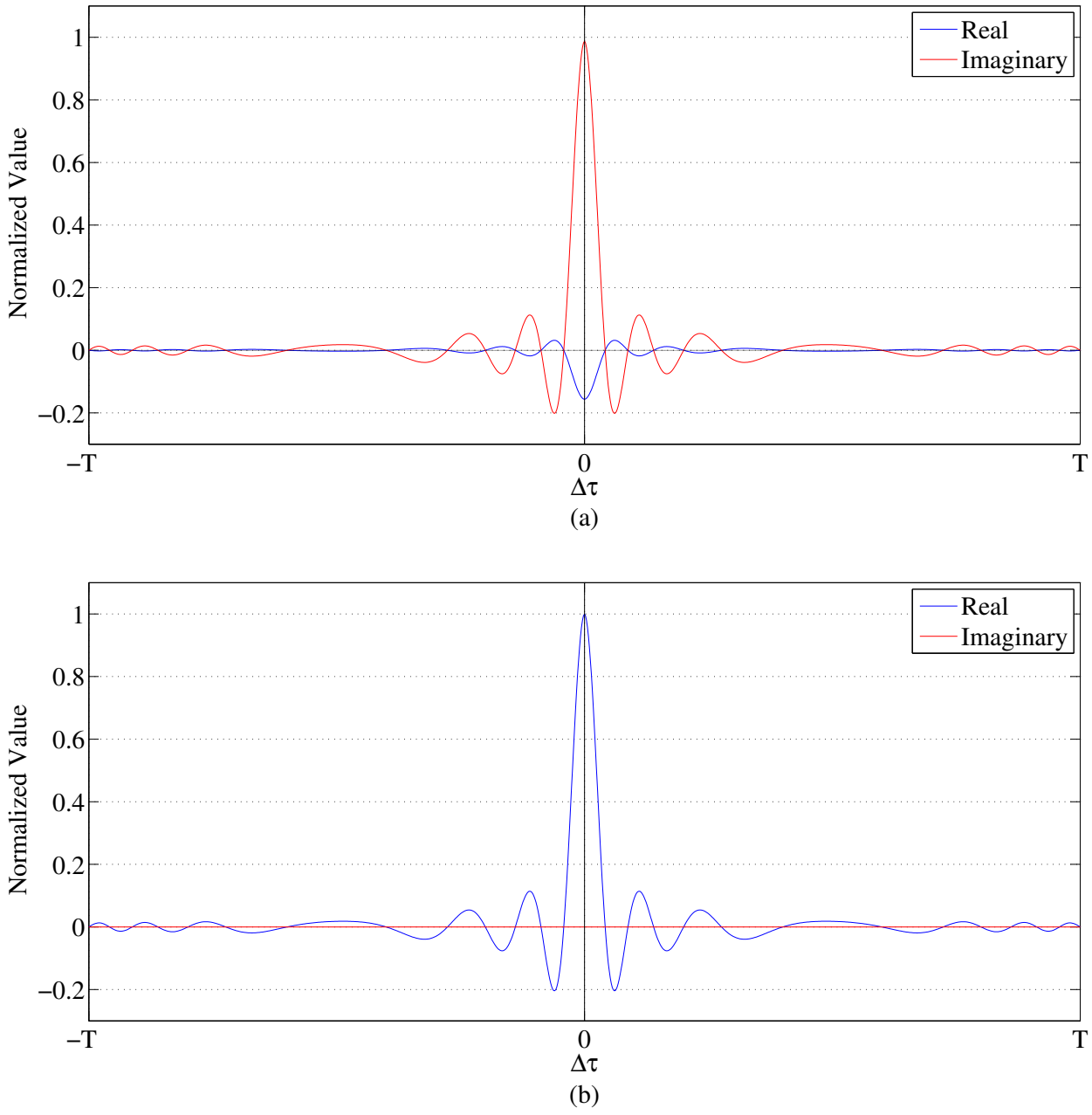

Figure 4.11: RC data for a single pulse. Panel (a) depicts RC data for a point target, where the data has an arbitrary phase shift ϕ due to the echo delay. In panel (b), the phase shift has been removed by multiplying the data by $e^{-j\phi}$, leaving a purely real result. When working with a pixel at a different slant range than the target, the data in panel (a) is reverse-phase-shifted by a different amount, leaving a complex result.

For any pixel not at the target position, its range history does not match the target's (this is not entirely true, as will be proved in Chapter 5, but it is true enough for this discussion). For a given pixel at a range different from the target range, the computed echo delay τ for the pixel is different from the echo delay for the target. Defining the target's true echo delay as τ_T, the time difference $\Delta\tau$ between the echo delays for the pixel and the target is

$$\Delta\tau = \tau - \tau_T. \tag{4.35}$$

An echo delay mismatch $\Delta\tau$ between a pixel and the target also includes an inherent phase mismatch $\Delta\phi$, which can be shown to be

$$\begin{aligned} \Delta\phi &= \omega_0 \Delta\tau \\ &= \omega_0(\tau - \tau_T) \\ &= \phi - \phi_T. \end{aligned} \tag{4.36}$$

For the rest of this thesis, a distinction is made between ϕ and ϕ_T, as well as between τ and τ_T. The phase shift ϕ is a variable that depends on which pixel is being computed, and ϕ_T is the RC data's true phase shift due to the target's range.

The echo delay mismatch $\Delta\tau$ can be thought of as a MF sample time mismatch because it makes the BPJ MF sample the RC data at a suboptimal index location away from the central peak. Because the SAR phase history contains all the Doppler information about the target scene, a phase mismatch is equivalent to a Doppler mismatch. As stated at the beginning of this section (4.4), timing and Doppler mismatches for BPJ are coupled together. This is shown by the first line of Eq. (4.36). The two mismatch quantities $\Delta\tau$ and $\Delta\phi$ are used to finish developing the BPJ AF.

At this point I replace the quantity Δt in Eq. (4.34) with $\Delta\tau$ from Eq. (4.35). This change of variables is acceptable because Δt and $\Delta\tau$ both represent time differences, and $\Delta\tau$ is more relevant to the intent of this discussion. Finally, using the definition of $\Delta\tau$ from Eq. (4.35), the RC data expression for one pulse is now

$$RC(\tau) = A^2 T \left(1 - \frac{|\tau - \tau_T|}{T}\right) e^{j\phi_T} \cdot \operatorname{sinc}\left[\frac{k_r T(\tau - \tau_T)}{2}\left(1 - \frac{|\tau - \tau_T|}{T}\right)\right]. \tag{4.37}$$

Computing the Backprojection Ambiguity Function

The BPJ equation [Eq. (2.11)] is repeated here for convenience. The references to (x,y,z,n) have been dropped, also for convenience:

$$P(x,y,z) = \sum_{n=1}^{N} RC[\tau] \cdot e^{-j\phi}. \tag{4.38}$$

Using Eq.(4.35), the value of τ for any pixel may be treated as the target's true echo delay τ_T plus an echo delay mismatch $\Delta\tau$. The phase shift ϕ for an arbitrary pixel may also be treated as a corresponding true phase shift ϕ_T due to the target's range, plus an phase mismatch $\Delta\phi$. These reinterpretations may be applied to the BPJ equation in Eq. (4.38):

$$P(x,y,z) = \sum_{n=1}^{N} RC[\tau_T + \Delta\tau] \cdot e^{-j(\phi_T + \Delta\phi)}. \tag{4.39}$$

Expanding out the definition of $RC(\cdot)$ using Eq. (4.37) and using the definitions of $\Delta\tau$ and $\Delta\phi$, the standard BPJ equation turns out, in an equivalent form, to be the tool necessary to compute the BPJ AF:

$$AF_{BPJ}(\Delta\tau) = \left| \sum_{n=1}^{N} A^2 T \cdot e^{-j\Delta\phi} \left(1 - \frac{|\Delta\tau|}{T}\right) \operatorname{sinc}\left[\frac{k_r T \Delta\tau}{2}\left(1 - \frac{|\Delta\tau|}{T}\right)\right] \right|. \tag{4.40}$$

It should be stressed that although the BPJ AF appears to depend on both $\Delta\tau$ and $\Delta\phi$, these mismatches are coupled through Eq. (4.36), and cannot be separated. This is why the left side of the BPJ AF is written as a function of $\Delta\tau$ only.

Computing the AF for BPJ is not nearly as simple as it is for single radar pulses. First, a decision must be made about which mismatch variables to use. These mismatches can be in position, velocity, or both. Then a set of image pixels and their initial time-zero positions must be chosen. Then the echo delay mismatch history $\Delta\tau(x,y,z,n)$ must be determined for each individual pixel as a function of its initial position and the mismatch variables chosen. Then each pixel's image value must be computed with the BPJ AF equation [Eq. (4.40)]. Finally, the resulting image is the BPJ AF.

For example, if the mismatch variables are position differences $(\Delta x, \Delta y)$ for pixels matched to the target's velocity vector, then an isolated point target's appearance in a conventional BPJ

image matched to the target's motion *is* the positional AF for BPJ. This assumes no clutter, noise, or other interference. Examples of this are Figs. 2.23 through 2.25, and Figs. 3.22 through 3.24. An important fact about the BPJ AF is that it is a BPJ image computed the same way as all the other BPJ images in this thesis, except that the pixels may or may not maintain constant spatial positions relative to each other. The BPJ AF is a function of the echo delay mismatch history $\Delta\tau(x, y, z, n)$ for each pixel relative to the target. The pixels' echo delay mismatch histories in turn depend on the mismatch variables chosen, the set of pixels chosen, their initial positions, and their velocity vectors as determined by the chosen mismatch variables.

For this thesis, the mismatch variables of interest for the BPJ AF are the velocity differences (ΔV_x, ΔV_y) between a target and pixels near it, where x and y respectively refer to the cross-track and along-track directions. The very nature of this choice of mismatch variables necessarily means the image pixels involved do not maintain their spatial positioning to one another over the course of the BPJ integration, because each pixel has a different velocity vector. The idea is to visualize how mismatches between the pixel and target velocities affect the final pixels' image values. For this thesis, I demonstrate three different BPJ AFs with three different pixel sets with a simple spatial symmetry relative to the target. There is no major significance to these three choices, except that they were simple to think of, and simple to code up to compute the BPJ AF for each one.

The first BPJ AF I demonstrate shows the effect on velocity-mismatched pixels that all coincide with the target position at time zero of the target's BPJ integration. As the BPJ integration progresses, the pixels move away from the target according to the pixels' various (ΔV_x, ΔV_y) values relative to the target's velocity. This set of pixels is depicted in Fig. 4.12. Figure 4.13 shows a 2-D image of the BPJ AF that results from the analysis between a target and this particular set of image pixels. Figure 4.14 show a 3-D version of this BPJ AF. Figures 4.15 and 4.16 show close-ups of the central peak in Figs. 4.13 and 4.14. Repeated runs for computing this AF show that it does not depend on the target's velocity vector. It only depends on the relative motion between the pixels and the target.

The BPJ AFs shown in this thesis are normalized to a maximum value of 1. However, the central peak value is so large and narrow compared to the rest of the AF that instead of plotting its direct magnitude, the square root of its magnitude is plotted to make the other features more visible.

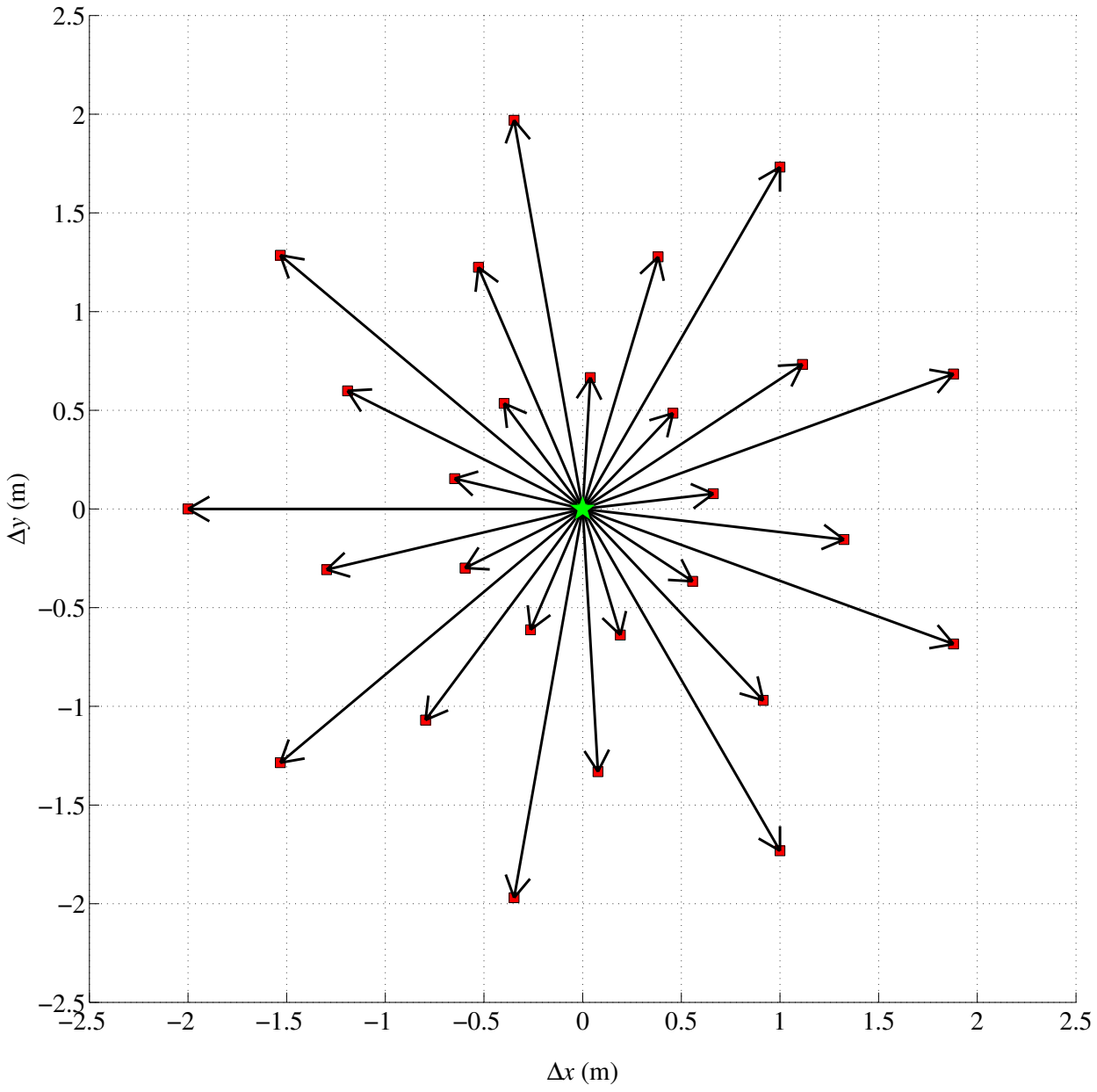

Figure 4.12: The set of moving pixels used to compute Example 1 of the BPJ AF in Figs. 4.13 through 4.16. At time zero, each pixel's initial position coincides with the target's position, represented by the green star. Once integration starts, the pixels move away from the target in all directions at different speeds. Regardless of the target's true velocity vector, each pixel moves relative to the target as a function of its own (ΔV_x, ΔV_y) value. The red squares represent final relative positions for pixels at the end of the integration process.

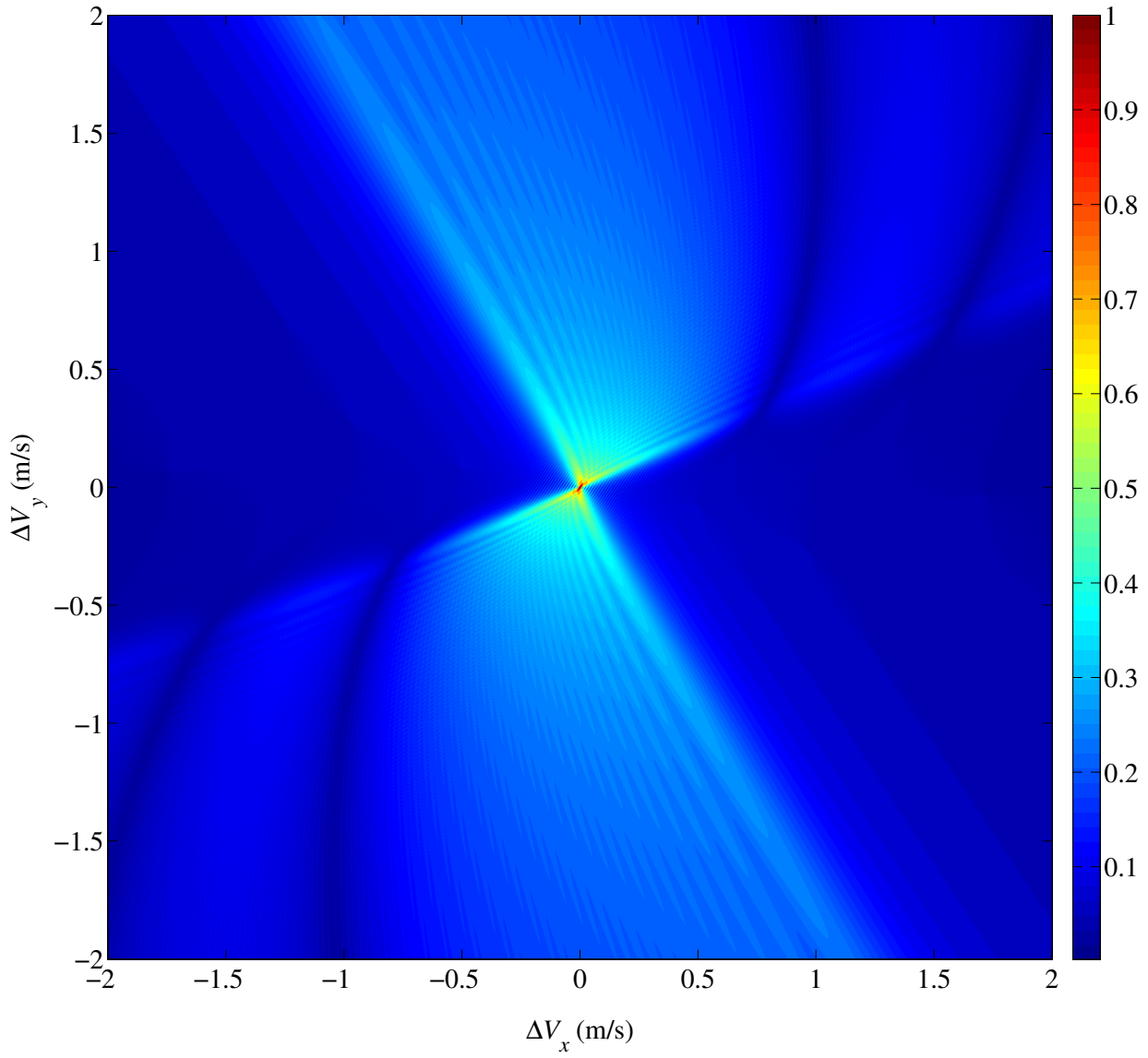

Figure 4.13: The BPJ AF for the pixel set shown in Fig. 4.12. At time zero, the pixels all start at the same position as the target, and then move away from it at different relative speeds according to the various values of $(\Delta V_x, \Delta V_y)$ for different pixels. The central peak is the pixel matched to the target's velocity vector for $\Delta V_x = \Delta V_y = 0$.

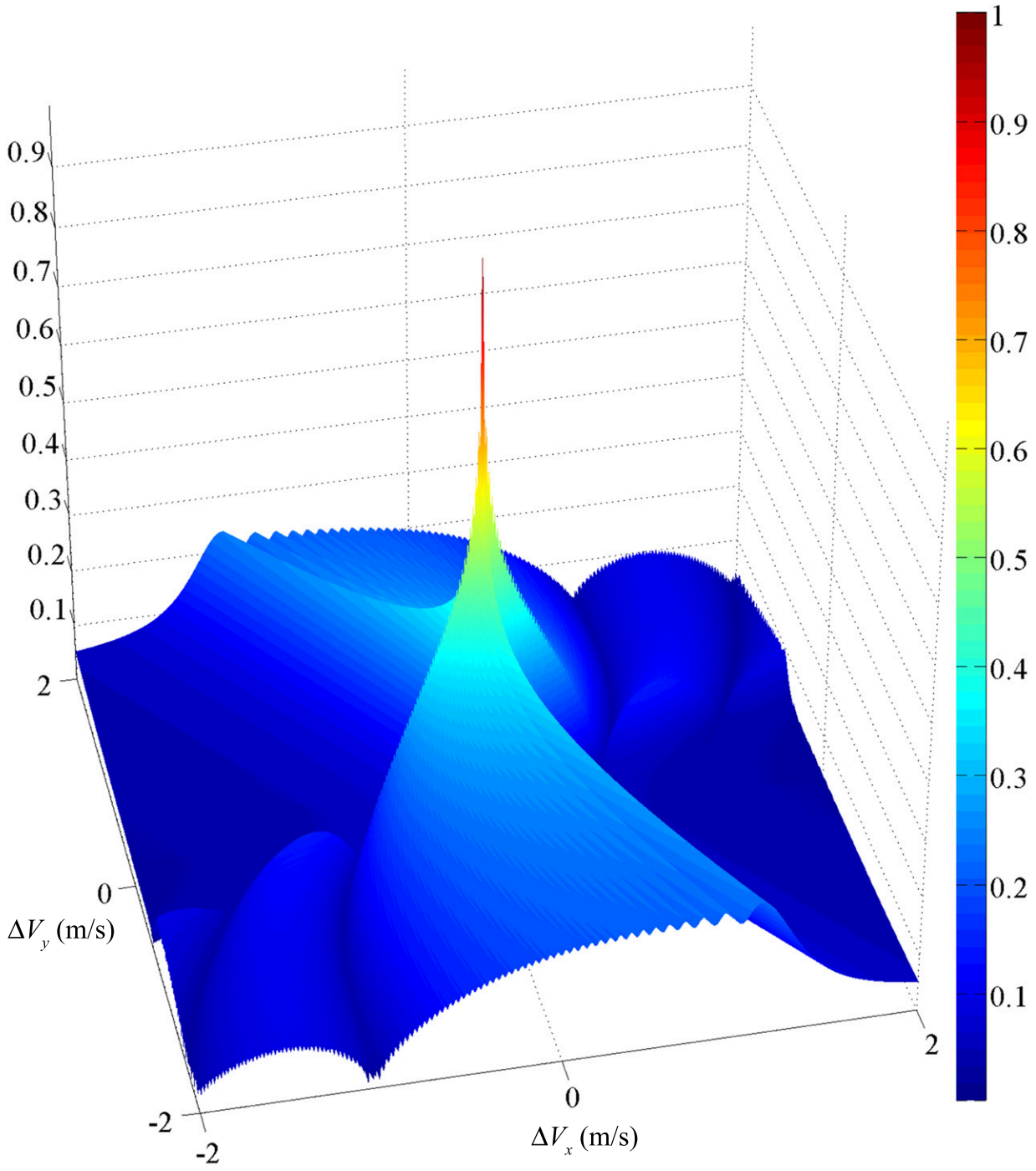

Figure 4.14: The BPJ AF in 3-D for the pixel set shown in Fig. 4.12. At time zero, the pixels all start at the same position as the target, and then move away from it at different relative speeds according to the various values of (ΔV_x, ΔV_y) for different pixels. The central peak is the pixel matched to the target's velocity vector for $\Delta V_x = \Delta V_y = 0$.

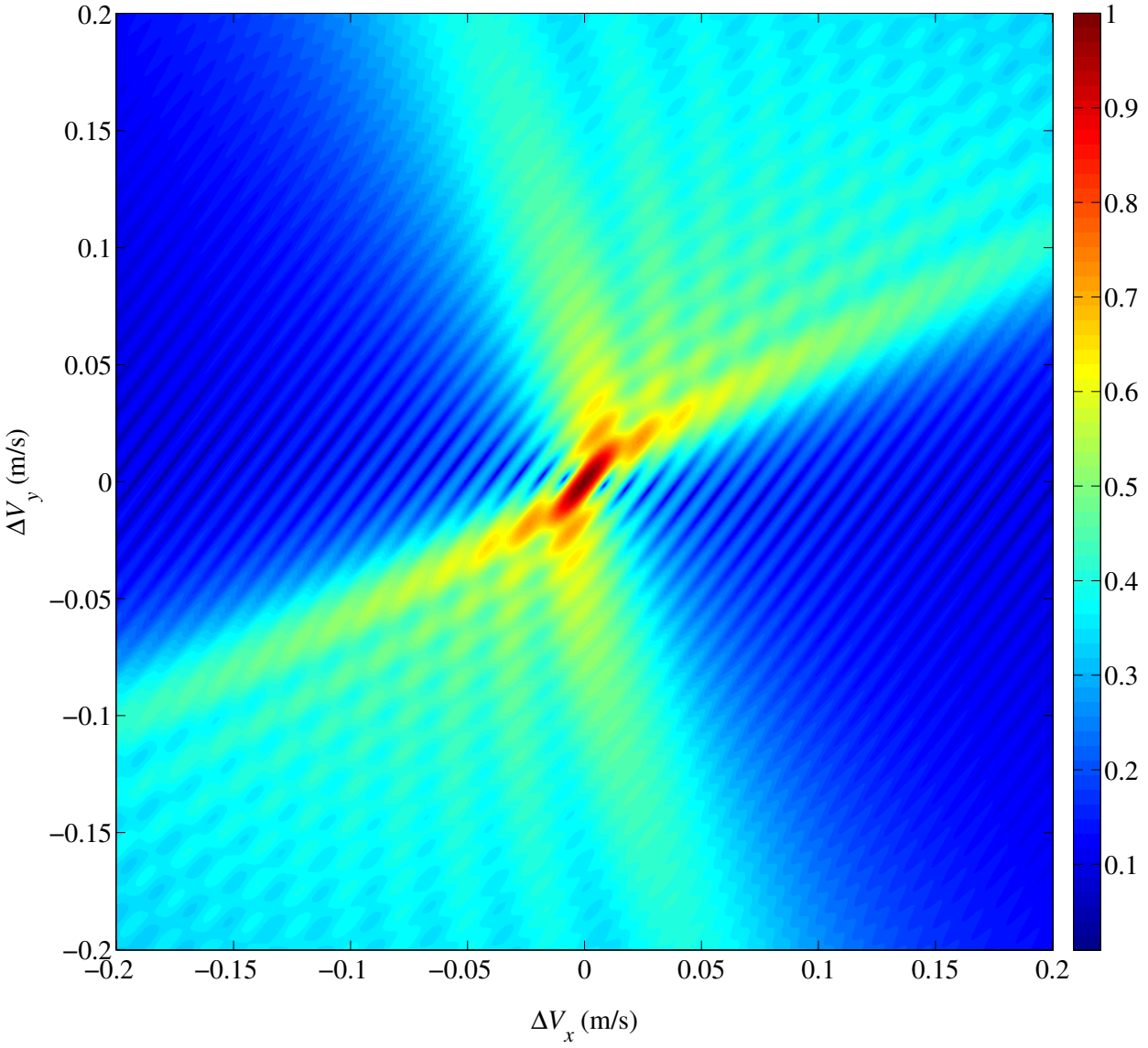

Figure 4.15: The BPJ AF for the pixel set shown in Fig. 4.12. This is a close-up of the central peak in Fig. 4.13. At time zero, the pixels all start at the same position as the target, and then move away from it at different relative speeds according to the various values of $(\Delta V_x, \Delta V_y)$ for different pixels. The central peak is the pixel matched to the target's velocity vector for $\Delta V_x = \Delta V_y = 0$.

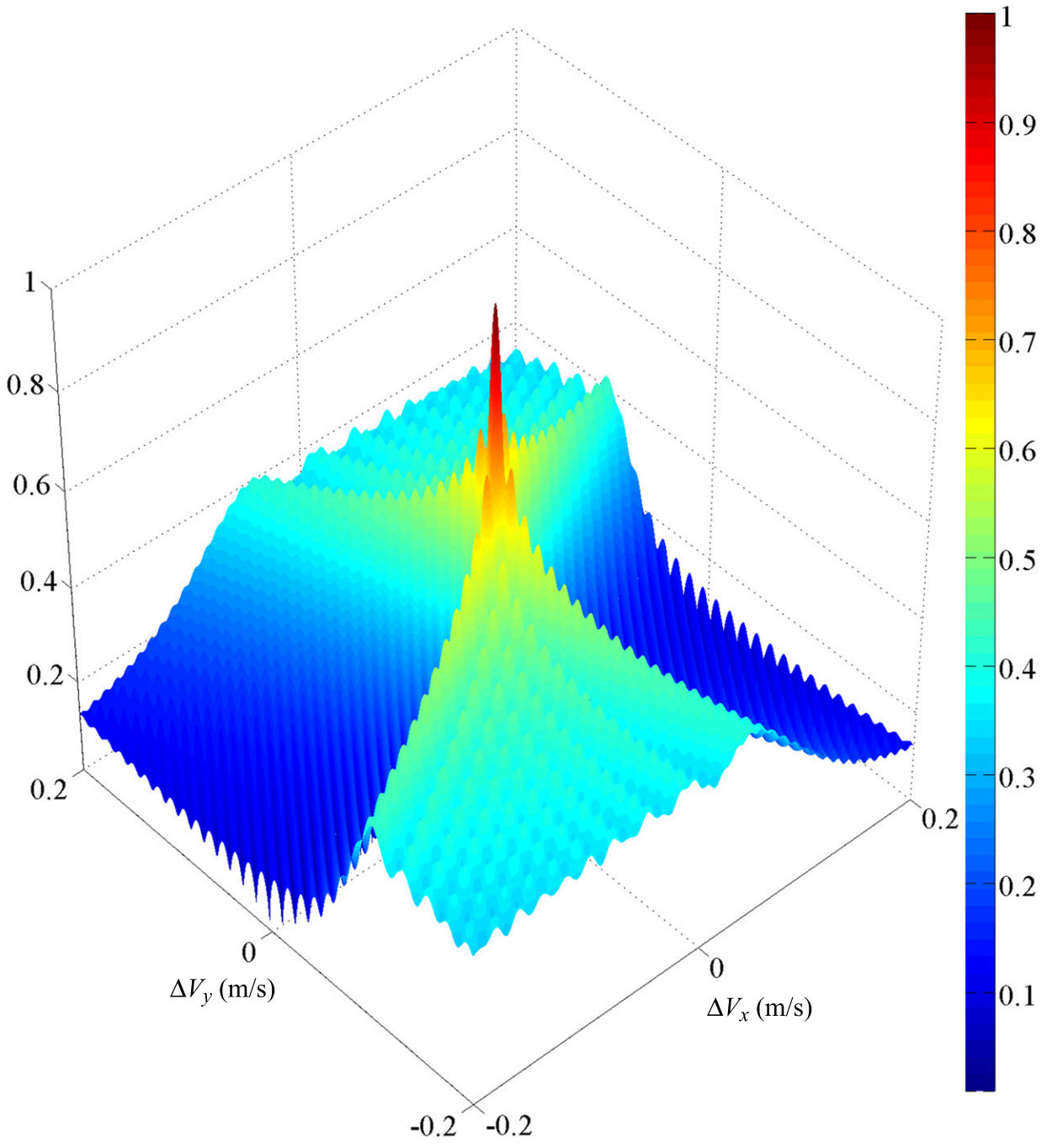

Figure 4.16: The BPJ AF for the pixel set shown in Fig. 4.12. This is a close-up of the central peak in Fig. 4.14. At time zero, the pixels all start at the same position as the target, and then move away from it at different relative speeds according to the various values of (ΔV_x, ΔV_y) for different pixels. The central peak is the pixel matched to the target's velocity vector for $\Delta V_x = \Delta V_y = 0$.

The second BPJ AF example is very similar to the first, except that the pixels start off-target at time zero, and converge toward it when integration starts. All the same values for (ΔV_x, ΔV_y) are used, except each pixel's initial position at time zero is chosen so that, according to its own (ΔV_x, ΔV_y), they all simultaneously coincide with the target position halfway through the integration time, then continue through the target position and diverge away from it. This pixel set is shown in Fig. 4.17, and the corresponding BPJ AF is shown in Fig. 4.18. Figure 4.18 shows the same four views that were shown for the first BPJ AF example in Figs. 4.13 through 4.16.

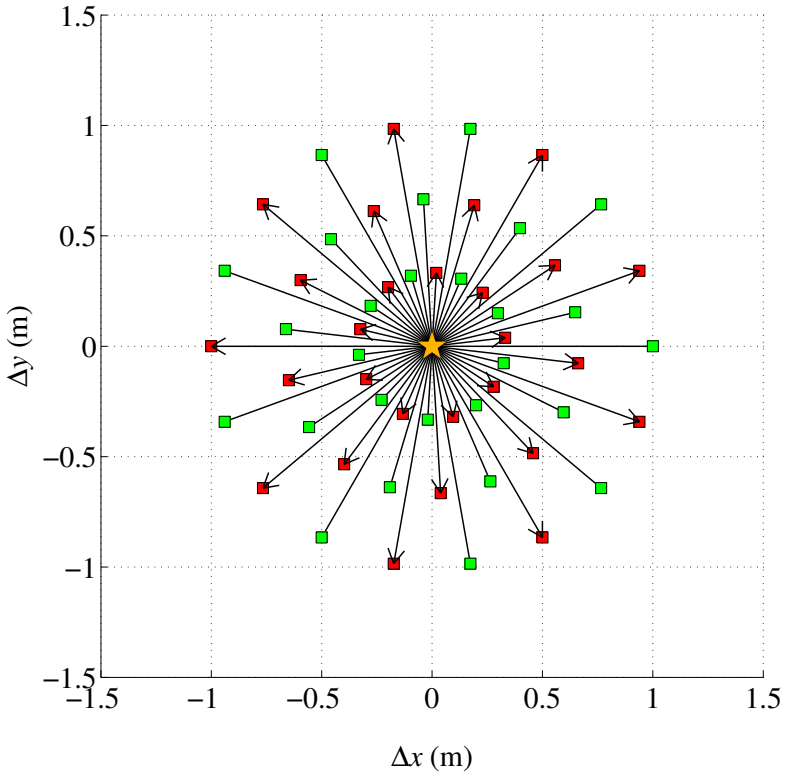

Figure 4.17: The set of moving pixels used to compute Example 2 of the BPJ AF in Fig. 4.18. This image is on the same physical scale as Fig. 4.12. At time zero, each pixel starts off-target. When integration starts, the pixels converge toward the target at different speeds. Their initial positions are chosen such that halfway through the integration time, the pixels all simultaneously pass through the target position. Regardless of the target's true velocity vector, each pixel moves relative to the target as a function of its own (ΔV_x, ΔV_y) value. The orange star represents the target, and the green and red squares respectively indicate initial and final pixel positions.

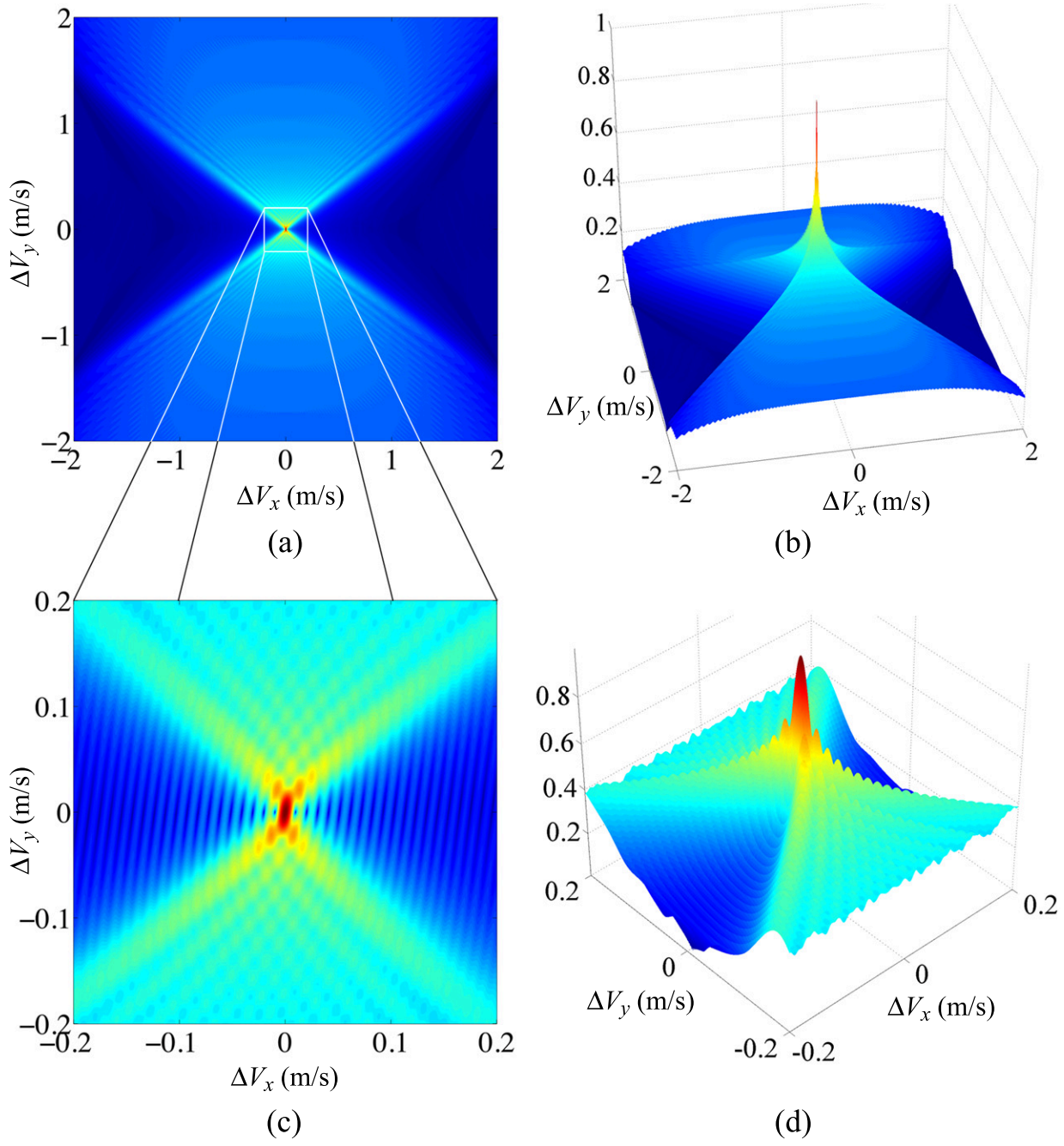

Figure 4.18: The BPJ AF for the pixel set shown in Fig. 4.17. At time zero, each pixel starts off-target. When integration begins, the pixels converge toward the target at different speeds. Halfway through the integration time, all pixels simultaneously pass through the target position. Regardless of the target's true velocity vector, each pixel moves relative to the target as a function of its own (ΔV_x, ΔV_y) value. Panel (a) is the BPJ AF in 2-D, panel (b) is the BPJ AF in 3-D, panel (c) is a close-up of the central peak in panel (a), and panel (d) is a close-up of the central peak in panel (b). The central peak is the pixel matched to the target's velocity vector for $\Delta V_x = \Delta V_y = 0$.

The third and final example of the BPJ AF is similar to the second example, with the pixels again starting off-target and converging toward it once integration starts at time zero. All the same values for (ΔV_x, ΔV_y) are used again. The difference, however, is that the pixels simultaneously converge at the target position at the end of the integration time. This pixel set is shown in Fig. 4.19, and is the complete opposite of the first example's pixel set in Fig. 4.12.

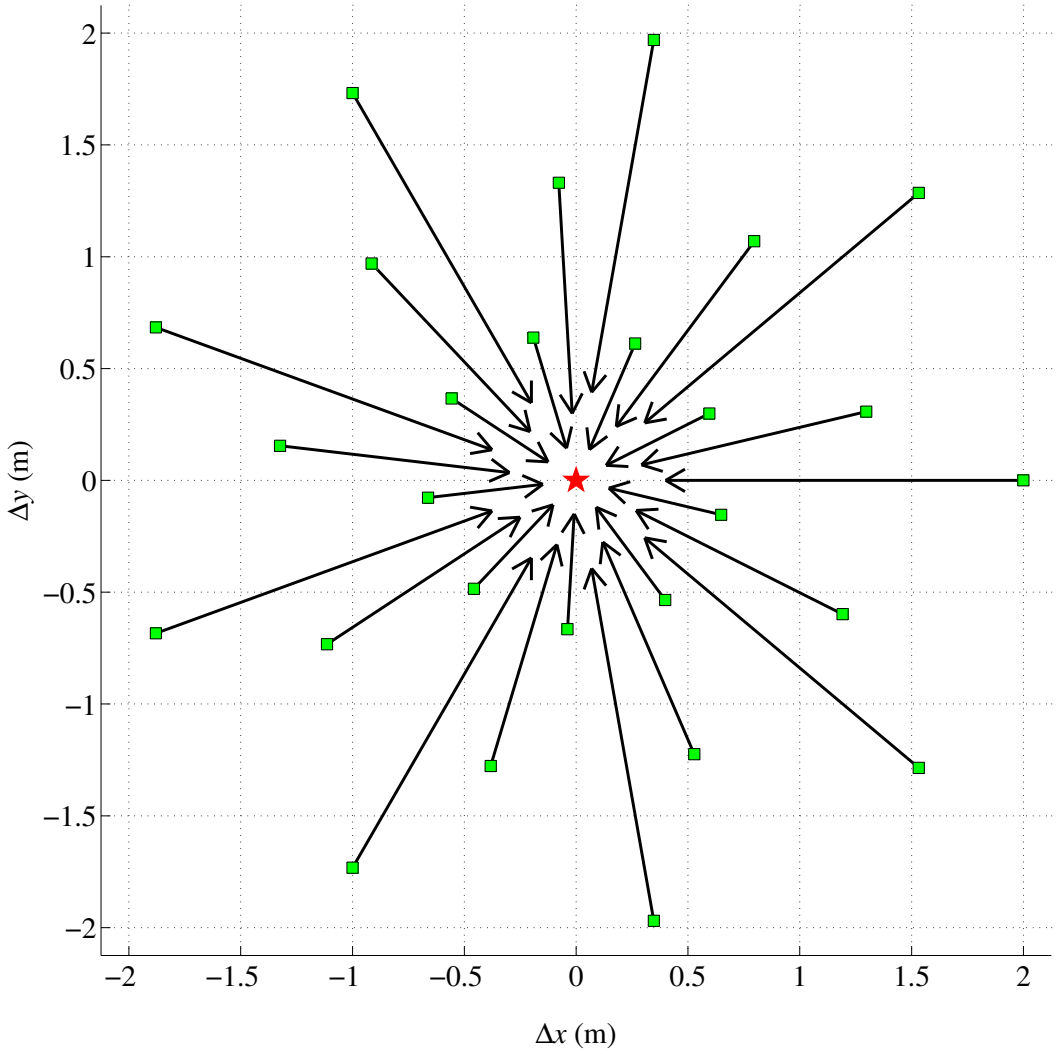

Figure 4.19: The set of moving pixels used to compute Example 3 of the BPJ AF in Fig. 4.20. At time zero, all pixels start off-target. When integration starts, the pixels move toward the target at different speeds, simultaneously converging at its position (the red star) at the end of the integration time. Regardless of the target's true velocity vector, each pixel moves relative to the target as a function of its own (ΔV_x, ΔV_y) value. The green squares represent starting positions for pixels at the beginning of the integration process.

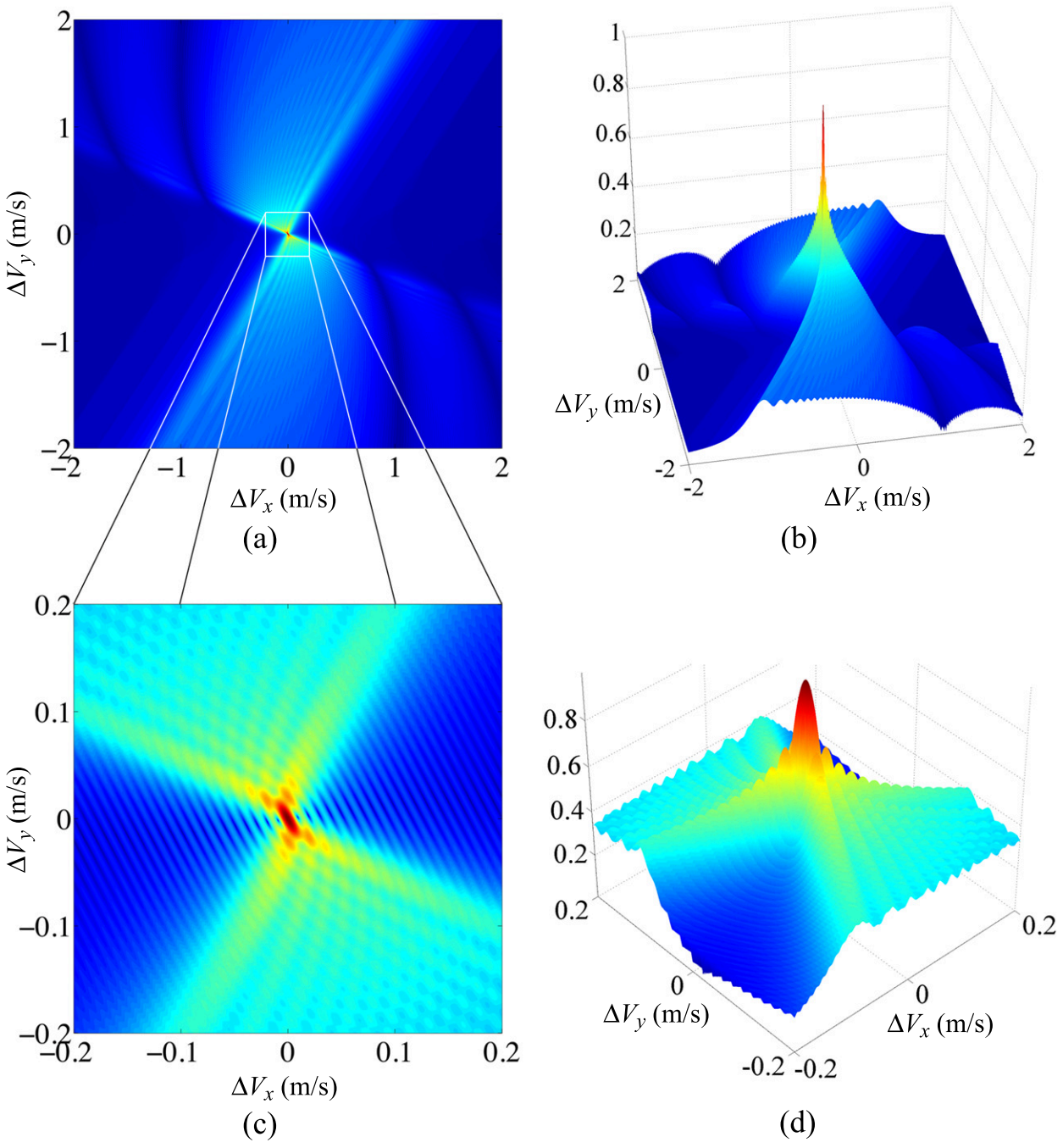

Figure 4.20: The BPJ AF for the pixel set shown in Fig. 4.19. At time zero, each pixel starts off-target. When integration begins, the pixels move toward the target at different speeds, simultaneously converging at its position at the end of the integration time. Regardless of the target's true velocity vector, each pixel moves relative to the target as a function of its own (ΔV_x, ΔV_y) value. Panel (a) is the BPJ AF in 2-D, panel (b) is the BPJ AF in 3-D, panel (c) is a close-up of the central peak in panel (a), and panel (d) is a close-up of the central peak in panel (b). The central peak is the pixel matched to the target's velocity vector for $\Delta V_x = \Delta V_y = 0$.

This chapter has presented and discussed an AF I developed for BPJ. I have shown that the BPJ AF has infinitely many possible manifestations because of the infinite number of ways to set up the moving pixel set. Moving targets and moving pixels introduce the idea of range mismatch history between them, which depends on the particular way the pixels are moved relative to the target during image formation. I have shown that a conventional BPJ image of a stationary, isolated point target in an ideal interference-free environment is a subset of the family of BPJ AFs. This kind of standard BPJ image can be interpreted as an AF for pixels in a $(\Delta x, \Delta y)$ position mismatch space, where the pixels' velocity vectors are matched to the stationary ground and the stationary targets in the scene. The BPJ AF examples shown in this section are velocity AFs for pixels in a $(\Delta V_x, \Delta V_y)$ velocity mismatch space, which pass through a moving target. In Chapter 6, the BPJ AF is used to implement my single-channel SAR GMTI method for pixels in a $(\Delta s, V)$ space for mismatches in both position and velocity. The BPJ AF appears to have much flexibility, so that it may potentially be used to analyze many possible imaging questions.

CHAPTER 5. TARGET SIGNATURE ANALYSIS IN SAR DATA

It is well known that when a SAR platform flies a straight path with uniform speed, the slant range between the SAR and a stationary ground target is a hyperbolic function of time [1, 2, 11, 21, 44, 52]. This chapter proves that the hyperbolic relationship still holds when the target is moving, as long as the target motion is also a straight path with uniform speed. This chapter also shows that the hyperbolic range relationship is the fundamental issue that makes general GMTI infeasible for a single-channel SAR.

As discussed previously in Section 2.3 and illustrated in Fig. 2.10, a target's signature in SAR RC data provides a history of the target's slant range from the SAR during data collection. When the target SNR is high enough, the hyperbolic slant range relationship between the SAR and the target is evident by the shape of the target's range migration curve (RMC). The target's range history may also be equivalently called phase history, as discussed in Section 2.4.2.

This chapter is organized as follows: Section 5.1 derives the hyperbolic relationship between the SAR and all targets, stationary or moving, and Section 5.2 demonstrates the underdetermined nature of the single-channel SAR (SCS) GMTI problem.

5.1 Mathematical Derivation of the Hyperbolic Range History for SAR Targets

The section derives the hyperbolic range history between a SAR and a moving ground target. This discussion and derivation are based on the geometry of the scenario depicted in Fig. 5.1, which shows a moving ground target present during a SAR data collection. In the SAR's coordinate system, the origin is the airplane's nadir point on the ground directly below it at time zero. Positive x (cross-track) is due east, and positive y (along-track) is due north. The SAR starts at position $(0,0,h)$, where h is the SAR's altitude, and the SAR flies due north looking to the right (east). The target starts at position $(x_0, y_0, 0)$. The SAR and target are both treated as point objects.

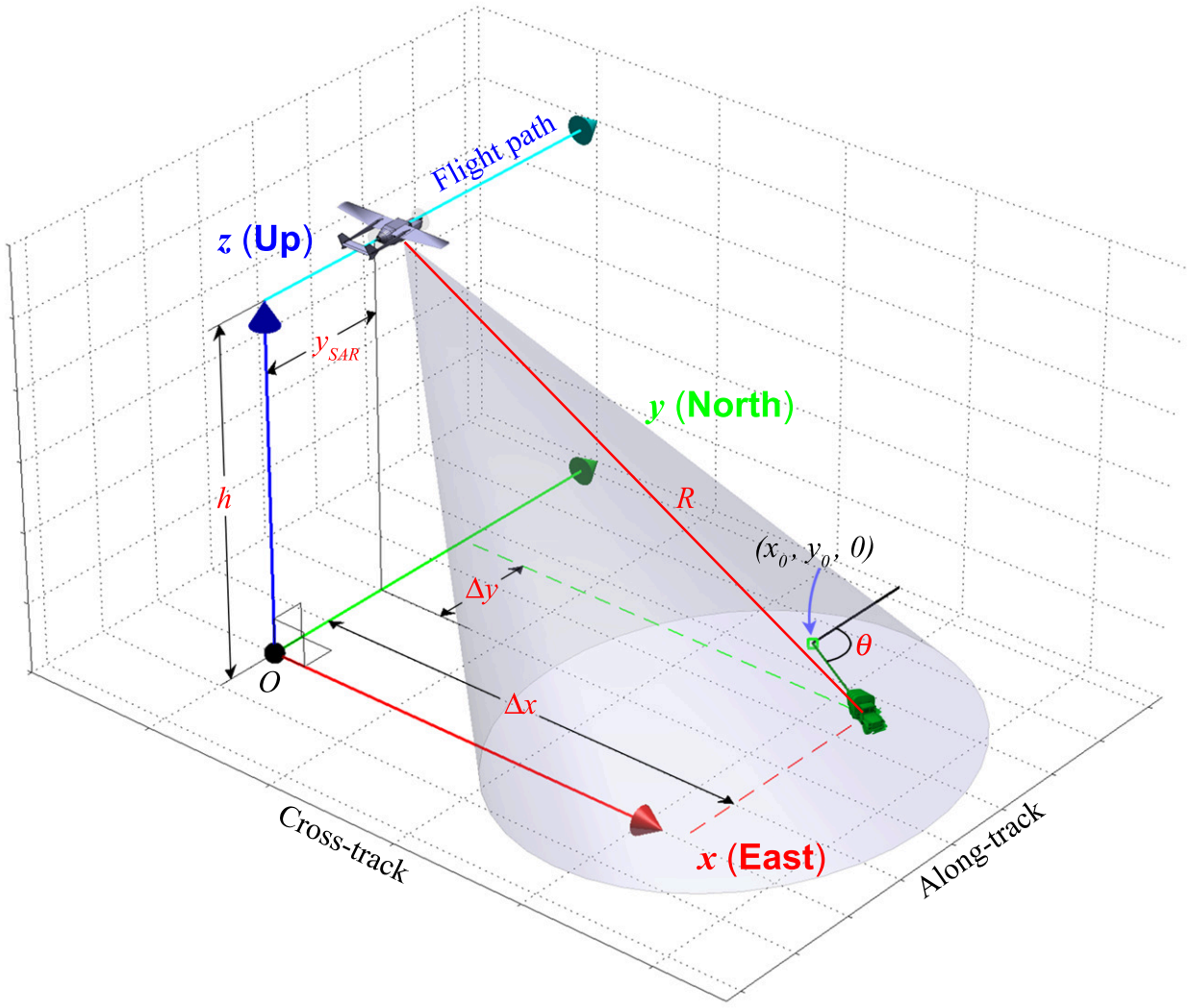

Figure 5.1: A SAR scenario illustrating the geometry and quantities used to derive the range history between the SAR and a ground target. The position marked O is the origin of the GMTI coordinate reference frame. Positive x is east, positive y is north, and positive z is up. At time zero, the SAR starts directly above the origin at position $(0,0,h)$ and the target starts at position $(x_0,y_0,0)$. The quantity h is the SAR altitude, y_{SAR} is the along-track distance the SAR platform has flown since time zero, θ is the target's heading relative to due north, R is the slant range between the SAR and the target, and Δx and Δy are the respective cross-track and along-track separations between the SAR and the target at any given moment.

A hyperbolic relationship between variables u and w is expressed mathematically as

$$\frac{(u-m)^2}{a^2} - \frac{(w-k)^2}{b^2} = 1, \tag{5.1}$$

where all quantities except u and w are constant. This formula can be verified in any algebra textbook.

The derivation starts with the Pythagorean Theorem. The slant range R between the SAR and the target is

$$R^2 = \Delta x^2 + \Delta y^2 + h^2. \tag{5.2}$$

The SAR altitude h is assumed constant, but Δx and Δy are not. At any given moment, the respective cross-track and along-track separations Δx and Δy between the SAR and the target depend on their velocity vectors, their initial positions, and how much time has elapsed since time zero.

The cross-track and along-track separations Δx and Δy are defined as

$$\Delta x = x_T - x_{SAR}, \tag{5.3}$$

$$\Delta y = y_T - y_{SAR}, \tag{5.4}$$

where $(x_T, y_T, 0)$ and (x_{SAR}, y_{SAR}, h) are the target's and SAR's respective time-changing positions on the ground and in the sky. Since the SAR in this discussion flies due north above the y-axis, x_{SAR} is zero by definition. The target's position depends on its speed, heading, and initial position, and is expressed as

$$\begin{aligned} x_T &= x_0 + v_{T,x}t \\ &= x_0 + \underbrace{v_T \sin\theta}_{v_{T,x}} \cdot t, \end{aligned} \tag{5.5}$$

$$\begin{aligned} y_T &= y_0 + v_{T,y}t \\ &= y_0 + \underbrace{v_T \cos\theta}_{v_{T,y}} \cdot t, \end{aligned} \tag{5.6}$$

where v_T is the target's linear speed, and $v_{T,x}$ and $v_{T,y}$ are the target's respective cross-track and along-track velocity components. The SAR's position along its flight path relative to its time-zero position is

$$y_{SAR} = v_{SAR} t. \tag{5.7}$$

Substituting Eq. (5.5) and $x_{SAR} = 0$ into Eq. (5.3), and Eqs. (5.6) and (5.7) into Eq. (5.4) yield the results

$$\Delta x = x_0 + v_T \sin\theta \cdot t, \tag{5.8}$$

$$\Delta y = y_0 + (v_T \cos\theta - v_{SAR})t. \tag{5.9}$$

Now, substituting Eqs. (5.8) and (5.9) into Eq. (5.2) yields

$$R^2 = \underbrace{(x_0 + v_T \sin\theta \cdot t)}_{\Delta x}^2 + \underbrace{[y_0 + (v_T \cos\theta - v_{SAR})t]}_{\Delta y}^2 + h^2. \tag{5.10}$$

Next Eq. (5.10) is expanded out so the time variable t is not enclosed inside any parentheses, powers of t are factored out, and the resulting terms listed in decreasing order of t:

$$\begin{aligned} R^2 = {} & (v_T^2 \sin^2\theta + v_T^2 \cos^2\theta - 2v_T v_{SAR} \cos\theta + v_{SAR}^2)t^2 \\ & + 2[x_0 v_T \sin\theta + y_0(v_T \cos\theta - v_{SAR})]t \\ & + x_0^2 + y_0^2 + h^2. \end{aligned} \tag{5.11}$$

Now Eq. (5.11) is abstracted to the form of

$$R^2 = At^2 + 2Bt + C, \tag{5.12}$$

where

$$A = v_T^2 \sin^2\theta + v_T^2 \cos^2\theta - 2v_T v_{SAR} \cos\theta + v_{SAR}^2, \tag{5.13}$$

$$B = x_0 v_T \sin\theta + y_0(v_T \cos\theta - v_{SAR}), \tag{5.14}$$

$$C = x_0^2 + y_0^2 + h^2. \tag{5.15}$$

Although the expressions for A, B, and C appear complicated, they are all constants. Two other options for expressing these constants are as follows:

1: Use the identity $\sin^2\theta + \cos^2\theta = 1$ to simplify the expression for A:

$$A = v_T^2 - 2v_T v_{SAR}\cos\theta + v_{SAR}^2. \tag{5.16}$$

2: Express A and B in terms of $v_{T,x}$ and $v_{T,y}$:

$$A = v_{T,x}^2 + v_{T,y}^2 - 2v_{SAR}v_{T,y} + v_{SAR}^2, \tag{5.17}$$

$$B = x_0 v_{T,x} + y_0(v_{T,y} - v_{SAR}). \tag{5.18}$$

Next the square is completed on Eq. (5.12):

$$\begin{aligned} R^2 &= A\left(t^2 + \frac{2B}{A}t\right) + C \\ &= A\left(t^2 + \frac{2B}{A}t + \frac{B^2}{A^2} - \frac{B^2}{A^2}\right) + C \\ &= A\left(t^2 + \frac{2B}{A}t + \frac{B^2}{A^2}\right) - \frac{B^2}{A} + C \\ &= A\left(t + \frac{B}{A}\right)^2 - \frac{B^2}{A} + C. \end{aligned} \tag{5.19}$$

Finally, Eq. (5.19) is manipulated into the hyperbolic structure of Eq. (5.1):

$$\begin{aligned} R^2 - A\left(t + \frac{B}{A}\right)^2 &= C - \frac{B^2}{A} \\ \Rightarrow R^2 - \frac{\left(t + \frac{B}{A}\right)^2}{\left(\frac{1}{A}\right)} &= \frac{AC - B^2}{A} \end{aligned}$$

$$\Rightarrow \boxed{\frac{R^2}{\left(\frac{AC - B^2}{A}\right)} - \frac{\left(t + \frac{B}{A}\right)^2}{\left(\frac{AC - B^2}{A^2}\right)} = 1}. \tag{5.20}$$

Equation (5.20) proves that when the SAR and the target both move rectilinearly with constant speeds, the slant range between them is always a hyperbolic function of time, whether the target is moving [21, 44, 75] or stationary. A careful comparison between the structures of Eqs. (5.1) and (5.20) confirms this. As explained in the next section, this hyperbolic relationship makes the SCS-GMTI problem underdetermined.

5.2 The Underdetermined Nature of the Single-Channel SAR GMTI Problem

For this discussion, a scenario is contrived for a single point target moving in an environment free of ground clutter or any other interference. Its RC data is shown, and the hyperbolic signature is analyzed and then mathematically characterized. It is then shown that the mathematical characterization for the target's hyperbolic signature in the RC data is not unique to the target's true GMTI solution, but rather corresponds to an infinite set of GMTI solutions, of which the target's true solution is just one element. I define a GMTI solution as specifying an initial position for the target and a velocity vector (heading and speed), which I express as (x_0, y_0, θ, v_T).

The target scenario for this discussion is this: at time zero the SAR starts at position $(0, 0, h)$, where the altitude h is 500 m. It flies due north at 50 m/s and looks to the right, using an azimuth beamwidth of 50° and a boresight look angle 45° from nadir. In this coordinate system, the target's initial position $(x_0, y_0, 0)$ is (500 m, 250 m, 0), and its velocity vector is 45° heading (NE) at 10 m/s. This scene is illustrated in Fig. 5.2, and the resulting RC data for a 10-second data collection is shown in Fig. 5.3.

It should be emphasized that as the target's hyperbolic RMC is analyzed and characterized for this discussion, the method used is not presented as a viable technique to be used in practice. This idealized analysis assumes a mathematically sterile scenario with a flat-Earth model, no ground clutter or other interference, a perfect SAR platform motion history, and a single point target whose RMC in the RC data is prominent and well-defined, in addition to the ideal motion for the SAR and target as mentioned throughout this thesis. This set of conditions is virtually impossible to realize in practice. However, these assumed conditions enable a conceptual investigation of the underlying math and physics that do affect an actual SAR data collection and a target's SAR signature in actual RC data. As the steps taken to perform the analysis and characterization in this section are explained, it is assumed that the reader understands this usability disclaimer.

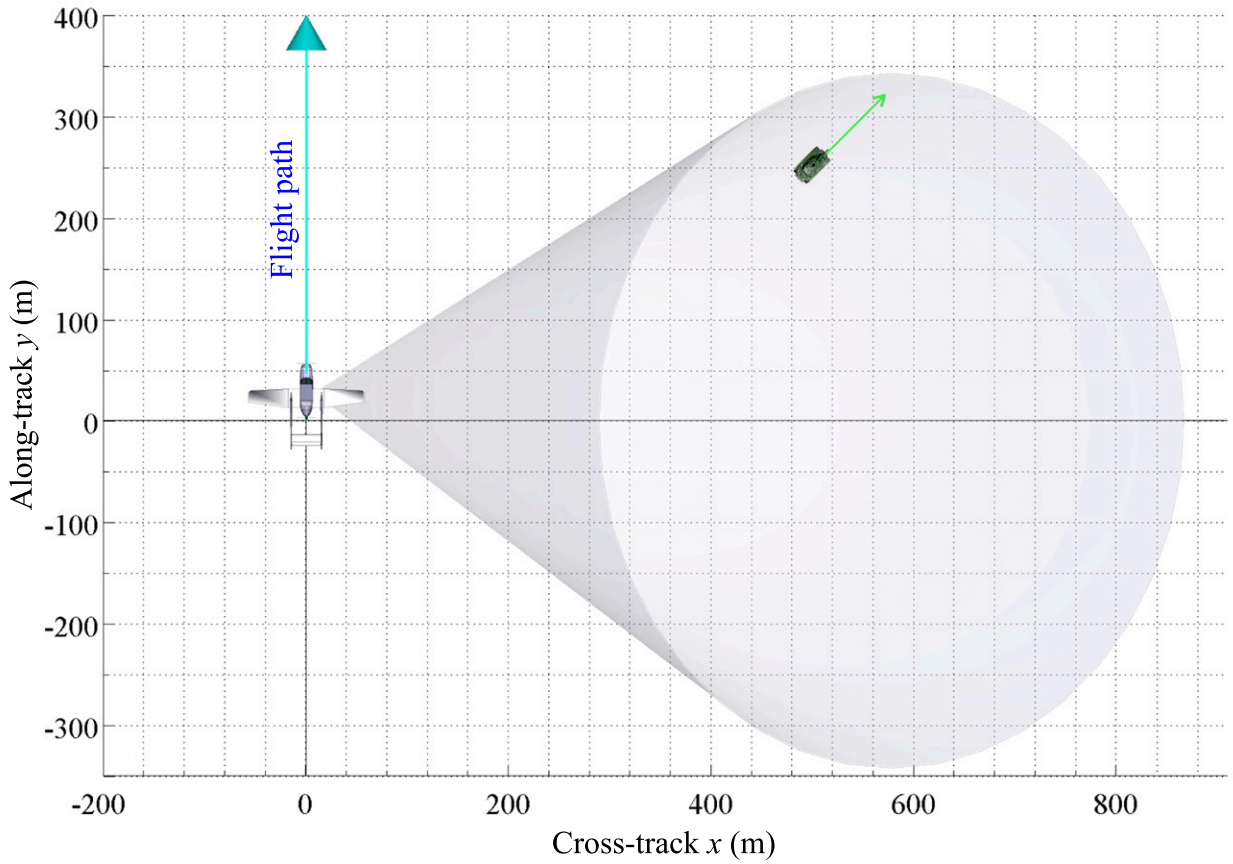

Figure 5.2: Top-down view of a SAR scenario with a single moving ground target. North is up. The scene shown here is a ground-truth snapshot at time zero. At time zero, the SAR is located at (0, 0, 500 m) and flies due north at 50 m/s. The target starts at (500 m, 250 m, 0) traveling at 45° heading (NE) at 10 m/s. The azimuth beamwidth shown here is 50°.

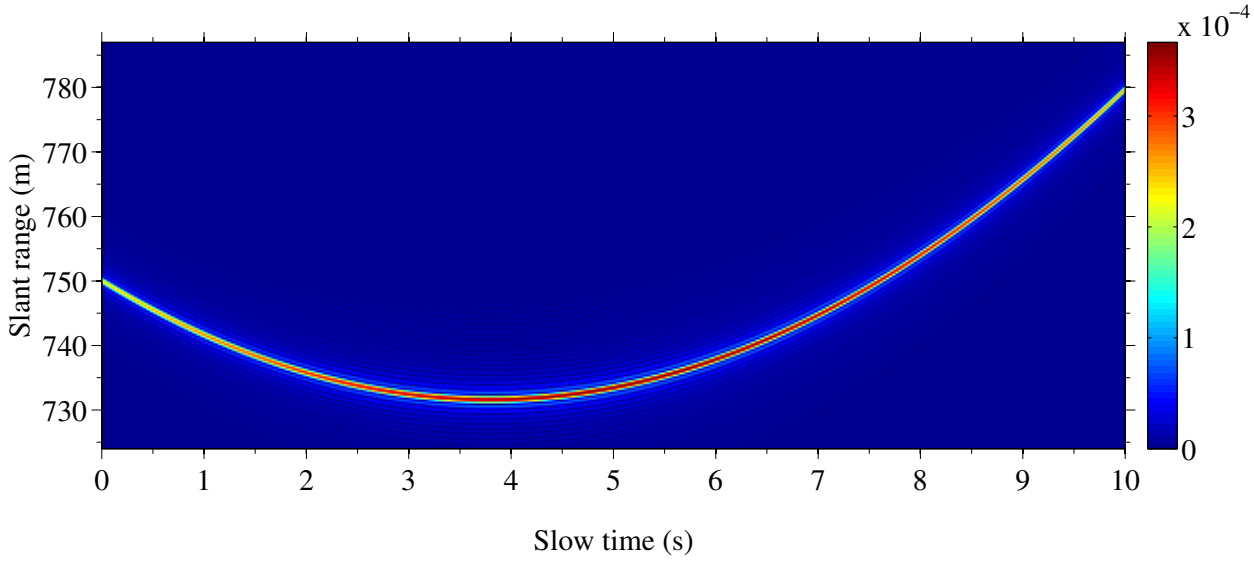

Figure 5.3: RC data for the SAR scenario depicted in Fig. 5.2 for a 10-second data collection.

During the course of this analysis, it is assumed that the slant range to the target, for any given pulse, can be accurately measured by finding the peak in the RC data for that pulse. If such "clean" RC data as that assumed here could be realized in practice, the RC data peak for any pulse could be found quite accurately by interpolating the RC data, which is how I did it in simulation. For this discussion, it is assumed that the target range can "somehow" be measured accurately for each pulse.

As Eq. (5.20) shows, the slant range R between the SAR and a target is always a hyperbolic function of time. As Eq. (5.12) shows, the quantity R^2 is a quadratic function of time. This shows that squaring a hyperbola produces a parabola. In a purely mathematical sense, a squaring operation is not one-to-one because information is lost in the process. For example, if a single number is squared to produce the value of 4, it is impossible to identify the root number based on the squared result alone. It is either 2 or -2. If a single root value is sought, it is impossible to determine with certainty which possible root is the correct answer. Fortunately, however, nature solves this problem for us because physical distances, such as slant range, are never negative. Therefore in a SAR context, the squaring operation *is* one-to-one and does preserve all information. This is important because if R^2 in Eq. (5.12) is characterized by the three coefficients A, B, and C, then these same three coefficients also fully characterize R for the hyperbolic RMC in Eq. (5.20). Therefore, it is desired to analyze the RMC and mathematically characterize it by extracting values for A, B, and C from the data.

To start this process, I chose N pulses at random from the data collection, with $N \geq 3$ and the pulses sufficiently far apart, and measured the target range for each pulse. The number of pulses N must be at least 3 because the RMC is described by the three coefficients A, B, and C. Knowing the PRI allows each pulse number to be turned into a time index. With N data points chosen for (t_n, R_n), they are all applied to Eq. (5.12) to produce the system of equations

$$\begin{aligned} R_1^2 &= At_1^2 + 2Bt_1 + C \\ R_2^2 &= At_2^2 + 2Bt_2 + C \\ &\vdots \\ R_N^2 &= At_N^2 + 2Bt_N + C, \end{aligned} \tag{5.21}$$

which can be written in matrix form as

$$\underbrace{\begin{bmatrix} t_1^2 & t_1 & 1 \\ t_2^2 & t_2 & 1 \\ & \vdots & \\ t_N^2 & t_N & 1 \end{bmatrix}}_{T} \cdot \underbrace{\begin{bmatrix} A \\ 2B \\ C \end{bmatrix}}_{\mathbf{x}} = \underbrace{\begin{bmatrix} R_1^2 \\ R_2^2 \\ \vdots \\ R_N^2 \end{bmatrix}}_{\mathbf{r}}, \tag{5.22}$$

or

$$T\mathbf{x} = \mathbf{r}. \tag{5.23}$$

The vector $\mathbf{x}$ contains the quadratic coefficients needed to characterize the RMC, and is computed via the Moore-Penrose pseudoinverse [76]:

$$\mathbf{x} = \left(T^H T\right)^{-1} T^H \mathbf{r}, \tag{5.24}$$

where the '^{H}' superscript is the Hermitian conjugation operator. This computation yields least-squares values for A, B, and C, effectively producing empirical data about the mathematical shape of the hyperbolic RMC. In simulation, using more pulses improves the accuracy of the coefficient estimates. But in the interference-free case, for as few as even three well-separated pulses, the computed value estimates for A, B, and C are accurate to within less than a tenth of a percent error from their true values based on target knowledge, with error due only to quantization. For the SAR scenario in Fig. 5.2 and the corresponding RC data in Fig. 5.3, the true coefficient values are

$$\begin{aligned} A &= 1,892.89, \\ B &= -7,196.7, \\ C &= 562,500, \end{aligned} \tag{5.25}$$

and it is assumed the values computed with Eq. (5.24) are accurate enough that any error between them and the true values is negligible. Once the RMC has been mathematically characterized with the coefficients A, B, and C, the solution space for the target can be computed.

According to the RC data of Fig. 5.3, the target's slant range at time zero is 750 m. At this point, I assume no knowledge of the target's ground truth, and that radar energy is only reflected from scatterers inside the radar beam's mainlobe. This constrains the target's initial position to lie somewhere on a circular iso-range arc segment centered on the SAR's nadir point on the ground directly below it at time zero, and bounded by the mainlobe, as shown in Fig. 5.4. All points on the iso-range are 750 m from the SAR itself. This is consistent with the definition of C in Eq. (5.15), which is simply the Pythagorean Theorem for the initial geometry between the SAR and the target.

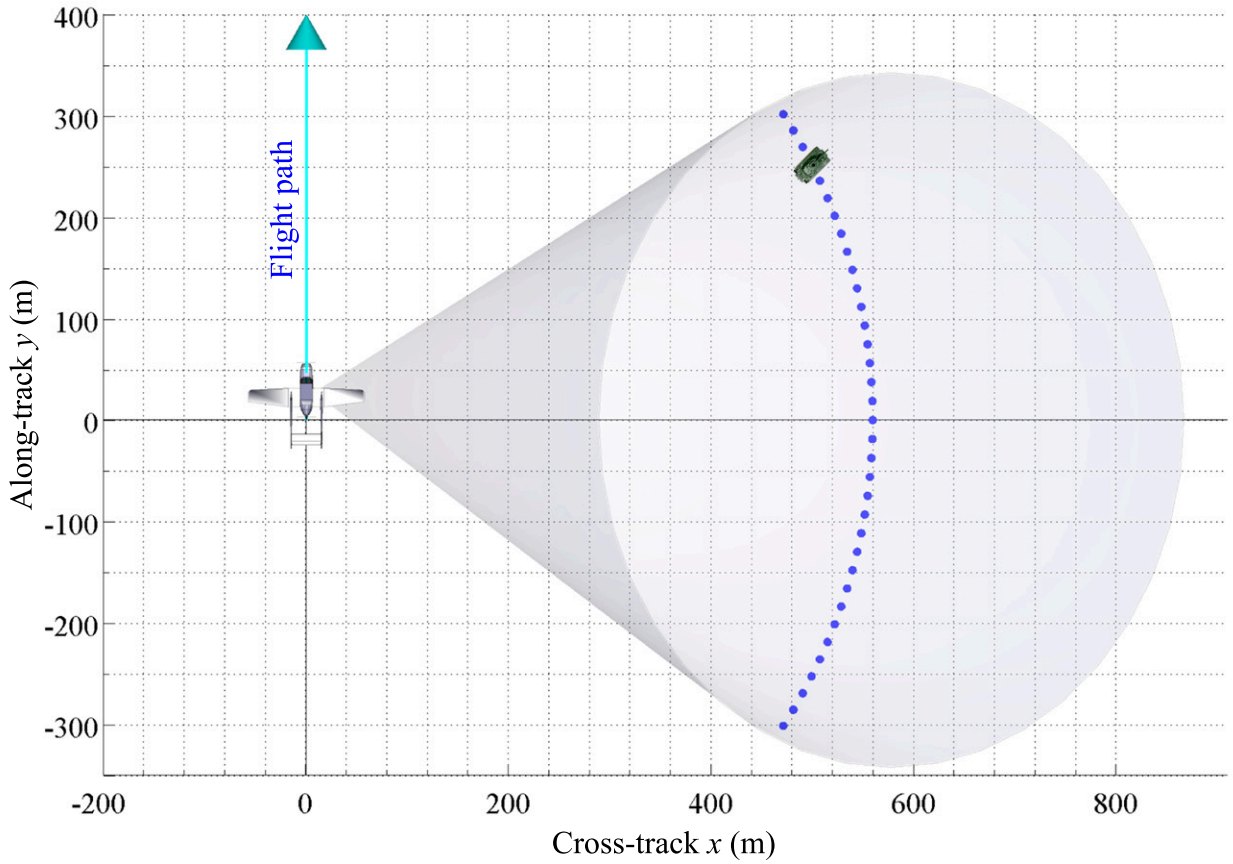

Figure 5.4: Top-down view of a SAR GMTI scenario with a single moving ground target. North is up. The azimuth beamwidth shown here is 50°. Based on the RC data in Fig. 5.3, the target range at time zero is 750 m. This constrains the target's initial position to lie somewhere on a circular iso-range arc segment centered on the SAR's initial nadir point and bounded by the mainlobe. All points on the iso-range are 750 m from the SAR. The iso-range is indicated by the blue points in this figure, with each point representing a potential starting position for the target.

To compute the corresponding velocity vector for a given candidate point for the target's initial position, I start by using the definitions for A and B from Eqs. (5.17) and (5.18), which are repeated here for convenience:

$$A = v_{T,x}^2 + v_{T,y}^2 - 2v_{SAR}v_{T,y} + v_{SAR}^2, \tag{5.26}$$

$$B = x_0 v_{T,x} + y_0(v_{T,y} - v_{SAR}). \tag{5.27}$$

These definitions are made more useful with some additional mathematical manipulation. First, A is factored:

$$A = v_{T,x}^2 + (v_{T,y} - v_{SAR})^2,$$

and then defining the velocity vector component differences between the target and the SAR as $\Delta V_x = v_{T,x}$ and $\Delta V_y = v_{T,y} - v_{SAR}$, A and B are now defined as

$$A = \Delta V_x^2 + \Delta V_y^2, \tag{5.28}$$

$$B = x_0 \Delta V_x + y_0 \Delta V_y. \tag{5.29}$$

Each possible time-zero position for the target's GMTI solution must be tested separately. First, a test point (x_0, y_0) is chosen from the set shown in Fig. 5.4, and then applied to the definition of B in Eq.(5.29). Equations (5.28) and (5.29) constitute a system of equations which must now be solved to obtain the velocity vector $(\Delta V_x, \Delta V_y)$ corresponding to the test position (x_0, y_0). The mathematical structures of the definitions for A and B indicate that the velocity vector is the intersection of a circle [from A in Eq. (5.28)] and a line [from B in Eq. (5.29)]. A conceptual visualization of this is shown in Fig. 5.5. The measured value for A from Eq. (5.25) determines the radius of this circle in $(\Delta V_x, \Delta V_y)$ space, which in this case is $r = \sqrt{A} \approx 43.51$ m/s. The circle described by A is the same for all possible time-zero test positions in Fig. 5.4, but the line described by B depends on which position (x_0, y_0) is being tested.

First, ΔV_x is algebraically isolated in the definition of B, and that result is then substituted into the definition of A, yielding

$$A = \left(\frac{B - y_0 \Delta V_y}{x_0}\right)^2 + \Delta V_y^2. \tag{5.30}$$

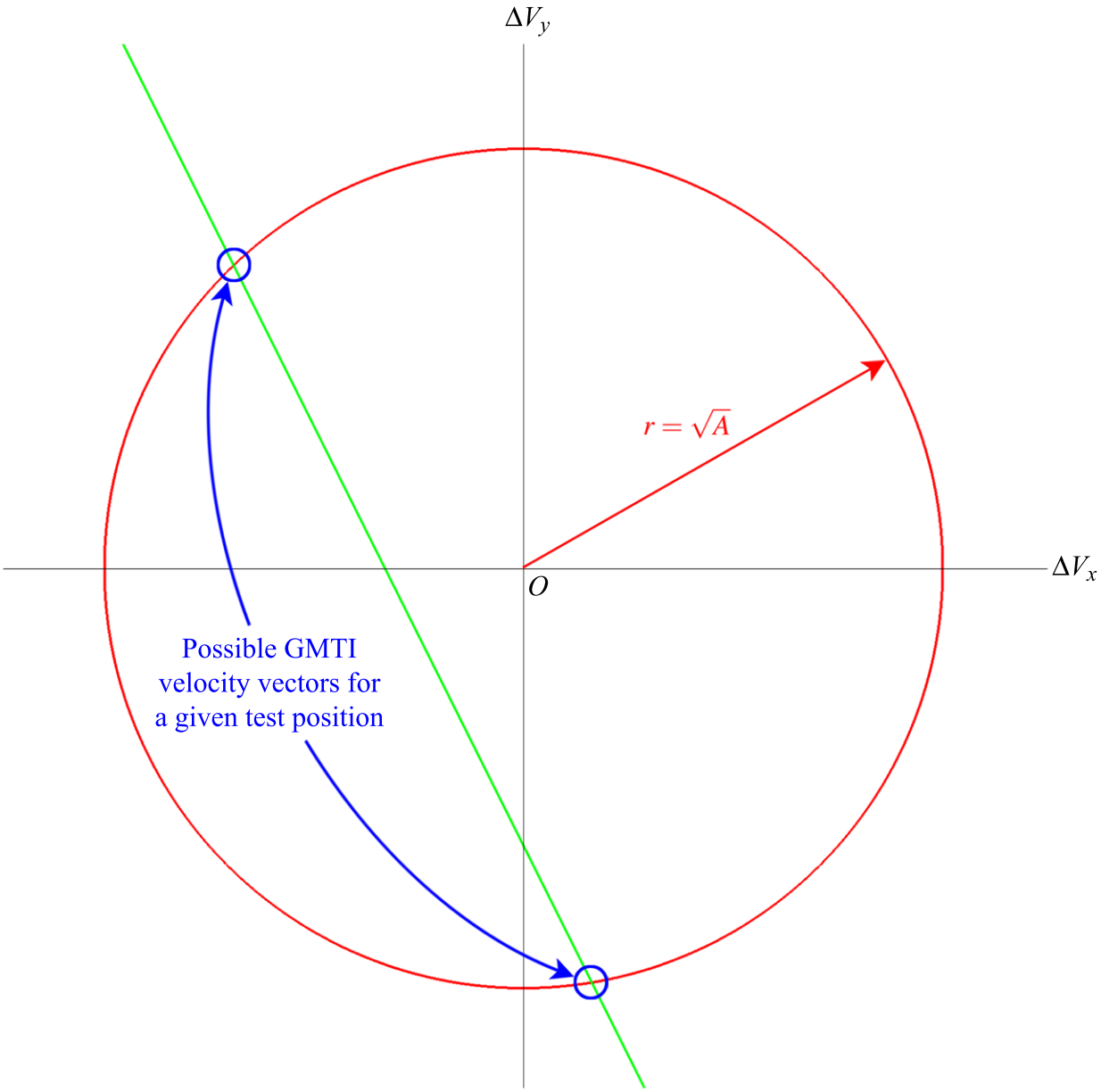

Figure 5.5: GMTI velocity vector solutions for a given (x_0, y_0) test position are found by solving the system of equations formed by Eqs. (5.28) and (5.29). Equation (5.28) describes the red circle, and (5.29) describes the green line. The quantities ΔV_x and ΔV_y respectively represent the target's apparent cross-track and along-track speeds in the moving SAR's reference frame. Since aircraft generally fly much faster than ground targets can travel, the solution containing a positive value for ΔV_y is discarded.

Expanding this out and grouping all terms on one side of the equation in decreasing powers of ΔV_y yields a quadratic equation in ΔV_y:

$$(x_0^2 + y_0^2)\Delta V_y^2 - 2By_0\Delta V_y + (B^2 - x_0^2 A) = 0. \tag{5.31}$$

Computing the roots of this quadratic produces two values for ΔV_y. These values are then applied to the definition of B in Eq. (5.29) to obtain the corresponding values for ΔV_x. These two velocity vector solutions are illustrated in Fig. 5.5, where the green line intersects the red circle.

Simulation results show that the green line always crosses the ΔV_x axis inside the red circle, which means that for a given test position, the two corresponding ΔV_y values have opposite signs. The quantity ΔV_y physically represents the target's apparent along-track speed in the SAR's reference frame. Since aircraft generally fly much faster than ground targets can travel, the solution containing a positive ΔV_y value is discarded.

By the process described in this section, a target's GMTI solution space can be found based on the hyperbolic shape of its RMC. For the GMTI scenario described in this section, illustrated in Fig. 5.2 and subsequently characterized by the three coefficients in Eq. (5.25), the resulting solution space is shown in Fig. 5.6. Figure 5.6 shows many GMTI solutions that all produce the same range history and the same hyperbolic RMC as in Fig. 5.3. Without additional information about the target, its GMTI solution cannot be uniquely determined by the target's SAR signature [15, 70, 77]. The single-channel SAR GMTI problem is underdetermined.

Technically, although the range and phase histories are identical for all the GMTI solutions in the solution space of Fig. 5.6, they would produce different amplitude histories because they would experience different radar illumination intensities due to their different paths through the radar beam's mainlobe. Accounting for the antenna radiation pattern could possibly help resolve the target motion ambiguity. However I did not study that effect, because it would depend on knowing beforehand the target's orientation-dependent RCS, and being able to remove the effects of interference and ground clutter. Since GMTI is primarily interested in cases where the target's presence and ground track are *not* known *a priori*, and since single-channel SAR cannot cancel the effects of ground clutter like multi-channel SARs can [13, 14, 20, 21, 28, 37, 78, 79], I decided it was not worth spending time studying radiation pattern effects.

In all the literature I studied for my research and this thesis, only one other author (Chapman, [44]) has studied the SCS-GMTI problem mathematically and demonstrated its underdetermined nature. Chapman approaches the problem from a purely mathematical standpoint, while in my research I approached it from the perspective of assuming that the target's unique GMTI solution could be found by analyzing the SAR data. This assumption led to a contradiction, as shown in this section.

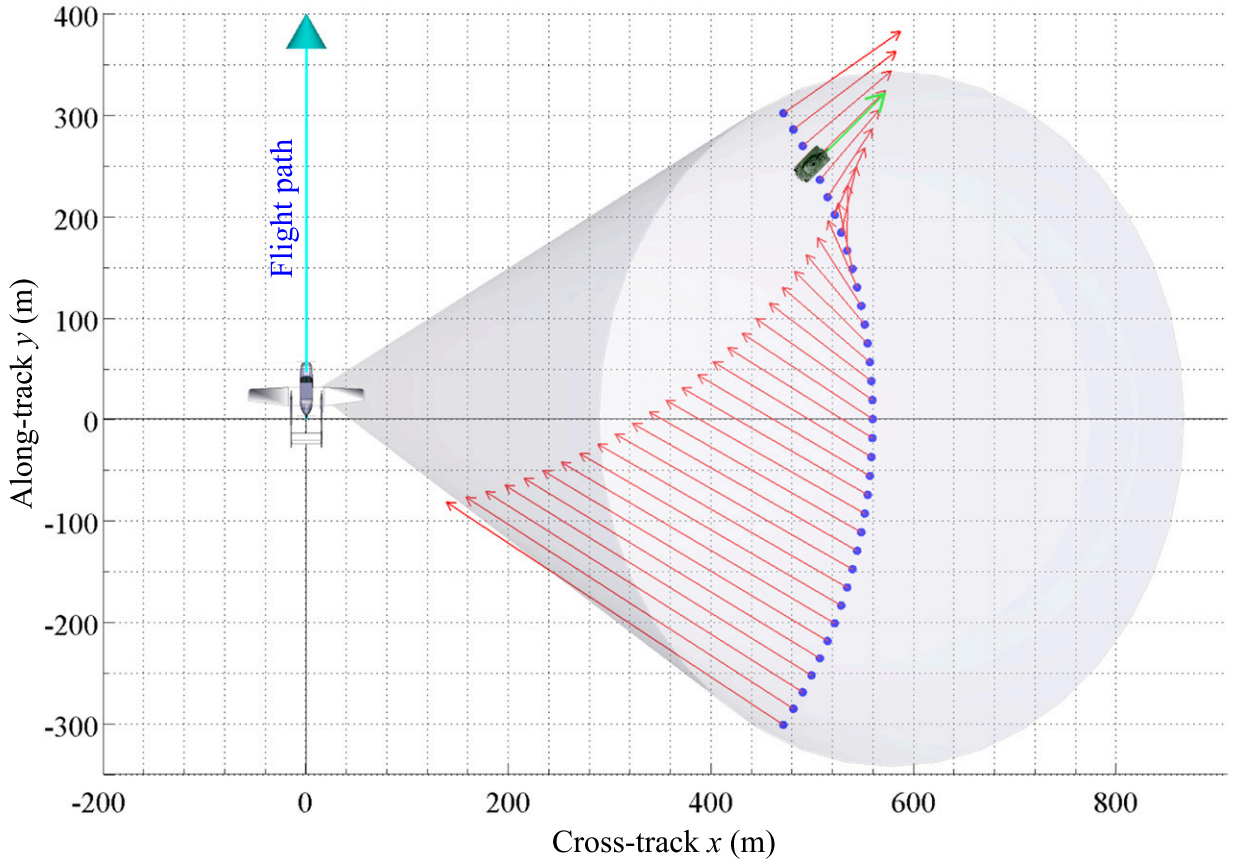

Figure 5.6: Top-down view of a SAR GMTI solution space based on the RC data in Fig. 5.3 produced by a single moving ground target. North is up. The azimuth beamwidth shown here is 50°. By considering only the mathematical shape of the hyperbolic RMC in the RC data of Fig. 5.3, the solution space contains infinitely many GMTI solutions, which means the SCS-GMTI problem is underdetermined. For each GMTI solution shown here, the initial position is indicated by a blue dot, and the corresponding velocity vector is indicated by the red arrow that extends from the dot. Arrow length indicates speed. All the computed solutions shown here produce the same range history as the actual target. The true solution for the target's (x_0, y_0, θ, v_T) is indicated by the tank and green arrow at (500 m, 250 m, 45°, 10 m/s).

This fundamental conclusion about single-channel SARs and GMTI merits some additional discussion. The GMTI solution space shown in Fig. 5.6 shows that a target signature corresponds to many different possible GMTI solutions, and conversely, many different GMTI scenarios leave the same signature in SAR data. This is also true for stationary targets. Assume a new SAR scenario identical to the moving target scenario in Fig. 5.2, except this time the target does not move from its initial position. It can be shown that by following the mathematical procedure outlined in this section, the RC data can be analyzed to produce the GMTI solution space shown in Fig. 5.7.

Figure 5.7 implies that targets moving primarily in the cross-track direction appear as stationary targets shifted in azimuth. This is consistent with the discussion in Section 3.2 on cross-

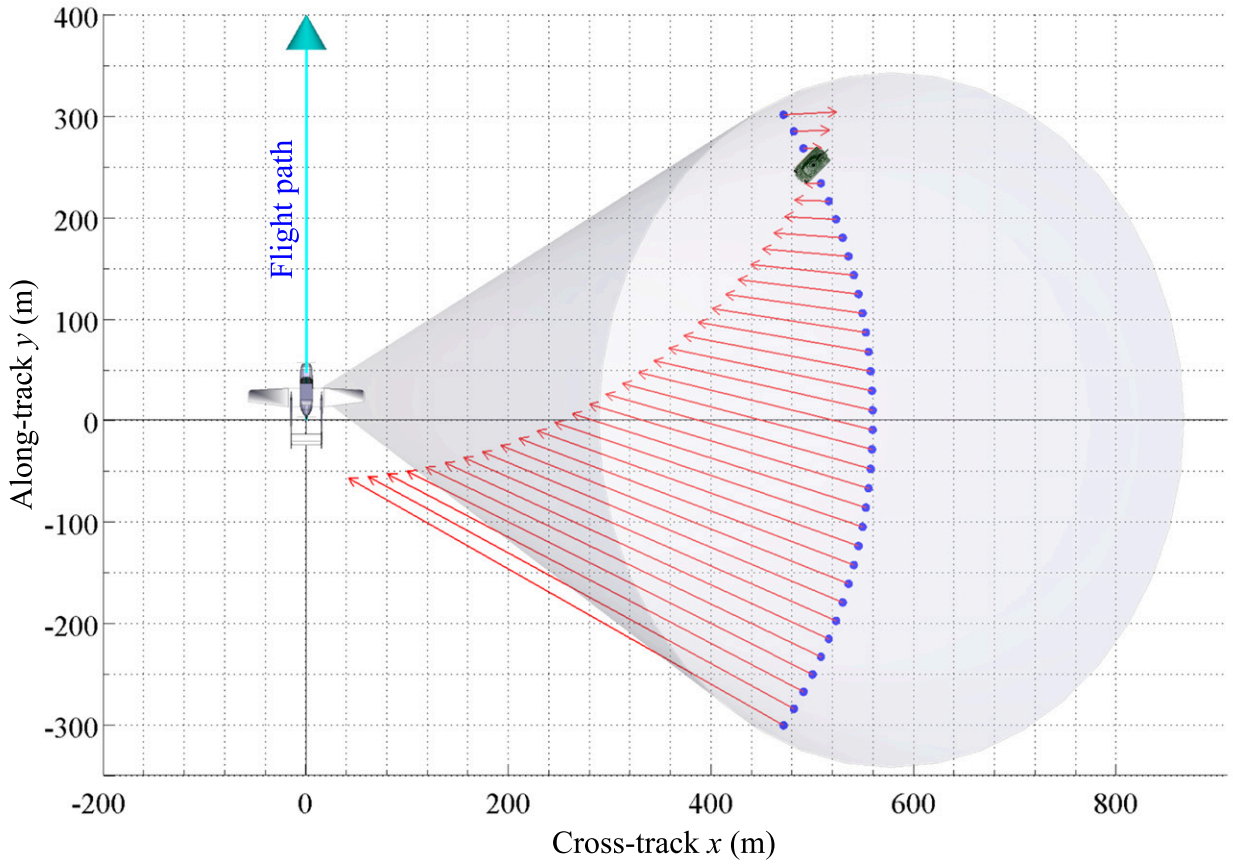

Figure 5.7: Top-down view of a SAR GMTI solution space based on the RC data produced by a single stationary ground target, indicated by the tank at position (500 m, 250 m, 0). North is up. The azimuth beamwidth shown here is 50°. This solution space implies that certain moving targets appear as stationary targets in a SAR image, especially targets that move primarily in the cross-track direction as discussed in Chapter 3.

track target motion effects. To illustrate this, Fig. 5.8 shows the RC data for the stationary target scenario of Fig. 5.7, and Fig. 5.9 shows a BPJ image of the target. The BPJ image in Fig. 5.9 is matched to the stationary ground and shows the target in its correct position. An arbitrary GMTI solution is then chosen from the solution space in Fig. 5.7 and fed back into the SAR simulator in place of the stationary target, and the results are compared. The GMTI solution used for this comparison is approximately (557.30 m, -43.89 m, 285.54° heading, 26.78 m/s).

The RC data for this moving target is shown in Fig. 5.10. Note that its RMC shape is identical to that of the stationary target in Fig. 5.8. However, the energy in its RMC is redistributed because the moving target took a different path through the radar beam's mainlobe.

The BPJ image for this moving target is formed while focusing on the same stationary patch of ground as for the stationary target in Fig. 5.9. As the resulting image in Fig. 5.11 shows, the moving target focuses as a stationary target in the exact same place. This is because the moving target and the stationary target are in the same GMTI solution space. Except for a slight rotation of the sidelobe structure, the two images in Figs. 5.9 and 5.11 are nearly identical.

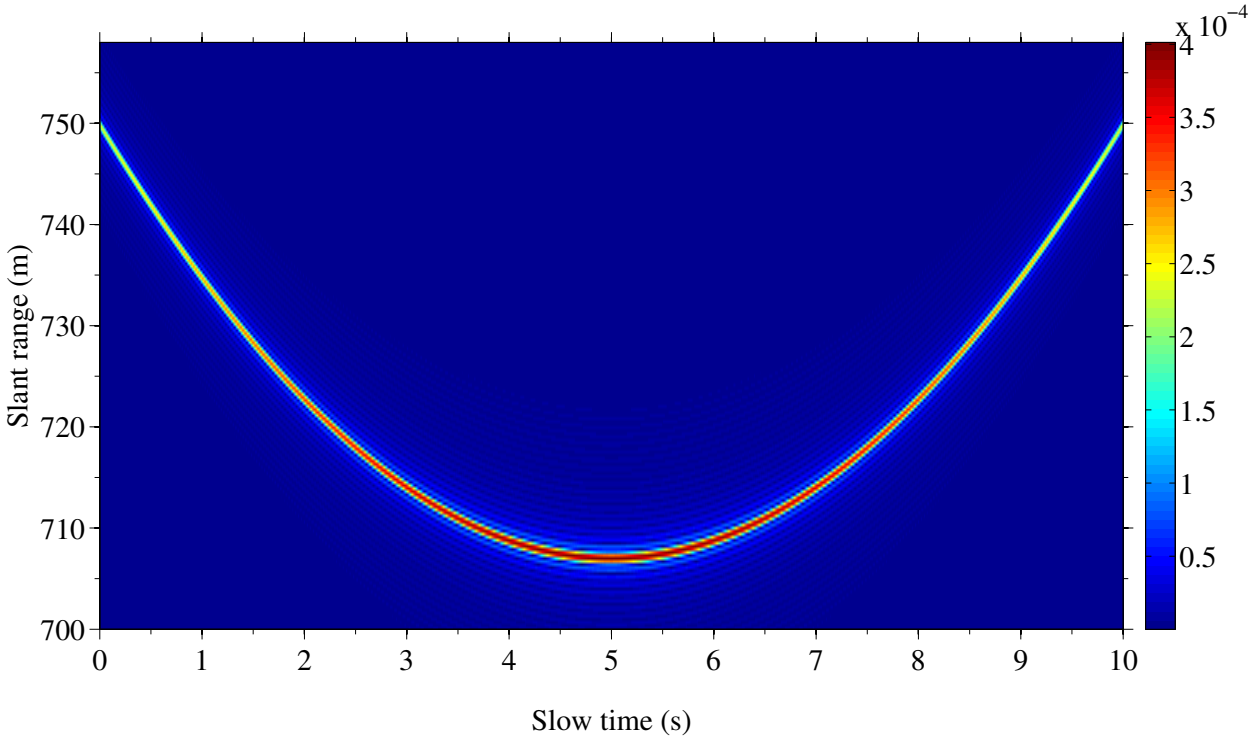

Figure 5.8: RC data for the stationary target depicted in the SAR scenario of Fig. 5.7.

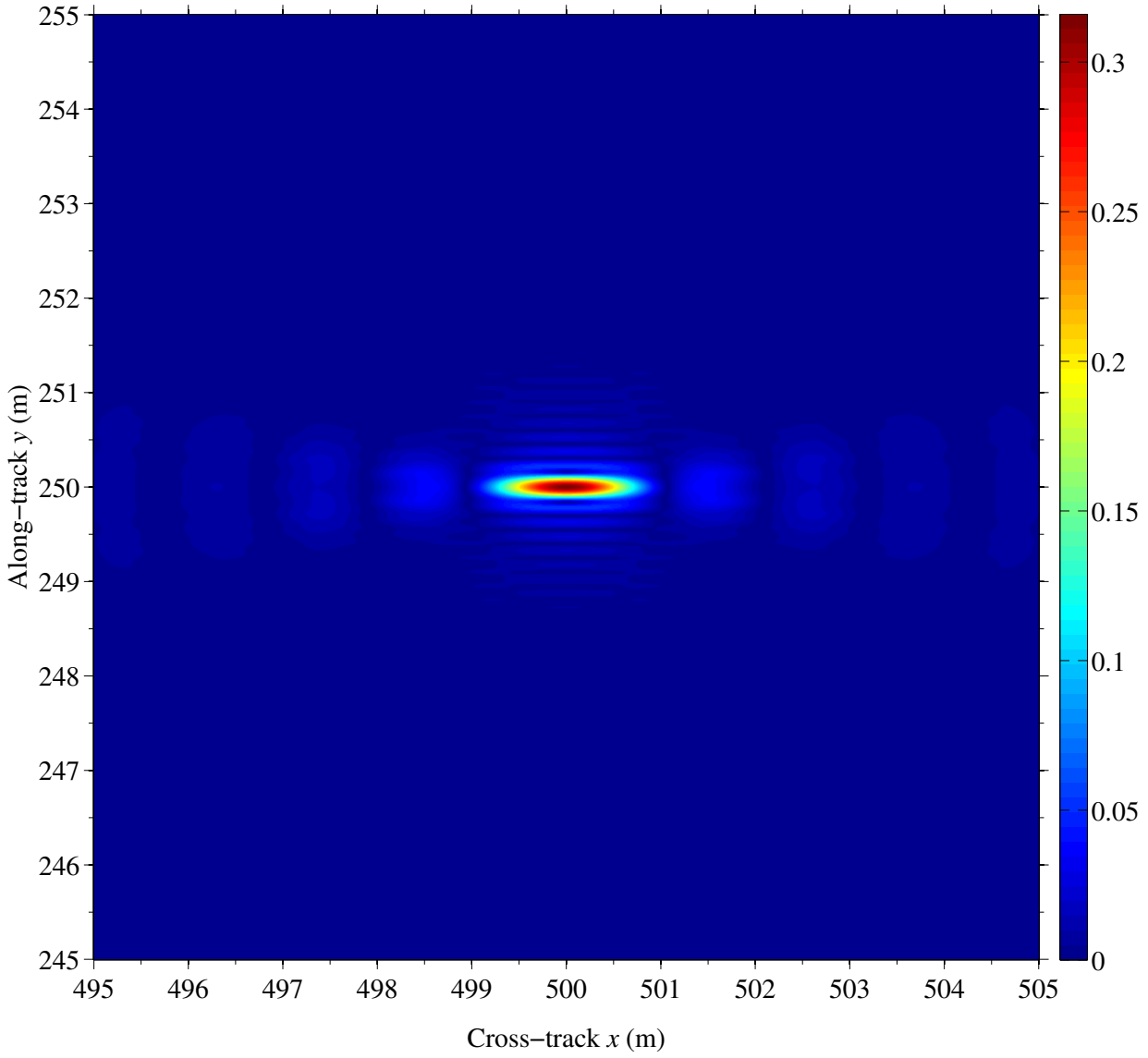

Figure 5.9: BPJ image of the stationary point target depicted in Fig. 5.7, whose RC data is shown in Fig. 5.8. North is up. The target's true ground position is $(500\text{ m}, 250\text{ m}, 0)$. In this image, matched to the stationary ground, the target appears in its correct position. The 50° wide integration angle yields an azimuth resolution much finer than the range resolution, causing the target's elongated appearance in ground range.

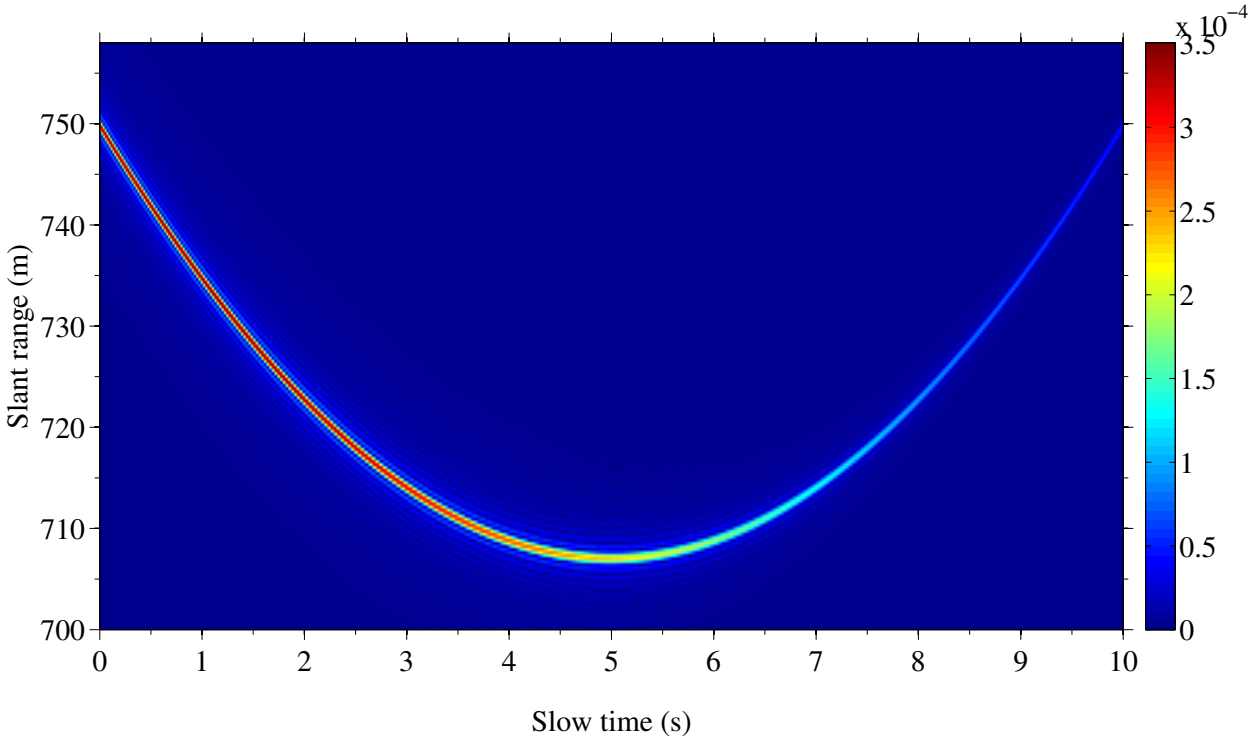

Figure 5.10: RC data for a moving target whose RMC shape is identical to the stationary target's RMC shown in Fig. 5.8. The moving target's velocity vector is taken from the stationary target's GMTI solution space in Fig. 5.7. The moving target's true GMTI solution is approximately (557.30 m, -43.89 m, 285.54° heading, 26.78 m/s). Comparing this figure to Fig. 5.8 shows that the two RMCs have the same shape, but different energy distributions since the moving target took a different path through the radar beam.

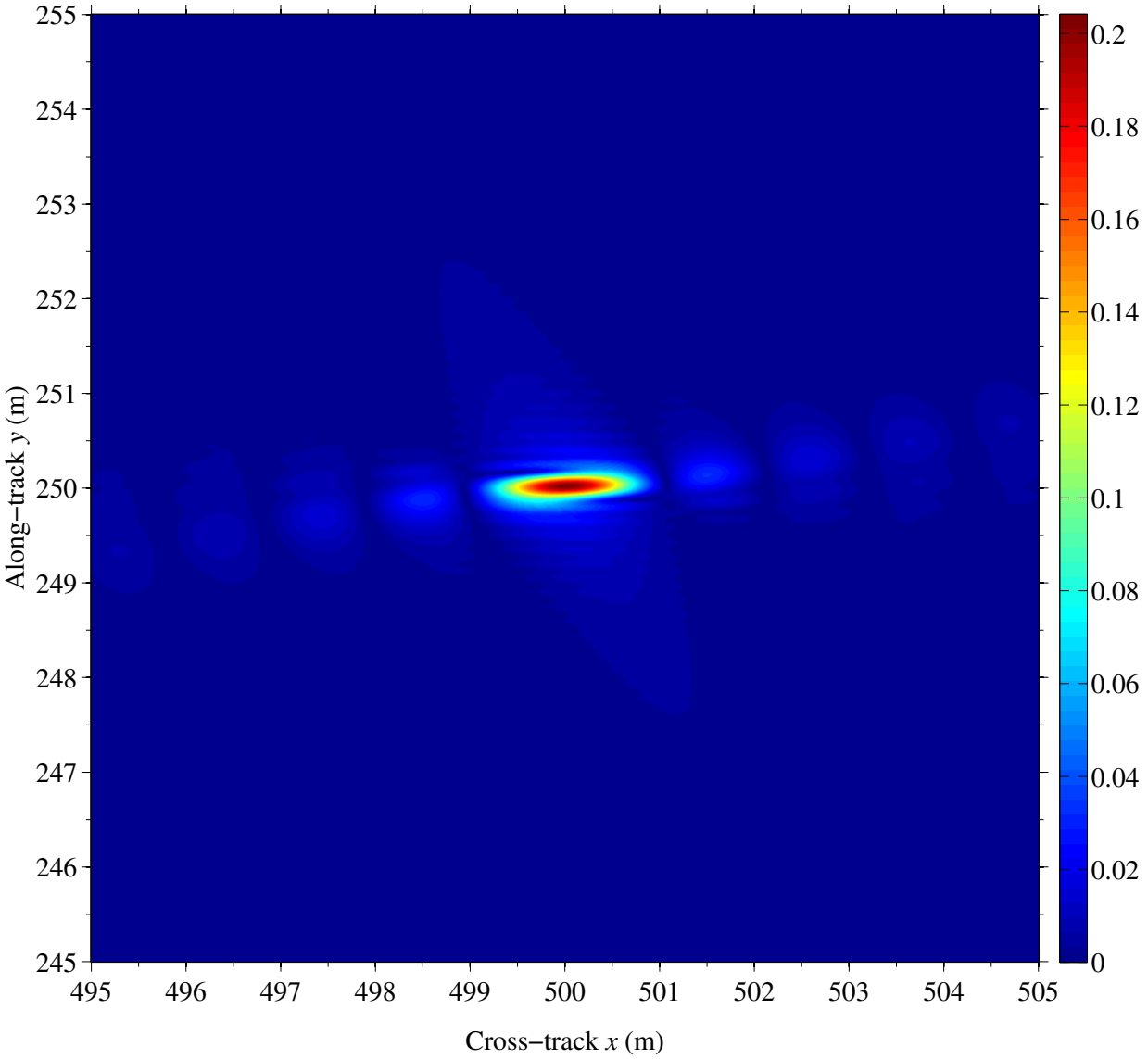

Figure 5.11: BPJ image of a moving point target from the same solution space as the stationary target in Fig. 5.7. North is up. The RMC for this target is shown in Fig. 5.10, and this image is focused on the same stationary patch of ground as in Fig. 5.9. Even though the target is moving and travels nowhere near this area, its image appears nearly identical to the stationary target image of Fig. 5.9, because the moving target's true GMTI solution is in the same solution space as the stationary target.

To summarize the point of this chapter, GMTI based solely on direct energy returns from a moving point target is not feasible for a single-channel SAR. This is because the SCS-GMTI problem attempts to find a four-dimensional target solution (x_0, y_0, θ, v_T) from a radar signature that is characterized by three parameters A, B, and C. This amounts to trying to solve for four unknowns using only three equations. It cannot be done based on the target's RMC alone because the problem is underdetermined. Conceptually, the best that can be done is to relate the four unknowns to an independent parameter. But unless a constraint is applied, no unique solution can be found. This idea of constraining the target is further explored in Chapter 6, where as it turns out, the target's path can be constrained to determine a unique GMTI solution when certain conditions are met.

CHAPTER 6. PERFORMING LIMITED GMTI WITH A SINGLE-CHANNEL SAR USING A BACKPROJECTION MATCHED FILTER

As shown in Chapter 5, a moving target's hyperbolic signature in SAR RC data is not sufficient by itself to uniquely specify the target's GMTI solution. The mathematical analysis in Chapter 5 reveals the fundamental reason why a single-channel SAR is not well-suited for performing GMTI. It also highlights the unavoidable need to somehow constrain the target's solution space if GMTI is to have any hope of being successfully performed with a single-channel SAR. This chapter presents such a way to constrain the target's GMTI solution space using contextual clues in the SAR data itself. This makes it theoretically possible to use a single-channel SAR to perform GMTI in a limited capacity. While the method shown in Chapter 5 is intended to be a conceptual analysis only, the method presented in this chapter may potentially be practical for implementing as a GMTI technique for a single-channel SAR.

The rest of this chapter is organized as follows: Section 6.1 shows how parameterizing the GMTI solution space helps identify a useful way to constrain the problem, and how the constraint could be conceivably be implemented in practice. Section 6.2 shows how the BPJ AF is used to implement my SCS-GMTI method after constraining the problem. Section 6.3 describes the nature of ground clutter and how the signal-to-clutter ratio (SCR) can be computed. Section 6.4 shows simulated GMTI results that demonstrate the theoretical feasibility of my single-channel SAR GMTI method, and discusses the conditions that must be met for my method to have any chance of working. Section 6.5 finishes this chapter by showing several cases of GMTI searches that do *not* adhere to proper path constraints, and the flawed results produced by those searches.

6.1 Parameterizing and Constrianing the SCS-GMTI Solution Space

Chapter 5 describes the underdetermined nature of the SCS-GMTI problem, and makes the point that for any underdetermined problem, a unique solution cannot be found without additional

constraining information. The most that can be done in SCS-GMTI without a constraint is that the GMTI variables x_0, y_0, θ, and v_T can each be related to an independent parameter. My purpose for parameterizing the GMTI solution space is to identify the best way to constrain the problem.

To show how parameterization applies to the SCS-GMTI problem, I first show a simple example using the following algebraic system of equations. Problems like this can be found in any algebra textbook (e.g., [80]).

$$\begin{cases} x+y+z=6 \\ 3x-2y+4z=9 \end{cases} \tag{6.1}$$

Geometrically, this system describes two nonparallel planes in 3-space that intersect along a line. Since there are three unknowns and only two equations, the system is underdetermined, and a unique solution cannot be found. But even though no unique solution exists, a relationship still exists between the variables x, y, and z that satisfies the underdetermined system. This relationship corresponds to the set of points on the intersection line where the two planes cross, and can be expressed by relating all three variables to an independent parameter, such as t. It can be shown that the parameterization of this system's solution space (the intersection line), can be expressed as

$$\begin{aligned} x &= t, \\ y &= 4t-1, \\ z &= 5t-7, \end{aligned} \tag{6.2}$$

where each value of t corresponds to a unique point on the line where the two planes intersect.

The system of equations in Eq. (6.1) is contrived to have a relatively simple solution space [Eq. (6.2)]. It should be no surprise, however, that solutions to real-world engineering problems are almost always far more complicated, and the SCS-GMTI problem is no exception. But even so, the idea of parameterizing the solution space can still be applied to the SCS-GMTI problem.

I now pick up where Chapter 5 left off with the SAR GMTI solution space in Fig. 5.6, which is repeated in Fig. 6.1 for convenience. To parameterize this GMTI solution space, I chose to relate each of the four GMTI solution components (x_0, y_0, θ, and v_T) to a parameter I call the *nadir azimuth angle*, represented as θ_N. The nadir azimuth angle is the angle between the Zero-Doppler (ZD) line and an imaginary line connecting the SAR's time-zero nadir point to a GMTI

solution's initial position on the ground. This is illustrated in Fig. 6.1 as a top-down map view, and in Fig. 6.2 as a 3-D perspective view. The SAR's nadir point at time zero is also the origin of the reference frame in which this thesis defines the SAR GMTI scenario. I chose the nadir azimuth angle as the parameter for two reasons: first, every value for θ_N corresponds to a unique GMTI solution; and second, the nadir azimuth angle is easy to visualize in the top-down map view which is characteristic of SAR imagery. The SCS-GMTI problem is too complicated to give algebraic relationships between θ_N and the four GMTI solution components, but plots of these relationships are shown in Fig. 6.3.

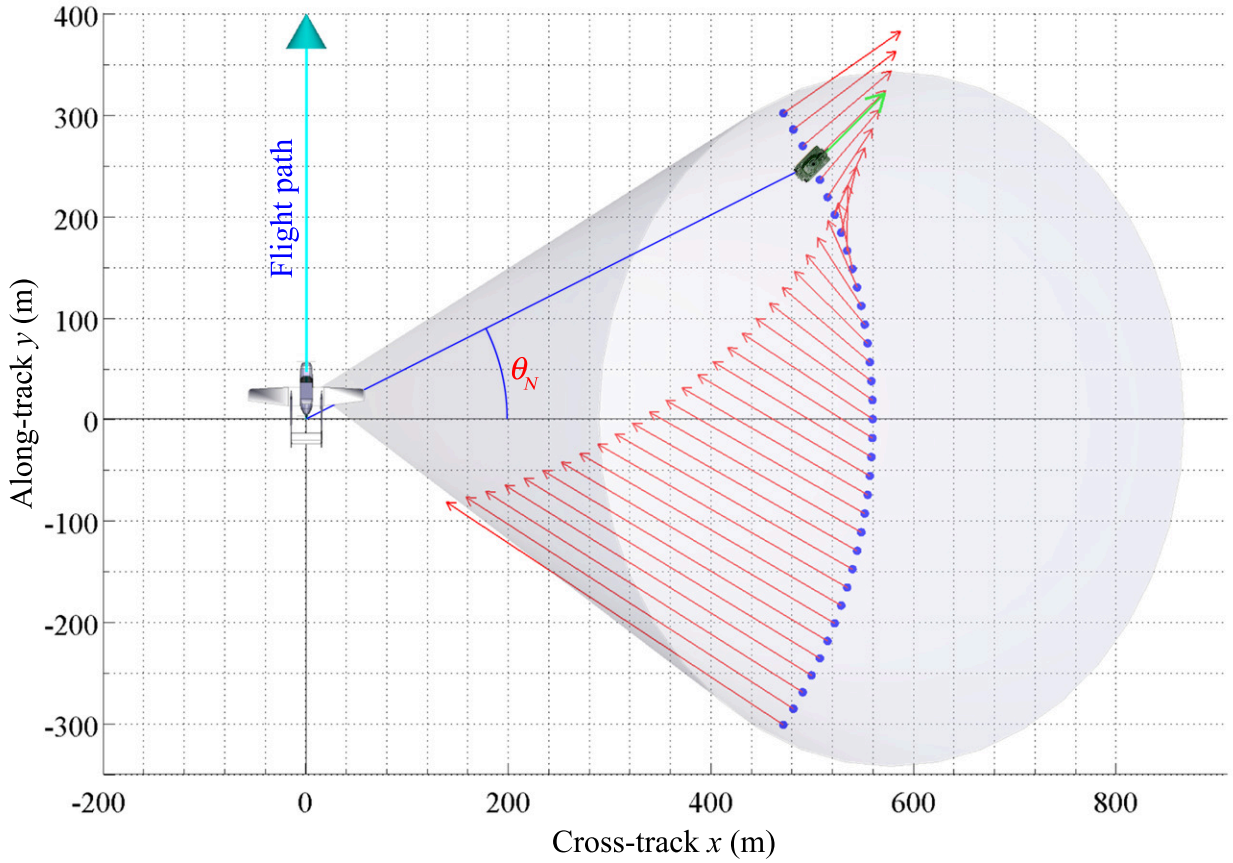

Figure 6.1: Top-down view of a SAR GMTI solution space for the moving target scenario discussed in Chapter 5. North is up. The azimuth beamwidth shown here is 50°. By considering only the mathematical shape of the hyperbolic RMC in the RC data of Fig. 5.3, the solution space contains infinitely many GMTI solutions, which means the SCS-GMTI problem is underdetermined. The quantity θ_N is the nadir azimuth angle. Every value for θ_N points to a unique initial target position within the GMTI solution space, and therefore corresponds to a unique GMTI solution.

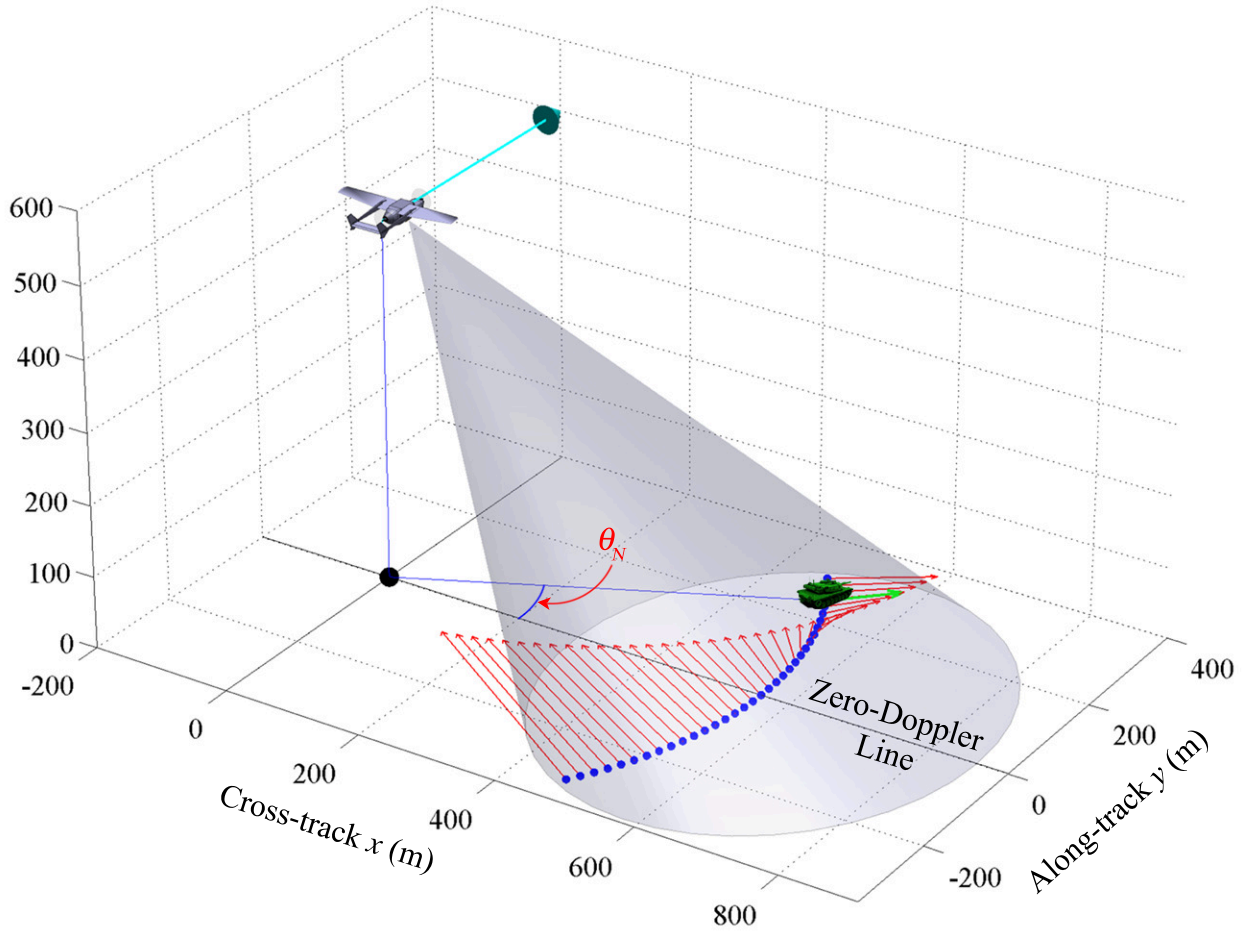

Figure 6.2: 3-D illustration of the nadir azimuth angle. The SAR's nadir point is on the ground directly below it. The nadir azimuth angle θ_N is the angle between the Zero-Doppler (ZD) line and an imaginary line connecting the SAR's time-zero nadir point to a GMTI solution's initial position on the ground. Positions ahead of the ZD line have positive values for θ_N, and positions behind it have negative values. Each value of θ_N represents a unique GMTI solution.

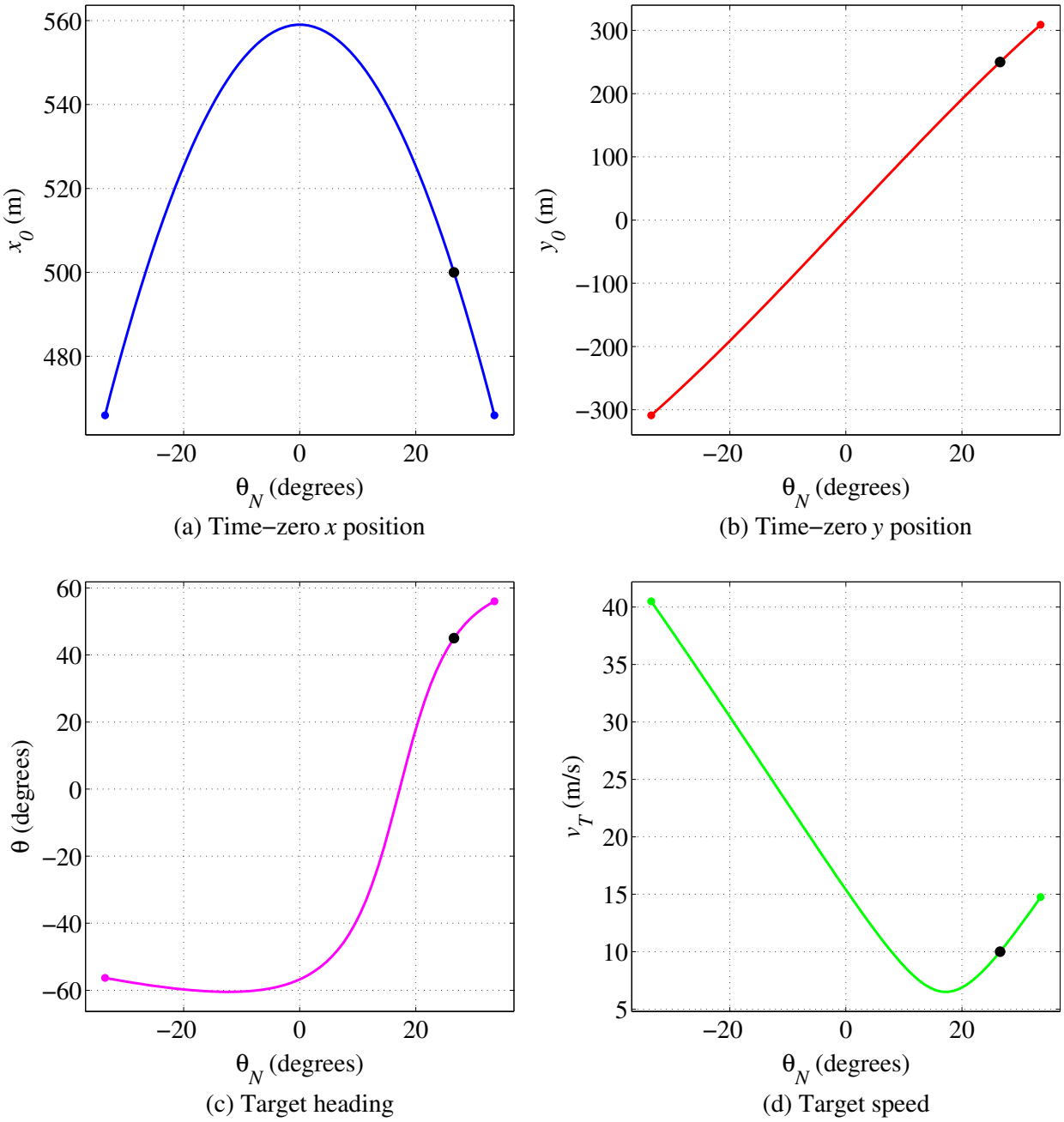

(a) Time−zero x position

(b) Time−zero y position

(c) Target heading

(d) Target speed

Figure 6.3: Parameterization of the SAR GMTI solution space shown in Figs. 6.1 and 6.2. Each GMTI solution component (x_0, y_0, θ, and v_T) is plotted against the nadir azimuth angle parameter θ_N. This particular set of plots is unique to the RMC shape in Fig. 5.3. The black dot in each plot indicates the target's true GMTI solution. The label under each panel states which GMTI component is plotted.

The plots in Fig. 6.3 show that out of the four GMTI solution components, only y_0 has a one-to-one relationship with the parameter θ_N. Because of this, the only mathematically unambiguous way to constrain the target's GMTI solution is to somehow constrain the target's initial along-track y-position. This requires some form of additional information [15, 70, 77] about the target's position beyond what can be inferred from just the target's hyperbolic signature in the SAR RC data. To complicate things further, SAR RC data in the real world almost never shows a target's RMC clearly against the overlapping RMCs from ground clutter, other targets, or structures, any of which may be much brighter in radar light than the target of interest. But as it turns out, additional useful information may be embedded in the SAR data itself.

6.2 Searching for Moving Targets in SAR Data with a Backprojection Matched Filter

Real ground targets almost never travel in clutter-free environments, and are not guaranteed to travel alone. As stated in Chapter 5, these two possibilities prevent the mathematical analysis in that chapter from being used as a viable GMTI technique for single-channel SAR. That analysis assumes an isolated target and "clean" RC data with no ground clutter or other interference present to distort the target's RMC. In addition, the analysis in Chapter 5 does not find the target's GMTI solution, it only proves that the problem is underdetermined.

My research and the existing literature show how ill-suited a single-channel SAR is for GMTI. In [15], Barbarossa makes the point that Doppler detection of moving targets requires a high PRF, which conflicts with how SAR works, as discussed in Section 2.2.4 of Chapter 2. In [13], Jao shows that with no prior information about the target, the GMTI search must be performed in a four-dimensional search space. My work in Section 5.2 of Chapter 5 shows that even a four-dimensional search does not produce a unique GMTI solution, as also shown by Chapman in [44].

However, despite these difficulties, in my research I found a way to potentially satisfy the constraint requirement. This enabled me to develop a method to perform limited GMTI. My method simultaneously detects multiple moving targets and estimates their GMTI solutions. If the SAR RC data is first formed into a conventional BPJ image matched to the stationary ground, it is entirely feasible that roads may be visible in the image. An actual SAR image containing roads is shown in Fig. 6.4, and an optical satellite photo of the same area is shown in Fig. 6.5. These roads can be used to provide the needed constraint on the target's GMTI solution space [44, 81, 82].

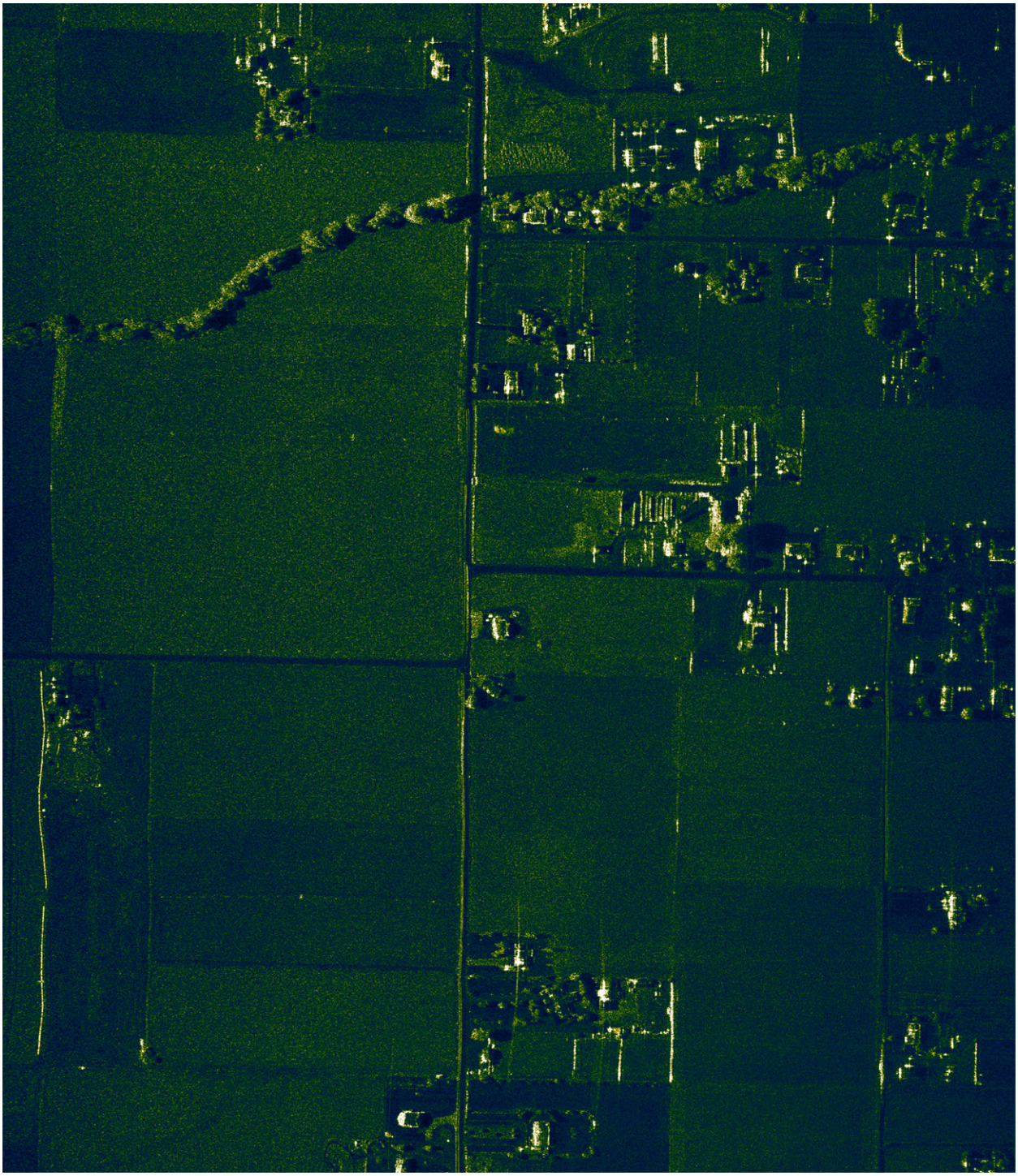

Figure 6.4: An actual SAR image (X-band) containing straight roads. North is up. The region in this image is just west of Smithfield, Utah. The SAR platform is off-image to the left, flying south and looking east. (Courtesy Space Dynamics Laboratory)

Figure 6.5: An optical satellite photo of the same ground scene as in Fig. 6.4. (Source: DigitalGlobe, Apple Maps)

My GMTI method involves using a form of the BPJ AF to search each road for moving targets. If a target travels along a road, its path is constrained by the road. It is also realistic to assume that the target(s) are moving at a constant speed. For this discussion I assume the road to be straight. A straight road has the benefit of constraining both the target's initial position and its heading, which can be one of only two possible directions 180° apart. To simplify the proof of my concept for this discussion, I also assume the road to be one-dimensional, with both directions of travel lying on the same line. If my GMTI technique is used in practice, it can be easily modified to account for the position difference between different lanes.

The search is performed by first choosing a segment of the road, and then defining a set of moving pixels that each act as a matched filter. The chosen road segment does not constitute the entire geographic search region: it only specifies where the moving pixels start at time zero. This set of positions is defined by specifying a reference point on the road, the length of the road segment to be searched, and a distance increment between adjacent search positions. This constitutes a search space in linear position relative to the reference point. Note the use of the phrase *linear position*, as opposed to along-track or cross-track position, because the road is not guaranteed to be oriented strictly in the along-track or cross-track direction.

A speed interval is then chosen for the pixels, with minimum and maximum searchable speeds, and a speed increment between adjacent speeds. This constitutes a search space in velocity along the road.

The search spaces in velocity and linear position together constitute a two-dimensional matched filter in target speed and time-zero linear position. The search direction is then specified, and the road is imaged via BPJ on the set of moving pixels that start at the time-zero positions specified in the position search space. Once BPJ integration starts, the pixels move along the road with various speeds as determined by the chosen velocity search space. In this way, each pixel is essentially a GMTI hypothesis that is tested by performing BPJ on it. With the road's direction constrained, all four GMTI solution components x_0, y_0, θ, and v_T are represented in this search scheme, which is depicted visually in Fig. 6.6. If a target is, in fact, traveling along the road with constant speed in the direction being searched, and if its speed and initial position fall in the 2-D search space, it appears as a bright peak in the final BPJ image. This bright peak fully indicates the target's true GMTI solution. Section 6.4 shows GMTI simulation results using this technique.

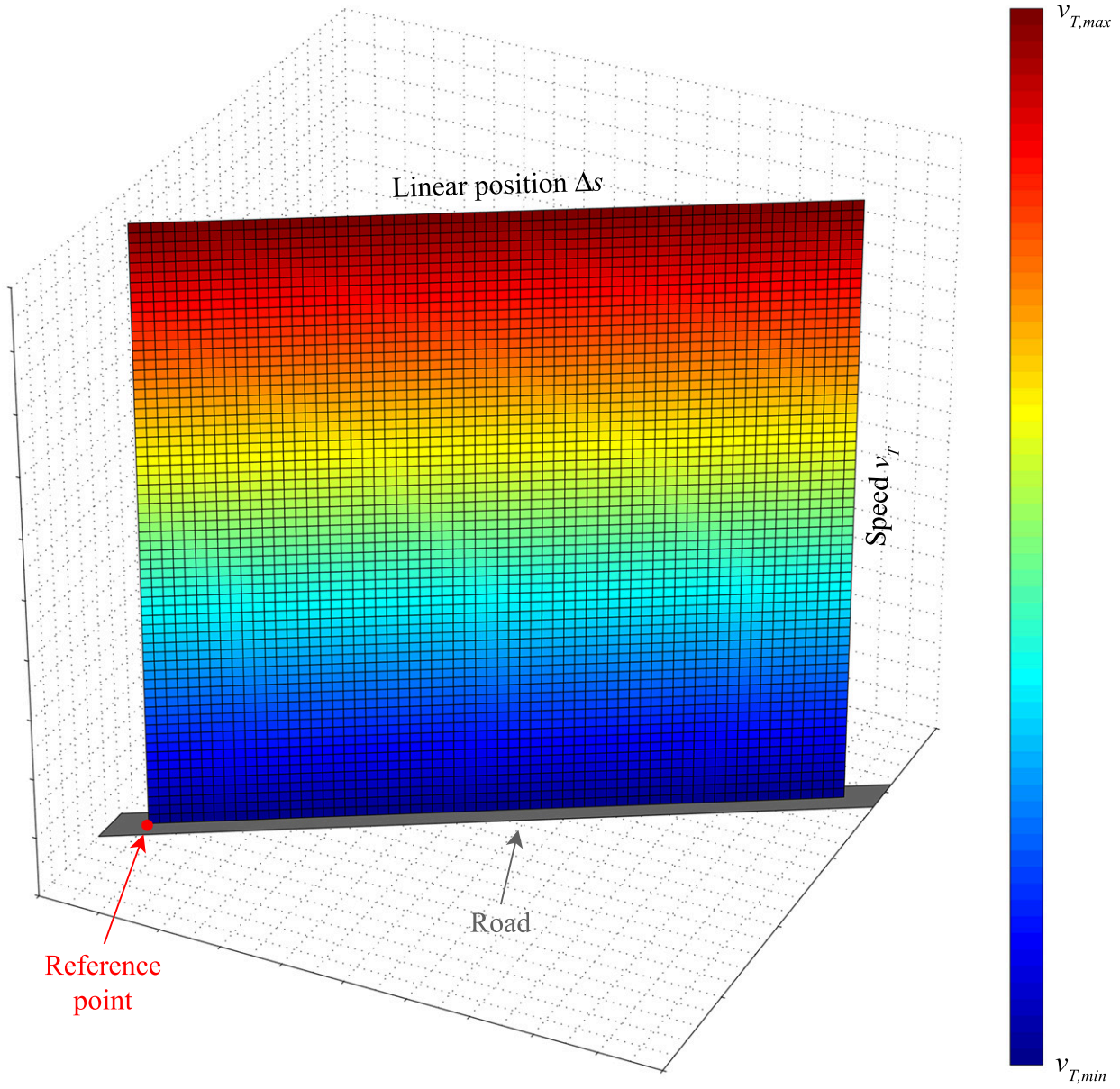

Figure 6.6: SAR GMTI search space. The colored grid represents a set of moving pixels which constitute the GMTI search space using a BPJ AF in a $(\Delta s, v_T)$ position-velocity space. The horizontal dimension is the linear position along the road, and the vertical dimension is speed. The red dot at the left end of the roadway represents the reference point. If the road's physical placement and direction are known, and if the reference point has been specified, then any position on the road can be specified by a single distance value Δs relative to the reference point. This couples x_0 and y_0 together, reducing the dimensionality of the SCS-GMTI problem from four to three. Each pixel's initial time-zero position is physically located at the road position on which its column is located, and each pixel's color in this figure represents a speed at which the pixel moves along the road after BPJ integration starts. In this sense, each pixel in the grid represents a particular matched filter, or a GMTI hypothesis that is tested by performing BPJ on it. If any pixel matches a target's GMTI solution, it appears as a bright peak in the final image, which fully indicates the target's true GMTI solution.

6.3 Ground Clutter and Signal-to-Clutter Ratio

In this thesis up until now, ground clutter has been given little mention aside from its brief appearances in Figs. 2.9 and 2.10b in Section 2.3. Ground clutter is an ever-present issue that SAR and GMTI must deal with, and is a major driving force behind ongoing research and advancements in these fields.

To demonstrate my GMTI technique, I show scenarios involving four different road orientations. In reality, roads contain asphalt which absorbs more radar energy than it reflects, making roads appear dark in SAR images and increasing a target's contrast against the road. However, in my GMTI simulations, I did not simulate an actual roadway surrounded by clutter. Instead, I simulated a uniformly distributed region of ground clutter, and had the targets travel through the clutter along a linear path that represented a road. This deprived the SAR of the benefit of having a radar-absorbent road surface against which to image the moving targets. However, this actually benefited my research, as the simulations were simpler to set up, and it turns out my GMTI technique still shows the targets very well against the background clutter.

For the GMTI results shown in Section 6.4, the SAR platform is west of the ground scene, flying north and looking east. Scenarios are shown for roads running north-south (N-S), E-W, NW-SE, and NE-SW. Each orientation is simulated with four point targets, two of which travel in each direction along the road. For each road orientation, two of the point targets represent cars, and two represent trucks. The cars were simulated to have RCS values of 100 m^2, and the trucks have RCS values of 200 m^2 [1]. A real truck generally has a larger RCS than a car due to the corner reflector effect of the truck bed. In each road orientation, the target positions and velocity vectors are selected to keep them within a certain region of ground clutter during the data collection.

The ground clutter region I used for my research and simulations is a square 50 m on a side, centered on the (500 m, 250 m) ground coordinate, with the clutter elements uniformly distributed, and a high average σ^0 of 2 m^2/m^2. A simulated BPJ image of this clutter region is shown in Fig. 6.7.

One key requirement to successfully image a target against ground clutter is that the target's radar signature must be sufficiently bright compared to the surrounding clutter. The relative radar brightness of a target compared to that of the surrounding ground clutter is referred to as the *signal-to-clutter ratio* (SCR).

A target's SCR has more than one way it can be defined in practice. The way I have chosen to define it in this thesis is based on several assumptions: first, I assume the point targets in this thesis to represent vehicles with typical dimensions (5 m $\times$ 2 m, illustrated in Fig. 6.8c). For SCR computations I also assume the target's RCS to be uniformly distributed over its footprint area. Although this thesis and my simulator model the targets as points with zero size, an SCR computation requires the targets to be treated as having measurable nonzero physical dimensions.

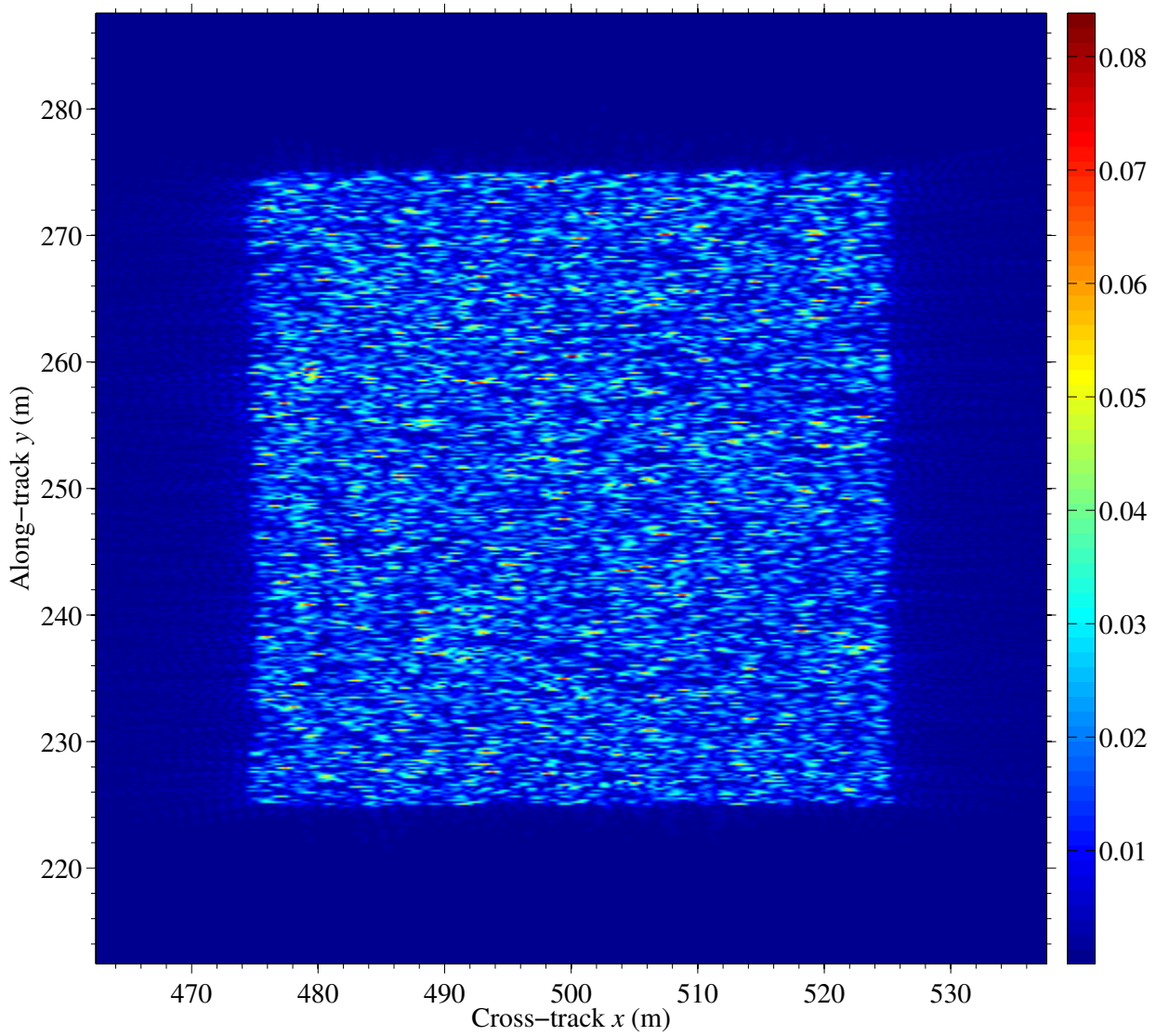

Figure 6.7: A conventional BPJ image of the ground clutter region used in this thesis. North is up. The SAR platform is off-image to the left, flying north and looking to the right. The clutter region is a square 50 m on a side, centered on the (500 m, 250 m) ground coordinate. The clutter is uniformly distributed with an average σ^0 of 2 m^2/m^2.

I also ignore localized statistical fluctuations in the ground clutter distribution. These fluctuations cause *speckle* [1], which is characteristic of coherent imaging systems. Speckle is the effect of constructive and destructive interference between individual clutter elements within a single resolution cell as they all echo the same radar pulse. Ignoring nonuniformities in the clutter distribution allows the total RCS of a given region on the ground to be approximated as the product of its area and the clutter's average σ^0.

Next, I assume a SAR image resolution cell to be a rectangle on the ground, with dimensions determined by the SAR's native azimuth resolution ΔAZ and ground range resolution ΔR_g as illustrated in Fig. 6.8b. For radar, ground range resolution depends on the incidence angle δ and the slant range resolution ΔR. The ground range resolution ΔR_g is the slant range resolution ΔR projected onto the ground plane along circular iso-range arc segments centered on the SAR according to the equation

$$\begin{aligned} \Delta R_g &= \frac{\Delta R}{\cos \delta} \\ &= \Delta R \cdot \sec \delta, \end{aligned} \tag{6.3}$$

and pictured in Fig. 6.8a. This discussion assumes a plane wave at the target location.

For a given target on the ground, the radar incidence angle δ depends on the right triangle formed by the SAR antenna, the SAR's nadir point, and the target position. With respect to ground range R_g, ΔR_g is not constant unless the radar is located at ground level, where $R_g = R$ and $\Delta R_g = \Delta R$. For SAR, ΔR_g is uselessly coarse near nadir (which is part of why active imaging radars never look straight down) where the incidence angle δ is 90°. For example, a SAR flying 500 m above ground level (AGL) and having a chirp bandwidth of 200 MHz has $\Delta R_g \approx 27.4$ m around its nadir point. At the other extreme, ground range resolution asymptotically approaches the slant range resolution as δ approaches zero for ground positions far from the the SAR's ground track.

Finally, I assume the target and ground clutter to be stationary. This set of assumptions (vehicle size, uniform RCS distributions, resolution cell shape, and absence of target motion) enables a precise definition of a target's SCR for this thesis: I define a target's SCR as the amount of radar energy reflected from a resolution cell on the target compared to the amount of energy

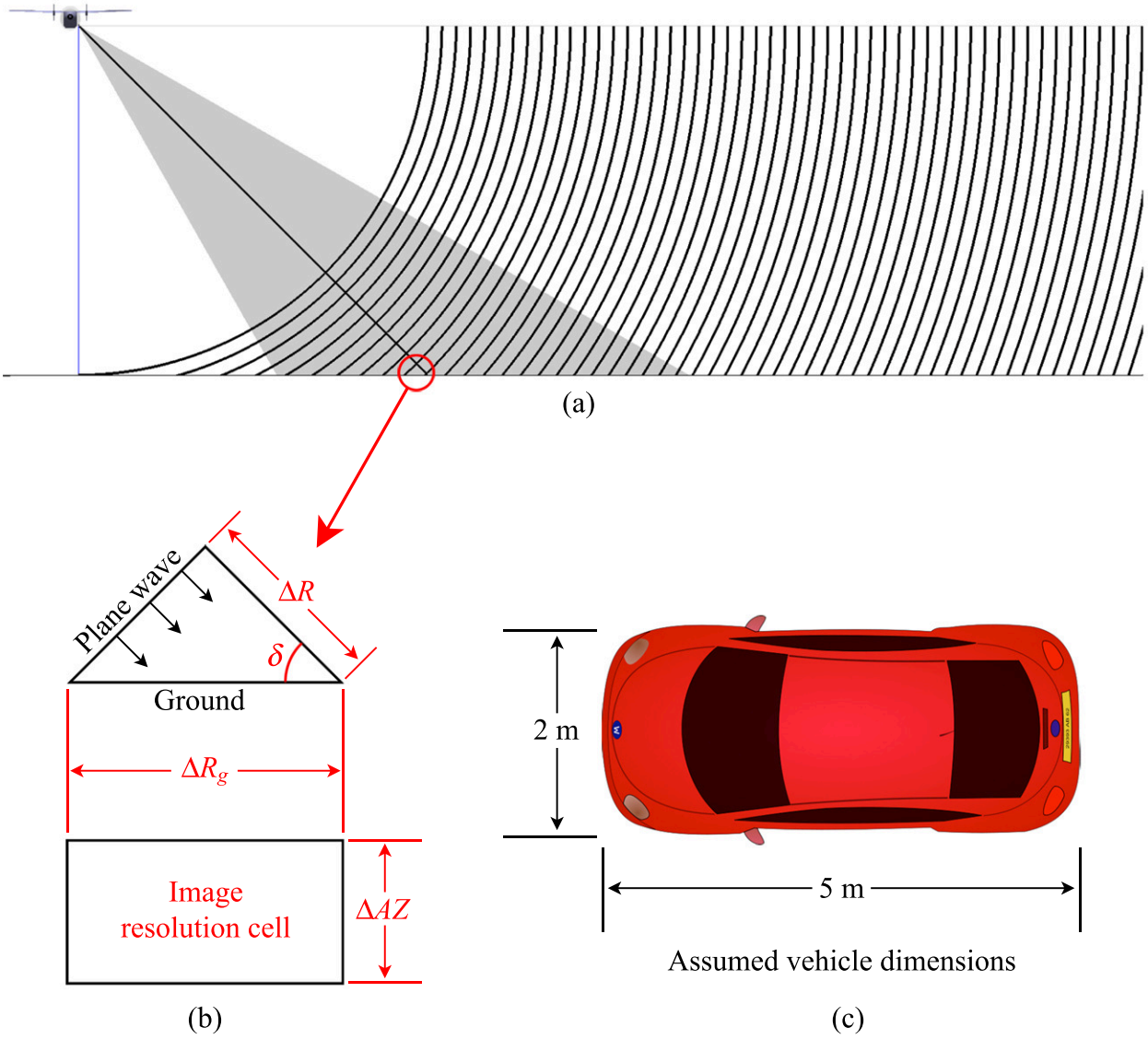

Figure 6.8: Factors used to compute the signal-to-clutter ratio (SCR) for a SAR in this thesis. The ground range resolution ΔR_g for SAR depends on its slant range resolution ΔR and the radar incidence angle δ at a given point on the ground. In panel (a), the SAR platform is flying into the page and looking to the right. The distance between adjacent iso-range arcs represents the slant range resolution ΔR, and ΔR_g for a given ground position is obtained by projecting ΔR onto the ground plane along the iso-range arcs. Ground range resolution is indicated by the horizontal distance between the ground intersection points for adjacent iso-range arcs. Note the coarseness of ΔR_g around nadir compared to distances further out. Panel (b) shows a two-dimensional resolution cell whose size is determined by the SAR's native azimuth resolution ΔAZ and the local ground range resolution. Panel (c) shows a car whose dimensions are assumed to be approximately equal to average dimensions for actual vehicles.

reflected from a resolution cell of ground clutter. Here I list the quantities used in the preceding assumptions:

Table 6.1: Quantities and parameters used to quantify the SCR for vehicle point targets used in this thesis.

Parameter Name:	Value
Assumed vehicle dimensions:	5 m $\times$ 2 m
Vehicle footprint area A_{target}:	10 m^2
Target position:	(500 m, 250 m)
Incidence angle δ at target:	45°
Chirp bandwidth BW:	200 MHz
Slant range resolution ΔR:	0.75 m [using Eq. (2.3)]
Ground range resolution ΔR_g at target position:	1.06 m [using Eq. (6.3)]
SAR's azimuth resolution ΔAZ for 50° beamwidth:	$\approx$ 15 cm
Image resolution cell area $A_{cell} = \Delta R_g \cdot \Delta AZ$:	$\approx$ 0.16 m^2
Car RCS σ_{car}:	100 m^2
Truck RCS σ_{truck}:	200 m^2
Ground clutter normalized RCS σ^0:	2 m^2/m^2

Using the values listed in Table 6.1, the SCR values can be computed for the target vehicles modeled in this thesis. First, assuming the target's RCS is evenly distributed over its footprint area, the target's normalized RCS σ^0_{target} is

$$\sigma^0_{target} = \frac{\sigma_{target}}{A_{target}}. \tag{6.4}$$

The amount of target RCS contained in a resolution cell is now

$$\sigma_{cell,\,target} = \sigma^0_{target} \cdot A_{cell} \tag{6.5}$$

and the amount of clutter RCS contained in a resolution cell is

$$\sigma_{cell,\,clutter} = \sigma^0_{clutter} \cdot A_{cell}. \tag{6.6}$$

Dividing Eq. (6.5) by Eq. (6.6) and converting to dB yields

$$\begin{aligned} SCR &= 10\log_{10}\left(\frac{\sigma_{cell,\,target}}{\sigma_{cell,\,clutter}}\right) \\ &= 10\log_{10}\left(\frac{\sigma^0_{target}\cdot A_{cell}}{\sigma^0_{clutter}\cdot A_{cell}}\right) \\ &= 10\log_{10}\left(\frac{\sigma^0_{target}}{\sigma^0_{clutter}}\right) \\ &= 10\log_{10}\left(\frac{\sigma_{target}}{A_{target}\cdot\sigma^0_{clutter}}\right). \end{aligned} \tag{6.7}$$

My definition for a target's SCR is based on how much radar energy is reflected from a single resolution cell on the target and in the clutter. Equation (6.7) shows that this definition leads to a SCR formula that does *not* depend on the size of the resolution cell, but depends only on the normalized σ^0 values for the target and the clutter. Applying the relevant terms from Table 6.1 to Eq. (6.7), the signal-to-clutter ratio for a car is 7 dB, and the SCR for a truck is 10 dB. These SCR values assume that the targets are stationary in the stationary ground clutter region pictured in Fig. 6.7. When the BPJ image formation process focuses on this stationary target scene, the image contrast of a hard target against the ground clutter can be quantified with these SCR values.

Because of the way I have defined a target's SCR for this thesis, it is difficult to express or quantify the SCR for scenarios that do not conform to the assumptions upon which my SCR definition is based. In such cases, I qualitatively describe the SCR as simply being "higher" or "lower" than the ideal stationary case as described at the end of the previous paragraph.

For example, if a target is moving, its energy in the BPJ image may or may not remain tightly focused as it does when stationary. It the target moves in the cross-track direction, its image remains well-focused but shifted in azimuth, and its SCR may remain approximately the same as if it was stationary. This assumes the target's shifted image is still positioned within the ground clutter region. But if the target moves in the along-track direction, its energy smears out in the image, and in a case like this the SCR is lower and the target is less detectable by a visual inspection of the BPJ image. This qualitative description of the SCR relative to the ideal stationary case is how I describe my SCS-GMTI results in the next section.

6.4 Single-Channel SAR GMTI Search Results

When simulating my GMTI technique, I had the SAR fly due north, and I placed all target scenes east of the SAR's flight track, with the SAR looking to the right. For my SCS-GMTI results, I first show the GMTI process for the NE-SW road orientation. I start by showing clean RC data (Fig. 6.9a) for the four targets on the road, and then the same RC data with ground clutter included (Fig. 6.9b). At $\sigma^0 = 2$ m^2/m^2, the ground clutter's normalized RCS in this thesis is high enough to almost completely "drown out" the target RMCs in the RC data. This is to demonstrate that my GMTI technique not only works in the presence of ground clutter, it works in the presence of *strong* ground clutter, it works for multiple targets simultaneously, and in fact it suppresses the ground clutter. The clutter is suppressed because each GMTI image is formed via BPJ matched filtering on a set of moving pixels, after the same manner as the BPJ AF [13]. The mismatch between the moving pixels and the stationary clutter reduces the clutter intensity in the final BPJ GMTI image. Pixels matched to moving targets increase the targets' brightness in the GMTI image. Overall, this boosts the SCR for moving targets, making them more detectable to the BPJ MF.

The RC data in Fig. 6.9 is used to form the conventional BPJ images in Figs. 6.10 and 6.11. These BPJ images are focused on the stationary 50 m x 50 m square region containing the moving targets and the ground clutter. The BPJ image in Fig. 6.10 is formed from the clean RC data in Fig. 6.9a to show how the moving targets smear, shift, and generally defocus due to their motion along the NE-SW road. The BPJ image in Fig. 6.11 shows the same ground scene, but is formed from the RC data in Fig. 6.9b, which includes the ground clutter. The high σ^0 for the ground clutter not only obscures the target signatures in the RC data of Fig. 6.9b, it also nearly completely drowns out the defocused target images in the conventional BPJ image of Fig. 6.11. Because of this, each target in this discussion has a low SCR in a conventional BPJ image. This is done intentionally to demonstrate the clutter-suppressing effects of my GMTI technique.

Figures 6.12 and 6.13 show GMTI images for the NE-SW road scenario using the BPJ MF technique described in this chapter. The true GMTI solutions for the targets are clearly visible as bright peaks, and the ground clutter is seen to be greatly suppressed. Figures 6.14 through 6.19 then show GMTI images for NW-SE, E-W, and N-S road orientations. For these other road orientations, I show only the GMTI results, and not their RC data or conventional BPJ images matched to the stationary ground.

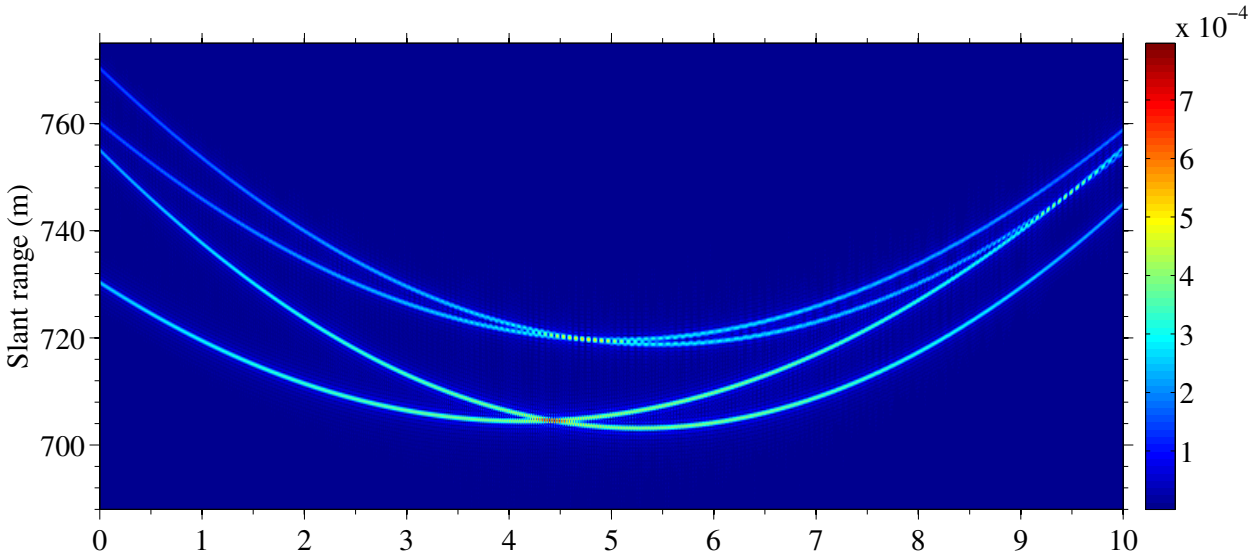

(a) Target data only

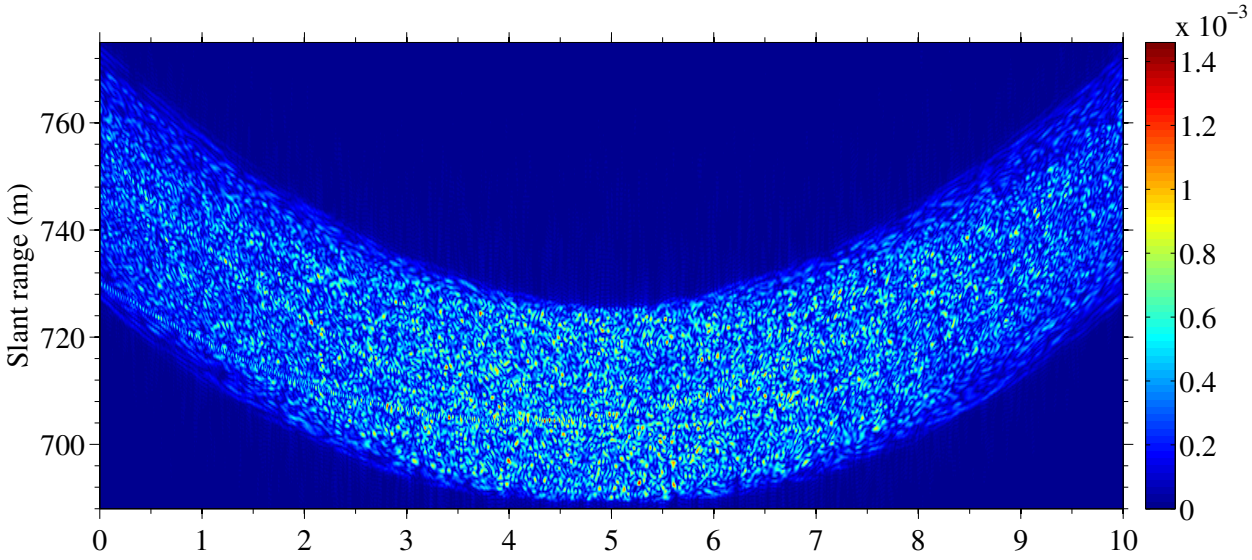

(b) Ground clutter included

Figure 6.9: RC data for four targets moving on a road oriented NE-SW. Panel (a) shows the clean RC data for the targets only, and panel (b) includes ground clutter, which has been deliberately intensified to $\sigma^0 = 2$ to give the targets a low SCR in the RC data. The BPJ image formed from this data is shown in Figs. 6.10 and 6.11. A BPJ image showing the clutter region only, with no targets, is shown in Fig. 6.7.

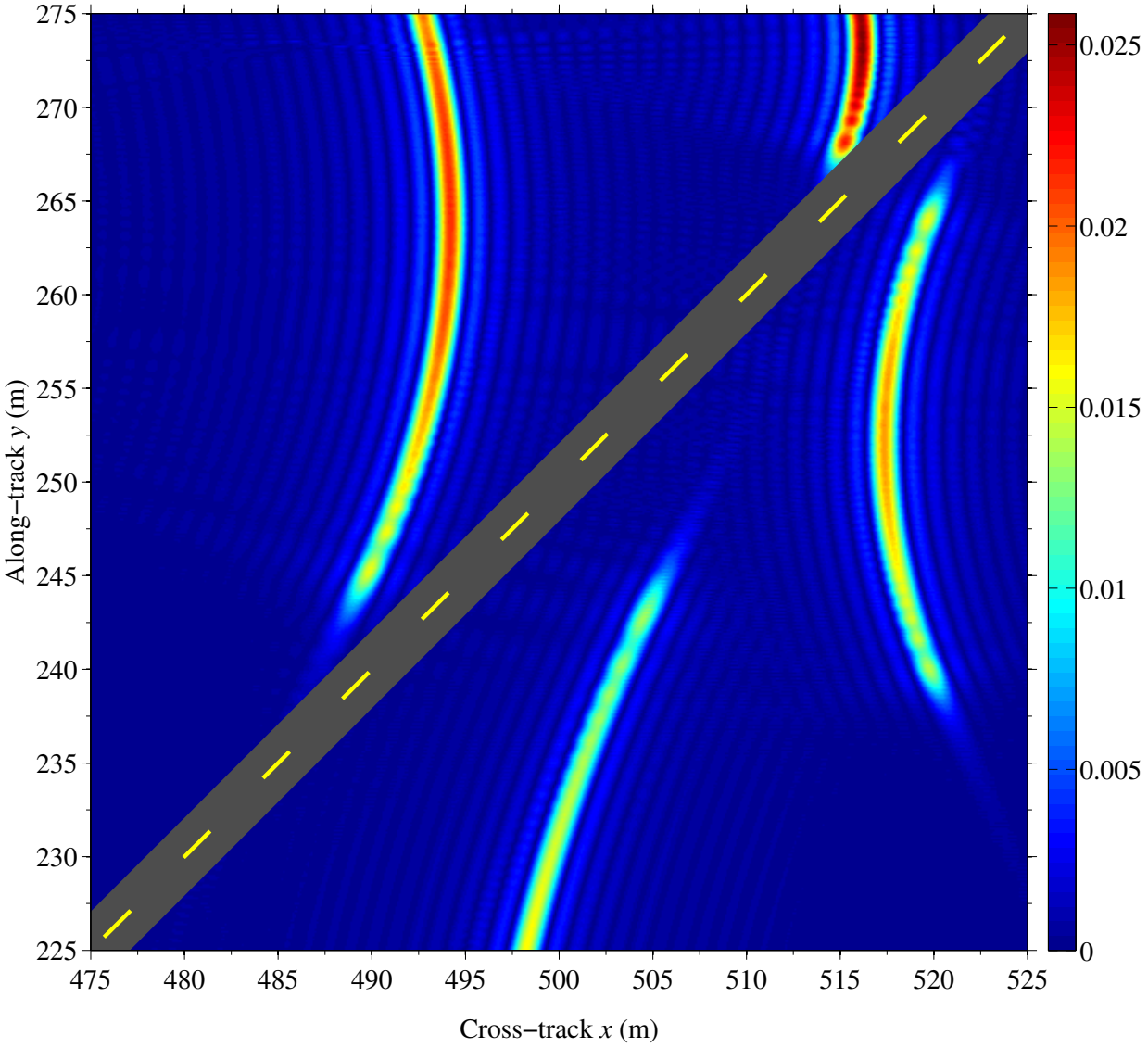

Figure 6.10: A conventional BPJ image of four targets moving on a NE-SW oriented road. North is up. The SAR platform is off-image to the left, flying north and looking to the right. This image was formed from the clean RC data in Fig. 6.9a, and the road graphic was added afterward. Two targets travel in each direction along the road. The targets' true GMTI solutions are listed in the table in Fig. 6.12.

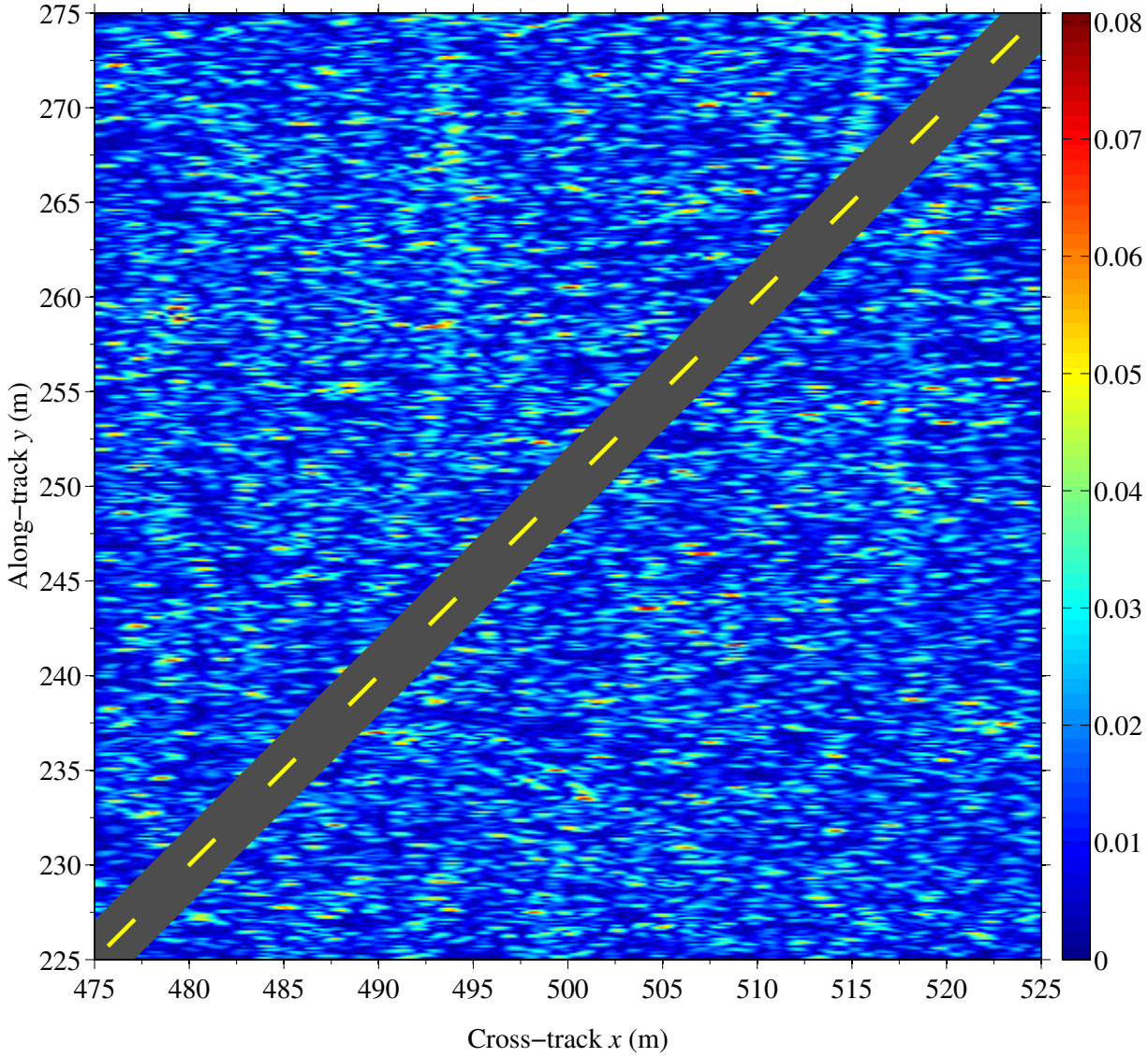

Figure 6.11: A conventional BPJ image of four targets moving on a NE-SW oriented road. North is up. The SAR platform is off-image to the left, flying north and looking to the right. This image was formed from the RC data in Fig. 6.9b which includes ground clutter, and the road graphic was added afterward. Two targets travel in each direction along the road. The targets' true GMTI solutions are listed in the table in Fig. 6.12. Note that based on this image alone, little useful information can be inferred about the targets, other than their possible existence due to the barely-visible curved smears. This is to provide a contrast to the clarity of my GMTI results, which are derived from the same data used to form this image.

As stated in Section 6.2, the BPJ AF technique is used to implement my SCS-GMTI method. For each road orientation, I provide a GMTI overview (Figs. 6.12, 6.14, 6.16, and 6.18), and close-ups of the individual GMTI target images (Figs. 6.13, 6.15, 6.17, and 6.19). The GMTI target images produced by this BPJ MF technique have all the characteristics of an AF, including central peaks and odd rotational symmetry. In the figures that show GMTI close-up images for individual targets, any imperfections to their odd rotational symmetry are due to ground clutter effects.

Concerning the ground clutter, it is apparent in the GMTI overview images that the background texturing effect due to the clutter does not cover the entire GMTI search space. This is because of the limited size of the ground clutter region I simulated for this research. During the BPJ GMTI computations, some of the moving pixels that constitute the GMTI MF move beyond the bounds of the ground clutter region, and no longer receive BPJ contributions from ground clutter as a result. This produces the "clear" regions in the GMTI images.

It is interesting to note that for each road orientation, the AF-like target images look completely different, yet still indicate valid GMTI solutions at their central peaks. This is an example of the point made at the end of Chapter 4 that the BPJ AF has infinitely many possible manifestations.

It is also interesting to observe the effect of placing two targets relatively close together in the GMTI search space. For the N-S road scenario shown in Fig. 6.18, targets 3 and 4 start one meter apart from each other at time zero, they travel in the same direction, and their speeds are separated by only half a meter per second. Fig. 6.18d shows how their BPJ MF responses interact and the complex wave interference between them, and Fig. 6.19c shows a close-up of these interfering target responses in the GMTI search space.

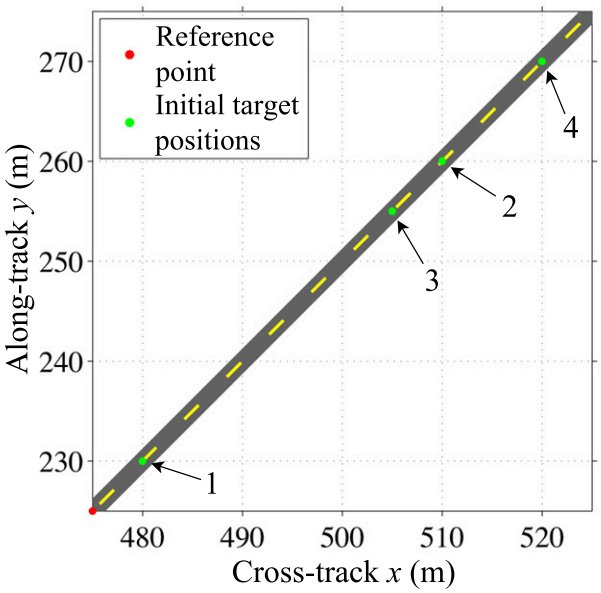

(a) NE-SW road

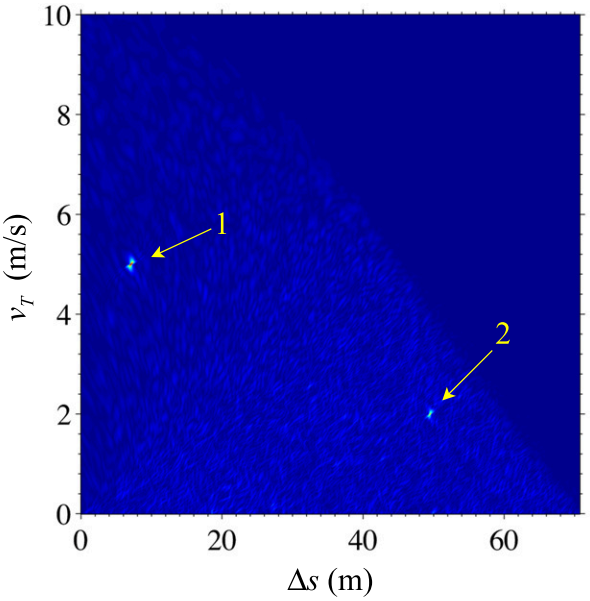

(b) 45° (NE) heading search

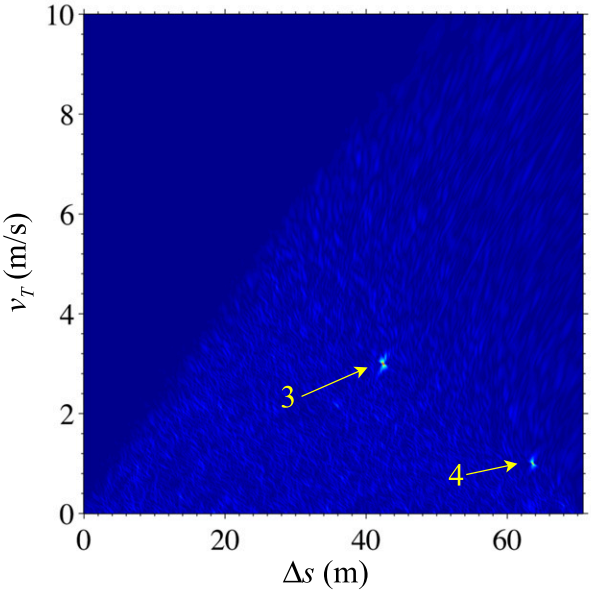

(c) 225° (SW) heading search

	x_0	y_0	θ	v_T
Target 1	480 m	230 m	45° (NE)	5 m/s
Target 2	510 m	260 m	45° (NE)	2 m/s
Target 3	505 m	255 m	225° (SW)	3 m/s
Target 4	520 m	270 m	225° (SW)	1 m/s

(d) Ground truth

Figure 6.12: GMTI results for four targets moving on a NE-SW oriented road. In panel (a), north is up, and the SAR platform is off-image to the left, flying north and looking to the right. These images are formed using the SCS-GMTI method described in this chapter. Two targets travel in each direction along the road. The targets' ground truths are listed in the table in panel (d). Figure 6.13 shows close-ups of each target's GMTI response.

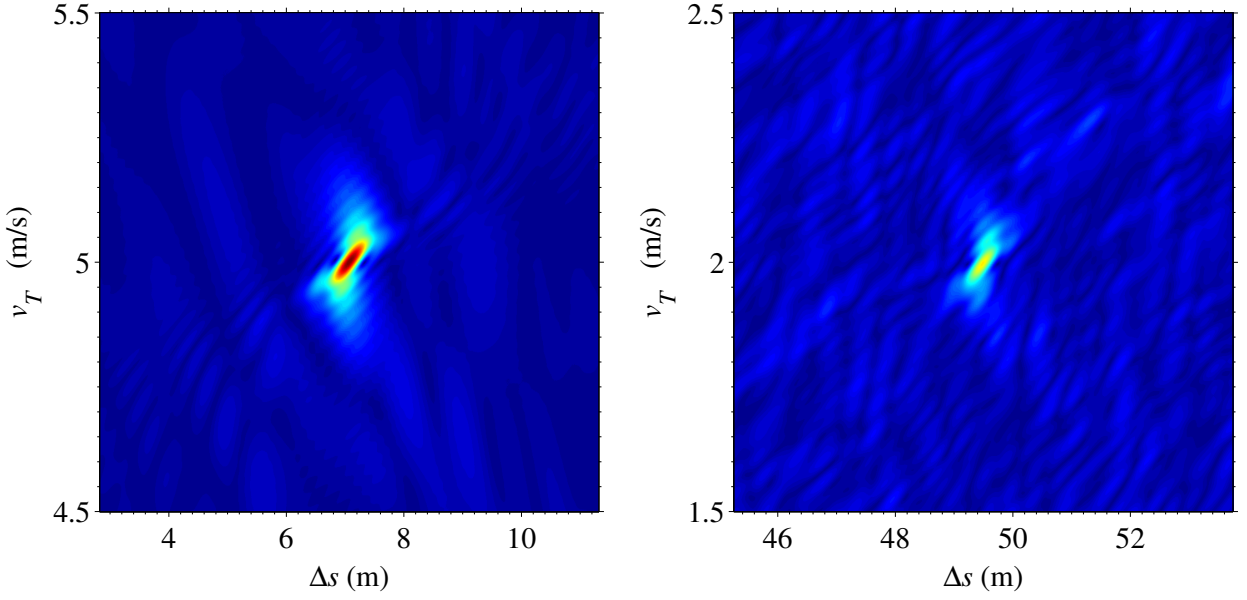

(a) Target 1, heading = 45° (NE)

(b) Target 2, heading = 45° (NE)

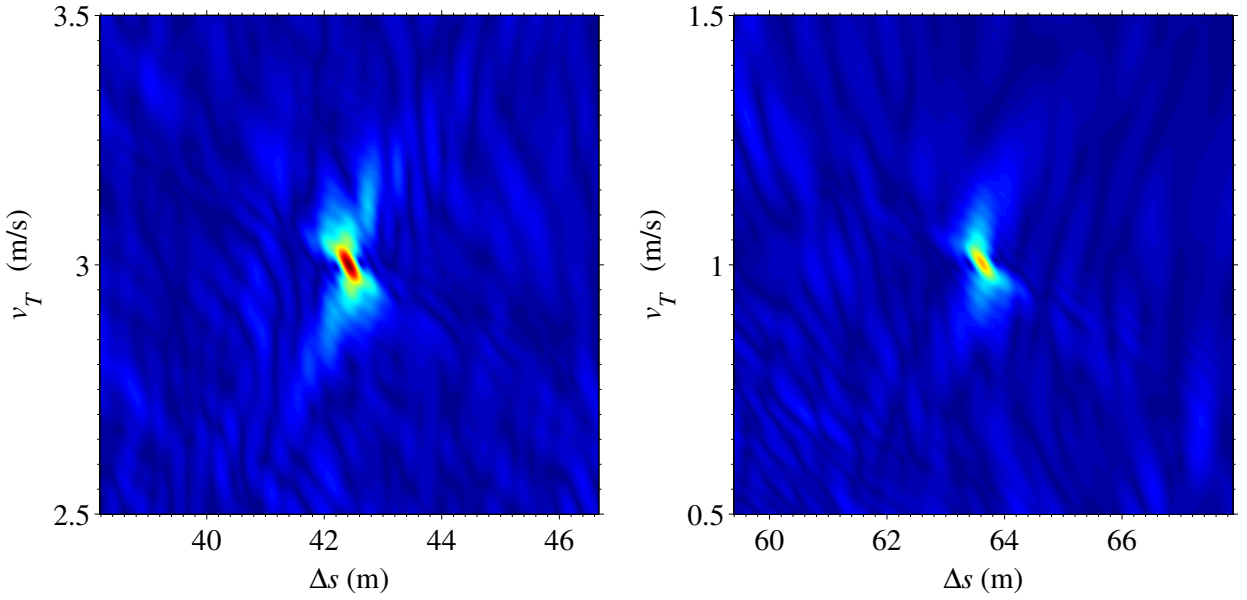

(c) Target 3, heading = 225° (SW)

(d) Target 4, heading = 225° (SW)

Figure 6.13: GMTI close-up images for the four targets in Fig. 6.12 moving on a NE-SW oriented road. These images are formed using the SCS-GMTI method described in this chapter.

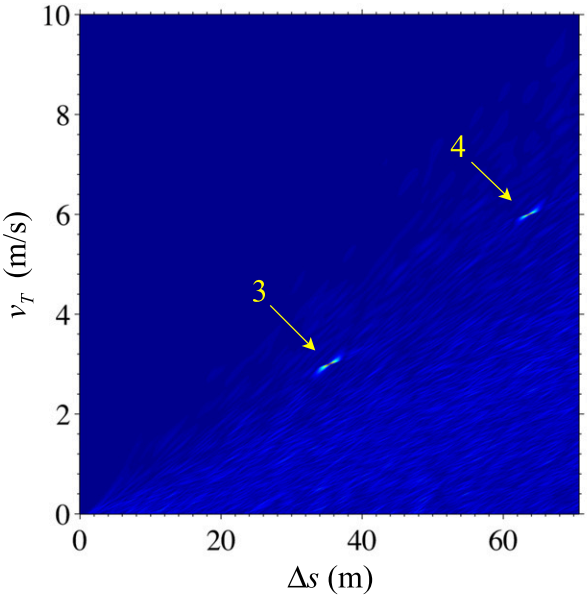

(a) 315° (NW) heading search

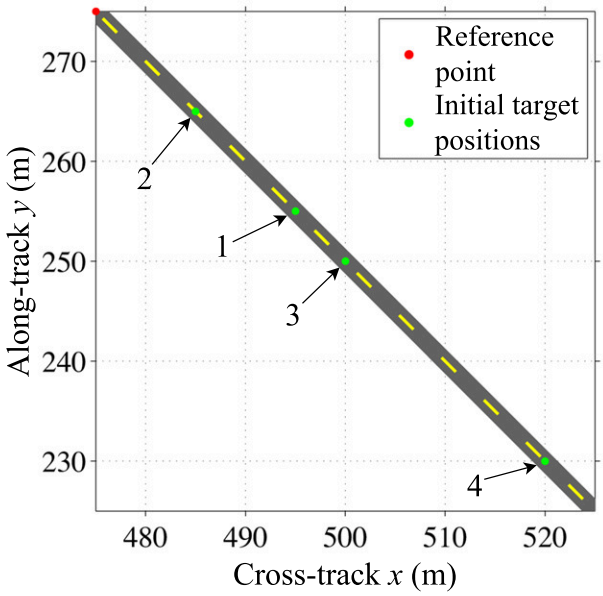

(b) NW-SE road

	x_0	y_0	θ	v_T
Target 1	495 m	255 m	135° (SE)	4 m/s
Target 2	485 m	265 m	135° (SE)	5 m/s
Target 3	500 m	250 m	315° (NW)	3 m/s
Target 4	520 m	230 m	315° (NW)	6 m/s

(c) Ground truth

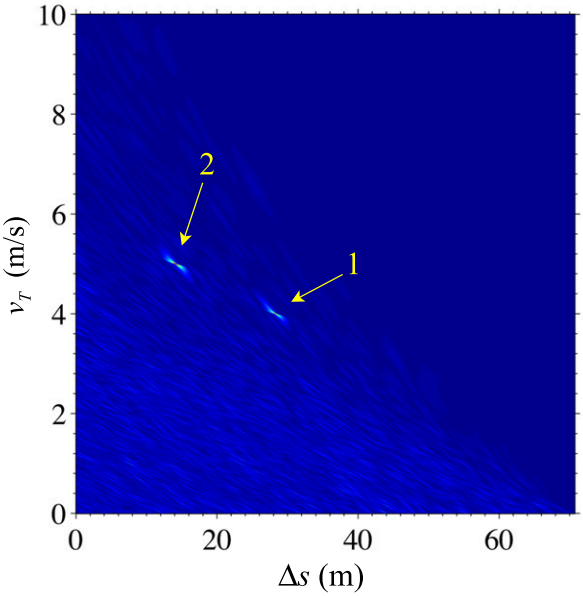

(d) 135° (SE) heading search

Figure 6.14: GMTI results for four targets moving on a NW-SE oriented road. In panel (b), north is up, and the SAR platform is off-image to the left, flying north and looking to the right. These images are formed using the SCS-GMTI method described in this chapter. Two targets travel in each direction along the road. The targets' ground truths are listed in the table in panel (c). Figure 6.15 shows close-ups of each target's GMTI response.

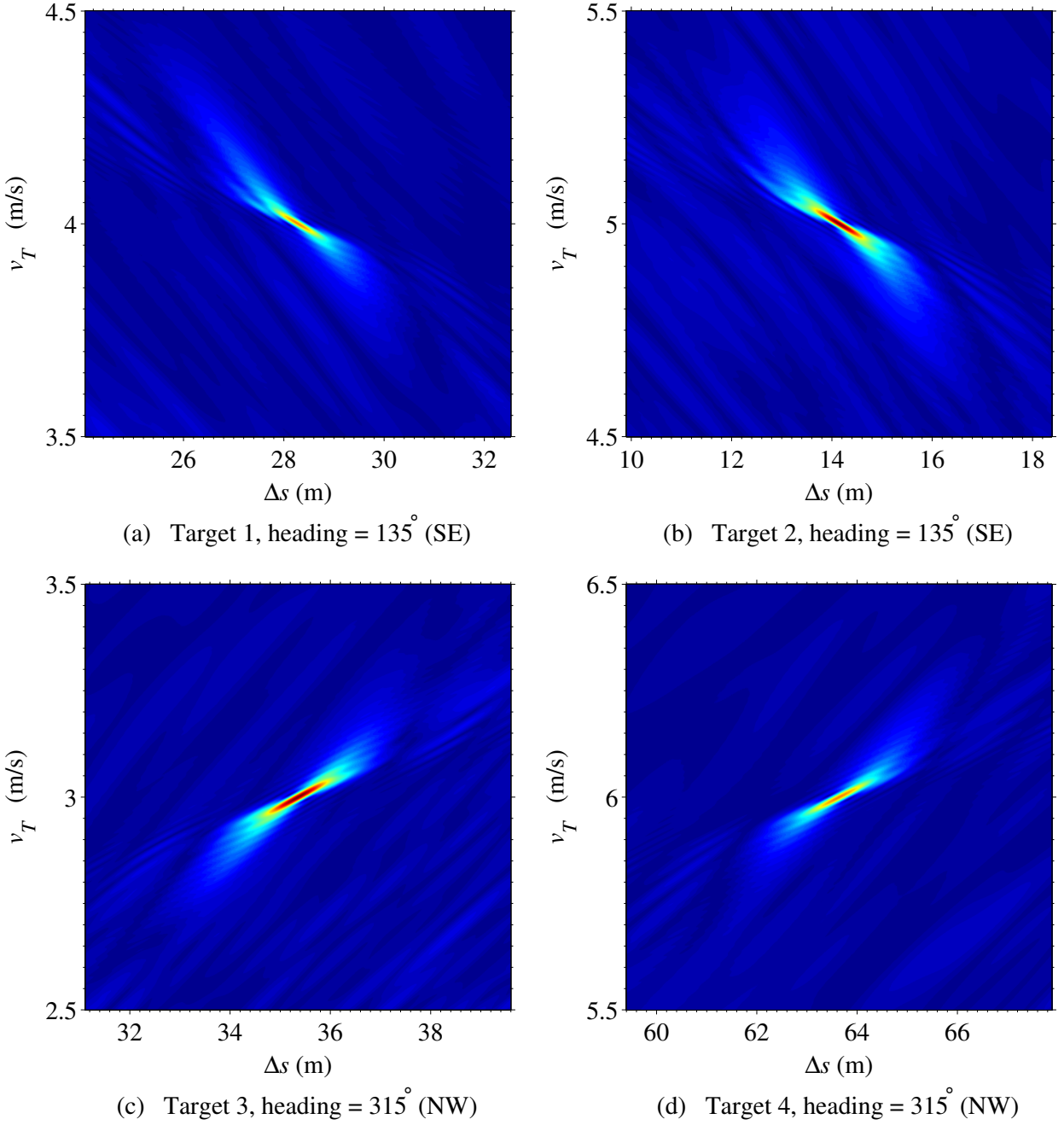

(a) Target 1, heading = 135° (SE)

(b) Target 2, heading = 135° (SE)

(c) Target 3, heading = 315° (NW)

(d) Target 4, heading = 315° (NW)

Figure 6.15: GMTI close-up images for the four targets in Fig. 6.14 moving on a NW-SE oriented road. These images are formed using the SCS-GMTI method described in this chapter.

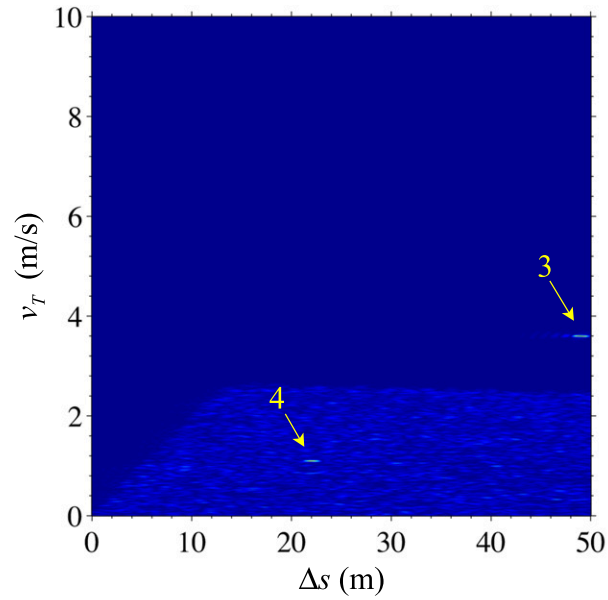

(a) 270° (W) heading search

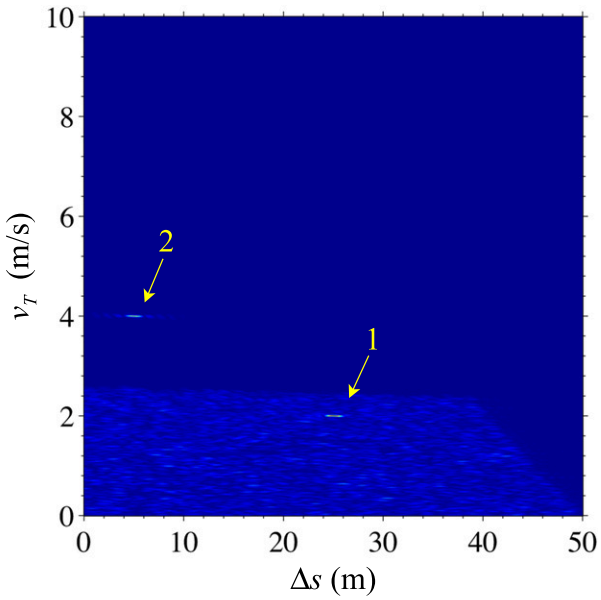

(b) 90° (E) heading search

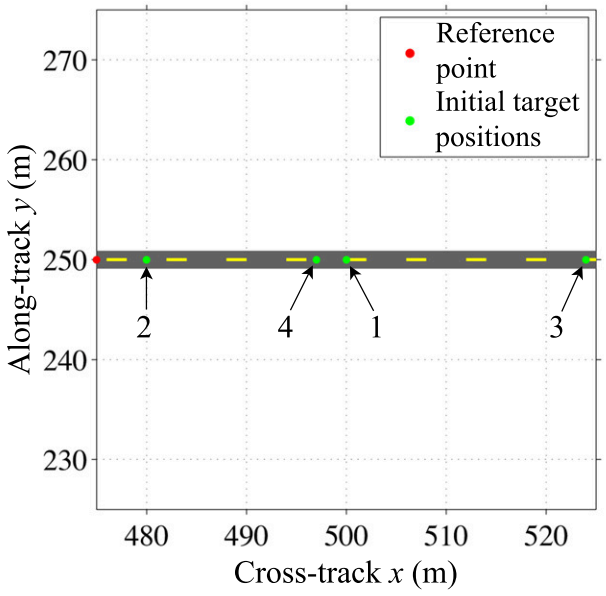

(c) E-W road

	x_0	y_0	θ	v_T
Target 1	500 m	250 m	90° (E)	2 m/s
Target 2	480 m	250 m	90° (E)	4 m/s
Target 3	524 m	250 m	270° (W)	3.6 m/s
Target 4	497 m	250 m	270° (W)	1.1 m/s

(d) Ground truth

Figure 6.16: GMTI results for four targets moving on an E-W oriented road. In panel (c), north is up, and the SAR platform is off-image to the left, flying north and looking to the right. These images are formed using the SCS-GMTI method described in this chapter. Two targets travel in each direction along the road. The targets' ground truths are listed in the table in panel (d). Figure 6.17 shows close-ups of each target's GMTI response.

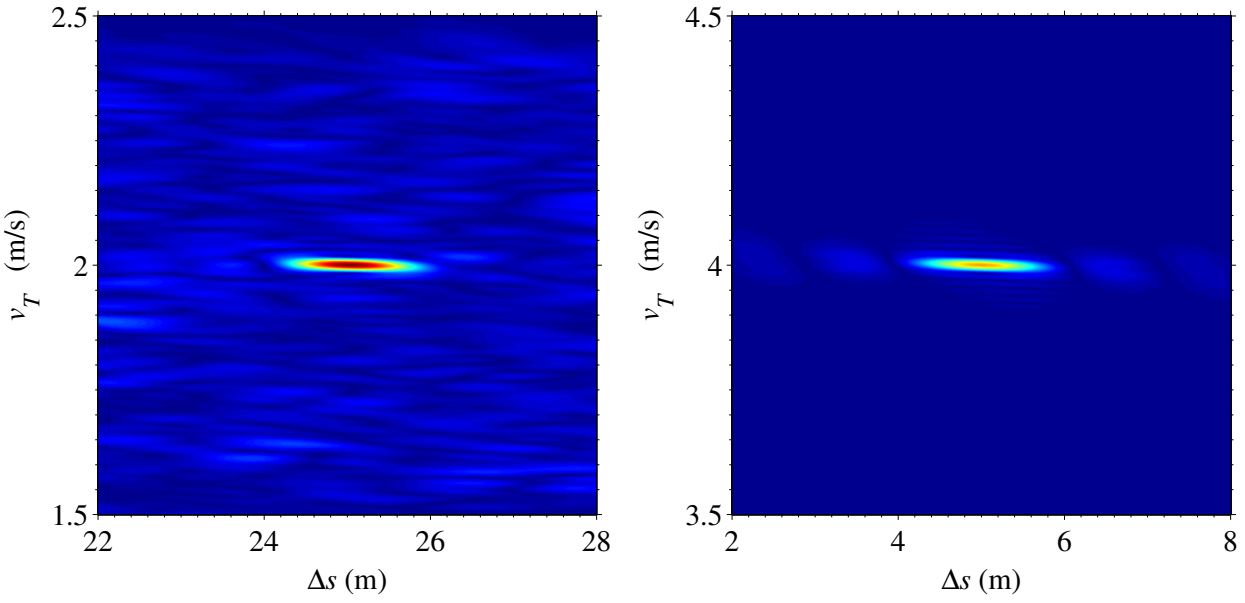

(a) Target 1, heading = 90° (E)

(b) Target 2, heading = 90° (E)

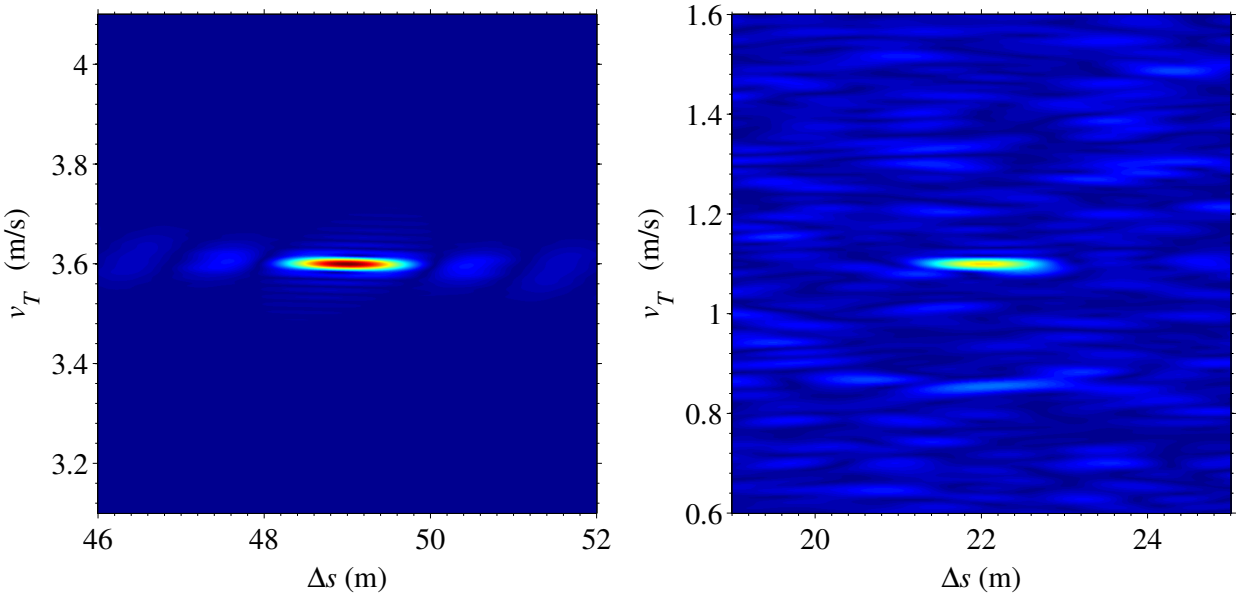

(c) Target 3, heading = 270° (W)

(d) Target 4, heading = 270° (W)

Figure 6.17: GMTI close-up images for the four targets in Fig. 6.16 moving on an E-W oriented road. These images are formed using the SCS-GMTI method described in this chapter.

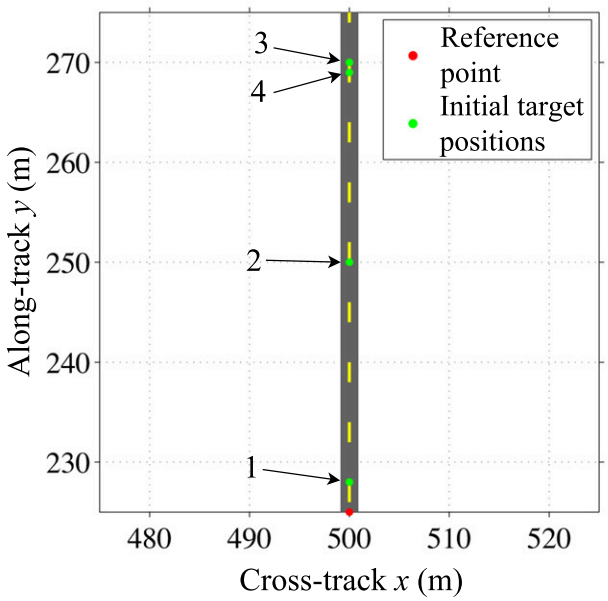

(a) N-S road

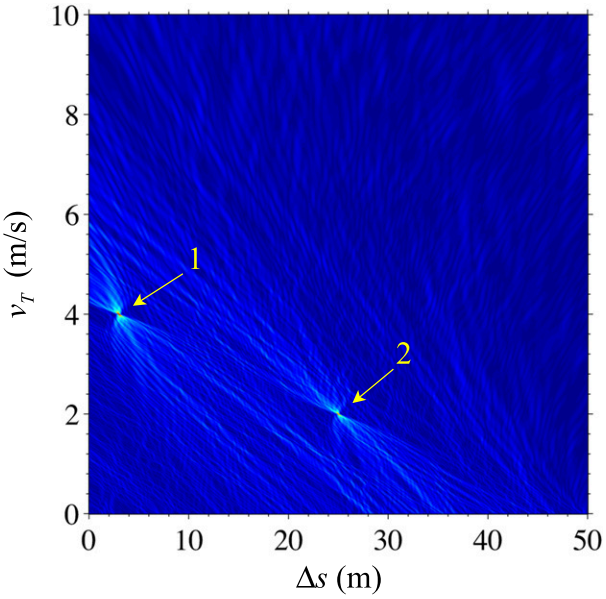

(b) 0° (N) heading search

	x_0	y_0	θ	v_T
Target 1	500 m	228 m	0° (N)	4 m/s
Target 2	500 m	250 m	0° (N)	2 m/s
Target 3	500 m	270 m	180° (S)	3.5 m/s
Target 4	500 m	269 m	180° (S)	3 m/s

(c) Ground truth

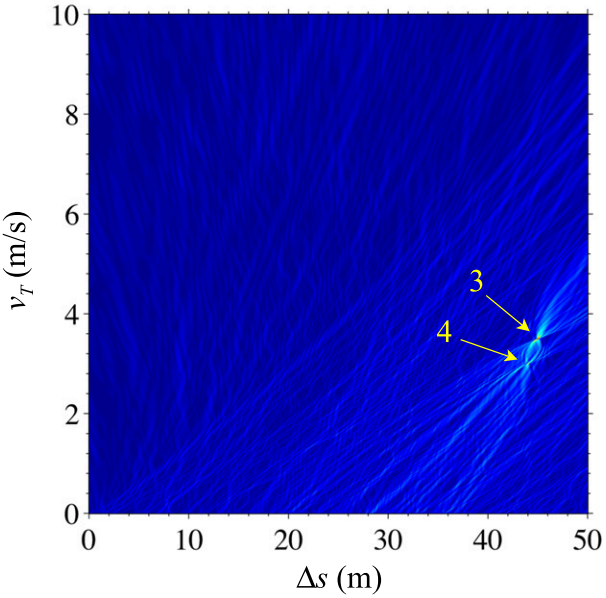

(d) 180° (S) heading search

Figure 6.18: GMTI results for four targets moving on a N-S oriented road. In panel (a), north is up, and the SAR platform is off-image to the left, flying north and looking to the right. These images are formed using the SCS-GMTI method described in this chapter. Two targets travel in each direction along the road. The targets' ground truths are listed in the table in panel (c). Targets 3 and 4 are intentionally placed near each other in position and speed to see how resolvable they are in the GMTI search results. Note their interaction and interference effects due to the complex-valued nature of BPJ computations. Figure 6.19 shows close-ups of each target's GMTI response.

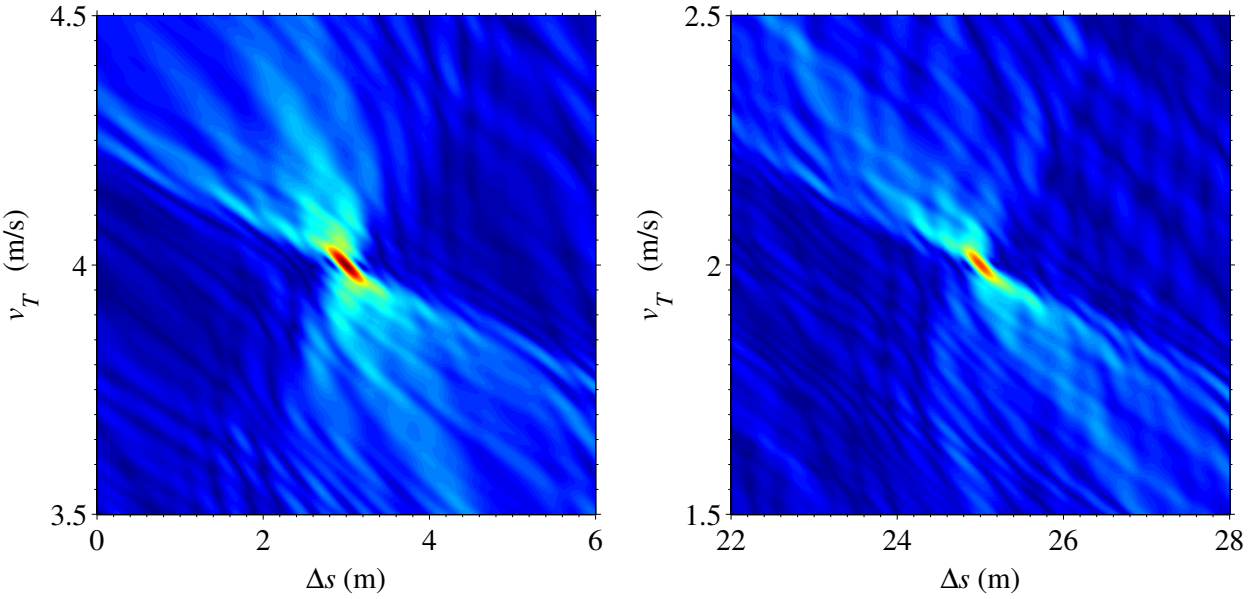

(a) Target 1, heading = 0° (N)

(b) Target 2, heading = 0° (N)

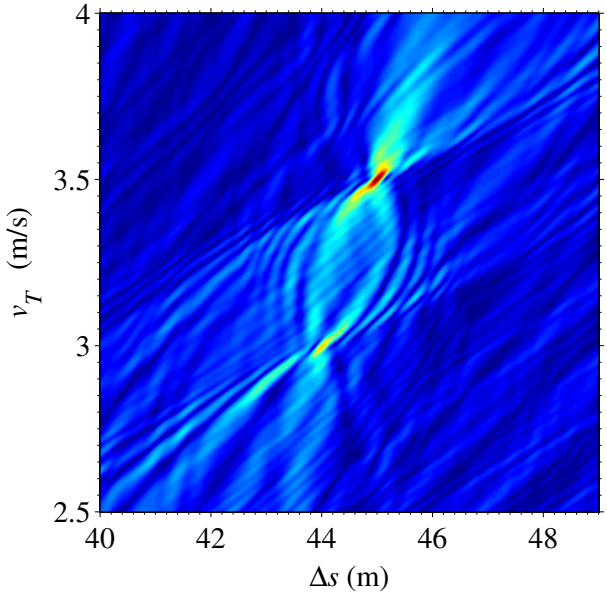

(c) Targets 3 and 4, heading = 180° (S)

Figure 6.19: GMTI close-up images for the four targets in Fig. 6.18 moving on a N-S oriented road. These images are formed using the SCS-GMTI method described in this chapter. In panel (c), targets 3 and 4 are the upper and lower GMTI images, respectively.

6.5 Erroneous GMTI Searches Without Proper Path Constraints

In this section I demonstrate the need for a correct path constraint when using this chapter's SCS-GMTI method of BPJ matched filtering. I demonstrate this need by showing what happens when the BPJ search path deviates from the correct path as determined by the actual roadway. I demonstrate the effects of two types of path deviations: heading errors, where the search path and the actual roadway intersect, but differ in direction by a few degrees; and parallel path errors, where the search heading is correct, but the search path is physically offset from the road by several meters.

I show the effects of each error type on two different road orientations: E-W (cross-track) and N-S (along-track). In each case, the GMTI target images blur out, defocus, and generally lose power compared to the correct search cases in Section 6.4, but these defocusing effects are much more sensitive to path errors when the road is oriented in the along-track direction. This result is consistent with the BPJ AFs as explained in Section 4.4 of Chapter 4. The BPJ AF images in that section indicate that accumulated pixel energy in BPJ drops off much more sharply and quickly when the motion mismatch is in the cross-track direction, and that pixel energy accumulation is more tolerant of along-track mismatches. This is also consistent with the way moving targets appear in stationary-focus BPJ images as discussed in Chapter 3. Pixels along or near a target's true path can still accumulate significant energy when the target motion is along-track to the SAR. But when the target moves cross-track to the SAR, virtually no energy appears along the target's true path in the image, and the target instead appears shifted elsewhere in azimuth. The error cases described in this section continue to support these pixel-energy-loss observations. In all the GMTI images that follow, I have pushed the search path error to the limit of target detectability.

Search Path Errors for a Cross-Track Oriented Road

Figures 6.20 and 6.21 respectively show search errors in heading and parallel path offset for the E-W road orientation, where the target motion is cross-track to the SAR. In this case, search errors are generally in the along-track direction. In Fig. 6.20, the GMTI target images smear out and lose cohesion, and for heading errors beyond about $\pm 10^{\circ}$, any discernible evidence of target presence is lost.

Interestingly however, in Fig. 6.21 where the search path is parallel but offset to the road, the GMTI target images migrate in the GMTI search space, but remain focused. This can easily cause high-confidence estimation errors for the target's GMTI solution. In simulation, this effect was observed for parallel search paths out to 30 meters on either side of the road before the GMTI target images migrated either to the edge of the GMTI search space or out of it completely. The GMTI target images did lose focus with more path offset error, but much more slowly than for any other search path error scenario I investigated for any other road orientation. The fact that the target images lost focus at all can be explained with Fig. 5.7. In that figure, a stationary target image can be produced by a cross-track moving target, but a *perfectly* focused stationary image alias is produced only by specific target tracks that are nearly, but not quite, oriented perpendicular to the SAR's flight path. In my research, the cross-track road orientation with a parallel path offset is the only search case that can tolerate significant error and still produce meaningful target detection, but false GMTI estimation.

It sometimes comes up in the course of writing a thesis or dissertation that the formatting does not satisfy department guidelines. Here, the word 'guidelines' is actually a gross misspelling of the words 'carved-in-stone rigidly inflexible requirements', quite unlike the Pirate's Code. When writing the thesis and relating the text to relevant figures, it is generally desirable to have them [text and related figures] close to each other in the thesis body. Sometimes, ensuring this proximity creates a gaping void of whitespace somewhere. Such whitespace provokes the wrath of the department, and results in having said thesis rejected until said whitespace has been filled somehow. Therefore, this paragraph exists solely to fill the lower half of this page so I can graduate and have a life again outside of my thesis. But in the interest of making this paragraph at least slightly useful, just for kicks please refer your attention to Fig. 3.1, which shows a rather striking photograph of a tracer round being fired from a military rifle. While great for visual wow-factor and training, it's probably not a good idea to use tracer rounds in actual combat. Because they work both ways. The enemy can see them too, and your tracers would do a most excellent job of revealing your position. When the enemy knows your position, it is generally bad for your health. There, you have now received potentially life-saving counsel. You may now continue learning the ways of SAR and GMTI in the following pages.

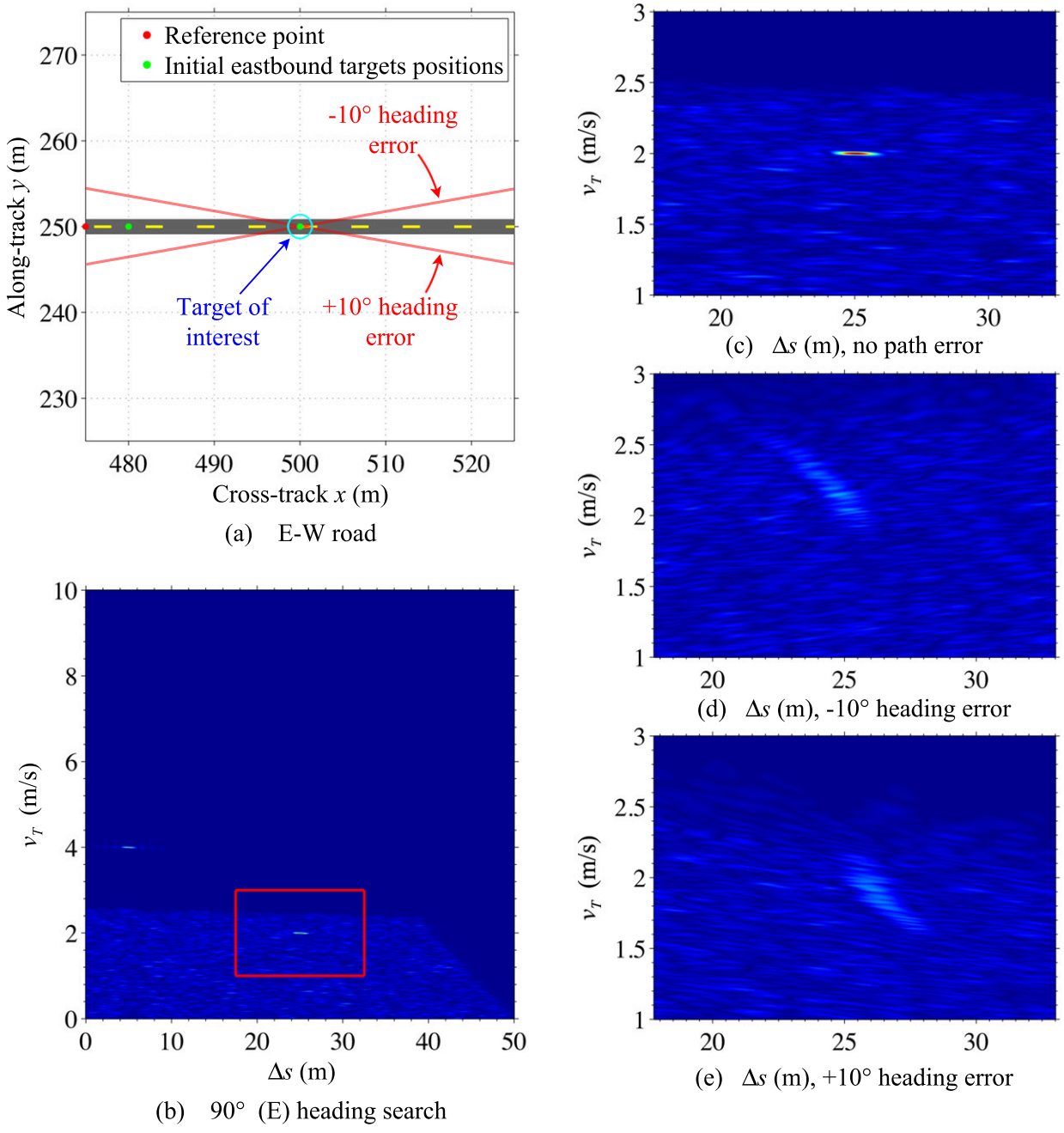

Figure 6.20: Search paths heading errors for an E-W (cross-track) oriented road. The SAR platform is left of the target scene, flying north (up) and looking to the right. Panel (a) shows the erroneous search paths in red, and the target of interest is in the blue circle at the center of the panel. Panel (b) shows the correctly-focused GMTI search space. The red box in panel (b) shows the GMTI search space in which the target of interest is imaged both with and without search path errors. Panel (c) shows the GMTI target solution correctly focused and estimated. Panels (d) and (e) show the deterioration of the target image as a result of searching the erroneous paths indicated in panel (a).

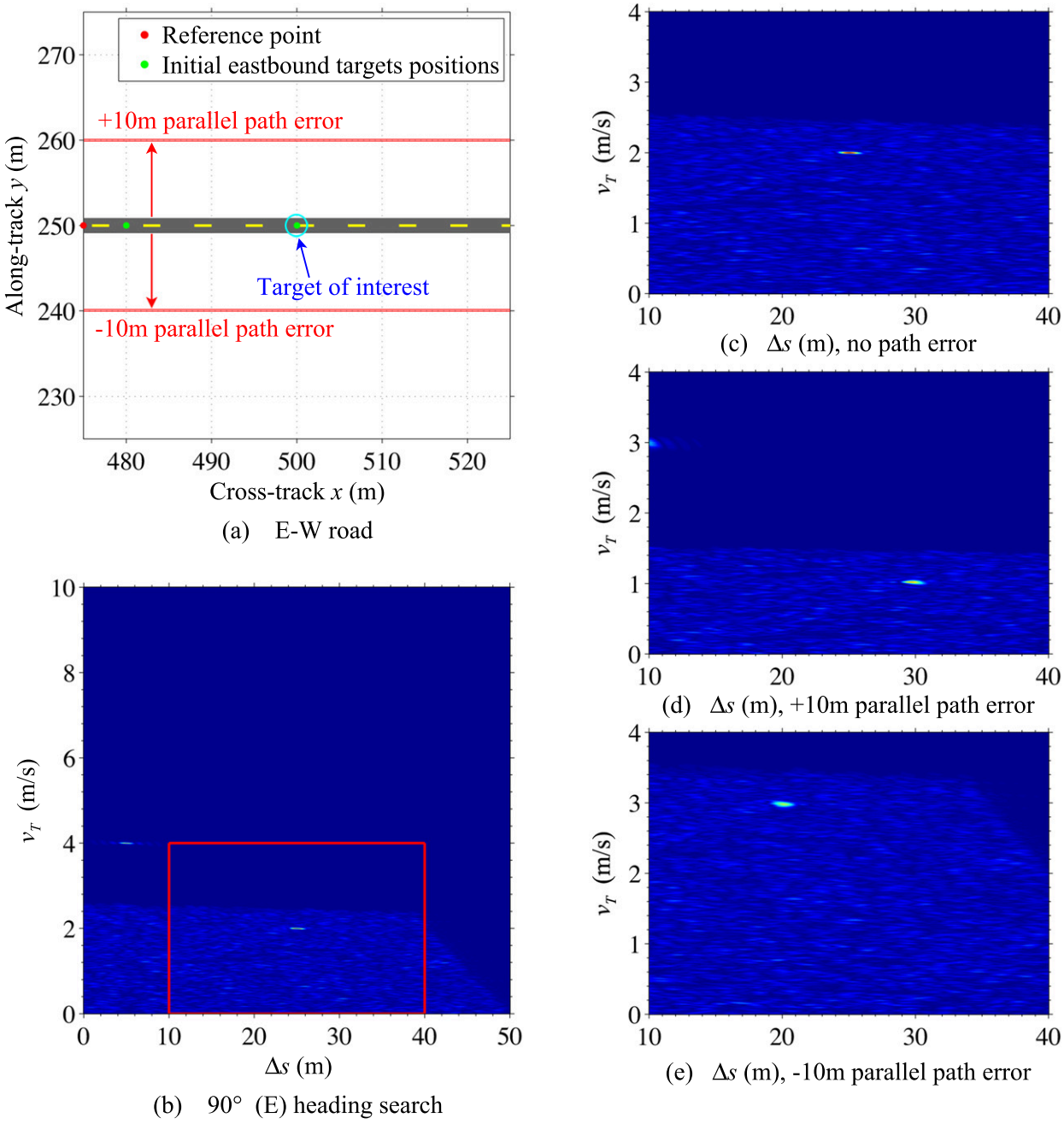

Figure 6.21: Parallel search path offset errors for an E-W (cross-track) oriented road. The SAR platform is left of the target scene, flying north (up) and looking to the right. Panel (a) shows the erroneous search paths in red, and the target of interest is in the blue circle at the center of the panel. Panel (b) shows the correctly-focused GMTI search space. The red box in panel (b) shows the GMTI search space in which the target of interest is imaged both with and without search path errors. Panel (c) shows the GMTI target solution correctly focused and estimated. Panels (d) and (e) show the migration of the target image as a result of searching the erroneous paths indicated in panel (a). This scenario can potentially lead to high-confidence false GMTI estimations.

Search Path Errors for an Along-Track Oriented Road

Figures 6.22 and 6.23 respectively show heading errors and parallel path offset errors for a N-S road, where target motion is along-track to the SAR, and search errors are generally in the cross-track direction from the correct search path. As these figures show, this scenario is much less tolerant of search errors before the GMTI process can no longer detect the target. While the E-W road orientation was able to maintain some semblance of target detection with heading errors out to roughly $\pm 10^{\circ}$, the N-S orientation's detectability interval is between about -4.5° and $+3^{\circ}$ to the road's true heading. And while the E-W road enabled clear target detection (and false estimation) for parallel search paths tens of meters off the actual roadway, the N-S road scenario loses all target detectability before a parallel search path has been offset by even one meter from the correct search path. Again, this is consistent with the behavior of the BPJ AF examples shown in Chapter 4.

Although this section demonstrates a few selected GMTI search-error scenarios, it should be understood that these error results cannot be generally applied to all SCS-GMTI error scenarios. There are several reasons for this: first, in cases where the search heading is in error, the deterioration of the GMTI target images versus heading error amount depends strongly on the target's initial position relative to the point where the askew search path intersects the roadway. Second, I only showed the cross-track and along-track road orientations. For intermediate road orientations, the GMTI target images exhibit a combination of the effects described in this section. Third, the simulated targets used for this research never moved faster than six meters per second, which is about 13 mph. Faster target speeds will produce different error effects and different detectability tolerances. The error effects in this section were shown strictly to give a qualitative general idea of search path error sensitivity, and how necessary it is to have a correct path constraint in place if SCS-GMTI is to have any hope of success. The only general conclusion I can draw about search path error effects is that if the target does not actually travel along the path being searched, a meaningful GMTI solution cannot be obtained for that target using a single-channel SAR.

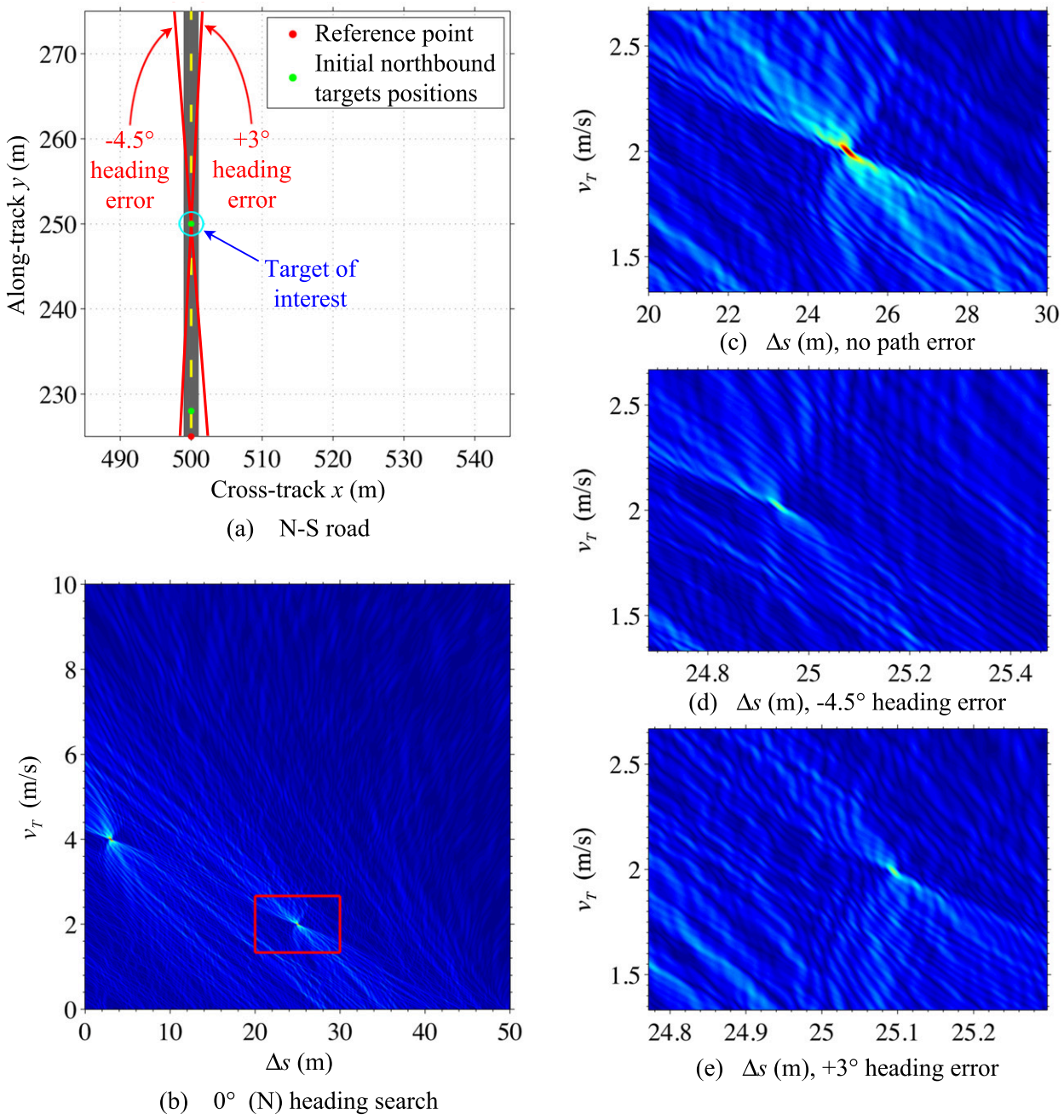

Figure 6.22: Search paths heading errors for a N-S (along-track) oriented road. The SAR is left of the target scene, flying north (up) and looking to the right. Panel (a) shows the erroneous search paths in red, and the target of interest is in the blue circle at the center of the panel. Panel (b) shows the correctly-focused GMTI search space. The red box in panel (b) shows the GMTI search space in which the target of interest is imaged both with and without search path errors. Panel (c) shows the GMTI target solution correctly focused and estimated. Panels (d) and (e) show the deterioration of the target image as a result of searching the erroneous paths indicated in panel (a). Note how much less error-tolerant this scenario is compared to that of heading errors for the cross-track oriented E-W road in Fig. 6.20.

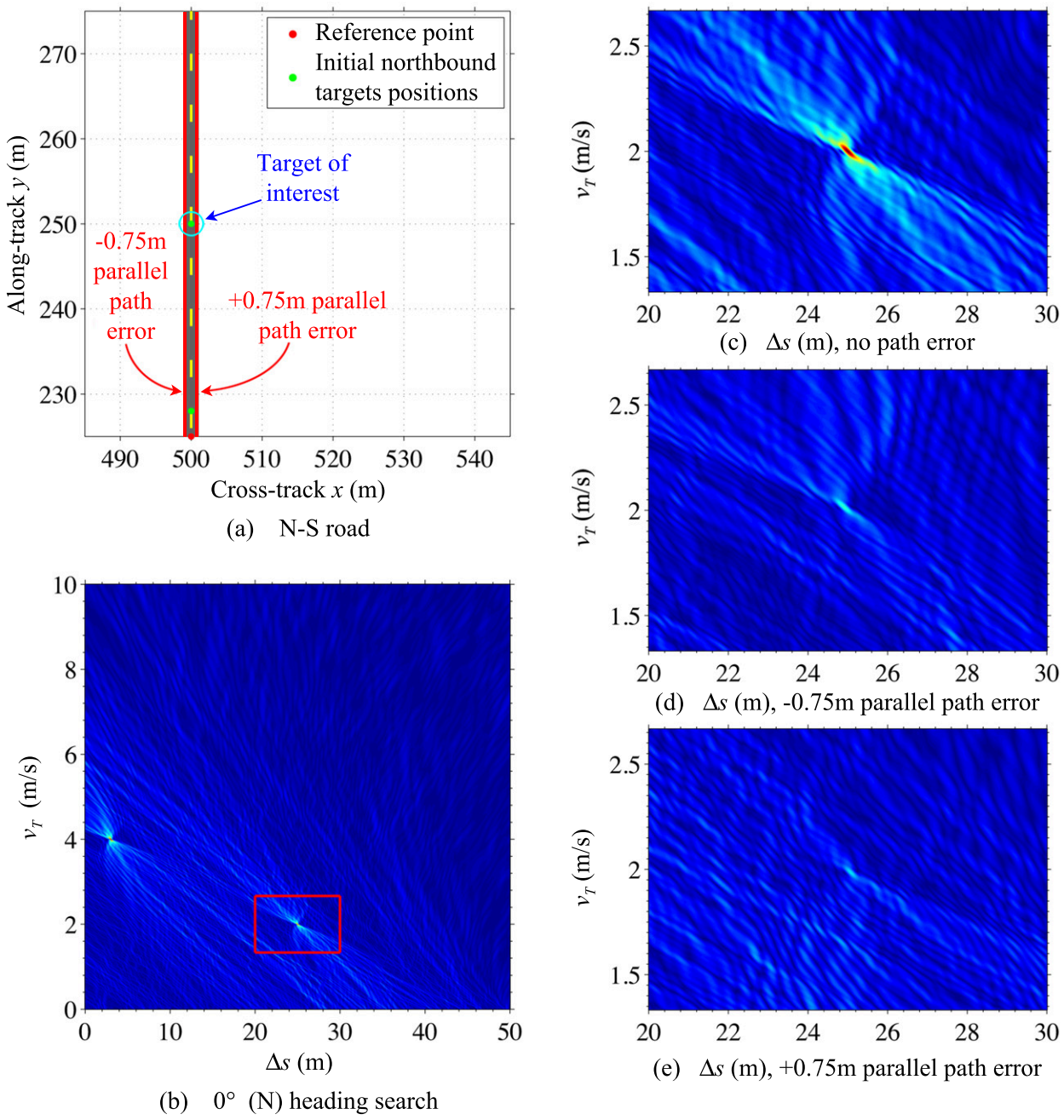

Figure 6.23: Parallel search path offset errors for a N-S (along-track) oriented road. The SAR is left of the target scene, flying north (up) and looking to the right. Panel (a) shows the erroneous search paths in red, and the target of interest is in the blue circle at the center of the panel. Panel (b) shows the correctly-focused GMTI search space. The red box in panel (b) shows the GMTI search space in which the target of interest is imaged both with and without search path errors. Panel (c) shows the GMTI target solution correctly focused and estimated. Panels (d) and (e) show the deterioration of the target image as a result of searching the erroneous paths indicated in panel (a). Note how much less error-tolerant this scenario is compared to that of parallel-path offset errors for the cross-track oriented E-W road in Fig. 6.21.

This chapter has demonstrated the theoretical feasibility of performing limited GMTI with a single-channel SAR. In my SCS-GMTI method, the road acts as a constraint. The BPJ matched-filter technique described in this section works only if the target(s) can be assumed to travel on the road being searched, and if the target is "well-behaved", meaning its speed and direction of travel do not change. If a target is not constrained to the road, my SCS-GMTI method is very unlikely to be of any practical use for correctly detecting the target and estimating its ground track. If the target is on the road, then my method *may* work. In theory and simulation, my method works because the technique of constraining the target's path to a straight road inherently satisfies the need to constrain the target's initial along-track y-position, as discussed at the end of Section 6.1. The road-constraint technique also provides useful constraints on the target's initial x-position and its heading. In a more abstract mathematical sense, if constrained to the target's correct path, the search space described in this section intersects the target's SAR GMTI solution space at only one point, which is the target's true GMTI solution for x_0, y_0, θ, and v_T.

I have also shown that when the path constraint does not match with the target's true path, the results are unpredictable. The target may defocus in the GMTI image, it may not be detectable at all, or it may have a solution space that intersects with the current road's GMTI search space, creating a false detection or estimation. This possibility is probably unavoidable due to the underlying math that makes the SCS-GMTI problem inherently underdetermined.

In conventional radar, an airborne or spaceborne target is detected with a surveillance radar before its position and velocity vector are estimated more precisely with a tracking radar. For SAR, however, Barbarossa [15] and Jao [13] make the point that moving target detection and parameter estimation are not separate operations. Also, Jao and Vu [81] both state that SAR GMTI can theoretically be performed by testing many different position/velocity solutions. By successfully performing these tasks simultaneously in simulation with my BPJ MF, this chapter provides theoretical support for these authors' statements.

CHAPTER 7. CONCLUSION

The desire exists to perform GMTI with a single-channel SAR. This thesis investigates the fundamental feasibility of doing so, and shows that a single-channel SAR is inherently ill-suited to performing general unconstrained GMTI. I show that the SCS-GMTI problem is underdetermined for the simplest GMTI scenario where both the SAR and the target are assumed to move rectilinearly with constant speeds. Under this assumption, I show that the range history between the SAR and a target is a hyperbolic function of time, whether the target is moving or stationary. I then show that this hyperbolic range history is the root source of the SCS-GMTI problem's underdetermined nature. This is because a GMTI solution has a dimensionality of four (x_0, y_0, θ, and v_T), while the hyperbolic range history is characterized by only three parameters (A, B, and C). This indicates, as proven in simulation, that there are infinitely many GMTI solutions that map to a given range history between the SAR and the target. Given only the range history, it is impossible to uniquely invert the problem to recover the target's true GMTI solution that produced the target's SAR signature in the range compressed data.

However, I show that when the problem is constrained by limiting the target's movement to a straight path, where the path's position and orientation are known, the problem becomes theoretically solvable. By constraining the target's path in this way, the target's initial position components (x_0, y_0) are coupled by the linear path, which reduces the problem's dimensionality from four to three. This dimensionality reduction conceptually enables the three-parameter hyperbolic range history to be uniquely inverted to identify the target's true GMTI solution, *if* the target can be constrained to a travel along a known straight path, with the target moving at a constant speed.

While this mathematical analysis is beneficial for illustrating the fundamentally underdetermined nature of the SCS-GMTI problem, the analysis may not be practical for use as a valid GMTI technique. It assumes the target's range history can be accurately determined from the RC data, which in practice would depend on clutter-free SAR data, and an isolated, prominent, undis-

torted range migration curve for the target in the RC data. The realities of SAR in practice do not typically allow for such ideal RC data. Because of this, even a path constraint is insufficient to find a target's GMTI solution from SAR RC data where the target's RMC is buried in clutter.

However, despite this inconvenience, I developed a method for performing limited SCS-GMTI that may work in practice if the right conditions are met. To satisfy the need to constrain the problem, I determined that if the SAR RC data is processed into a conventional BPJ image, and if straight roads are visible in the image, each road can serve as a linear path constraint. My SCS-GMTI method is based on a modified use of the backprojection image formation algorithm to search these linear paths. However, I do not claim that the target can or must be detected first before searching a road for it. But if moving targets *are* on the path and moving with constant speed, their existence may well be detectable, and their correct GMTI parameters estimated simultaneously with the detection by applying my GMTI method.

Conventional BPJ forms an image with a set of stationary pixels arranged on the ground in such a way that the final image product represents a map of the ground scene's σ^0. This σ^0 map can look nearly photographic, as if from the isometric perspective of a camera high above the ground looking straight down. A BPJ image is formed by sampling the RC data according to the range/phase history of each pixel in the image over the course of the SAR data collection. But there is nothing in the BPJ algorithm that requires the pixels to remain stationary during image formation. My GMTI technique involves applying the BPJ algorithm to a set of *moving* image pixels. These pixels move in such a way that for a given stretch of straight road, my technique amounts to using the SAR as a BPJ matched filter for moving targets on the road. In Chapter 6, I show that when the assumed target path is correct, this GMTI technique does produce correct target solution estimates.

In the process of developing a theoretical GMTI method for single-channel SAR, I also developed a new ambiguity function. In the radar literature, AFs are typically described in terms of single radar pulses, where the amplitude and frequency modulations on the pulse solely determine the mathematical nature of the resulting AF. The AF I developed is for BPJ, and takes advantage of the BPJ algorithm's flexibility in allowing for moving image pixels. My BPJ AF shows how a pixel accumulates energy during BPJ integration, which depends on how well the pixel matches

(or mismatches) the target's velocity vector and initial position. The flexible nature of BPJ makes my BPJ AF a suitable tool for performing a GMTI search along a linear road for moving targets.

However, there are some major differences between my BPJ AF and a single-pulse AF. A single-pulse AF is a 2-D surface plot, where each point on the surface is a prediction of the radar receiver's MF response to a certain Doppler shift and a certain time difference relative to the MF's peak output instant t_{MF}. The single-pulse AF predicts the result of a fast-time operation (matched filtering) in response to one radar pulse.

My BPJ AF, on the other hand, predicts a pixel's final image value, or how much energy the pixel accumulates over the course of an entire BPJ integration process for many pulses. Like a single-pulse AF, the BPJ AF is also a 2-D surface plot, but while computing the ambiguity surface for a single pulse requires $O(N^2)$ operations, the number of operations required to compute a BPJ ambiguity surface is $O(N^3)$. While the single-pulse AF predicts a fast-time MF output response, the BPJ AF predicts a slow-time BPJ pixel response. The BPJ AF depends not only on the pulse modulation parameters, but also on the relative positioning and velocity vectors between the target and each pixel in a set of moving pixels. The difference between the range history of a given moving pixel versus the target's true range history is the "range mismatch" history that determines the BPJ AF value for that pixel.

The BPJ AF is essentially the BPJ algorithm applied to a set of moving pixels that exhibit some type of mismatch relative to the target's true initial position and velocity vector. The pixel mismatches can be in relative position, relative velocity, or a combination of the two. A conventional BPJ image of a stationary, isolated point target in a sterile, clutter-free environment, focused on the stationary ground, can be interpreted as a BPJ AF in position mismatch. The BPJ AF examples given in Chapter 4 show the effects of velocity mismatches for moving pixels that pass through the target. The SCS-GMTI search results in Chapter 6 are BPJ AFs that use position *and* velocity mismatches to estimate the target's GMTI parameters.

Although my SCS-GMTI technique was formulated under the assumption that the SAR and the target both behave ideally, i.e., moving along straight lines with constant speeds, it turns out that for the BPJ MF search scheme I developed, it does not matter how the SAR moves. All that matters is that the target moves along the assumed path with a constant speed. The reason the SAR's motion is no longer required to be linear and unaccelerated is due to the nature of how BPJ

works. BPJ assumes an accurate motion record for the SAR's path through the sky. As long as this flight path and the precise timing of each pulse is known, the slant range between the SAR and every image pixel can be correctly computed for each pulse. This ultimately means that even though the SCS-GMTI problem is underdetermined, my constrained SCS-GMTI technique relaxes the need for a perfectly hyperbolic range history between the SAR and the target, which supports its possible implementation in practice.

However, my method depends on factors outside of the radar designer's control. Such factors include the target possibly changing speed or direction during the SAR data collection, and the possible existence of other moving targets on different nearby roads whose GMTI solutions intersect with the current road's BPJ MF search space. Such a scenario could produce false detections for the road being searched and/or false GMTI estimations. There may also be other complicating factors. For a moving target whose path cannot be constrained, the target might be visually detectable in the SAR image, but a reliable estimate of the target's GMTI solution is likely to be impossible. This is due to the ambiguous way moving targets shift and defocus in SAR imagery, which is tied to the underdetermined nature of the SCS-GMTI problem.

In conclusion, I have shown that it is theoretically possible to perform limited, constrained GMTI using a single-channel SAR based on direct energy returns from a moving target. However, general unconstrained GMTI, which is clearly far more useful, appears to be impossible for a single-channel SAR. This is because of single-channel SAR's inability to separate the target return from the clutter return on a pulse-by-pulse basis, and the need to constrain the target's path, the need for the target to be "well-behaved" from the perspective of the BPJ MF search scheme (i.e., no speed or direction changes), and the high probability for ambiguity or error in a target's GMTI estimation if the target does not actually follow the path being searched.

This thesis has investigated the fundamental question of whether or not GMTI can be feasibly done with a single-channel SAR based on direct energy reflections from moving point targets. I have developed a theoretical method that *might* work in practice if a somewhat restrictive set of conditions is met, but I have concluded that implementation in practice seems unlikely.

If further research into SCS-GMTI is conducted, possibilities for future work could include the following items:

- Perform experiments to determine if my GMTI technique has potential in practice
- Investigate the effects of noise and ground clutter, and determining a lower bound on SCR for my method to work
- Investigate the resolving limit of two targets close together in a GMTI search space for various road orientations
- Extend my GMTI technique to nonlinear target paths and target acceleration
- Automate the detection of straight roads in SAR imagery, possibly using some form of the Hough Transform

REFERENCES

[1] M. A. Richards, *Fundamentals of Radar Signal Processing*. New York, New York: McGraw-Hill, 2005. 1, 2, 4, 9, 13, 14, 15, 17, 18, 19, 23, 27, 40, 43, 44, 45, 84, 90, 95, 96, 97, 114, 144, 146

[2] M. A. Richards, J. A. Scheer, and W. A. Holm, Eds., *Principles of Modern Radar: Basic Principles*. Raleigh, NC: Scitech Publishing, Inc., 2010. 1, 2, 9, 13, 23, 25, 28, 45, 70, 84, 96, 114

[3] C. W. Sherwin, J. P. Ruina, and R. D. Rawcliffe, "Some early developments in synthetic aperture radar systems," *Military Electronics, IRE Transactions on*, vol. MIL-6, no. 2, pp. 111–115, Apr. 1962. 1, 9, 10, 11

[4] W. M. Brown and L. J. Porcello, "An introduction to synthetic-aperture radar," *Spectrum, IEEE*, vol. 6, no. 9, pp. 52–62, Sep. 1969. 1, 25

[5] K. Graf and H. Guthart, "Velocity effects in synthetic apertures," *Antennas and Propagation, IEEE Transactions on*, vol. 17, no. 5, pp. 541–546, Sep. 1969. 1

[6] L. J. Cutrona and G. O. Hall, "A comparison of techniques for achieving fine azimuth resolution," *Military Electronics, IRE Transactions on*, vol. MIL-6, no. 2, pp. 119–121, Apr. 1962. 1, 10

[7] W. M. Brown, "Synthetic aperture radar," *Aerospace and Electronic Systems, IEEE Transactions on*, vol. AES-3, no. 2, pp. 217–229, Mar. 1967. 1, 18, 25

[8] J. Munson, D.C. and R. Visentin, "A signal processing view of strip-mapping synthetic aperture radar," *Acoustics, Speech and Signal Processing, IEEE Transactions on*, vol. 37, no. 12, pp. 2131–2147, Dec. 1989. 1, 9, 45

[9] A. Currie, "Synthetic aperture radar," *Electronics Communication Engineering Journal*, vol. 3, no. 4, pp. 159–170, Aug. 1991. 1

[10] D. A. Ausherman, A. Kozma, J. L. Walker, H. M. Jones, and E. C. Poggio, "Developments in radar imaging," *Aerospace and Electronic Systems, IEEE Transactions on*, vol. AES-20, no. 4, pp. 363–400, July 1984. 1, 25, 45, 46

[11] R. Rau and J. McClellan, "Analytic models and postprocessing techniques for UWB SAR," *Aerospace and Electronic Systems, IEEE Transactions on*, vol. 36, no. 4, pp. 1058–1074, Oct. 2000. 1, 9, 25, 27, 114

[12] M. Fennell and R. Wishner, "Battlefield awareness via synergistic SAR and MTI exploitation," *Aerospace and Electronic Systems Magazine, IEEE*, vol. 13, no. 2, pp. 39–43, Feb. 1998. 2

[13] J. K. Jao, "Theory of synthetic aperture radar imaging of a moving target," *Geoscience and Remote Sensing, IEEE Transactions on*, vol. 39, no. 9, pp. 1984–1992, Sep. 2001. 2, 4, 50, 52, 53, 54, 59, 126, 139, 150, 170

[14] V. C. Chen and H. Ling, *Time-Frequency Transforms for Radar Imaging and Signal Analysis*. Boston, Massachusetts: Artech House Publishers, 2002. 4, 18, 45, 59, 80, 84, 126

[15] S. Barbarossa, "Detection and imaging of moving objects with synthetic aperture radar, part 1: Optimal detection and parameter estimation theory," *Radar and Signal Processing, IEE Proceedings F*, vol. 139, no. 1, pp. 79–88, Feb. 1992. 4, 18, 25, 45, 59, 126, 139, 170

[16] J. Moreira and W. Keydel, "A new MTI-SAR approach using the reflectivity displacement method," *Geoscience and Remote Sensing, IEEE Transactions on*, vol. 33, no. 5, pp. 1238–1244, Sep. 1995. 4, 59

[17] M. Soumekh, "Moving target detection in foliage using along track monopulse synthetic aperture radar imaging," *Image Processing, IEEE Transactions on*, vol. 6, no. 8, pp. 1148–1163, Aug. 1997. 4

[18] J. Entzminger, J.N., C. Fowler, and W. Kenneally, "JointSTARS and GMTI: past, present and future," *Aerospace and Electronic Systems, IEEE Transactions on*, vol. 35, no. 2, pp. 748–761, Apr. 1999. 4

[19] M. Soumekh, "Moving target detection and imaging using an X band along-track monopulse SAR," *Aerospace and Electronic Systems, IEEE Transactions on*, vol. 38, no. 1, pp. 315–333, Jan. 2002. 4

[20] J. Meyer-Hilberg, B. Bickert, and K.-P. Schmitt, "Results of flight tests of a two-channel radar system with real-time MTI processing," *Radar, Sonar and Navigation, IEE Proceedings* -, vol. 150, no. 1, pp. 23–27, Feb. 2003. 4, 126

[21] M. Pettersson, "Detection of moving targets in wideband SAR," *Aerospace and Electronic Systems, IEEE Transactions on*, vol. 40, no. 3, pp. 780–796, July 2004. 4, 9, 25, 71, 114, 119, 126

[22] G. Wang, X.-G. Xia, V. Chen, and R. Fielder, "Detection, location, and imaging of fast moving targets using multifrequency antenna array SAR," *Aerospace and Electronic Systems, IEEE Transactions on*, vol. 40, no. 1, pp. 345–355, Jan. 2004. 4

[23] A. Brenner and J. Ender, "Demonstration of advanced reconnaissance techniques with the airborne SAR/GMTI sensor PAMIR," *Radar, Sonar and Navigation, IEE Proceedings* -, vol. 153, no. 2, pp. 152–162, Apr. 2006. 4

[24] A. Damini, B. Balaji, G. Haslam, and M. Goulding, "X-band experimental airborne radar-Phase II: synthetic aperture radar and ground moving target indication," *Radar, Sonar and Navigation, IEE Proceedings* -, vol. 153, no. 2, pp. 144–151, Apr. 2006. 4

[25] B. Himed and M. Soumekh, "Synthetic aperture radar-moving target indicator processing of multi-channel airborne radar measurement data," *Radar, Sonar and Navigation, IEE Proceedings*, vol. 153, no. 6, pp. 532–543, Dec. 2006. 4

[26] A. Budillon, V. Pascazio, and G. Schirinzi, "Estimation of radial velocity of moving targets by along-track interferometric SAR systems," *Geoscience and Remote Sensing Letters, IEEE*, vol. 5, no. 3, pp. 349–353, July 2008. 4

[27] E. Chapin and C. Chen, "Along-track interferometry for ground moving target indication," *Aerospace and Electronic Systems Magazine, IEEE*, vol. 23, no. 6, pp. 19–24, June 2008. 4

[28] D. Cerutti-Maori, J. Klare, A. Brenner, and J. Ender, "Wide-area traffic monitoring with the SAR/GMTI system PAMIR," *Geoscience and Remote Sensing, IEEE Transactions on*, vol. 46, no. 10, pp. 3019–3030, Oct. 2008. 4, 126

[29] L. Yang, T. Wang, and Z. Bao, "Ground moving target indication using an InSAR system with a hybrid baseline," *Geoscience and Remote Sensing Letters, IEEE*, vol. 5, no. 3, pp. 373–377, July 2008. 4

[30] X. Lv, M. Xing, Y. Wu, and S. Zhang, "Azimuth-invariant bistatic multichannel synthetic aperture radar for moving target detection and location," *Radar, Sonar Navigation, IET*, vol. 3, no. 5, pp. 461–473, Oct. 2009. 4

[31] D. Cerutti-Maori, C. Gierull, and J. Ender, "Experimental verification of SAR-GMTI improvement through antenna switching," *Geoscience and Remote Sensing, IEEE Transactions on*, vol. 48, no. 4, pp. 2066–2075, Apr. 2010. 4

[32] X. Lv, M. Xing, Z. Bao, S. Zhang, and Y. Wu, "Coherence improving algorithm for airborne multichannel SAR-GMTI," *Radar, Sonar Navigation, IET*, vol. 4, no. 3, pp. 336–347, June 2010. 4

[33] V. T. Vu, T. Sjogren, M. Pettersson, A. Gustavsson, and L. Ulander, "Detection of moving targets by focusing in UWB SAR-theory and experimental results," *Geoscience and Remote Sensing, IEEE Transactions on*, vol. 48, no. 10, pp. 3799–3815, Oct. 2010. 4, 57, 58, 73, 74, 75, 76

[34] C. Gierull, "Analysis of the multimode feedhorn concept for multichannel SAR-GMTI," *Geoscience and Remote Sensing, IEEE Transactions on*, vol. 49, no. 10, pp. 3611–3621, Oct. 2011. 4

[35] B. Guo, D. Vu, L. Xu, M. Xue, and J. Li, "Ground moving target indication via multichannel airborne SAR," *Geoscience and Remote Sensing, IEEE Transactions on*, vol. 49, no. 10, pp. 3753–3764, Oct. 2011. 4

[36] J. Qian, X. Lv, M. Xing, L. Li, and Z. Bao, "Motion parameter estimation of multiple ground fast-moving targets with a three-channel synthetic aperture radar," *Radar, Sonar Navigation, IET*, vol. 5, no. 5, pp. 582–592, June 2011. 4

[37] S. Zhu, G. Liao, Y. Qu, Z. Zhou, and X. Liu, "Ground moving targets imaging algorithm for synthetic aperture radar," *Geoscience and Remote Sensing, IEEE Transactions on*, vol. 49, no. 1, pp. 462–477, Jan. 2011. 4, 126

[38] A. Budillon, A. Evangelista, and G. Schirinzi, "GLRT detection of moving targets via multibaseline along-track interferometric SAR systems," *Geoscience and Remote Sensing Letters, IEEE*, vol. 9, no. 3, pp. 348–352, May 2012. 4

[39] P. Guccione, A. Monti-Guarnieri, and S. Tebaldini, "Stable target detection and coherence estimation in interferometric SAR stacks," *Geoscience and Remote Sensing, IEEE Transactions on*, vol. PP, no. 99, pp. 1–8, 2012. 4

[40] J. Xu, Y. Zuo, B. Xia, X. Xia, Y. Peng, and Y. Wang, "Ground moving target signal analysis in complex image domain for multichannel SAR," *Geoscience and Remote Sensing, IEEE Transactions on*, vol. 50, no. 2, pp. 538–552, Feb. 2012. 4

[41] D. Cerutti-Maori, I. Sikaneta, and C. H. Gierull, "Optimum SAR/GMTI processing and its application to the radar satellite RADARSAT-2 for traffic monitoring," *Geoscience and Remote Sensing, IEEE Transactions on*, vol. 50, no. 10, pp. 3868–3881, 2012. 4

[42] C. Wiley, "Synthetic aperture radars," *Aerospace and Electronic Systems, IEEE Transactions on*, vol. AES-21, no. 3, pp. 440–443, May 1985. 9, 25, 46

[43] F. T. Ulaby, R. K. Moore, and A. F. Kung, *Microwave Remote Sensing: Active and Passive*. Norwood, Massachusettes: Artech House, Inc., 1981. 9, 11, 25, 27, 43, 84

[44] R. Chapman, C. Hawes, and M. Nord, "Target motion ambiguities in single-aperture synthetic aperture radar," *Aerospace and Electronic Systems, IEEE Transactions on*, vol. 46, no. 1, pp. 459–468, Jan. 2010. 9, 114, 119, 127, 139

[45] J. Goldstein, M. Picciolo, M. Rangaswamy, and J. Griesbach, "Detection of dismounts using synthetic aperture radar," in *Radar Conference, 2010 IEEE*, May 2010, pp. 209–214. 9, 71

[46] F. T. Ulaby and D. G. Long, Eds., *Microwave Remote Sensing: Modern Edition (in press)*. Norwood, Massachusettes: Artech House, Inc., 2013. 9, 28

[47] C. A. Wiley, "Pulsed Doppler Radar Methods and Apparatus," US Patent US 3,196,436, July 20, 1965. [Online]. Available: http://www.google.com/patents/US3196436, 11

[48] J. Peyton Z. Peebles, *Radar Principles*. New York, New York: John Wiley & Sons, Inc., 1998. 13, 80, 83, 84

[49] W. Wirth, "High resolution in azimuth for radar targets moving on a straight line," *Aerospace and Electronic Systems, IEEE Transactions on*, vol. AES-16, no. 1, pp. 101–104, Jan. 1980. 25

[50] S. Werness, W. Carrara, L. Joyce, and D. Franczak, "Moving target imaging algorithm for SAR data," *Aerospace and Electronic Systems, IEEE Transactions on*, vol. 26, no. 1, pp. 57–67, Jan. 1990. 25

[51] H. Yang and M. Soumekh, "Blind-velocity SAR/ISAR imaging of a moving target in a stationary background," *Image Processing, IEEE Transactions on*, vol. 2, no. 1, pp. 80–95, Jan. 1993. 25

[52] L. Ulander, H. Hellsten, and G. Stenstrom, "Synthetic-aperture radar processing using fast factorized back-projection," *Aerospace and Electronic Systems, IEEE Transactions on*, vol. 39, no. 3, pp. 760–776, July 2003. 25, 28, 29, 114

[53] M. Albuquerque, P. Prats, and R. Scheiber, "Applications of time-domain back-projection SAR processing in the airborne case," *Synthetic Aperture Radar (EUSAR), 2008 7th European Conference on*, pp. 1–4, June 2008. 25, 28, 29

[54] O. Frey, C. Magnard, M. Ruegg, and E. Meier, "Focusing of airborne synthetic aperture radar data from highly nonlinear flight tracks," *Geoscience and Remote Sensing, IEEE Transactions on*, vol. 47, no. 6, pp. 1844–1858, June 2009. 25, 28, 29, 46, 47, 48, 70

[55] A. Yegulalp, "Fast backprojection algorithm for synthetic aperture radar," in *Radar Conference, 1999. The Record of the 1999 IEEE*, 1999, pp. 60–65. 25, 26, 28, 29

[56] G. Zeoli, "The effect of constant velocity error on SAR focus," *Aerospace and Electronic Systems, IEEE Transactions on*, vol. AES-22, no. 5, pp. 657–659, Sep. 1986. 25

[57] E. C. Zaugg, "Generalized Image Formation for Pulsed and LFM-CW Synthetic Aperture Radar," Ph.D. dissertation, Brigham Young University, April 2010. 28

[58] A. Ellis, "The processing of synthetic aperture radar signals," *Radio and Electronic Engineer*, vol. 53, no. 3, pp. 107–114, Mar. 1983. 44, 46

[59] M. Sack, M. Ito, and I. Cumming, "Application of efficient linear FM matched filtering algorithms to synthetic aperture radar processing," *Communications, Radar and Signal Processing, IEE Proceedings F*, vol. 132, no. 1, pp. 45–57, Feb. 1985. 45

[60] E. Banta, "Limitations on SAR image area due to motion through resolution cells," *Aerospace and Electronic Systems, IEEE Transactions on*, vol. AES-22, no. 6, pp. 799–803, Nov. 1986. 45

[61] J. Kirk, "A discussion of digital processing in synthetic aperture radar," *Aerospace and Electronic Systems, IEEE Transactions on*, vol. AES-11, no. 3, pp. 326–337, May 1975. 46

[62] R. Wu and J. Li, "Autofocus and super-resolution synthetic aperture radar image formation," *Radar, Sonar and Navigation, IEE Proceedings*, vol. 147, no. 5, pp. 217–223, Oct. 2000. 46

[63] K. Liu, "Aircraft on-board SAR processing using a frequency-domain fast correlation technique," in *Radar Conference, 1988., Proceedings of the 1988 IEEE National*, Apr. 1988, pp. 165–170. 46

[64] C. Oliver, "Towards perfect SAR imagery," in *Synthetic Aperture Radar, IEE Colloquium on*, Nov. 1989, pp. 4/1–4/4. 46

[65] R. Goodman, S. Tummala, and W. Carrara, "Issues in ultra-wideband, widebeam SAR image formation," in *Radar Conference, 1995., Record of the IEEE 1995 International*, May 1995, pp. 479–485. 46

[66] E. Yadin, "Modern synthetic aperture radar systems," in *Electrical and Electronics Engineers in Israel, 2002. The 22nd Convention of*, Dec. 2002, pp. 333–335. 46

[67] W. Carrara, R. Goodman, and M. Ricoy, "New algorithms for widefield SAR image formation," in *Radar Conference, 2004. Proceedings of the IEEE*, Apr. 2004, pp. 38–43. 46

[68] M. Kirscht, "Detection and imaging of arbitrarily moving targets with single-channel SAR," *Radar, Sonar and Navigation, IEE Proceedings* -, vol. 150, no. 1, pp. 7–11, Feb. 2003. 52, 59

[69] H. Chen and C. McGillem, "Target motion compensation by spectrum shifting in synthetic aperture radar," *Aerospace and Electronic Systems, IEEE Transactions on*, vol. 28, no. 3, pp. 895–901, July 1992. 52, 59, 61

[70] T. Sparr, "Moving target motion estimation and focusing in SAR images," in *Radar Conference, 2005 IEEE International*, May 2005, pp. 290–294. 56, 126, 139

[71] R. Raney, "Synthetic aperture imaging radar and moving targets," *Aerospace and Electronic Systems, IEEE Transactions on*, vol. AES-7, no. 3, pp. 499–505, May 1971. 59

[72] H. Chen and C. McGillem, "Target motion compensation in synthetic aperture radar," *Aerospace and Electronic Systems Magazine, IEEE*, vol. 6, no. 2, pp. 14–18, Feb. 1991. 59

[73] K. Ouchi, "On the multilook images of moving targets by synthetic aperture radars," *Antennas and Propagation, IEEE Transactions on*, vol. 33, no. 8, pp. 823–827, Aug. 1985. 61

[74] H. Griffiths, "Developments in modern synthetic aperture radar," in *Sensor Array and Multichannel Processing, 2006. Fourth IEEE Workshop on*, July 2006, pp. 0/38–0/113. 68, 69

[75] G. Li, X. Xia, J. Xu, and Y. Peng, "A velocity estimation algorithm of moving targets using single antenna SAR," *Aerospace and Electronic Systems, IEEE Transactions on*, vol. 45, no. 3, pp. 1052–1062, July 2009. 119

[76] T. K. Moon and W. C. Stirling, *Mathematical Methods and Algorithms for Signal Processing*. Upper Saddle River, New Jersey: Prentice-Hall, Inc., 2000. 122

[77] J. Dias and P. Marques, "Multiple moving target detection and trajectory estimation using a single SAR sensor," *Aerospace and Electronic Systems, IEEE Transactions on*, vol. 39, no. 2, pp. 604–624, Apr. 2003. 126, 139

[78] R. Perry, R. DiPietro, and R. Fante, "SAR imaging of moving targets," *Aerospace and Electronic Systems, IEEE Transactions on*, vol. 35, no. 1, pp. 188–200, Jan. 1999. 126

[79] J. Fienup, "Detecting moving targets in SAR imagery by focusing," *Aerospace and Electronic Systems, IEEE Transactions on*, vol. 37, no. 3, pp. 794–809, July 2001. 126

[80] M. Sullivan, *College Algebra*, 7th ed. Upper Saddle River, New Jersey: Prentice-Hall, Inc., 2005. 135

[81] V. Vu, T. Sjö Andgren, M. Pettersson, and P. Marques, "Application of the moving target detection by focusing technique in civil traffic monitoring," in *Geoscience and Remote Sensing Symposium (IGARSS), 2010 IEEE International*, July 2010, pp. 4118–4121. 139, 170

[82] P. Marques, “SAR-MTI improvement using a-priori knowledge of the road network,” in *Radar Conference (EuRAD), 2010 European*, Sep.-Oct. 2010, pp. 244–247. 139